

The Al-Pt-Ru ternary phase diagram

Sara Natalia Prins

Submitted in partial fulfilment of the requirements for the degree Master of Science in the Faculty of Engineering, Built Environment and Information Technology, University of Pretoria

1 April 2003



Declaration

I declare that this dissertation is my own work. It is being submitted for the degree of Masters of Science in the Faculty of Engineering, Build Environment and Information Technology, University of Pretoria, South Africa. It has not been submitted before for any degree or examination at any other University.

A handwritten signature in black ink, appearing to be 'Sara Natalia Prins'.

Sara Natalia Prins
1 April 2004



Table of Contents

Chapter 1	Introduction	1
1.1	Introduction	1
1.2	Background	1
1.3	Motivation	3
Chapter 2	Literature Review – The Phase Diagrams	8
2.1	The Elements: Al, Pt and Ru	8
2.2	The Al-Pt Binary System	
2.2.1	Phase Diagram Data	9
2.2.2	Thermodynamic Data	14
2.3	The Al-Ru Binary System	15
2.2.1	Phase Diagram Data	15
2.2.2	Thermodynamic Data	19
2.2.3	Applications of Al-Ru Intermetallics	20
2.3	The Pt-Ru system	21
2.4	The Al-Pt-Ru Ternary System	22
Chapter 3	Experimental Investigation	23
3.1	Introduction	23
3.2	Sample Preparation	23
3.3	Analyses	24
3.3.1	Scanning Electron Microscopy and Energy Dispersive X-Ray Analysis	24
3.3.2	X-Ray Diffraction	25
3.4	Methodology to Determine a Solidification Sequence for a Ternary Alloy	27
3.4.1	Analyses of As-Cast Alloys	27
3.4.2	Fundamental and theoretical considerations	28
3.4.2.1	Phase diagram considerations	28
3.4.2.2	Liquid-solid interactions and transformations	30
3.4.2.3	Deriving the solidification sequence and liquidus surface projection	32
3.5	Syntax and Terminology	34
Chapter 4	Experimental Results and Discussion	35
4.1	Introduction	35
4.2	Microstructures and proposed solidification sequences	36
4.2.1	PAR 1 - Al ₈₆ :Pt ₇ :Ru ₇ alloy	36
4.2.2	PAR 2 - Al ₆₆ :Pt ₂₆ :Ru ₆ alloy	39
4.2.3	PAR 3 - Al ₅₇ :Pt ₁₂ :Ru ₃₁ alloy	41
4.2.4	PAR4 - Al ₅₄ :Pt ₃₈ :Ru ₈ alloy	43

4.2.5	PAR5 - Al ₅₀ :Pt ₂₅ :Ru ₂₅ alloy	45
4.2.6	PAR6 - Al ₂₅ :Pt ₅₅ :Ru ₂₀ alloy	46
4.2.7	PAR7 - Al ₇₃ :Pt ₂₂ :Ru ₅ alloy	49
4.2.8	PAR 8 – Al ₇₁ :Pt ₇ :Ru ₂₂ alloy	50
4.2.9	PAR 9 - Al ₅₉ :Pt ₃₃ :Ru ₈ alloy	52
4.2.10	PAR10 - Al ₃₄ :Pt ₄₆ :Ru ₂₆ alloy	54
4.2.11	PAR 11 - Al ₄₂ :Pt ₅₂ :6 alloy	56
4.2.12	PAR 12 - Al ₃₃ :Pt ₅₉ :Ru ₈ alloy	58
4.2.13	The PAR 13- Al ₈₅ :Pt ₁₀ :Ru ₅ alloy	59
4.2.14	The PAR14- Al ₆₆ :Pt ₁₃ :Ru ₂₁ alloy	61
4.2.15	The PAR 15- Al ₄₇ :Pt ₅₁ :Ru ₂ alloy	63
4.2.16	The PAR 16- Al ₇₄ :Pt ₈ :Ru ₁₈ alloy	65
4.3	XRD results	67
4.4	Solidification projection.	72
4.4.1	Liquidus surface projection	73
4.4.2	Solidification reaction sequence	75
4.5	Conclusions	76
Chapter 5 The CALPHAD Method		77
5.1	Introduction	77
5.2	History	77
5.3	Current Status	79
5.4	CALPHAD Methodology	80
5.5	CALPHAD Thermodynamics	84
5.5.1	Some basic principles	84
5.5.2	Thermodynamics of Pure Elements	84
5.5.3	Thermodynamics of solutions	85
5.5.3.1	Substitutional Solutions	86
5.5.3.2	Sublattice Model / Compound Energy Formalism	87
5.5.3.2.1	CEF applied to B2/A2 order/disorder transformation	90
5.5.3.2.2	CEF applied to fcc ordering	91
5.6	CALPHAD Optimisations	93
5.7	Prediction of higher order systems	94
5.8	Conclusions	95
Chapter 6 The Assessments – Results and Discussion		95
6.1	The Models	95
6.2	Some basic concepts	97
6.3	Assessment procedures	
6.3.1	Al-Ru	98
6.3.2	Al-Pt	100
6.3.3	Al-Pt-Ru	101
6.4	Results and discussion	
6.4.1	Al-Ru	102



6.4.2	Al-Pt	107
6.4.3	Al-Pt-Ru	115
6.5	Conclusions	119
Chapter 7 Comparison Experimental and Calculated		120
7.1	Introduction	120
7.2	Results and Discussion	120
7.3	Conclusions	124
Conclusions and Recommendations		125
References		127
<u>Appendices</u>		
Appendix A Papers and Presentations		
Appendix B XRD refinement example		
Appendix C Al-Pt-Ru Database (SGTE format)		
Appendix D Thermo-Calc Binary and ternary TDB and POP files (on CD)		
Appendix E XRD spectra in .wmf format (on CD)		

List of Figures

Figure 2.1. The Al-Pt phase diagram after [1990Mas].	10
Figure 2.2. Revised Pt-rich portion of the Al-Pt phase diagram [1987Oya].	13
Figure 2.3. The calculated Al-Pt phase diagram by Wu and Jin [2000Wu].	14
Figure 2.4. The Al-Ru phase diagram after Massalski [1990Mas].	16
Figure 2.5. The modified Al-Ru phase diagram after Boniface and Cornish [1996Bon2].	16
Figure 2.6. The phase diagram of Anlage et al. [1988Anl] for the high-Al corner in the Al-Ru system.	18
Figure 2.7. The Pt-Ru phase diagram [1990Mas].	21
Figure 2.8. Calculated Pt-Ru phase diagram, from Spencer [1996Spe].	22
Figure 2.9. Isothermal section of the Al-Pt-Ru system at 1350°C [2001Big2].	22
Figure 3.1. Ternary plot showing the EDS phase analyses. The square indicates the overall composition, the triangles the phase analysis and the solid circle indicates a two-phase area.	27
Figure 3.2. Ternary invariant reactions, after West [1965Wes]	27
Figure 3.3. Phase diagram of two components showing the influence of solute diffusion on solidification, a phenomenon called coring [1990Tom]	31
Figure 3.4. Sample PAR14 on the liquidus surface.	33
Figure 4.1. Overall compositions of the Al-Pt-Ru alloys studied.	35
Figure 4.2. (a) and (b) show the two distinct different microstructure areas observed in the PAR1 alloy. (c) shows the detail of the finer (darker) microstructure and (d) shows the detail of the lighter, coarser microstructure area.	37
Figure 4.3. A ternary plot of the overall and phase compositions in the PAR 1 alloy.	38
Figure 4.4. (a) shows the dendrite structure of PAR 2 and (b) shows the remnants of primary T in the light PtAl ₂ dendrites.	40
Figure 4.5. A ternary plot of the overall and phase compositions in the PAR 2 alloy.	40
Figure 4.6. BSE images of PAR 3. (a) shows the overall microstructure. (b) shows the X phase as well as the two areas where Ru ₂ Al ₃ and T decomposed.	41
Figure 4.7 A ternary plot of the overall and phase compositions in the PAR 3 alloy.	42
Figure 4.8. BSE images of PAR 4. (a) shows dark primary ~RuAl dendrites, coated by a PtAl layer (the light phase) in a Pt ₂ Al ₃ matrix. (b) shows the detail of the PtAl coating layer.	43
Figure 4.9. A ternary plot of the overall and phase compositions in the PAR 4 alloy.	44
Figure 4.10. BSE image on the right showing dark ~RuAl dendrites in a light two-phase matrix. The light matrix consists of PtAl and Pt ₃ Al ₃ , which is the very light phase.	45
Figure 4.11. A ternary plot of the overall and phase compositions in the PAR 5 alloy.	46
Figure 4.12. (a) The BSE image of PAR 6. (a) shows the long dark (Ru) needles in the light ~Pt ₃ Al matrix, with a finer dark phase present between the long needles. (b) shows that the fine (Pt) blob-like phase, and the finer (Ru) needles which formed in the ternary eutectic.	47
Figure 4.13. A ternary plot of the overall and phase compositions in the PAR 6 alloy.	48

Figure 4.14. The BSE images of PAR 7. (a) shows white PtAl ₂ dendrites in a darker X matrix. (b) shows precipitates of X in the PtAl ₂ dendrites.	49
Figure 4.15. A ternary plot of the overall and phase compositions in the PAR 7 alloy.	50
Figure 4.16. BSE images of PAR 8. (a) shows dark ~RuAl dendrites in a medium grey X phase. A very light phase ~PtAl ₂ is present in the medium grey phase. (b) shows the microstructure in more detail.	51
Figure 4.17. A ternary plot of the overall and phase compositions in the PAR 8 alloy.	51
Figure 4.18. BSE microstructure of PAR 9. (a) shows the dendritic structure. (b) shows the coring of the dark grey ~RuAl phase.	53
Figure 4.19. A ternary plot of the overall and phase compositions in the PAR 9 alloy.	53
Figure 4.20. BSE images of PAR10. (a) shows the 'feather-like' dendrite solidification structure, with some areas which appear 'cloudy'. In the close up, (b), the dark (Ru) needles, coated by a medium phase, ~RuAl in a light (Pt ₅ Al ₃ + PtAl) matrix. Between the dendrites, a fine eutectic structure is visible.	54
Figure 4.21 A ternary plot of the overall and phase compositions in the PAR 10 alloy.	54
Figure 4.22. BSE images of PAR 11. (a) shows the dendritic structure of the alloy. (b) clearly shows the presence of a fine phase in the dark dendrite phase as well as the area surrounding the dark dendrite.	56
Figure 4.23. A ternary plot of the overall and phase compositions in the PAR 11 alloy.	57
Figure 4.24. BSE images of PAR 12. (a) shows long thin and small fine (Ru) needles in a light Pt ₃ Al matrix. (b) shows the microstructure at a higher magnification.	58
Figure 4.25. A ternary plot of the overall and phase compositions in the PAR 12 alloy.	59
Figure 4.26. BSE images of PAR 13. (a) and (b) show the general microstructure. In (c) the ternary eutectic structure between the primary X dendrites can be seen. (d) shows the presence of another phase (lighter than dendrites) on the edges of the X dendrites.	60
Figure 4.27 A ternary plot of the overall and phase compositions in the PAR 13 alloy.	61
Figure 4.28. BSE images of PAR 14. (a) shows the dark RuAl ₂ dendrites surrounded by a medium X phase in a light ~PtAl ₂ matrix. (b) shows a higher magnification of the microstructure.	62
Figure 4.29. A ternary plot of the overall and phase compositions in the PAR 14 alloy.	62
Figure 4.30. (a) shows the overall microstructure of PAR 15. (b) shows the 'island'-like structure. (c) shows the solid state decomposition of a primary b grain while (d) shows the difference in decomposition microstructures.	63
Figure 4.31. A ternary plot of the overall and phase compositions in the PAR 15 alloy.	64
Figure 4.32. Schematic development of the solidification microstructure of the PAR15 alloy.	65
Figure 4.33. (a) shows the overall microstructure of PAR 16. (b) shows the medium primary RuAl ₂ dendrites coated by the black Ru ₄ Al ₁₃ phase. Small, very light areas of PtAl ₂ can be seen in the cored X phase.	65
Figure 4.34. A ternary plot of the overall and phase compositions in the PAR 16 alloy.	66
Figure 4.35. Summary of results for ternary Al-Pt-Ru alloys (square = overall composition, triangle = phase composition).	72



Figure 4.36. Proposed experimental liquidus surface projection.	74
Figure 4.37. Overall alloy compositions on the liquidus surface projection.	74
Figure 4.38. Experimental liquidus surface projection for the Al-Pt-Ru system, showing the solidification reactions.	75
Figure 5.1. Flowchart of the CALPHAD method, adapted from [2001Kum].	81
Figure 5.2. Phase diagram showing regions where only composition can be reliably measured at a given temperature and vice versa [2001Kum].	82
Figure 5.3. Composition space and reference energy surface for $(A,B)_1(C,D)_1$ [1998Sau].	87
Figure 5.4. Schematic crystallographic structure of the A2 and B2 phases. (a) A2, the disordered structure, where all the sites are equivalent. (b) B2, the ordered structure where the occupation of the site in the centre of the cube is different to the one on the corner.	89
Figure 5.5. The face-centred cubic (fcc) structure. The numbers indicate the four sublattices for ordering.	91
Figure 5.6. Extrapolation to higher order systems [1997Kat].	93
Figure 6.1. The calculated Al-Ru phase diagram showing B2 calculated using the SL (—) and MSL (---) models.	104
Figure 6.2. Comparison between the calculated Al-Ru phase diagram and experimental data	104
Figure 6.3. Phase diagram of temperature against chemical potential of Al.	106
Figure 6.4. Comparison of calculated enthalpy of formation for the SL (—) and MSL (---) RuAl-B2 models with experimental results [1992Jun] and ab initio [1992Lin, 1998Wol, 1999Man, 2002Gar] predictions.	106
Figure 6.5. The calculated Al-Pt phase diagram.	110
Figure 6.6. The calculated Al-Pt phase diagram compared with experimental invariant data points [1986McA].	110
Figure 6.7. Enlargement of the Al-Pt binary system to show the reactions for PtAl, β and the liquid phases	112
Figure 6.8 The Al-Pt phase diagram of temperature against chemical potential of Pt.	112
Figure 6.9. The Al-Pt phase diagram of temperature against chemical potential of Al.	113
Figure 6.10 Comparison of calculated enthalpy of formation for Pt_3Al ($L1_2$) phase with experimental results [1968Fer, 1981Wor, 1993Mes], Miedema estimations [1989deB] and ab initio predictions [2002Ngo].	113
Figure 6.11 Liquidus surface projection for Al-Pt-Ru, indicating liquidus surface areas for the phases.	115
Figure 6.12 Enlargement of the Al-corner of the Al-Pt-Ru liquidus projection.	116
Figure 6.13 Projection of temperature against composition to identify the reaction types.	118
Figure 6.14 Solidification reactions, as listed in Table 6.8.	118
Figure 6.15 Solidification reactions, as listed in Table 6.8 (enlargement of the Al-corner in Figure 6.14).	119
Figure 7.1. Experimental liquidus surface projection.	121
Figure 7.2. Predicted liquidus surface projection.	121

List of Tables

Table 1.1. Platinum demand and supply [2002Joh]	4
Table 2.1. Properties of the pure elements [1985Vil, 2001ICD].	9
Table 2.2. Crystal structure data for the stable phases in the Al-Pt binary system.	11
Table 2.3 Crystal structure data for the metastable phases in the Al-Pt binary system.	11
Table 2.4. Enthalpies of formation for the stable phases in the Al-Pt system.	15
Table 2.5. The compositions and crystal data for the elements and compounds in the Al-Ru system.	17
Table 2.6 Enthalpies of formation for the phases in the Al-Ru system.	20
Table 4.1. Targeted and analysed compositions for the experimental alloy samples.	36
Table 4.2. Summary of phase and composition analysis for the PAR1 alloy.	38
Table 4.3 Summary of the phase and composition analyses for the PAR 2 alloy.	40
Table 4.4. Summary of phase and composition analysis for the PAR 3 alloy.	42
Table 4.5. Summary of phase and composition analysis for the PAR4 alloy.	43
Table 4.6. Summary of phase and composition analysis for the PAR 5 alloy.	45
Table 4.7. Summary of phase and composition analysis for the PAR 6 alloy.	47
Table 4.8. Summary of phase and composition analysis for the PAR 7 alloy.	49
Table 4.9. Summary of phase and composition analysis for the PAR 8 alloy.	51
Table 4.10. Summary of phase and composition analysis for the PAR 9 alloy.	53
Table 4.11. Summary of phase and composition analysis for the PAR 10 alloy.	54
Table 4.12. Summary of phase and composition analysis for the PAR 11 alloy.	56
Table 4.13. Summary of phase and composition analysis for the PAR 12 alloy.	58
Table 4.14. Summary of phase and composition analysis for the PAR 13 alloy.	60
Table 4.15. Summary of phase and composition analysis for the PAR 14 alloy.	62
Table 4.16. Summary of phase and composition analysis for the PAR 15 alloy.	64
Table 4.17. Summary of phase and composition analysis for the PAR 16 alloy.	66
Table 4.18. The XRD results	69
Table 4.19. Solidification reactions for Al-Pt-Ru.	76
Table 5.1. Applications of the compound energy formalism.	88
Table 6.1. Thermodynamic models of the intermetallic phases in Al-Ru.	95
Table 6.2 Thermodynamic models of the intermetallic phases in Al-Pt.	95
Table 6.3 Calculated thermodynamic parameters for the Al-Ru system [J/mol]	102
Table 6.4 Calculated and Experimental invariant temperatures and compositions for the Al-Ru system.	105
Table 6.5. The calculated model parameters for Al-Pt [J/mole of atoms].	108
Table 6.6. Experimental and calculated invariant temperatures and compositions for the Al-Pt system.	111
Table 6.7. Experimental and calculated enthalpies of formation for the Al-Pt system.	114
Table 6.8. Solidification sequence for Al-Pt-Ru.	117
Table 7.1. Experimental solidification reactions for Al-Pt-Ru.	122
Table 7.2. Predicted solidification reactions for the calculated Al-Pt-Ru system.	123

Chapter 1 Introduction

1.1 Introduction

This study evaluates the phase diagram of the Al-Pt-Ru ternary system. The study consists of two parts: an experimental part and a computational part.

This chapter gives a background to the development of platinum-based alloys and states the motivation of this work in the light of the current platinum market.

The phase diagrams pertaining to the Al-Pt-Ru system are reviewed in Chapter 2.

Chapters 3 and 4 cover the experimental work. Chapter 3 discusses the experimental methodology used in this study. The experimental results for the Al-Pt-Ru system are discussed, the results reported and a liquidus surface projection is proposed in Chapter 4.

In the computational part, an overview of computational thermodynamics and the principles of the CALPHAD method are presented in Chapter 5. Chapter 6 describes the calculation of the binary phase diagrams with the CALPHAD method, using the Thermo-Calc software, and the extrapolation of the ternary system from the binaries is discussed. A liquidus surface projection is predicted by calculation.

The experimental and calculated phase diagrams are compared in Chapter 7. Conclusions and recommendations are listed.

1.2 Background

Since World War II, Ni-based superalloys (NBSAs) have been developed to become highly successful, operating at high temperatures in the severe environmental conditions in turbine engines, while maintaining their strength. However, NBSAs are approaching the limit of their capabilities, despite advanced processing technologies like single-crystal technology and thermal barrier coatings.

There is a present and future need for a new ultra-high temperature alloy that will still maintain its mechanical properties at least 200 degrees above the maximum operating temperature of the current advanced NBSAs. A number of studies [2000Fai, 2001Hil1] have indicated the potential of platinum-based alloys as the future ultra-high structural alloy since platinum is similar to nickel in crystal structure and chemistry, but has a much higher melting point (2042 K for platinum and 1725 K for nickel) as well as improved corrosion resistance. Platinum forms phases similar to Ni₃Al (the principal strengthening precipitate in superalloys) with a number of elements (e.g. Al, Zr) and initial studies have shown that these alloys have an analogue microstructure of small, semi-coherent

precipitates in a softer matrix, with improved mechanical properties, strength and high-temperature corrosion resistance in comparison to Ni-based superalloys.

Although platinum-based alloys are unlikely to ever replace Ni-based superalloys on account of both higher price and higher density, it is likely that they can be used for the highest application temperature components, in static components in gas turbines and for rockets. Platinum is also extensively used in the protective environmental coatings on Ni-based superalloys, as platinum forms a very stable aluminide with better properties than nickel aluminides, thus shielding the underlying Ni-based superalloy bulk from the high temperatures and corrosive environment.

The development of the Ni-based superalloys spans more than sixty years. In the early years, research and development were based on experimental work alone. However, ways to predict phase diagrams were systematically developed and increasingly assisted alloy development during this period [1998Sau]. There were different ways of thinking, from first principle calculations to neural networks. As computational power became available, the development of these predictions accelerated. One of the successful methods is called the CALPHAD method, an acronym for 'CALculation of PHase Diagrams', which was developed by Larry Kaufman and a number of co-workers [1970Kau]. This method has led to the development of databases for many systems, and a number of them are specifically for Ni-based superalloys. The CALPHAD method is based on Gibbs energy functions for elements and phases and predicts equilibrium phase diagrams from thermodynamic principles. One of the major advantages of the CALPHAD method is that experimental work can be limited for a system where a database is available, thus saving time and costs.

A thorough experimental study of Pt-Al-X based alloys (X=Ru, Cr, Ni, Ti, Ta, Re) to identify a base alloy for further development to a potential Pt-based alloy superior to Ni-based alloys, reported that Pt-Al-Ru and Pt-Al-Cr alloys had the best potential properties for high temperature applications [2001Hil1]. Further to that work, the quaternary alloy Pt₈₄:Al₁₁:Ru₂:Cr₃ was identified to be a two phase alloy of fine precipitates in a platinum matrix, with good oxidation resistance and a high hardness [2000Süs]. Thus to facilitate the further development of these Pt-based alloys, a thermodynamic database will be developed, initially covering the Pt-Al-Cr-Ru quaternary system [2002Cor].

In order to understand a multi-component alloy system, one first should understand the binary and ternary phase diagrams that are part of the multi-component system. Not all the binaries in this suggested quaternary Pt-base system are well defined, and for the Pt-based ternaries relevant to the quaternary, no data are available.

In this study, the Al-Pt-Ru ternary alloy system was studied experimentally and the microstructure was characterised over the complete composition ranges. Although the platinum-rich corner is the important area for Pt-based superalloys, all three of the elements play a significant role in the coating technology of Ni-based superalloys since both platinum and ruthenium form stable aluminides. These are still not well characterised in the coating technology, prompting the full ternary to be determined.

1.3 Motivation

The Platinum Development Initiative (PDI) is supporting a drive to investigate new applications for platinum. A Mintek – Department of Science and Technology (DS&T) (previously the Department of Arts, Culture, Science and Technology – DACST) Lead Fund project to identify Pt-base alloy compositions for further investigation lead to a second DS&T Lead Fund project, with the aim to develop a thermodynamic database to facilitate Pt-based alloy design in future. This work is the first contribution to the Pt-database.

As one of the most frequent questions posed when ‘platinum-based alloys’ are mentioned is 'Cost!!!!', an overview of the platinum market and platinum applications is presented here to give the reader some background and understanding of the market, as well as to place this study in perspective with the bigger platinum picture.

Platinum is an expensive precious metal, and very few people really understand the dynamics of supply and demand in the platinum market. The platinum market is dynamic and vibrant, with some new applications emerging while many other applications decline as substitute materials are found to reduce costs. Furthermore, significant expansion of the South African platinum mining sector might bring changes in the always-complicated balance between supply and demand.

South Africa is the major platinum producer in the world; in 2002 more than 70% of the total world production (5860 million oz = 182.3 tons) was produced, well ahead of Russia which supplies 22% of the total world platinum [2002Joh]. With the current and planned mining expansions in South Africa, a supply of 10 000 million oz are predicted for 2010. In 2000, Pt also took over from gold as the 'forex roost' of South African exports. While gold is continuing a long-term trend of declining production, the platinum industry seems to be forging ahead. It is not expected that supply will balance demand before 2005. The world supply and demand figures for platinum are summarised in Table 1.1.

The PGM applications fall broadly into the following categories:

- Automotive
- Jewellery
- Processing/Production
- Electronics
- Petroleum refining
- Dental/Medical
- Investment

The automotive sector is the largest consumer of platinum, with catalytic converters and the possibility of fuel cells in the near future, immediately coming to mind. Platinum is, with palladium and rhodium, an active element in catalytic converters that convert unburned hydrocarbons into carbon dioxide and water vapour in fossil fuelled automotives. The amount of palladium in the catalytic converters was increased a few

years ago, but it is inevitable that the platinum and rhodium content will have to be raised again to meet the ever-increasing stricter emission control requirements. Diesel powered automotives, a market which increased sharply over the last few years, can use only platinum as a catalyst. On the other side of the coin, automakers are aggressively researching ways to eliminate the expensive platinum group metals (PGM) based emission control components, especially with new 'lean-burn' technologies that will reduce or even eliminate the need for PGM catalytic converters.

Table 1.1. Platinum demand and supply [2002Joh]

Platinum supply and demand										
'000 oz	1992	1993	1994	1995	1996	1997	1998	1999	2000	2001
Supply										
South Africa	2,750	3,360	3,160	3,370	3,390	3,700	3,680	3,900	3,800	4,100
Russia	750	680	1,010	1,280	1,220	900	1,300	540	1,100	1,300
North America	200	220	220	240	240	240	285	270	285	350
Others	120	130	140	100	130	120	135	160	105	110
Total Supply	3,820	4,390	4,530	4,990	4,980	4,960	5,400	4,870	5,290	5,860
Demand by application										
Auto catalyst: Gross	1,550	1,685	1,870	1,850	1,880	1,830	1,800	1,610	1,890	2,520
Recovery	-230	-255	-290	320	-350	-370	-405	-420	-470	-520
Chemical	215	180	190	215	230	235	280	320	295	290
Electrical	165	165	185	240	275	305	300	370	455	385
Glass	80	80	160	225	255	265	220	200	255	285
Investment: small	145	125	155	75	110	180	210	90	-100	30
Large	110	180	240	270	130	60	105	90	-100	30
Jewellery	1,510	1,615	1,740	1,810	1,990	2,160	2,430	2,880	2,830	2,550
Petroleum	120	105	90	120	185	170	125	115	110	125
Other	150	165	190	225	255	295	305	335	375	435
	3,815	4,045	4,530	4,710	4,960	5,130	5,370	5,590	5,680	6,150
Western sales to China*	0	20	50	130						
Total demand	3,815	4,065	4,580	4,840	4,960	5,130	5,370	5,590	5,680	6,150
Movements in stocks	5	325	-50	150	20	-170	30	-720	-390	-290
	3,820	4,390	4,530	4,990	4,980	4,960	5,400	4,870	5,290	5,860
Demand by region										
Europe	860	895	935	880	840	875	910	995	1,150	1,490
Japan	1,870	1,975	2,145	2,215	2,005	1,885	1,795	1,820	1,410	1,250
North America	705	760	940	1,015	1,180	1,250	1,325	1,080	1,225	1,285
Rest of the world	380	415	510	600	935	1,120	1,340	1,695	1,895	2,125
	3,815	4,045	4,530	4,710	4,960	5,130	5,370	5,590	5,680	6,150
Western sales to China *	0	20	50	130						
Total demand	3,815	4,065	4,580	4,840	4,960	5,130	5,370	5,590	5,660	6,150

*Before 1993, estimates include Eastern Europe; for 1993 and subsequent years, demand in this region is included in the European figures. From 1996, demand in China is incorporated in our Rest of the World estimates

The use of fuel cell technology to replace fossil fuel in the automotive industry is a strong likelihood, as international emission and fuel-efficiency mandates are becoming more challenging. Prototypes of this new generation of automobiles have been released by some of the major automotive manufacturers. Catalysts are the only way to increase the efficiency of proton exchange membrane fuel cells (PEMFC), the most suitable fuel cell for automotive applications. While platinum was initially the main catalyst in PEMFC technology, which could have resulted in a complete world shortage of platinum, recent developments have shrunk the amount of platinum from 26 mg/cm² to only 0.2 mg/cm² [2001 Wil] as Pt is replaced by a Pt-FeO_x compound.

Other automotive applications include PGMs used in oxygen and ozone sensors for anti-pollution subsystems. Both platinum and ruthenium are also used in life-long spark plugs.

The demand for platinum jewellery increased sharply in the mid-nineties mainly due to consumers in the eastern markets switching from gold to platinum. However, since 2000 there has been a 13% decline in this demand, as the Japanese economy is in recession. On the other hand, China is still a growing market for platinum jewellery as gold trade is strictly controlled in China. This is a market driven by Asian and other ethnic groups feeling that platinum has a more pleasing contrast with their skin colour than other metals. Jewellery is an extremely fickle market, and specifically in platinum based jewellery, the market share is directly proportional to the marketing effort, whereas gold and diamond sales are not related to marketing input.

It is estimated that platinum is used as a catalyst in about 20 % of products purchased by modern consumers. Platinum is a catalytic agent in the processing of nitric acid, fertilizers, synthetic fibres and a number of other materials. Although platinum is essential in these processes and there are few satisfactory substitutes, it is not consumed in the process and can be recycled for future use.

The glass industry uses platinum dies extensively. Platinum is also used in fibreglass production. While the initial amount of platinum needed for bushings and claddings is high, these components only need a ~1% refurbishing per year.

Various kinds of PGM alloy combinations are used in thermocouple devices to measure temperature with high accuracies, while a platinum silicide is used in thin film optical and temperature sensing systems. Platinum is used in the semi-conductor industry for wire and electrical contacts in corrosive or high-voltage environments, as well as for magnetic coatings for high-density hard disk drives and optical storage systems. Hewlett Packard recently announced a new memory storage device, based on rotaxane molecules, where they plant these molecules between tiny platinum and titanium layers. This could revolutionise memory storage as it has at least 10 times the memory density of the best DRAM (silicon based memory). HP will partly disclose their results to 'seed their own competition', thus the use of platinum in the semiconductor industry can increase significantly over the next few years [2002Eco].

Platinum and palladium catalysis is an environmentally-friendly way to perform crude oil separation. While a significant amount of platinum is needed for the fine meshed nets used in this industry, the platinum is not consumed by the separation process and only needs a refurbishment after the initial capital outlay to procure the nets.

Investment demand for platinum is unpredictable. Investment is usually related to the platinum price. When the price falls, the interest in platinum investment products is high. During the first six months of 2001, demand for the US Mint's platinum Eagle series of proof and bullion coins fell as the platinum price hovered around \$600 per oz and only increased as the platinum price began to fall.

Platinum use in medicine is a growing market. In the USA, the annual revenue from platinum used in medicine was \$1billion, and the market is growing at ~15% per year. Most of these drugs are used in the treatment of cancer. Due to the complexity in identifying an active unit, these drugs will remain a platinum domain as all research on substituting the platinum in the active unit has failed to date.

Other application demands increased steadily from 4% in 1992 to 7% in 2001. One of the growing applications in this field is the use of Pt in environmentally protective coatings especially on the Ni-based superalloys to enhance their properties, as Pt additions to the aluminide coatings significantly increase the oxide scale adherence at high temperatures [2000Hay].

The platinum supply is further boosted by an 11% increase in 2001 in the platinum recovered from autocatalysts. This figure is likely to keep on increasing in the future as a new smelter plant in South Africa is planned, dedicated to the recovery of platinum, and in Europe legislation will require that at least 85 % of a car's weight is recycled.

It is thus clear that, as the South African platinum industries are increasing their mining operations and world research is focused on reducing platinum to reduce cost, efforts must be maintained to search for future applications for platinum to avoid an over-supply on the market. It is, therefore, to the advantage of the South African platinum market that studies such as this are conducted, as they might open up other opportunities for platinum demand along the way.

So what is the future of platinum in high temperature applications? As previously mentioned, platinum already plays an important role in environmentally protective coatings on Ni-based superalloys. The extreme high-temperature components in a turbine (e.g. blades, vanes and airfoils) are typically coated with a 2-10 μm thick layer of platinum by electrolysis or PVD. An aluminide coating is then grown by a diffusion treatment as platinum promotes the formation of a slow growth, very adherent and stable Al_2O_3 layer on the surface. With roughly 600-700 new commercial aircraft per year, a current fleet of about 12 000 commercial aircraft and 12 000 business aircraft, at 2-4 engines per aircraft, it amounts to about 60 000 engines. Blades are recoated every 10 000 - 150 000 hours. The current military fleet is estimated to about 15 000 aircraft, with 5 000 new aircraft planned for the next 10 years. At 2-3 engines per aircraft, another at

least 32 000 engines, which have shorter lifespans due to the higher demands placed on them. At roughly 50g of platinum per aircraft engine, the aerospace industry uses at least 4500 kg platinum per year. It is nearly impossible to account for industrial gas turbines on land. These typically have a 15m² blade surface area per turbine and it has been estimated that the land turbine industry could use 10 000 kg of platinum per year [2001Hil1].

Looking at a platinum-based superalloy, and not a Ni-based superalloy coated with a few microns of platinum, the picture is different. No detailed study has yet been done on the feasibility of such an option, but platinum-based superalloys are not an impossibility. There will be advantages of a higher operating temperature, which will increase the efficiency of the turbines dramatically and reduce the thrust fuel cost. However, platinum is very dense (21.5 g/cm³ against ~8 g/cm³ for NBSAs) and the cost of platinum as base material will significantly change the cost-breakdown for turbine engines. The raw material cost is currently 2% of the total turbine cost for NBSAs, while nearly 45% of the cost is due to the highly specialised casting, machining and coating costs, as well as another 25% for quality management, which is critical as the coatings must be fail-proof. Platinum-based turbine blades might not need these specialized coating technologies. The use of platinum based alloys as high temperature alloys in turbines will be limited to only the components exposed to the highest temperatures: first stage blades and vanes, combustors, transitions and shrouds.

This might just be what South African platinum production needs to increase the demand and justify the current expansions to increase the platinum supply, especially since there are platinum reserves for the next 500 years. It is thus important that opportunities for new applications for platinum are explored and investigated beyond the present limits, to ensure the future of this white metal as South Africa's main foreign currency commodity.

Chapter 2

Literature review - The Phase Diagrams

The Al-Pt-Ru ternary phase diagram is virtually unstudied, as only one partial isothermal section at 1350°C for the high-platinum corner has been reported [2001Big1,2001Big2, 2001Hil1].

In order to evaluate a ternary system accurately and completely, the binary systems making up the ternary diagram must be well defined, as they are the 'building blocks' of the system. Discrepancies must be addressed and assumptions well identified. As both the Al-Pt and Al-Ru phase diagrams published in the Binary Alloy Phase Diagrams series of Massalski *et al.* [1990Mas] show some discrepancies with later results published in the literature, this chapter gives a detailed overview of the phases found in the Al-Pt, Al-Ru and Pt-Ru binary phase diagrams and the data used in this determination of the Al-Pt-Ru phase diagram.

2.1 The Elements: Al, Pt and Ru

Aluminium is a soft, lightweight silvery-white metal, the third most abundant metal in the earth's crust, mostly occurring in the form of Al_2O_3 . Too soft in its pure form, it is alloyed with other metals to harden and strengthen it. Aluminium alloys are used for many purposes from airplanes to beverage cans. Bonded to the transition metals, highly ordered aluminides, such as MAI , MAI_3 and M_3Al ($M=Ni, Fe, Ti, etc$), can form. These intermetallic phases possess many remarkable properties. Their high temperature strength is often very attractive (some aluminide intermetallic phases get stronger as the temperature increases over certain temperature ranges), and they frequently exhibit very good resistance to high temperature corrosion, due to the formation of stable Al_2O_3 rich oxide films. However, an inherent brittleness at room temperature has hampered their fabrication to date.

Platinum and ruthenium belong to the so-called platinum group metals (PGMs), the six metal group of platinum, palladium, rhodium, iridium, ruthenium and osmium. Platinum is soft, ductile, and resistant to oxidation and high temperature corrosion. Platinum is one of the densest known metals. Ruthenium is hard, brittle, shows poor oxidation resistance at high temperatures and is almost unworkable in the metallic state. Alloys of the PGMs are used for their exceptional catalytic properties. Other distinctive properties include resistance to chemical attack, excellent high-temperature characteristics, and stable electrical properties. The properties of Al, Pt and Ru are given in Table 2.1.

Table 2.1. Properties of the pure elements [1985Vil, 2001ICDD].

	Aluminium	Platinum	Ruthenium
Chemical symbol	Al	Pt	Ru
Crystal structure	fcc-Al	fcc-A1	hcp-A3
Space Group	Fm-3m	Fm-3m	P6 ₃ /mmc
Lattice parameter [nm]	0.40496	0.39239	0.27057
Melting point [K]	933.5	2 042	2 583
Density [g/cm ³]	2.698	21.45	12.45

2.2 The Al-Pt Binary System

2.2.1 Phase Diagram Data

The Al-Pt phase diagram is complex, with nine intermetallic phases present in the equilibrium diagram, of which two phases have transformations to polymorphic phases at lower temperatures. The diagram is shown in Figure 2.1 and the stable intermetallic phases are listed in Table 2.2. Six metastable phases have been reported (Table 2.3).

While certain features in the system had been determined reliably, other aspects of this diagram, especially at the Pt-rich end, remain problematic. McAlister and Kahan reviewed the Pt-Al system in 1986 for the Bulletin of Alloy Phase Diagrams [1986McA]. The transformation temperatures for the formation of the low temperature polymorphs of the Pt₃Al and Pt₂Al phases are uncertain, and the presence of the β phase had not been confirmed. Oya, Mishima and Suzuki [1987Oya] proposed a revised phase diagram for the platinum rich area (Figure 2.2).

Huch and Klemm [1964Huc] reported platinum to be practically insoluble in (Al). They reported an eutectic reaction $L \rightarrow (Al) + Pt_5Al_{21}$ at 700 K. Extrapolation of this reaction by McAlister [1986McA] places the eutectic composition at 0.44 at. % Pt, which is in agreement with experimental unidirectional solidification work by Piatti and Pellegrini [1980Pia].

Pt₅Al₂₁ forms by a peritectic reaction $L + Pt_8Al_{21} \rightarrow Pt_5Al_{21}$ at 1079 K. Pt₅Al₂₁ is a complex cubic stoichiometric phase. Huch and Klemm [1964Huc] reported a cubic 'PtAl₄' with ~20 at. % Pt. They suggested the phase might rather be of the form Pt₅Al₂₁. Guex [1976Gue] also reported a complex cubic phase of either PtAl₄ or Pt₅Al₂₁ structure.

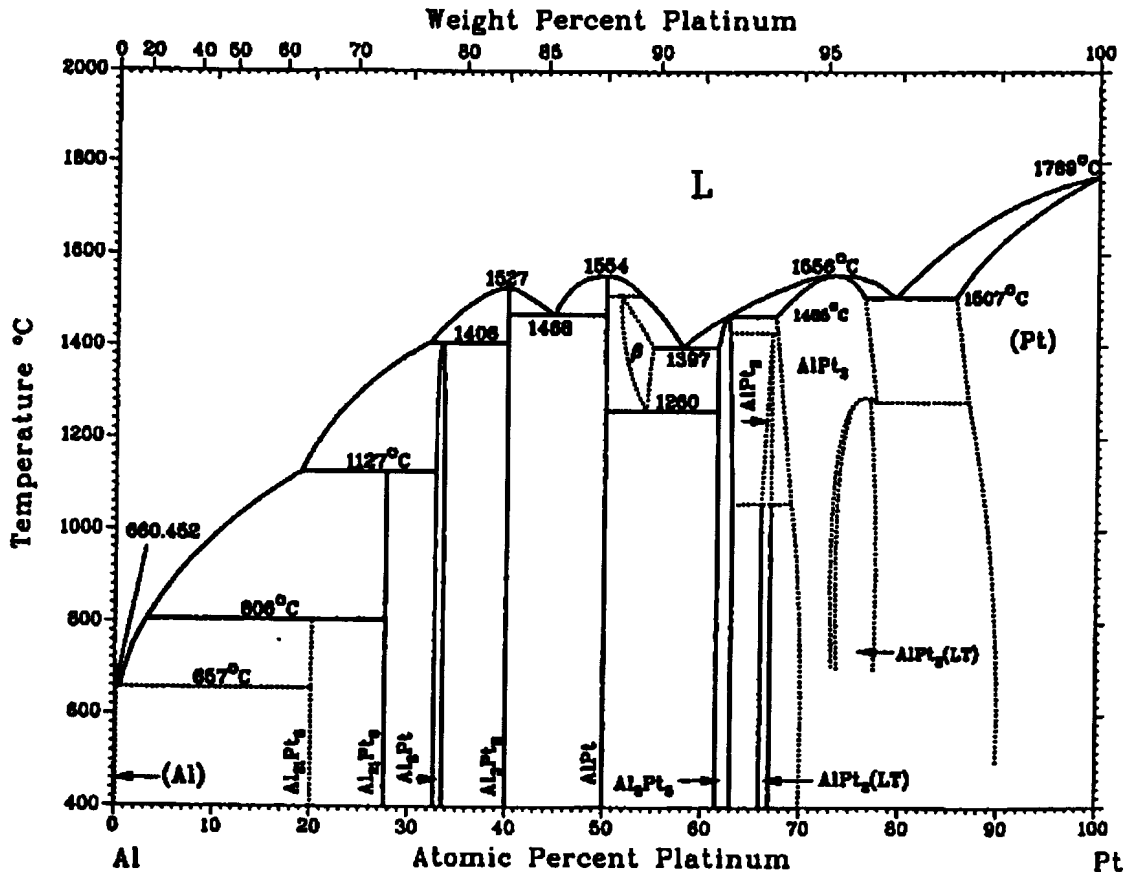


Figure 2.1. The Al-Pt phase diagram from Massalski [1990Mas].

Schaller [1979Sch] reported, without experimental detail, a hexagonal Pt_5Al_{21} phase while Ellner, Kattner and Predel [1982Ell] confirmed the hexagonal structure of the phase and suggested it to be a $PtAl_4$ phase. Piatti and Pellegrini [1980Pia] also reported a hexagonal phase in this composition range, which they suggested to be Pt_6Al_{21} , but also noted a transformation from hexagonal to cubic phases after treatment at 473 K for several hours. Careful analysis of thermal arrest data reported by Huch and Klemm [1964Huc] confirmed the phase as Pt_5Al_{21} [1986McA]. $PtAl_4$ has thus been suggested as a metastable phase in the Pt-Al system. A crystal structure of Pt_5Al_{21} has not been published.

The stoichiometric Pt_8Al_{21} phase at 27.5 at. % Pt has been confirmed by Edshammer [1965Eds] and Ellner *et al.* [1982Ell] after earlier reports of a $PtAl_3$ -like phase by Huch [1964Huc] and Guex [1976Gue]. Pt_8Al_{21} forms by the peritectic reaction $L + PtAl_2 \rightarrow Pt_8Al_{21}$ at 1400 K.

Huch and Klemm [1964Huc], Guex [1976] and Ellner *et al.* [1982Ell] reported the $PtAl_2$ phase which forms through a peritectic reaction $L + Pt_2Al_3 \rightarrow PtAl_2$ at 1952 K. The $PtAl_2$ phase is of the cubic CaF_2 type. It has been reported as a stoichiometric compound by Guex [1976Gue], while the other workers reported a ~1 at. % phase range up to 1123 K.

Table 2.2. Crystal structure data for the stable phases in the Al-Pt binary system.

Phase	Composition range (at. %Pt)		Pearson symbol	Space Group	Strukturbericht	Prototype	Reference
(Al)	0		<i>cF4</i>	Fm3m	A1	Cu	
Pt ₅ Al ₂₁	19.2		<i>c**</i>				[1964Huc] [1980Pia]
Pt ₈ Al ₂₁	27		<i>tI116</i>	I4 _{1α}			[1968Eds] [1982Ell]
PtAl ₂	31.5	33.5	<i>cF12</i>	Fm3m	C1	CaF ₂	[1937Zin] [1963Fer] [1982Ell]
Pt ₂ Al ₃	40		<i>hP5</i>	P3m1			[1978Bah]
PtAl	50		<i>cP8</i>	P2 ₁ 3	B20	FeSi	[1957Sch] [1963Fer]
β	52	56	<i>cP2</i>	Pm3m	B2	CsCl	[1975Cha1] [1978Bha]
Pt ₅ Al ₃	61.5	63	<i>oP16</i>	Pbam		Ge ₃ Rh ₅	[1964Huc]
Pt ₂ Al	66	67	<i>oP12</i>	Pnma	C23	PbCl ₂	[1975Cha1]
Pt ₂ Al (LT)	66	67	<i>oP24</i>	Pmma		GaPt ₂ (LT)	[1976Cha]
Pt ₃ Al	67.3	77.7	<i>cP4</i>	Pm3m	L1 ₂	AuCu ₃	[1962Bro] [1964Huc] [1963Mag]
Pt ₃ Al (LT)	73.5	100	<i>tP16</i>	P4/mbm	DO _c '	GaPt ₃ (LT)	[1975Cha1]
(Pt)	83.8	100	<i>cF4</i>	Fm3m	A1	Cu	

(LT – Low Temperature, HT – High Temperature)

Table 2.3 Crystal structure data for the metastable phases in the Al-Pt binary system.

Phase	Composition (at. % Pt)	Pearson symbol	Space Group	Strukturbericht	Prototype	Reference
α'		<i>cF4</i>	Fm3m	A1	Cu	[1964Com]
PtAl ₄	20	<i>hP*</i>				[1978Sch] [1980Pia] [1982Ell]
PtAl ₅		<i>P4</i>				[2001Lab]
PtAl ₆	14	<i>o**</i>				[1975Ton] [1979Cha]
ε'		<i>c**</i>				[1979Cha]
λ'	10-25					[1982Ell]

Pt₂Al₃ forms congruently $L \leftrightarrow \text{Pt}_2\text{Al}_3$ at 1800 K and 40 at. % Pt. Huch and Klemm [1964Huc], Guex [1976Gue] and Ellner *et al.* [1982Ell] reported that Pt₂Al₃ has a structure related to, but not isotypic with, hexagonal Ni₂Al₃ and essentially has no solubility range.

PtAl is a stoichiometric intermetallic phase and has a cubic FeSi structure. It forms congruently from the liquid at 1827 K and 50 at. % Pt by the reaction $L \leftrightarrow \text{PtAl}$.

Experimental evidence of a β -phase existing between 1533 - 1733 K, with a composition range from 51 - 56 at. % Pt, has been reported by Chattopadhyay and Schubert [1975Cha1], as well as by Bhan and Kudielka [1978Bha]. McAlister and Kahan [1986McA] included these observations in their assessment of the Pt-Al system and proposed a peritectic reaction $\text{PtAl} + L \rightarrow \beta$. No temperature was reported for this reaction. The eutectoid decomposition $\beta \leftrightarrow \text{PtAl} + \text{Pt}_5\text{Al}_3$ has also been proposed by McAlister and Kahan [1986McA] to correspond with a thermal arrest reported by Huch and Klemm [1964Huc].

A Pt₃Al₂ phase was reported by Huch and Klemm [1964Huc] after observing a thermal arrest at 1533 K between 50 to 60 at. % Pt. Guex [1976Gue] also reported this phase, but it was referenced to the work of Huch and Klemm [1964Huc] and not an experimental observation. Subsequent studies have failed to confirm the existence of this phase and it has been suggested by McAlister and Kahan [1986McA] that Huch and Klemm most likely misinterpreted the solubility range of Pt₅Al₃, and that what they observed was the eutectoid decomposition of the β phase.

Pt₅Al₃ is rhombohedral of the Rh₅Ge₃ type and forms by peritectically $L + \text{PtAl}_3 \rightarrow \text{Pt}_5\text{Al}_3$ at 1738 K. McAlister's version of the phase diagram [1986McA] shows Pt₅Al₃ having a solubility range 61.5 to 63 at. % Pt, as reported by Ellner *et al.* [1982Ell] and Oya *et al.* [1987Oya].

A peritectoid reaction $\text{PtAl}_3 + \text{Pt}_5\text{Al}_3 \rightarrow \text{Pt}_2\text{Al}$ occurs at about 1703 K and 67.5 at. % Pt, forming Pt₂Al with a phase range of ~ 2 at. %. Two crystal variants of the Pt₂Al phase have been reported, a high temperature (HT) form similar to the PbCl₂ type and a low temperature (LT) form relating to the GaPt₂ (LT) type. While the nature of the reaction is still unknown, it is accepted that the reaction occurs at ~ 1333 K [1986McA,1987Oya]. Biggs [2001Big2] suggested a martensitic-type reaction.

The highest Pt-containing intermetallic phase is Pt₃Al. Pt₃Al forms congruently $L \rightarrow \text{Pt}_3\text{Al}$ at 1829 K at 73.2 at. % Pt. A phase width of ~ 4-6 at. % has been reported for Pt₃Al. A martensitic type transformation has been reported where the cubic L1₂ structure of Pt₃Al, transforms to a tetragonal DO'_c Pt₃Al during cooling. There are many discrepancies, and to further complicate matters, the temperature of the transformation is composition dependent. It has been reported as either a congruent transformation at 1563 K or an eutectic reaction at 1553 K, depending on the composition. Oya *et al.* [1987Oya] reported an intermediate phase between the HT and LT Pt₃Al phases (Figure 2.2). The intermediate phase forms at ~ 613 K and the low temperature phase at ~ 400 K. The DO'_c

phase was reported to be extremely unstable. Biggs [2001Big2] reported the $L1_2$ to DO'_c transformation at between 623 to 673 K.

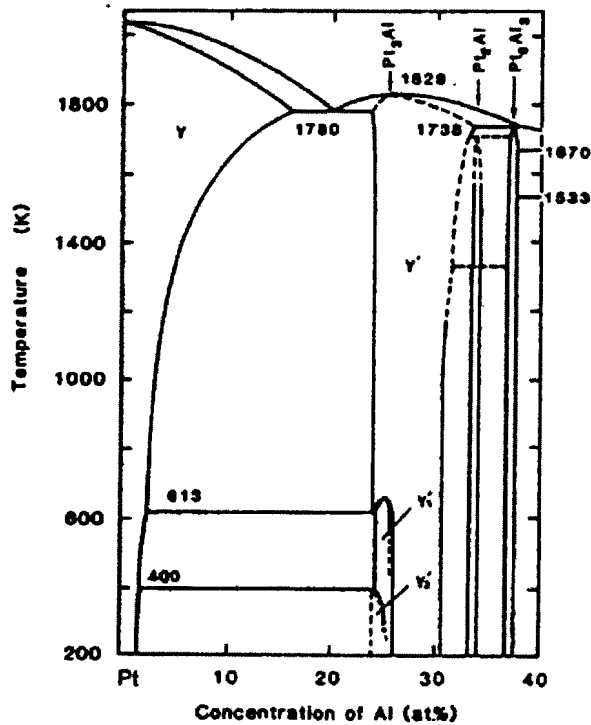


Figure 2.2. Revised Pt-rich portion of the Al-Pt phase diagram [1987Oya].

An eutectic reaction $L \rightarrow (Pt) + Pt_3Al$, reported by Huch and Klemm [1964Huc] and confirmed by Darling, Selman and Rushforth [1970Dar], occurs at 1780 K and 79.5 at. % Pt.

From the combined data of Huch and Klemm [1964Huc] and Darling *et al.* [1970Dar], (Pt) dissolves about 14 at.% Al at 1783 K. Darling *et al.* [1970Dar] suggested a lower solubility of Al in (Pt) at lower temperatures, confirmed as 10 at. % Pt at 1473 K by Bronger and Klemm [1962Bro] and 10 and 5 at. % Pt at 1273 K and 573 K respectively by Schaller [1979Sch].

Wu and Jin [2000Wu] calculated the Al-Pt phase diagram with the CALPHAD technique (Figure 2.3). The calculation did not include the β and the Pt_2Al phases. The Pt_3Al phase was not described as an ordered phase and the order/disorder transformation had not been included. The low temperature Pt_3Al phases have not been included either. Both $PtAl_2$ and Pt_5Al_3 have been modelled as stoichiometric compounds, making no provision for the composition ranges reported above.

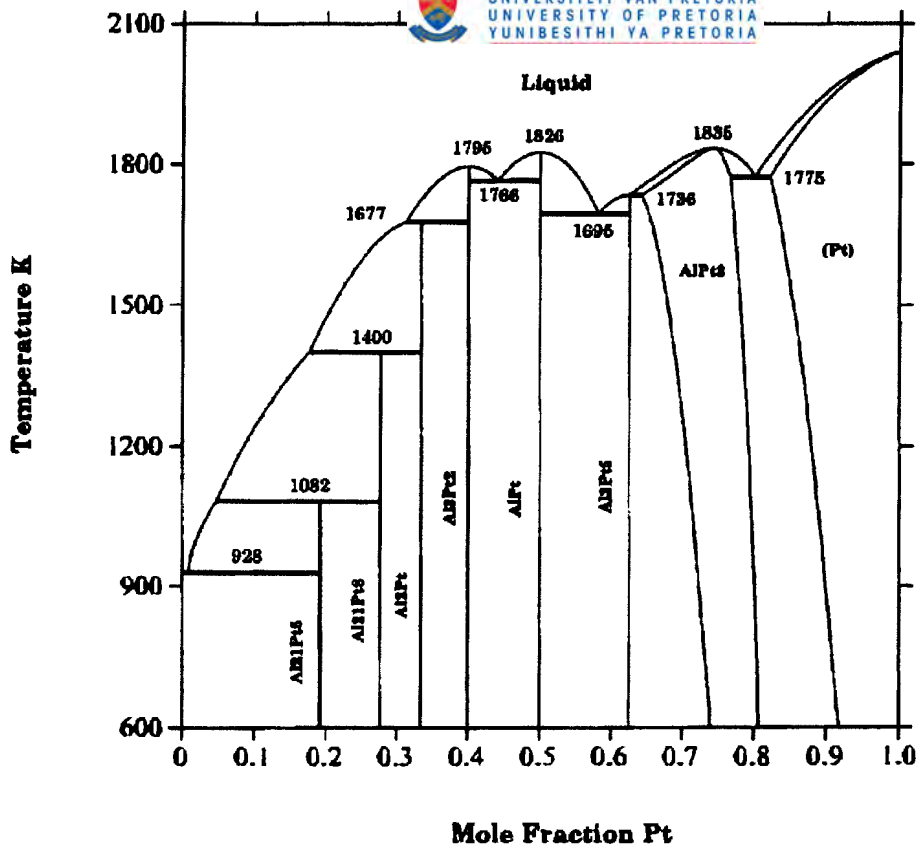


Figure 2.3. The calculated Al-Pt phase diagram by Wu and Jin [2000Wu].

2.2.2 Thermodynamic data

Ferro *et al.* [1968Fer] determined the heat of formation (ΔH_f) for alloys in the Al-Pt system experimentally by solute solvent drop calorimetry. Worrel and Ramanarayanan [1981Wor] determined the Gibbs energy of mixing (ΔG_m) for the 75 at. % Pt composition by an electrochemical cell technique. Lee and Sommer [1985Lee] determined the partial enthalpies of mixing (ΔH_m) of liquid aluminium-rich Pt alloys at ~ 1200 K using solution calorimetry. Jung and Kleppa [1991Jun] determined the enthalpy of formation for PtAl by direct synthesis calorimetry at 1473 ± 2 K. Meschel and Kleppa [1993Mes] determined the enthalpies of formation for Pt₂Al₃ and Pt₃Al in the same way.

Miedema's semi-empirical model has been used to estimate enthalpies of formation for some of the phases [1988deB].

Ab initio techniques have also been applied to predict the enthalpies of formation. Ngoepe [2002Ngo] used a pseudo-potential total energy package (CASTEP) approach to calculate heats of formation for PtAl and Pt₃Al.

The thermodynamic data for the Al-Pt system are listed in Table 2.4.

Table 2.4. Enthalpies of formation for the stable phases in the Al-Pt system.

Phase	ΔH_f [kJ/mole atoms]	Method	Reference
Pt ₅ Al ₂₁	-57.320	Solute solvent drop calorimetry	[1968Fer]
Pt ₈ Al ₂₁	-71.130	Solute solvent drop calorimetry	[1968Fer]
PtAl ₂	-100.420	Solute solvent drop calorimetry	[1968Fer]
Pt ₂ Al ₃	-94.980	Solute solvent drop calorimetry	[1968Fer]
	-79.000	Miedema semi-empirical method	[1988deB]
	-96.500	Direct Synthesis Calorimetry	[1993Mes]
PtAl	-100.420	Solute solvent drop calorimetry	[1968Fer]
	-100.000	Direct Synthesis Calorimetry	[1991Jun]
	-82.000	Miedema semi-empirical method	[1988deB]
	-67.440	<i>Ab initio</i>	[2002Ngo]
β			
Pt ₅ Al ₃	-90.730	Miedema semi-empirical method	[1998Wol]
Pt ₂ Al	-88.280	Miedema semi-empirical method	[1998Wol]
Pt ₂ Al (LT)			
Pt ₃ Al	-69.870	Solution Calorimetry	[1968Fer]
	-63.600	Direct Synthesis Calorimetry	[1993Mes]
	-50.990	Miedema semi-empirical method	[1988deB]
	-76.000*	Electrochemical	[1981Wor]
	-74.380	<i>Ab initio</i>	[2002Ngo]
Pt ₃ Al (LT)**	-79.100	<i>Ab initio</i>	[2002Ngo]

* Gibbs energy of mixing: $-76\,460 + 7.48 \cdot T$ [1981Wor], which gives an estimated enthalpy of formation of $-76\,000$ J/mol of atoms

** DO_c structure

2.3 The Al-Ru Binary System

2.3.1 Phase Diagram Data

The Al-Ru phase diagram from the Binary Alloy Phase Diagrams series [1990Mas] includes five stable intermetallic phases as shown in Figure 2.4. However, the phase boundaries are in dashed lines, indicating that uncertainties are associated with the phases and their homogeneity ranges. Most of the invariant reaction temperatures are also not well determined. Subsequent work by Anlage [1988Anl] and Boniface and Cornish [1996Bon1, 1996Bon2] clarified some of these uncertainties. Boniface and Cornish [1996Bon2] proposed a revised phase diagram, incorporating the results from Anlage [1988Anl] (Figure 2.5). Okamoto [1997Oka] reviewed the Al-Ru system and reported the diagram proposed by Boniface and Cornish to be the more acceptable phase diagram. However, the liquidus surface on the cascade of peritectic reactions did not obey all phase diagram rules and a modification was suggested by Prins and Cornish [2000Pri].

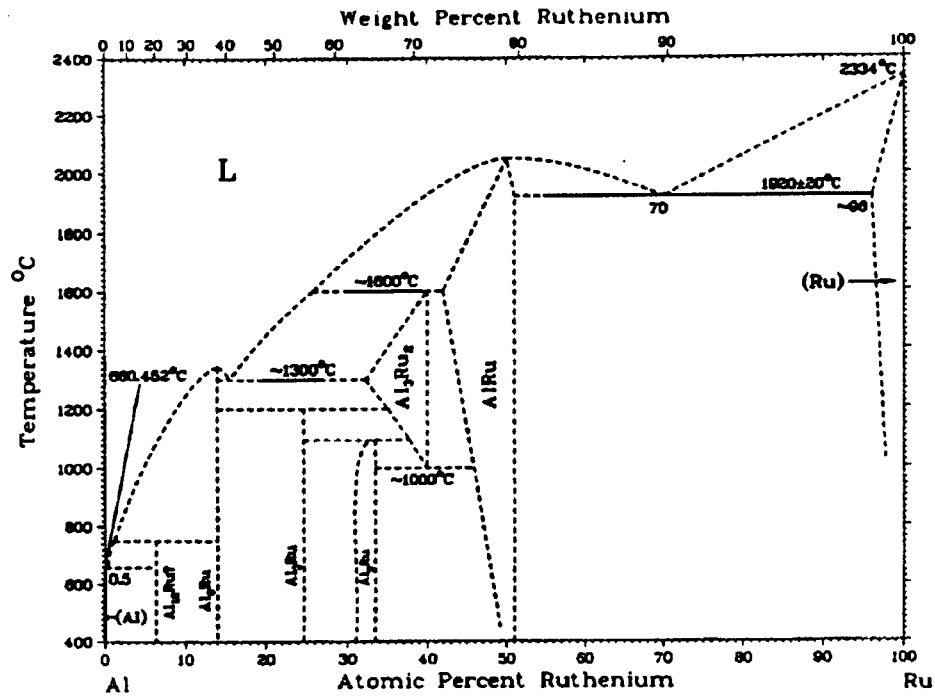


Figure 2.4 The Al-Ru phase diagram after Massalski [1990Mas].

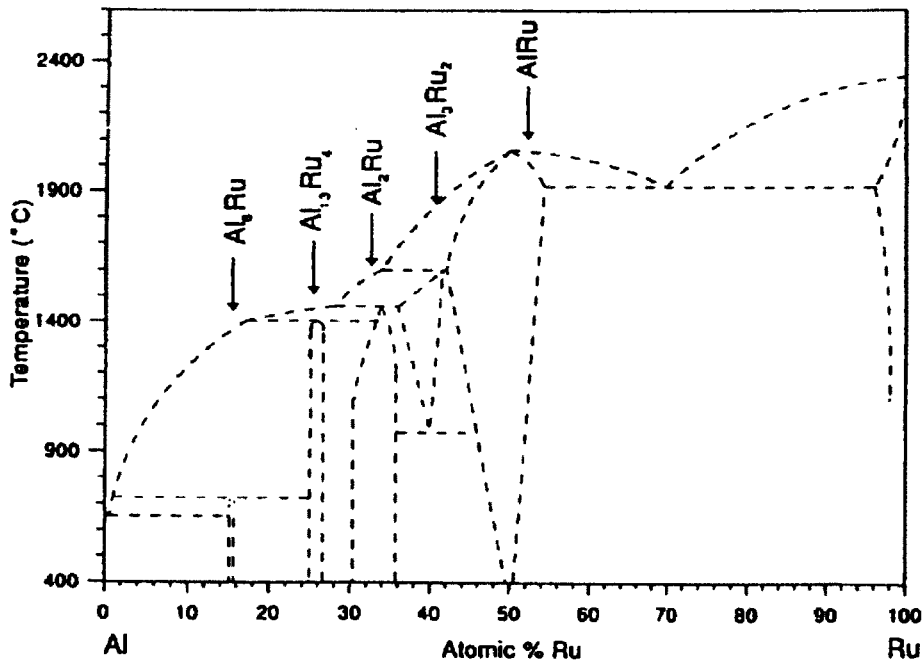


Figure 2.5. The modified Al-Ru phase diagram after Boniface and Cornish [1996Bon2].

The peritectic formation temperatures of the RuAl₂ and Ru₂Al₃ phases were raised to 1873K and 1973 K respectively, to agree with reaction temperatures reported by Obrowski [1860Obr]. The crystal structure data for the stable intermetallic phases are listed in Table 2.5. Only one metastable phase, RuAl_{2.5}, has been reported for the Al-Ru system [1968Eds].

Obrowski [1960Obr] reported the first phase diagram for the Al-Ru system and this was based on microscopic, X-ray and thermoanalytical observations. Six intermetallic phases were reported: RuAl₁₂ (although some uncertainty existed of the exact composition), RuAl₆, RuAl₃, RuAl₂, Ru₂Al₃ and RuAl, taking part in eight invariant reactions. The Ru-rich solid solution was reported to comprise ~ 4 at. % Al at the eutectic temperature. No solubility of Ru in (Al) was detected and it was also concluded that all the Al-rich intermetallic compounds were stoichiometric line compounds. The RuAl phase was observed to melt at 2333 ± 20 K and the eutectic reaction between RuAl + (Ru) at 2193 ± 20 K. Reactions were observed at 1573 and 1873 K and these were assigned to eutectic and peritectic reactions respectively. However, it was concluded that some uncertainty existed of the solid-state reactions between 20 and 40 at. % Ru. Apart from Obrowski, no subsequent workers have reported the existence of RuAl₁₂. Other reactions reported by Obrowski, but not found by other workers are:

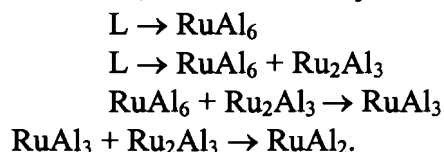


Table 2.5. The compositions and crystal data for the elements and compounds in the Al-Ru system.

Phase	Composition (at. % Ru)		Pearson symbol	Space Group	Strukturbericht	Prototype	Reference
Al			<i>cF4</i>	<i>Fm3-m</i>	A1	Cu	
RuAl ₆	14.3	14.3	<i>oC28</i>				[1968Eds]
						MnAl ₆	[1982Cha]
	15.1±1	15.7±1					[1996Bon2]
Ru ₄ Al ₁₃			<i>mC102</i>	<i>C2/m</i>		Fe ₄ Al ₁₃	[1965Eds]
	23.6	23.6					[1988Anl]
	25.0±1.5	26.6±1.5					[1996Bon2]
RuAl ₂	30.35	33	<i>tI6</i>	<i>I4/mmm</i>	C11 _α	CaC ₂	[1960Obr]
			<i>oF24</i>	<i>Fddd</i>	C54	TiSi ₂	[1966Eds]
	30.4±1	35.8±1					[1996Bon2]
Ru ₂ Al ₃			<i>hP5</i>	<i>P3-m1</i>	D5 ₁₃	Ni ₂ Al ₃	[1960Obr]
			<i>tI10</i>	<i>I4/mmm</i>		Os ₂ Al ₃	[1966Eds]
RuAl			<i>cP2</i>	<i>Pm3-m</i>	B2	CsCl	[1960Obr]
Ru			<i>hP2</i>	<i>Fm3-m</i>	A3	Mg	

Schwomma [1963Sch] undertook X-ray work on a 33.3 at. % Ru sample, and found RuAl_2 and RuAl . Uncertainty through the contamination of the samples by silicon and oxygen was, however, raised as a possible problem by the author.

Edshammar determined the crystal structure for $\text{Ru}_4\text{Al}_{13}$ [1965Eds] (Obrowski's RuAl_3 [1960Obr]), and noted the similarity with $\text{Fe}_4\text{Al}_{13}$ because of the twinned prismatic structure and co-ordination numbers, although $\text{Ru}_4\text{Al}_{13}$ showed even better agreement with $\text{Os}_4\text{Al}_{13}$. It was also found that Al atoms were absent from some of the sites which were partially occupied by Al in $\text{Fe}_4\text{Al}_{13}$ and $\text{Co}_4\text{Al}_{13}$. $\text{Ru}_4\text{Al}_{13}$ was, therefore, considered to be the ideal structure of RuAl_3 [1960Obr]. Subsequently with X-ray powder methods, Edshammar reported the crystal structures for five more intermetallic phases: RuAl , Ru_2Al_3 , RuAl_2 , $\text{RuAl}_{-2.5}$ and RuAl_6 [1966Eds, 1968Eds]. The phase $\text{RuAl}_{-2.5}$ was observed only in arc-melted samples. There were some additional CsCl-like phases reported around the composition RuAl , but no further details were given. No evidence of the RuAl_{12} phase was found, and there were other inconsistencies with Obrowski's phase diagram [1960Obr] concerning the Ru_2Al_3 and RuAl_2 phases.

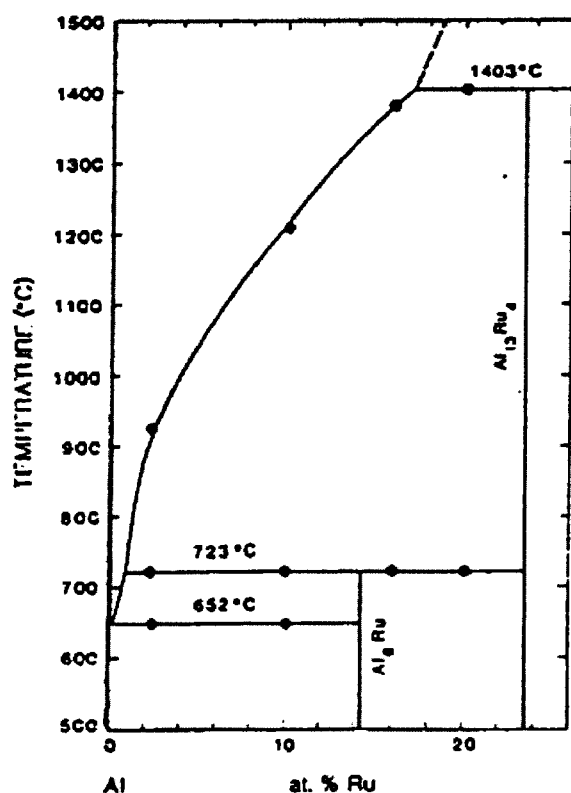


Figure 2.6. The phase diagram of Anlage *et al.* [1988Anl] for the high-Al corner in the Al-Ru system.

Anlage, Nash and Ramachandran [1988Anl] undertook experiments up to 26 at. % Ru using scanning electron microscopy, X-ray diffraction and thermal analysis (DSC) and proposed a revised phase diagram for the Al-rich portion of the Al-Ru phase diagram

(Figure 2.6). Confirmation of the RuAl₁₂ phase was not found. Edshammar's [1965Eds] notation for the Ru₄Al₁₃ phase was used. It was also reported that both RuAl₆ and Ru₄Al₁₃ melt by a peritectic reaction at 996 K and 1676 K respectively, and not congruently as suggested by Obrowski [1960Obr]. Some liquidus temperatures were provided. Problems with homogeneity of the alloys were reported, and also that the peritectic reaction forming RuAl₆, was sluggish. Under rapid solidification conditions, icosahedral phases were reported between 2.4 and 23.5 at. % Ru.

Boniface and Cornish [1996Bon1] confirmed Anlage's results for the high-Al end of the phase diagram. No evidence of the L ↔ Ru₂Al₃ + RuAl₆ eutectic reaction, reported by Obrowski [1960Obr], was found and the presence of RuAl₂ in as-cast samples over a specific range indicated stability at higher temperatures. The microstructures revealed that there was a peritectic cascade of reactions from the formation of Ru₂Al₃ to the formation of RuAl₆. A slight endothermic peak at 1733 K suggested the formation temperature for RuAl₂ [1996Bon2]. The Ru₂Al₃ phase was found to decompose at ~ 1223K.

Although Varich and Luykevich [1973Var] found a maximum solubility of Ru in (Al) of 3.23 at.% Ru by rapid solidification techniques, this solubility has not been reported for equilibrium conditions.

No assessment of the Al-Ru phase diagram, based on the CALPHAD method, had been published prior to this work.

2.3.2 Thermodynamic data

The only experimental thermodynamic value for the Al-Ru system was determined by Jung and Kleppa [1992Jun] by dropping a mixed 1:1 powder mixture (atomic percent) of the elements into the calorimeter, which showed that RuAl (B2) has a high heat of formation, $\Delta H_f = -124.1 \text{ kJ.mol}^{-1}$.

Miedema's method was used to estimate values for the heats of formation for the intermetallic phases [1998Wol], as no other data were available.

Neumann, Chang and Lee [1976Neu], without using Obrowski's experimental data [1960Obr] used a theoretical method to predict that the RuAl phase has a very narrow phase width, probably not exceeding 1 at. % on either side of the stoichiometric composition. They suggested that RuAl is slightly off-stoichiometric and that the disorder parameter is less than 3.10^{-3} , indicating that RuAl is a highly ordered phase.

Several *ab initio* results have been reported for the enthalpy of formation of RuAl. However, the data are scattered, probably due to the different assumptions for defect formation in RuAl, which have been implied to be vacancies [1993Fle] or anti-structure defects [1976Neu]. Ngyen-Manh and Pettifor [1999Man] used the full-potential linear muffin-tin orbital (FP-LMTO) method within a local-density-function approximation

(LDA), while Gargano, Mosca, Bozolla and Noebe. [2002Gar] used the Bozzolo-Ferrante-Smith-based (BFS) Monte Carlo simulations. Hu *et al.* [1999Hu] applied an embedded atom model to calculate the enthalpies of formation for the phases, though most of their data differed vastly from the values estimated by Miedema's semi-empirical model. They have also misquoted data from the literature for the RuAl phase. However, their result for the Ru₄Al₁₃ phase is in better agreement with the Miedema estimation.

The thermodynamic data are listed in Table 2.6.

2.3.3 Applications of Al-Ru intermetallics

The RuAl compound has an unusual combination of properties. Fleischer and co-workers [1991Fle] first reported the excellent room temperature toughness, compared to other intermetallic compounds, and recommended its potential for structural applications because of its high melting point and good oxidation resistance. The improved toughness is due to five independent slip systems in the crystal.

The excellent corrosion resistance of RuAl in hot, concentrated mineral acids was first reported by Wopersnow and Raub [1979Wop], and more recently, McEwan and Biggs [1996McE] demonstrated its capability as a coating in a range of aqueous media. They recognised that it has potential in corrosion-resistant coatings and electrochemical applications. The electrical conductivity of RuAl is high, almost metallic in value, and it exhibits good work function attributes [1995Smi]. This, and the good thermal conductivity [1998And] and a high wear resistance [1994Ste] also render the material suitable for lifelong spark-plug electrodes [1997Wol].

Although RuAl is difficult to manufacture by melting because of its high melting point, it can be manufactured by powder processing techniques, especially by reactive powder processing [1996Cor], or reactive hot isostatic processing (RHIP) [1996Wol].

Table 2.6 Enthalpies of formation for the phases in the Al-Ru system.

Phase	ΔH_f [kJ/mol of atom]	Method	Reference
RuAl ₆	-17.930 ± 10%	Miedema semi-empirical method	[1998Wol]
Ru ₄ Al ₁₃	-30.030 ± 10% -28.940	Miedema semi-empirical method Ab initio	[1998Wol] [1999Hu]
RuAl ₂	-38.260 ± 10%	Miedema semi-empirical method	[1998Wol]
Ru ₂ Al ₃	-44.040 ± 10%	Miedema semi-empirical method	[1998Wol]
RuAl	-47.320 ± 10% -62.050 ± 3000 -70.740 -58.150 -95.510	Miedema semi-empirical method Direct Solution Calorimetry <i>Ab initio</i> <i>Ab initio</i> <i>Ab initio</i> (BFS method)	[1998Wol] [1992Jun] [1992Lin] [1999Man] [2002Gar]

2.4 The Pt-Ru Binary System

The Pt-Ru phase diagram is rather simple in that there are no phases other than the two end-member solid solutions (Pt) and (Ru) and a two phase area comprising of (Pt) and (Ru). The phase diagram [1990Mas] is shown in Figure 2.7.

About 62% Ru dissolves in (Pt) at 1000 °C. A two-phase region of (Pt) and (Ru) exists between ~62 and ~80 at. % Pt. A ruthenium solid solution is observed above ~80 at. % Pt at 1000 °C. (Pt) forms by a peritectic reaction at ~2120 °C.

The Pt-Ru phase diagram has been calculated by Spencer using the CALPHAD method [1996Spe] and is shown in Figure 2.8. The calculated diagram is just an extrapolation of the elemental data. It is only in relative good agreement with the published ASM diagram [1990Mas], as it shows an eutectic reaction instead of the peritectic reaction, as in Figure 2.7. However, there are limited data available for the liquidus and solidus curves.

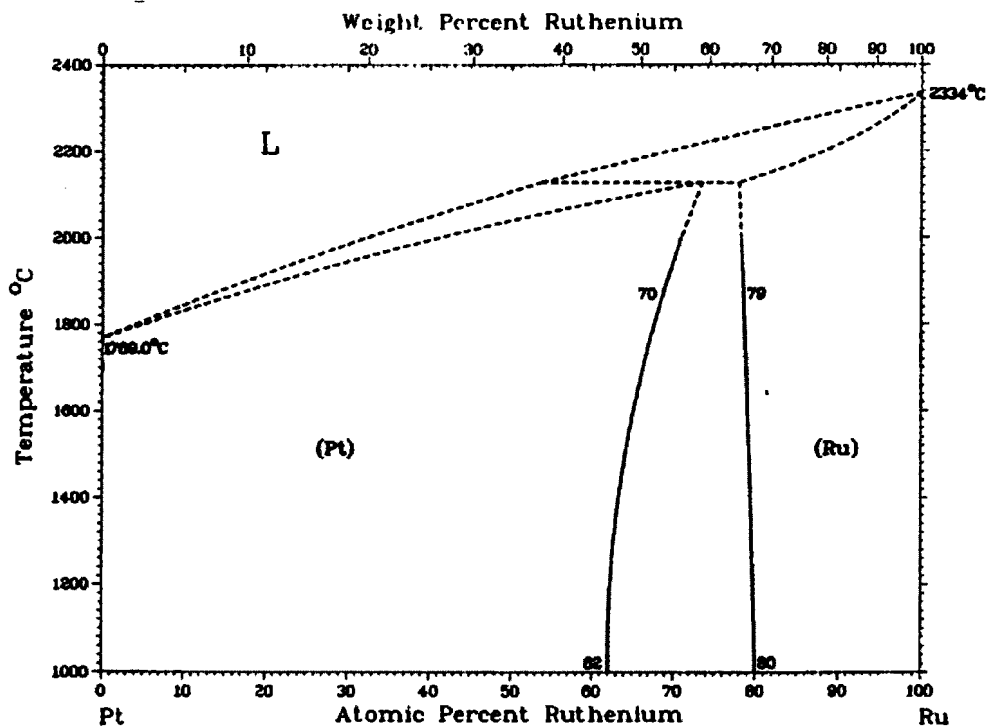


Figure 2.7. The Pt-Ru phase diagram [1990Mas].

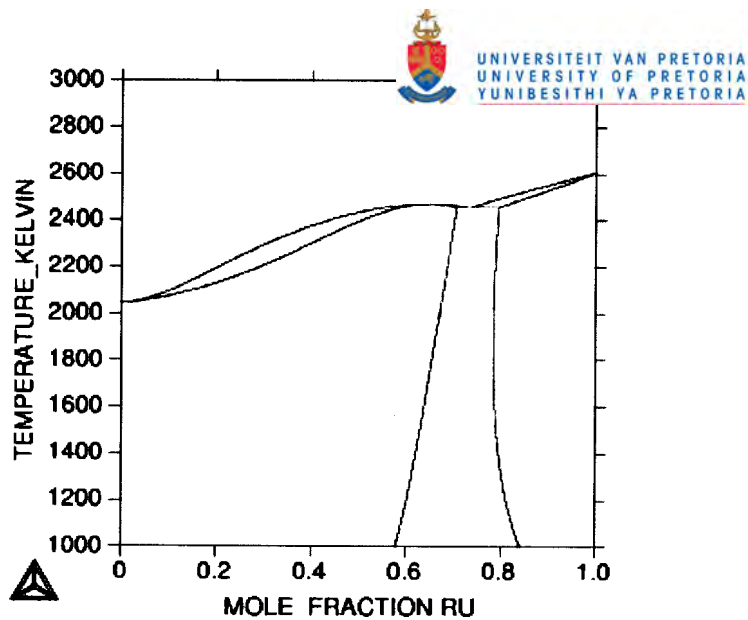


Figure 2.8. Calculated Pt-Ru phase diagram, from Spencer [1996Spe].

2.5 The Pt-Al-Ru Ternary System

The only published data is an isothermal section at 1350°C [2001Big1, 2001Big2, 2001Hil1]. No ternary reactions or ternary phases have been reported and very limited extension of the $\sim\text{Pt}_3\text{Al}$ phase into the ternary was observed. The isothermal section is shown in Figure 2.9.

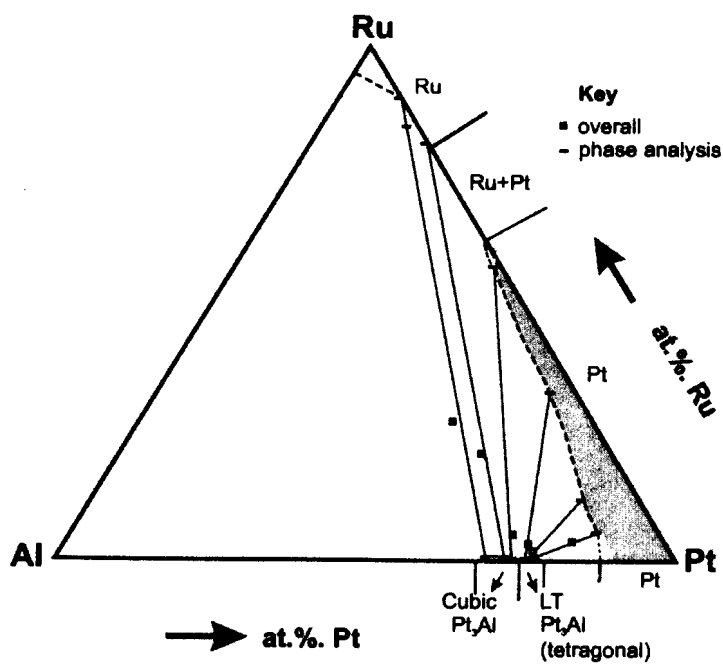


Figure 2.9. Isothermal section of the Al-Pt-Ru system at 1350°C [2001Big2].

Chapter 3

Experimental Procedure

This chapter describes the basic experimental procedures that were followed in this study. The methodology on how the solidification sequences and liquidus surface projection were determined is also presented.

3.1 Introduction

Sixteen samples were prepared in four stages. An initial set of six alloy compositions was selected after extrapolations from the binary phase diagrams to identify possible two-phase areas in the ternary. Two-phase samples were targeted because more information could be gleaned per sample. Samples were selected to have a lower Pt-content than the alloys investigated by Biggs [2001Big1] and Hill [2001Hil1], as their work covered the platinum-rich corner. The highest platinum composition sample was selected to be the same composition as the lowest platinum composition sample from Biggs [2001Big1] in order to benchmark this set of samples. Samples were also selected away from the ruthenium-rich corner since previous experimental work on the Al-Ru system indicated that there is only the eutectic reaction above 50 at. % Ru and such a sample would not give new information.

Six more alloy compositions were selected later to clarify uncertainties raised by the results of the first set of samples. Three more samples were subsequently prepared in order to complete the liquidus surface projection. A final sample was prepared to confirm a ternary phase found in the alloy system.

3.2 Sample Preparation

The as-cast samples were prepared at Mintek, according to their standard preparation method PMD-SOP-037. The samples were prepared by arc-melting on a water-cooled copper hearth, using elemental powders of at least 99.9 percent purity. Three grams of powder were mixed by hand. No binders were used. The powders were compressed before melting under a protective argon atmosphere. Samples were re-melted five times to ensure homogeneity. Samples were turned upside down between each re-melt. Six samples could be prepared per arc-melt.

The arc-melting electrode was equipped with a tungsten-metal tip. No mass-loss measurements were performed on the electrode tip, but no evidence of any detectable tungsten uptake by the samples was found in the composition analyses of any of the phases.

The mass losses of the samples were monitored. All the recorded weight losses were less than 5 %, which were considered acceptable since aluminium is almost always lost during a re-melting as it has a much lower melting point than platinum and ruthenium, and a very high partial pressure. Mass losses were only recorded for the first six samples.

The cooling rate of the arc-melted samples is not known, but it was not sufficiently fast enough to totally freeze in the as-solidified liquidus-solid structure, as some coring was observed in some samples, which indicated that there was time for some diffusion on cooling.

Additionally, the cooling rate was also not fast enough to freeze in the high temperature binary phases or a new high temperature ternary phase, which was found in this study, as solid-state decompositions were observed in the microstructures.

Arc-melted samples were cut into two pieces. The high aluminium content samples were brittle and cracked when they were fastened in the vice for cutting. The more ductile samples were cut with a diamond wheel in a Struers Accutome. One half was mounted in a conductive resin and prepared metallographically to a 0.25 μm finish.

3.3 Analyses

3.3.1 Scanning electron microscopy and Energy Dispersive X-ray Analysis (SEM/EDS)

All imaging was conducted in the backscattered electron (BSE) mode for phase contrast, on a LEO 1525 field-emission scanning electron microscope (FE-SEM). BSE mode is suitable for phase analysis, as the intensity of the backscattered electrons is a function of the atomic number of the phase, so different phases have a different amount of backscattered electrons associated with them and this shows as different shades of grey in the resulting micrograph. The higher the average atomic number of the phase, the more electrons are backscattered and the brighter the phase appears in the micrograph.

The overall and phase compositions of the samples were determined using an Oxford INCA energy dispersive X-ray (EDS) system attached to the abovementioned SEM. The resolution of the EDS detector was 132 eV. The accelerating voltage was optimised for the alloys using the Oxford Inca Spectrum Synthesiser, since all samples could only contain Al, Pt and Ru. The synthesiser program models the spectrum, taking into account the input variables for EDS, as well as the energy lines which will be used for analysis. The acquisition conditions can be optimised taking into account the elements present in the sample. This ensured that excessive over-voltages were not used in generating the X-rays for EDS, as this could influence the results significantly. All samples were analysed at 12 mm working distance (optimum for the SEM used) and 12 kV accelerating voltage. All the EDS analyses were done quantitatively against pure element standards.

The microstructures of the samples were visually inspected in the SEM prior to analysis to ensure they were homogenous. Some samples had a small fraction of unreacted Ru in them. In these cases, the areas adjacent to the Ru were avoided in the analysis. The presence of the Ru was not considered a problem as previous sample preparations involving Ru at Mintek has shown that Ru tends to agglomerate and form lumps, especially in the small samples which are mixed by hand. It is also possible that the Ru did not melt properly, as Ru has a very high melting point (2701 K).

Overall compositions were determined by scanning a sufficiently large area of the sample, 200 – 1000 times magnification, depending on how coarse the microstructure was. Five overall analyses were recorded per sample.

The composition of each phase was recorded in spot mode in the SEM. At least five spots were measured for each phase and for each phase the standard deviation was calculated. In some samples the phases were present on a very fine scale, which complicated results, since the spatial resolution of EDS analysis is not lower than 1 μm . X-ray information in EDS comes from an interaction volume from about 5 to 2 μm under the surface of the sample,

depending on the operating conditions and average atomic number of the phase, which means that for fine particles, there could be a big matrix contribution. In these cases, more analysis points were recorded, and were taken into account in the plotting of the results on a ternary projection, as the composition of the two phases must lie on the tie-line between the two phases. Due to this, phases could not always be assigned beyond doubt using EDS, thus X-ray diffraction (XRD) was used to confirm phases.

It should be noted that since all samples were analysed at the same conditions, the standard deviations reported in this study only reflect the composition deviations and are not true uncertainties associated with EDS analysis. EDS is only accurate to a minimum of ± 1 at. % due to counting statistics, detector resolution, beam-sample interactions and a number of other factors. However, these factors have been assumed constant in this study as all the samples contained the same elements and all the conditions were constant. Depending on operating conditions, EDS also has a minimum detection limit of 0.5 - 2 at. %, which means that low concentrations of one of the elements in a binary phase could not always be detected. Thus, the uncertainty for elements present in low atomic percentages was much higher. Again, all factors were assumed constant and low atomic concentrations have been reported in the same way as higher concentrations.

3.3.2 X-Ray Diffraction

The samples were broken out of the resin mounts and analysed in a Philips XRD, with monochromated Cu K α radiation using a continuous scan from 4 to 90° 2 θ with step size of 0.02° and dwell time of 0.5 s, to confirm the phases found in EDS.

XRD is a suitable technique for phase analyses incorporating lattice parameter and lattice-type determinations on crystalline materials. XRD can also be used to determine and evaluate the effect of a solute on the lattice parameter of a phase.

XRD is based on Bragg diffraction. When a crystalline material is irradiated by a monochromatic source of X-rays, reflections will occur from the various lattice planes in the crystal. Each reflecting plane will diffract a portion of the X-ray beam as governed by the relationship

$$n\lambda = 2d \sin \theta$$

where

λ = wavelength of the incident radiation

d = interplanar spacing

θ = incident angle of radiation with the plane

n = a small integer.

The reflections are characteristic for a specific crystal structure and give the d -values for a phase, from which the lattice parameter can be calculated through the relationship (for a cubic phase)

$$d^2 = \frac{a^2}{h^2 + k^2 + l^2}$$

where d is the interplanar spacing, a is the lattice parameter and h , k and l are the Miller indices, referring to the plane from which the reflection originates. The positions of the atoms in the unit cell are then determined by the space group.

Phases are identified in XRD by matching the phase under investigation to standard patterns, which are available in the International Crystallography Diffraction Database (ICDD) [2001ICD] and International Crystal Structure Database (ICSD) [2002ICS]. However, there are many phases not yet included in these databases, and the standard patterns are normally only for end-member phases, solid solutions are usually not included.

Many of the phases found in the Al-Pt and Al-Ru binaries are not included in the ICDD or ICSD. Most of the binary phases showed solubility for the third element in the system, which shifts the position of the reflections. Some of the diffraction patterns also had overlaps on the major peaks. These complicated the XRD identification significantly and a different approach to only matching recorded and standard patterns had to be followed to confirm the phases proposed by EDS analyses.

A method that is used at the CSIR-NML has been followed to identify the phases. This method uses a software program WinCell [2002Raj], a freeware program from the internet, to refine lattice parameters, based on the crystal structure, d -values and (hkl) values for a phase. From the crystal structure data reported in the literature for the pure binary phases, the lattice parameter and reflections present in the spectra were known.

The method comprised the following steps:

1. For the phases that were present in the ICDD or ICSD, the lattice parameters were calculated in WinCell from the standard pattern data in the database. For phases which were not in the databases, but for which prototypes have been suggested in the literature, the lattice parameters of the prototypes have been calculated. For some phases very limited data were available and in those cases related binary systems were searched to find suitable prototypes. Some phases have more than one prototype suggested in the literature, in these cases all the prototypes were evaluated, as there are some discrepancies in the binary phase diagrams. This provided a starting set of values for each phase.
2. Once a 'standard' has been set up in WinCell, the corresponding phase was evaluated. The corresponding 2θ values from the diffractogram were selected for input to WinCell and a lattice parameter was calculated and refined through a non-linear regression method. A standard deviation and an overall coefficient of determination, R^2 , are also calculated for each phase.

In Appendix B the XRD spectrum, the ICDD data of the phases to be confirmed, the WinCell inputs and results are presented as an example.

Unfortunately, in WinCell it was not possible to assign different weights to the relative intensities of the reflections in the diffractogram, which sometimes complicated the calculations. But this method also ensured that all phases were, as far as possible, identified, as the number of lines in the diffractogram that were not already assigned to a phase could be identified.

The advantage of this approach was that phases could be identified with a figure of merit, the R^2 value, and that the shifts due to the presence of a third element in the binary phase lattice were taken into account, making it possible to calculate the solid solubilities of the phases.

Two new ternary phases were also found in the study. The one phase is a high temperature phase and was found in only one sample. It was not quenched into the microstructure, and decomposed. This phase is referred to as phase T in this study. The other ternary phase, called phase X in this study, was stable to room temperature and present in a number of samples. Through a search and match procedure, a structure was found which matched the diffraction patterns of this phase. This was then used as a prototype for phase X.

3.4 Methodology to determine a solidification sequence for a ternary alloy

In order to determine a solidification sequence of an alloy and then propose a liquidus surface projection, also called the polythermal projection of the liquidus, fundamental thermodynamic principles as well as practical experimental observations have to be considered. This section attempts to describe the basic method which was used to propose the solidification sequences and liquidus surface projection.

3.4.1 Analyses of as-cast alloys

Overall compositions were determined for the samples. The phases in the microstructure were then analysed. EDS is a useful tool to determine the compositions of the phases as well as the overall composition of the alloy. The composition results from the EDS analyses were plotted on a ternary composition triangle. In this study all the overall compositions are indicated with a solid square on the diagrams and the phase compositions are indicated with solid triangles. These are shown in Figure 3.1. When there were only two phases present in a sample, the overall composition had to be on the line connecting the two-phase compositions. When there were three or four phases present, the overall composition had to fall within the area formed when the phase compositions are connected, as shown below for the triangular area.

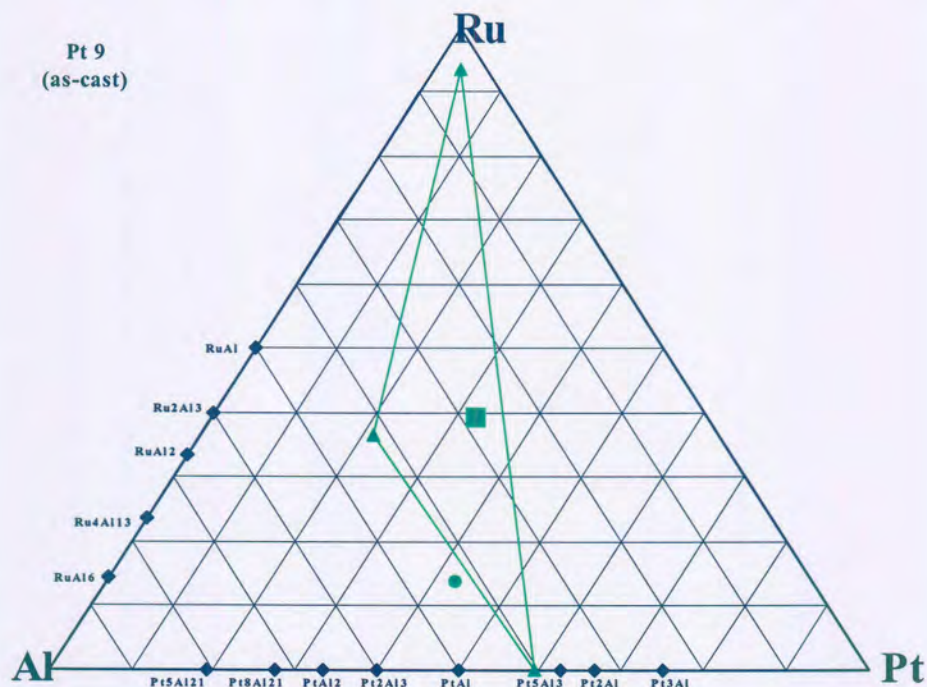


Figure 3.1. Ternary plot showing the EDS phase analyses. The square indicates the overall composition, the triangles the phase analysis and the solid circle indicates a two-phase area.

Since EDS only gives the compositions of the phases, and not the structures, XRD analyses had to be used to confirm the phases in the sample. The phases confirmed by XRD were assigned to the phase compositions on the ternary plot. This had to be in agreement with the binary phases on the axes of the ternary diagram, unless it was a ternary phase, for which there is no extrapolation to the binaries that make up the ternary diagram.

The shapes of the phases in the microstructures were also evaluated qualitatively. Did the phase form dendrites in a matrix? Were the dendrites coated with another phase? Was the area between the dendrites a mixture of two phases? Which phase was coating what? These are important considerations in determining the solidification sequence and in identifying what type of reaction (monotectic, eutectic or peritectic) occurred.

Phases solidify in a sequence. The order of the sequence is very important, because it gives the order of the reactions.

3.4.2 Fundamental and theoretical considerations

Once the experimental analysis data were consolidated, certain fundamental and theoretical factors were considered to propose a solidification reaction sequence and to plot a proposed liquidus surface projection for the Al-Pt-Ru system. These are outlined below. Although discrepancies can occur between the theory and experiment, these should not detract from the usefulness of the theoretical approach, since the theory can provide useful ideas on the phase growth and resulting experimental microstructures.

This discussion is only a rough guideline to the possible fundamental and theoretical considerations, as non-equilibrium solidification of multi-element liquids is complex and it is influenced by many factors. Predicting what will happen only theoretically is, today, still nearly impossible.

3.4.2.1 Phase Diagram Considerations

The Phase Rule

During equilibrium solidification, the phase rules must be obeyed. The phase rule is

$$F = C - P + 2$$

where F is the degrees of freedom, C is the number of components and P is the number of phases, and it describes the relation between the phases and system variables (temperature, pressure and composition). At constant pressure, the rule reduces to

$$F = C - P + 1.$$

Although the non-equilibrium freezing of the arc-melted samples is too fast for equilibrium solidification, and compositions constantly change during the non-equilibrium freezing, a local equilibrium at each interface can be assumed, and the basic principles of the phase rule should be considered in considering and evaluating the invariant reactions.

Reactions in a ternary system

In a ternary system, all the reactions from the binary systems are possible in the ternary system, as well as some ternary reactions. The most commonly observed ternary reactions are [1965Wes]:

- (i) ternary eutectic reactions $L \rightarrow \alpha + \beta + \gamma$,
- (ii) ternary quasi-peritectic reactions $L + \alpha \rightarrow \beta + \gamma$
- (iii) true ternary peritectic reactions $L + \alpha + \beta \rightarrow \gamma$.

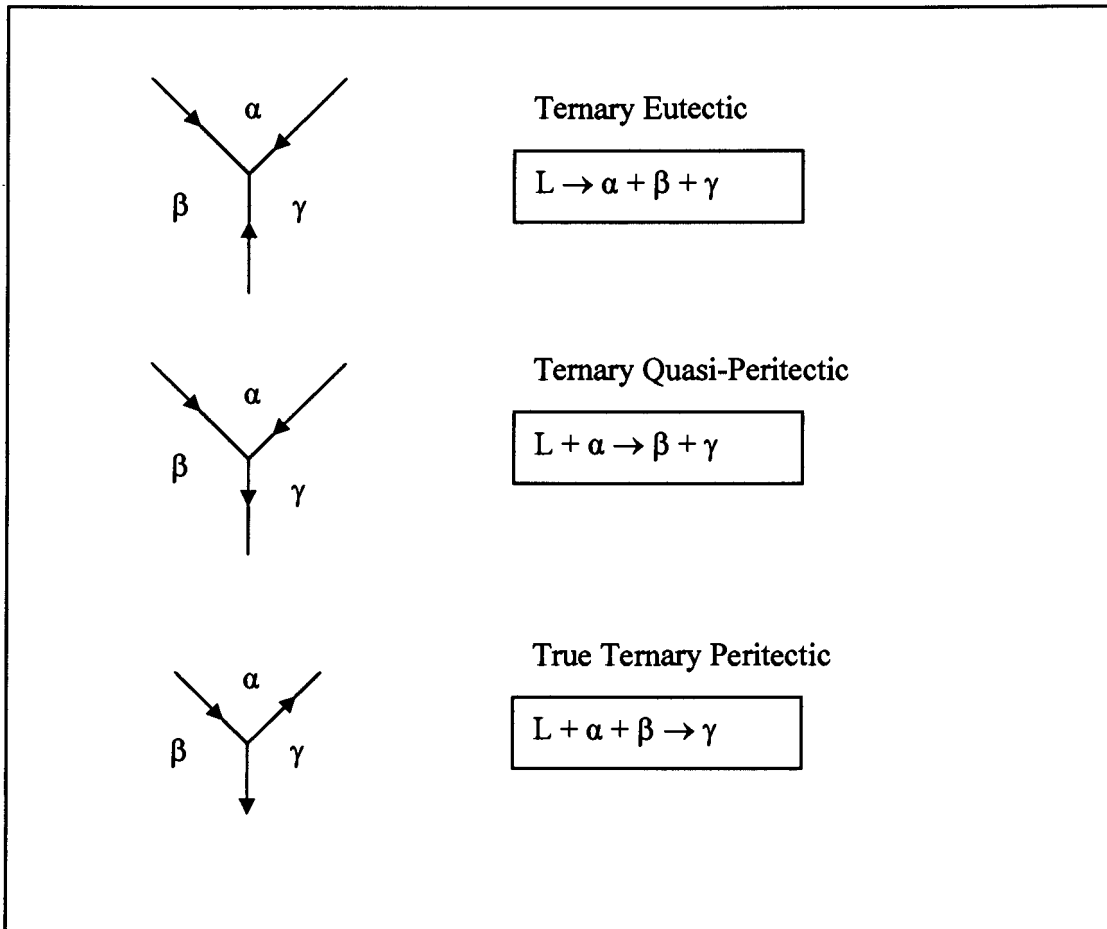


Figure 3.2 Ternary invariant reactions, after West [1965Wes].

These ternary reactions are illustrated in Figure 3.2, where the arrows on the liquid surface point in the direction of decreasing temperature. Reaction (ii) is also sometimes referred to as a 'weak' peritectic reaction.

It is important to note that a reaction which is an eutectic reaction in the binary, can appear as a peritectic reaction in the ternary. The presence of a third element in the ternary can change the compositions of the binary phases when the third element is dissolved in the binary phase in the ternary system. This can change the Gibbs energy of the phase so that the relative stabilities of the phases change. Thermodynamically, a eutectic reaction can become a peritectic reaction. In some cases, the eutectic reaction was observed before the conditions for the eutectic became unstable, in other cases the eutectic from the binary was not observed at all, only the peritectic reaction was observed. Also, if cooled too quickly, a stable eutectic reaction can become a metastable peritectic reaction.

3.4.2.2 Liquid-solid interactions and transformations

Some fundamentals on liquid-solid transformations were considered. Solidification of an alloy from the liquid consists of nucleation of the primary solidification phase in the liquid, and then the growth of the phase into the liquid, consuming the liquid, until all the liquid is solidified.

Nucleation

Nucleation is always associated with a change in crystal structure, a change in volume or a change in composition. Embryos form in the liquid, and once these reach a critical size and become thermodynamically stable, a stable nucleus is formed.

Solid-liquid interactions

The liquid-solid interface of the growing solid nucleus shows three characteristic features [1972Cha]:

- (i) the interface is non-crystallographic and atomically rough;
- (ii) the interface is planar, i.e. contains no projections;
- (iii) the interface is isothermal and undercooled by an amount ΔT related to the growth rate.

Not all of above is necessarily observed.

The growth of the nuclei is then dependent on the interface energy, surface energy of the nuclei and amount of undercooling. Liquid metal must undercool by a few degrees before solidification begins. The type and direction of grain growth is controlled by the temperature gradients at the solid-liquid interface. It is also dependent on the alloy composition.

As solidification continues after nucleation, temperature gradients develop. The gradients develop during the transport of the latent heat of fusion from the interface, produced by the formation of the solid phase. If the liquid-solid interface grows into a supercooled liquid (negative temperature gradient), protrusions at the interface can grow into the liquid without being melted back, resulting in dendritic growth. If the temperature gradient ahead of the interface is positive, then grain growth occurs by the advancement of a more stable solid-liquid interface. The liquid can also be supercooled by both thermal and constitutional effects, then seed crystals can appear, which can grow into equiaxed, dendritic or columnar crystals.

It is often that the bulk sample solidifies with a dendritic morphology. Dendrites grow in quite specific crystallographic directions. Dendrites can have a cellular appearance, or branches can develop to produce a tree-like appearance, depending on the composition and temperature gradients. However, the morphology of the primary phase also depends on the surface energy of the primary phase, and when growth in a specific crystal direction in the liquid is not thermodynamically favoured, discrete particles can form in the liquid. The discrete particles grow without direction preference or they can form faceted crystals.

The growth of the primary phase continues until the remaining liquid composition is too saturated with elements rejected from the solid and the phase cannot grow anymore. This is assuming that most of the partitioning of the elements occurs in the liquid and not in the solid. Then three types of liquid-solid interactions are possible. Eutectic, peritectic and monotectic reactions occur most often in a ternary system. For eutectic and peritectic reactions, the liquid phase is in equilibrium with two solid phases. These are recognised by their different morphologies [1972Cha]. The peritectic reaction can continue only whilst the phase being

coated is still in contact with the liquid. For a monotectic type reaction, a miscibility gap must exist in the liquid.

The further sequence of solidification is then determined taking into account the shape of the microstructure.

Eutectic reactions are the simultaneous solidification of two phases and the two phases are always finely dispersed. The morphology could include globular, rod-like, lamellar and more irregular shapes (see Chadwick [1972Cha] for detail on eutectic morphologies). In peritectic reactions, the phase which formed peritectically formed directly on the phase which reacted with the liquid, in other words, the phase which formed peritectically 'coated' the primary phase. Since the liquid reacted with the primary phase, the latter could have an uneven appearance.

Solid-state eutectoid reactions occur where a phase had been formed during solidification and it is not stable at lower temperatures. A solid-state decomposition is characterized by a very fine structure if a high nucleation rate was attained. In the time during rapid solidification, the structure remains fine, as the diffusion rates are much less in the solid, and at a lower temperature than solidification from the liquid.

Coring is also possible in as-cast samples. Coring means that individual dendrites do not have the same composition from the center to the outer edge of the dendrite. This is due to the fact that the composition of the solidifying liquid, as well as the temperature of the liquid, is changing as the dendrite grows from the liquid. The composition of the liquid is either enriched or depleted of a solute, thus the solute concentration in the dendrite differs from the surrounding liquid, and the phase solidifies in a continuous layered structure until the liquid concentration has changed and the phase cannot precipitate anymore (Figure 3.3).

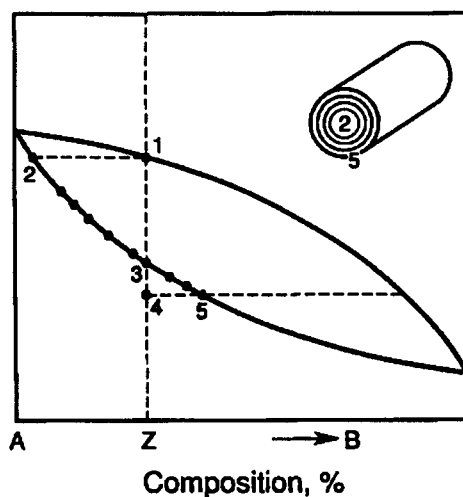


Figure 3.3. Phase diagram of two components showing the influence of solute diffusion on solidification, a phenomenon called coring [1990Tom].

3.4.2.3 Deriving the solidification sequence and liquidus surface projection

The proposed solidification sequence and liquidus surface projection were derived from the experimental microstructures. Drawing a liquidus surface projection is a bit like building a jigsaw puzzle, as a number of factors need to be considered.

For each alloy a solidification sequence was deduced. The primary phase was identified, and the solidification reactions were proposed as eutectic or peritectic, following the shape of the microstructure. These deduced solidification sequences for the alloys were used to derive the liquidus surface projection.

The overall composition of an alloy falls on the liquid surface of the primary phase. Furthermore, the surfaces of phases in a particular solidification reaction had to be in contact on the liquidus surface projection. The solidification reactions also had to agree with the liquid reactions found in the binaries, although, as described above, the reaction types could have changed based on the relative thermodynamic stabilities of the phases when third elements are dissolved in the binary crystal structures.

The proposed solidification sequence had to be consistent with the microstructure. The order of the phases in the microstructure, from the primary phase to the final phase solidified, had to be such that there were no extra phases in the microstructure between two consecutive phases in the solidification sequence. The cooling of the as-cast alloys was too fast to allow phases to form through diffusion alone, although it was not fast enough to prevent coring and solid state decomposition. Although quite unusual in as-cast alloys, it is possible that in some cases a phase is not observed, since in some peritectic reactions all the previously formed phase can be consumed during the reaction. In such cases, only a small part of the liquid surface of the consumed phase could fall on the solidification path on the liquidus surface projection. The solidification reactions had to agree with the liquid reactions found in the binaries, although, as described above, the reaction types can change based on the relative thermodynamic stabilities of the phases when third elements are dissolved in the binary crystal structures.

Since three binary systems were involved, and ternary phases could be present, the solidification microstructures were used as input to the solidification sequence. Usually the same order of formation for the phases from the liquid had to occur in the ternary system. It was also considered that the presence of a third element in a binary structure could change the composition range and formation temperature of the phase. The formation temperatures of the phases from the liquid in the binary systems were also used to give an indication of the solidification sequence.

The proposed liquidus surface projection was evaluated against the solidification sequences to ensure consistency between them. This is best explained with an example. If one considers the alloy composition 14 (overall and the phase compositions) plotted on a liquidus surface projection (Figure 3.4), the primary crystallisation product will be RuAl_2 , since the overall composition lies on the RuAl_2 liquidus surface. RuAl_2 is not a stoichiometric line compound in the binary system; it shows a small solubility range, which extends more to the Al-side than the Ru-side (Figures 2.4 and 2.5 in Chapter 2). The crystallisation path of the liquid will be along a line roughly towards the overall composition and the phase composition of RuAl_2 . If RuAl_2 had been a line compound, the crystallisation path of the liquid would have been on the straight line between the overall composition and the RuAl_2 composition on the Al-Ru side of the ternary plot. The solidification of RuAl_2 continues until the liquid attains a composition on

the univariant valley, the boundary between the $RuAl_2$ and X liquidus surfaces. The direction of continued solidifications is determined by the direction of the liquidus slope (valley or 'kink'), as well as the steepness of the slopes of the adjoining liquidus surfaces. The solidification can continue down the valley in a eutectic, or go over the adjoining liquidus surface if the slope permits it in a peritectic. In the example, the solidification continues in a peritectic way over the liquidus surface of phase X, until the liquid compositions reach the univariant boundary between X and $PtAl_2$. The solidification continues down the valley, until there is no more liquid to consume.

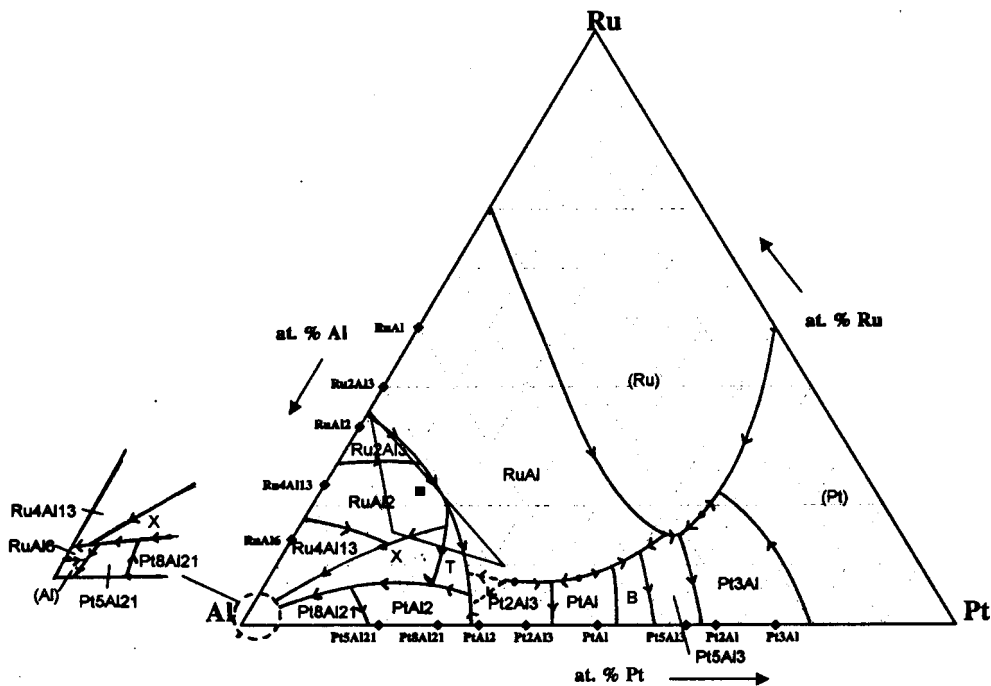


Figure 3.4. Sample 14 on the liquidus surface.

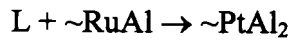
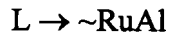
Pelton [1995Pel] presented the solidification of a ternary alloy in more detail. However, only stoichiometric line compounds were considered in the discussion.

It is possible that, in some cases, the path of solidification crossed a liquidus surface of a phase which is not observed. In such a case, the phase probably was consumed during a peritectic reaction and it was not observed in the solidification microstructure, especially for a small liquidus surface. In cases where the two adjacent liquidus slopes are both very steep, the solidification path might have 'jumped' to the other surface before the univariant boundary between the two phases was reached.

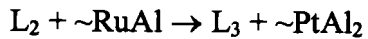
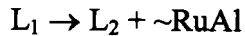
Although the solidification occurred under non-equilibrium conditions, the Gibbs phase rule should be obeyed in the liquidus surface projection. For a ternary system at constant pressure, the phase rule becomes $F = 4 - P$, where F is the degrees of freedom and P is the number of phases. When the liquid and one solid phase are in equilibrium, $P = 2$, thus $F = 2$ and the system is bivariant. A ternary liquidus is thus a two-dimensional surface. At a ternary eutectic point, $F = 0$ as the temperature and the composition for all four phases (liquid, α , β and γ) in equilibrium are fixed. Thus, in a ternary system, only three phases can be in equilibrium at any stage, so no more than three lines could meet in an invariant point on the liquidus surface.

3.5 Syntax and terminology

Solidification reaction sequences are sometimes written in “short hand”, without indicating the remaining liquid on the right hand side of the equation. Thus, in this work, solidification reactions were written as



with the above actually implying more explicitly, the following



In some instances, a ‘~’ sign is put in front of a binary phase. This indicates that the binary phase shows some solubility for the third element in the system, and that the phase is slightly changed from the pure binary phase. The ‘~’ sign is also sometimes used to represent a non-stoichiometric binary phase.

The end members of the ternary phase diagram (the corners) are the solid solutions of aluminium, platinum and ruthenium, dissolving varying amounts of the other two elements in the system. These solid solutions are indicated in parentheses: (Al), (Pt) and (Ru).

A line compound describes a phase with no solubility range. A phase is stoichiometric when it appears at its stoichiometric composition in the phase diagram.

Chapter 4

Results and Discussion of the Experimental Investigation.

This chapter presents and discusses the results of the experimental work.

The first part of the chapter deals with the analyses of the alloy samples, evaluating the microstructures and proposing a solidification sequence. The XRD results and observations are discussed. An overall solidification sequence for the Al-Pt-Ru system is presented and a liquidus surface projection is proposed. Some conclusions are made from the experimental results.

4.1 Introduction

Sixteen samples were analysed in the as-cast condition. The alloy compositions of the alloys studied are shown in Figure 4.1. The targeted and analysed compositions are listed in Table 4.1. The microstructures were investigated in the SEM, the overall compositions determined and the phase compositions were analysed with EDS, and confirmed by XRD where possible.

Six samples (1-6) were initially selected. A further six (7-12) was prepared to shed more light and clarify discrepancies from the first six samples. A further three samples (13-15) were prepared to glean more information in unclear areas of the system. As new ternary phase was suspected, a final sample (16) was prepared, the composition of this sampled was specifically targeted in the are of this sample. Samples were not prepared for the high platinum side, since that have been covered in two previous studies [2001Big, 2001Hil]

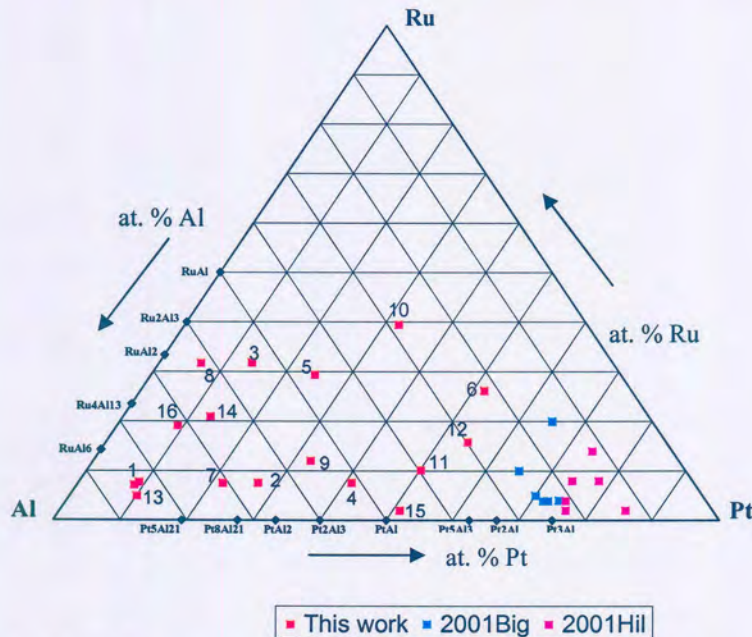


Figure 4.1. Overall compositions of the Al-Pt-Ru alloys studied.

Table 4.1. Targeted and analysed compositions for the experimental alloy samples.

Sample	Targeted Composition (at. %)			Analysed Composition (at. %)		
	Al	Pt	Ru	Al	Pt	Ru
PAR 1	86	7	7	84	8.5	7.5
PAR 2	66	26	6	65	26.9	7.6
PAR 3	57	12	31	54.4	13.8	31.8
PAR 4	54	38	8	51.6	40.9	7.6
PAR 5	50	25	25	43.6	26.5	29.9
PAR 6	25	55	20	21.4	51.7	26.2
PAR 7	73	22	5	70.8	21.6	7.6
PAR 8	71	7	22	62.0	6.2	31.8
PAR 9	59	33	8	55.4	32.5	12.1
PAR 10	34	40	26	28	32.6	39.5
PAR 11	42	52	6	39.7	50.1	10.2
PAR 12	33	59	8	29.9	54.3	15.8
PAR 13	85	10	5	87.6	8.5	4
PAR 14	66	13	21	64.0	13.6	22.4
PAR 15	47	51	2	42.0	55.7	2.3
PAR 16	74	8	18	71.9	8.9	19.2

From Table 4.1 it can be seen that in most cases the analysed Al composition was lower than the targeted composition, while the Ru composition was higher. This was expected, as Al has a much lower melting point than both Pt and Ru. Since some unreacted Ru was observed in some samples, the lower Al content observation was not consistent throughout all the samples, e.g. PAR13, which showed a higher Al content in the analysed results than what was targeted.

Porosity was observed in a number of samples. This was probably due to the fast cooling rates and the presence of Al, which has a much lower solidification temperature and higher partial pressure than Pt and Ru, leading to vaporisation. It could also have been due to traces of water vapour, despite precautions, in the samples prior to the arc-melting.

4.2 Microstructures and proposed solidification sequences

Each alloy sample was analysed, the phases determined and a solidification sequence was proposed for each alloy. These are discussed here, the XRD results will be discussed separately in paragraph 4.3.

4.2.1 PAR 1 - Al₈₆:Pt₇:Ru₇ alloy

The as-cast button was extremely brittle and crumbled into small pieces while clamping it in a vice to cut in half.

The PAR 1 alloy exhibited two distinctly different regions in the microstructure (Figure 4.2a and b). The composition of the two areas, however, was not significantly different. The origin of the two different structures is difficult to explain due to a lack of data, but,

since the coarser phase was observed mostly on the outside of the sample, it could be that columnar liquid dendrites with a very slight difference in composition formed and that it was enough to follow different solidification paths. The ‘coarser’ microstructure (Figure 4.2 d) shows light dendrites in a dark matrix, with some precipitation in the matrix. The ‘finer’ microstructure (Figure 4.2 c) shows a light phase coated by a darker phase in a dark matrix, also with some precipitation in the dark matrix.

The phase compositions are given in Table 4.2 and are plotted on a ternary projection in Figure 4.3.

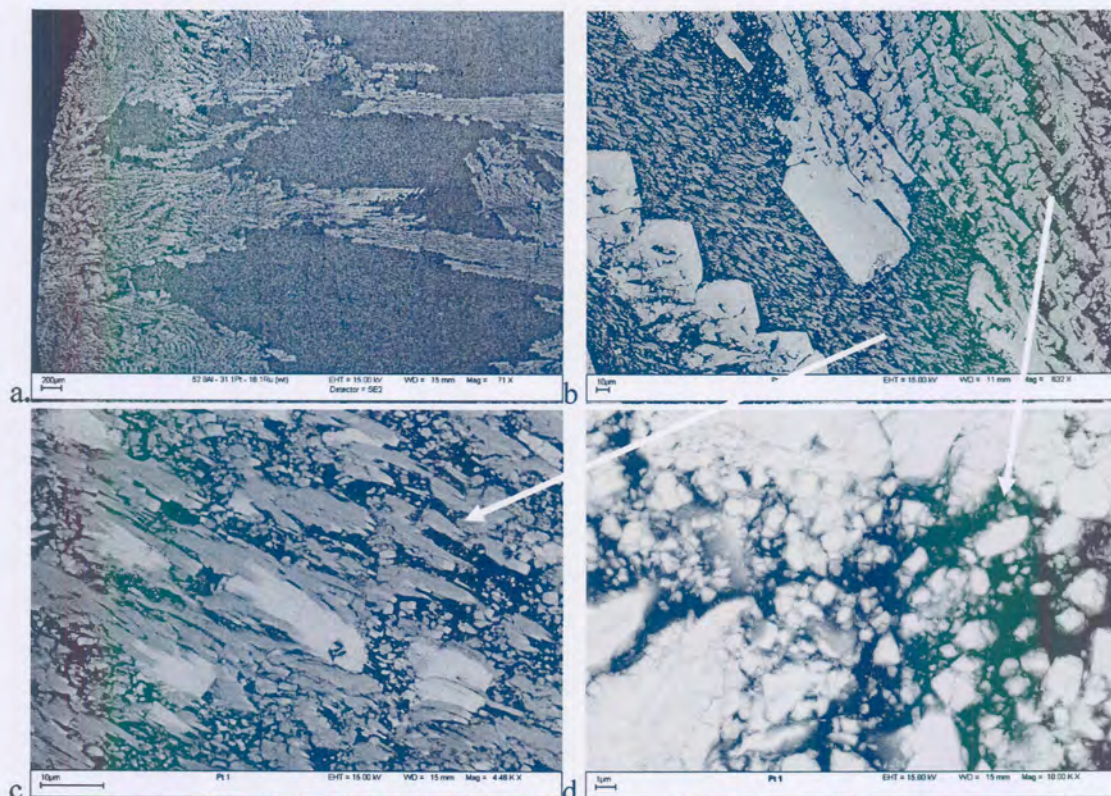


Figure 4.2. (a) and (b) show the two distinct different microstructure areas observed in the PAR1 alloy. (c) shows the detail of the finer (darker) microstructure and (d) shows the detail of the lighter, coarser microstructure area.

Table 4.2. Summary of phase and composition analysis for the PAR1 alloy.

Sample	Condition	Phase Description	Composition			Proposed phase(s)	No of analyses
			Al	Pt	Ru		
PAR 1	Arc-melted	Overall	84.0 ± 0.6	8.5 ± 0.5	7.5 ± 0.6		5
		Fine microstructure	84.3 ± 0.6	8.5 ± 0.6	7.2 ± 0.6		5
		Black	100			(Al)	3
		Grey	76.1 ± 1	10.5 ± 0.7	13.4 ± 0.6	X	10
		Light	75.1 ± 0.2	20.8 ± 0.5	4.1 ± 0.5	~Pt ₅ Al ₂₁	9
		Coarse microstructure	83.3 ± 0.6	8.9 ± 0.6	7.8 ± 0.6		5
		Black	100			(Al)	3
		Very light	75.1 ± 0.3	14.1 ± 1.3	10.8 ± 1.1	X	6
		Grayish	72.8 ± 0.2	13.9 ± 0.7	13.3 ± 0.7	~RuAl ₆	5

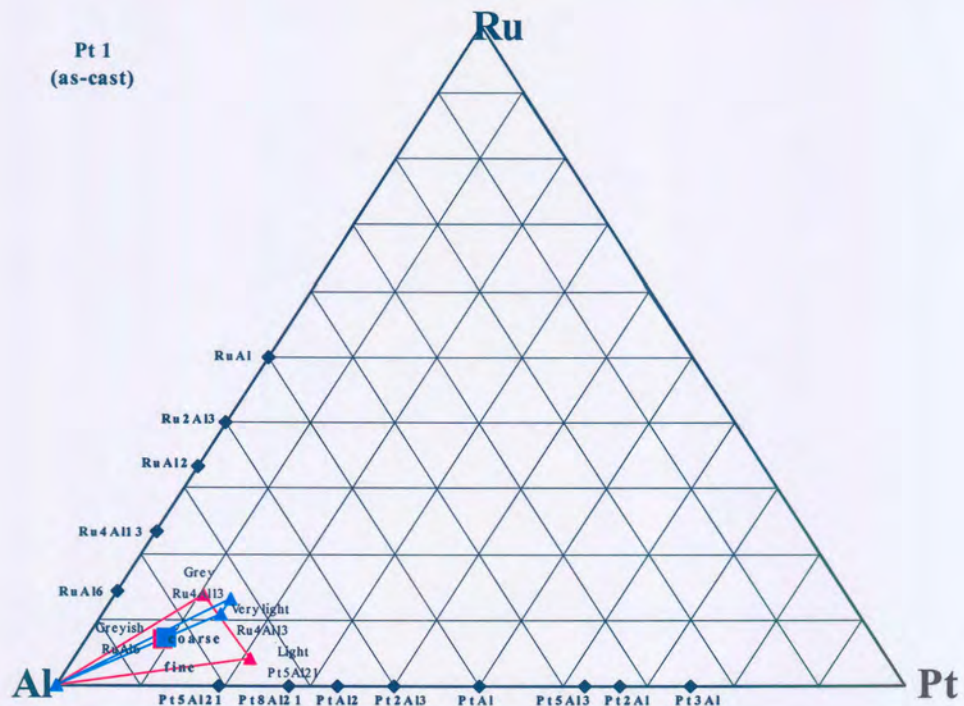


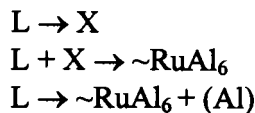
Figure 4.3. A ternary plot of the overall and phase compositions in the PAR 1 alloy.

In the 'coarse' microstructure, the ternary phase X solidified first in the liquid as dendrites. ~RuAl₆ then formed peritectically, coating the X-phase dendrites. The final liquid solidified eutectically, forming ~RuAl₆ and (Al).

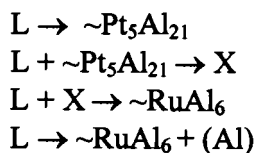
In the 'fine' microstructure alloy, the primary phase is different to the primary phase in the coarse microstructure. $\sim\text{Pt}_5\text{Al}_{21}$ solidified from the liquid. The X phase coated the primary phase, indicating that it solidified peritectically. On the outside of the X, a phase is seen as small light specs, it is probably $\sim\text{RuAl}_6$ that has formed peritectically. The final liquid solidified eutectically, forming (Al) and a small amount of $\sim\text{RuAl}_6$.

From the phase and composition analyses of this alloy, the following solidification sequence is proposed

Coarse area



Fine area



Not all the proposed reactions were observed in the solidification microstructure, as the phases were too fine to identify all of them accurately.

Since the last part of the proposed solidification sequences for the two microstructures are the same, that one part of the liquid was slightly enriched in Ru and depleted in Pt relative to the other part, if columnar type solidification is assumed, leading to different primary solidification. The composition difference might have been big enough for such a phenomenon and the EDS technique may not have been sensitive enough to pick up the real composition difference.

The phases were very finely dispersed and it was difficult to analyse the phases accurately with EDS. Unfortunately, in this sample, most of the proposed phases did not have prototypes suggested in the literature, which made confirmation by XRD difficult/impossible. The solidification for this alloy thus has some uncertainty associated with it.

4.2.2 PAR 2 - $\text{Al}_{66}:\text{Pt}_{26}:\text{Ru}_6$ alloy

The PAR 2 alloy was extremely brittle and broke into pieces while fastening in a vice to cut the button-melt sample in half. The sample was also very porous.

The BSE images in Figure 4.4 show a light dendritic phase in a dark matrix. In the light phase, another dendritic structure can be observed. This is not a continuous dendrite, as can be seen in Figure 4.4(b).

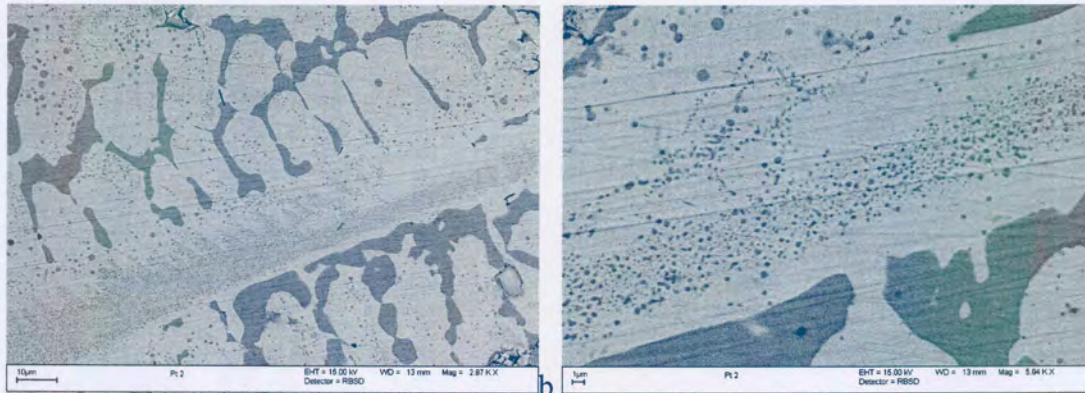


Figure 4.4. (a) shows the dendrite structure of PAR 2 and (b) shows the remnants of primary T in the light $PtAl_2$ dendrites.

Table 4.3 Summary of the phase and composition analyses for the PAR 2 alloy.

Sample	Condition	Phase Description	Composition			Proposed phase(s)	No of analyses
			Al	Pt	Ru		
PAR 2	Arc-melted	Overall	65.5 ± 0.5	26.9 ± 0.4	7.6 ± 0.4		5
		Light	61.5 ± 0.3	32.6 ± 0.3	5.9 ± 0.5	$\sim PtAl_2$	5
		Dark	70.5 ± 0.4	16.6 ± 0.2	12.9 ± 0.4	X	5
		Two phase (in light phase)	64.0 ± 0.3	28.2 ± 0.2	38.8 ± 0.3	T+ $\sim PtAl_2$	5

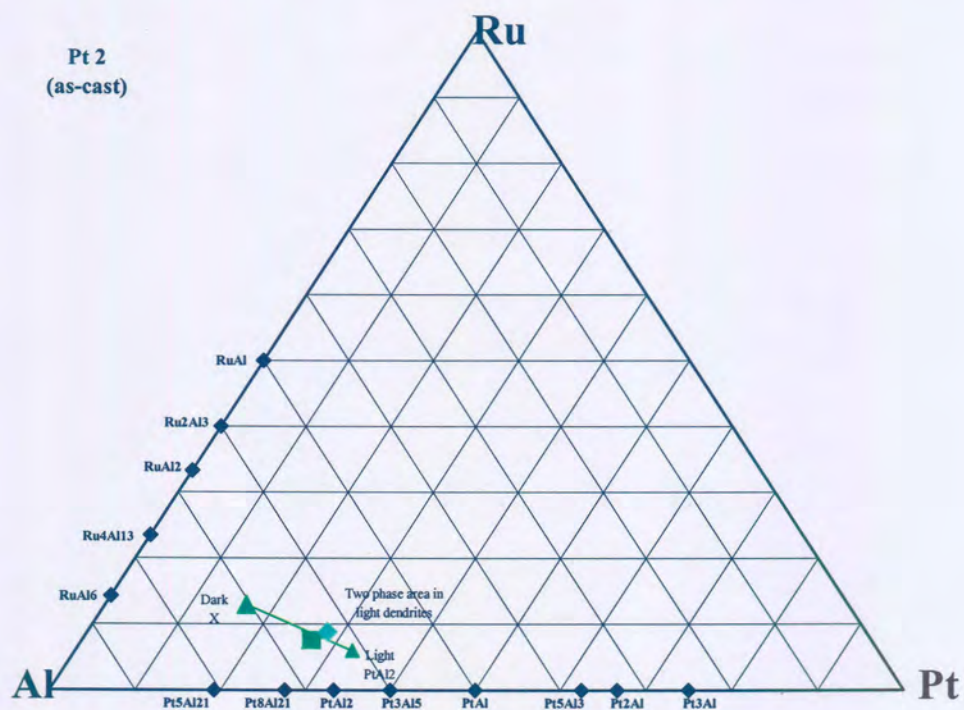
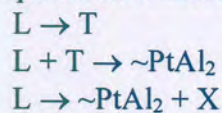


Figure 4.5. A ternary plot of the overall and phase compositions in the PAR 2 alloy.

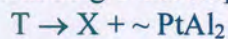
The phase compositions determined by EDS analyses are listed in Table 4.3 and have been plotted on a ternary projection in Figure 4.5.

The PAR 2 alloy first solidified from the liquid by forming phase T dendrites. Phase T is a proposed new ternary phase of composition $\text{Ru}_{18}\text{Pt}_{28}\text{Al}_{64}$. The liquid then reacted peritectically with phase T to form PtAl_2 . Most of the T was consumed in the peritectic reaction, leaving traces of phase T dendrites in the PtAl_2 dendrites. This is confirmed by EDS analysis, which found the composition of the two-phase area to be between the phase T composition and PtAl_2 composition (Figure 4.5 d). The last liquid transformed eutectically to PtAl_2 and phase X, a ternary phase stable at low temperatures.

The proposed solidification sequence can be summarised as follows:



Any remaining T decomposed



4.2.3 PAR 3 - $\text{Al}_{57}\text{Pt}_{12}\text{Ru}_{31}$ alloy

The PAR 3 alloy showed limited brittleness and little porosity.

The BSE images in Figure 4.6 show a dark grey dendritic phase in a light matrix. The dark grey dendrites are coated by a black phase. Between the dark grey dendrites and black phase, a fine two-phase area formed. On the outside of the black phase, another fine grey phase formed. A two-phase area also exists between the black and fine grey phase. Some of the grey phase is in the light matrix phase.

The phase compositions determined by EDS analyses are listed in Table 4.4 and have been plotted on a ternary projection in Figure 4.7.

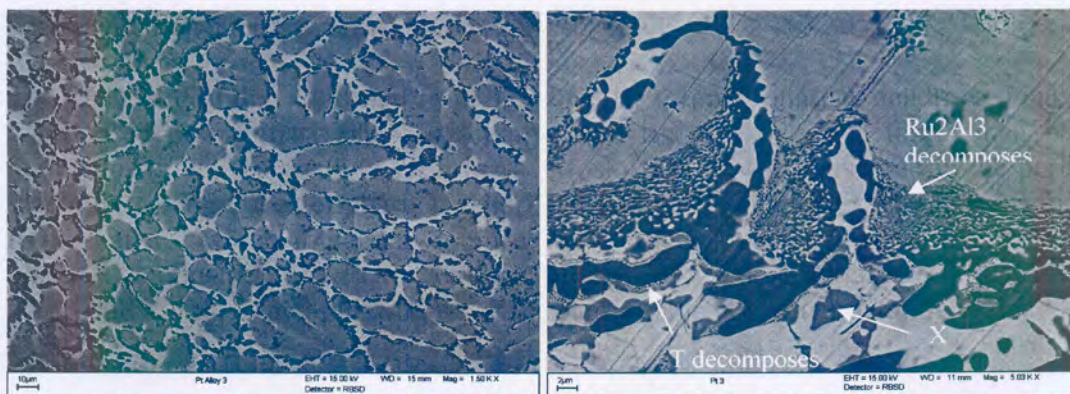


Figure 4.6. BSE images of PAR 3. (a) shows the overall microstructure. (b) shows the X phase as well as the two areas where Ru_2Al_3 and T decomposed.

Table 4.4. Summary of phase and composition analysis for the PAR 3 alloy.

Sample	Condition	Phase Description	Composition			Proposed phase(s)	No of analyses
			Al	Pt	Ru		
PAR 3	Arc-melted	Overall	65.5 ± 0.8	26.9 ± 0.9	7.6 ± 0.9		5
		Grey dendrites	49.4 ± 3	12.3 ± 1	38.3 ± 3.2	~RuAl	5
		Dark	63.2 ± 1.1	1.3 ± 0.5	36.6 ± 1.8	~RuAl ₂	5
		Light	57.3 ± 1.3	31.1 ± 1	11.6 ± 1.9	~PtAl ₂	5
		Darker Grey	69.6 ± 1.1	14.0 ± 1.4	16.4 ± 1.9	X	8

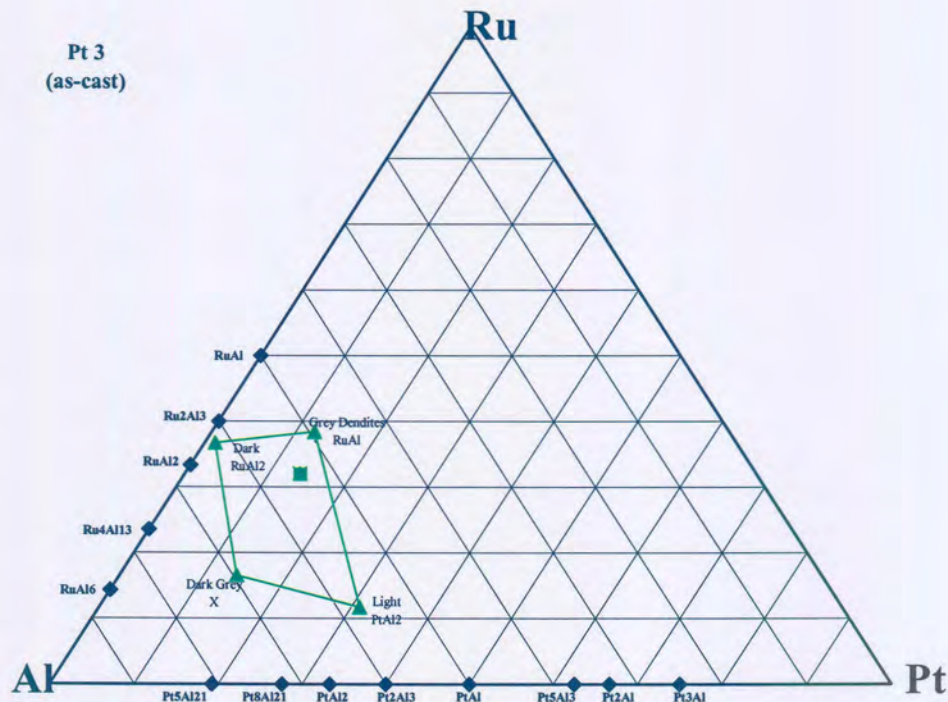
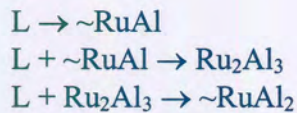


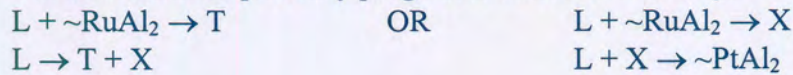
Figure 4.7 A ternary plot of the overall and phase compositions in the PAR 3 alloy.

The liquid first solidified as ~RuAl, the grey primary dendrite phase. Through a peritectic reaction, Ru₂Al₃ formed, coating the ~RuAl dendrites. The Ru₂Al₃ reacted with the liquid to form ~RuAl₂, the black phase. The solidification then proceeded in one of two ways: either the ~RuAl₂ reacted with the liquid to form X, which was consumed in a subsequent peritectic reaction between the liquid and X, or the ~RuAl₂ reacted with the liquid to form a ternary phase T, which coated the ~RuAl phase before it formed X, a ternary phase, through a peritectic reaction. Ru₂Al₃ decomposed through a solid-state reaction to ~RuAl and ~RuAl₂, thus explaining the dark 'messy' two-phase structure that coated the primary ~RuAl dendrites. The ternary phase T also decomposed at lower temperatures, which explained the fine structures between ~RuAl₂ and the ternary phase X.

The proposed solidification sequence can be summarised as follow:



The solidification probably progressed in one of two ways



Ru_2Al_3 decomposed in the solid state:



4.2.4 PAR4 - $\text{Al}_{54}:\text{Pt}_{38}:\text{Ru}_8$ alloy

The PAR4 alloy showed some brittleness and the sample broke into four equal pieces when fastened in a vice for cutting.

The BSE images in Figure 4.8 show dark cored dendrites coated by a light phase in a medium matrix. The light coating phase is not continuous; a fine structure is present in it.

The phase compositions determined by EDS analyses are listed in Table 4.5 and have been plotted on a ternary projection in Figure 4.9.

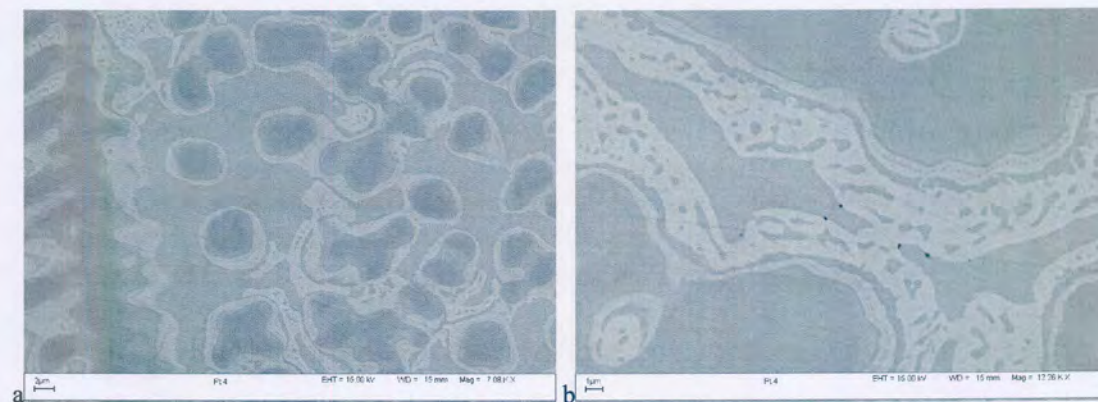


Figure 4.8. BSE images of PAR 4. (a) shows dark primary $\sim\text{RuAl}$ dendrites, coated by a PtAl layer (the light phase) in a Pt_2Al_3 matrix. (b) shows the detail of the PtAl coating layer.

Table 4.5. Summary of phase and composition analysis for the PAR4 alloy.

Sample	Condition	Phase Description	Composition			Proposed phase(s)	No of analyses
			Al	Pt	Ru		
PAR4	Arc-melted	Overall	51.6 ± 0.5	40.9 ± 3	7.6 ± 3.2		5
		Dark	45.3 ± 1.2	27.3 ± 1.4	27.4 ± 1.6	$\sim\text{RuAl}$	7
		Medium	55.2 ± 0.6	44.8 ± 0.6	0	Pt_2Al_3	6
		Light	47.4 ± 2	52.6 ± 2	0	PtAl	6

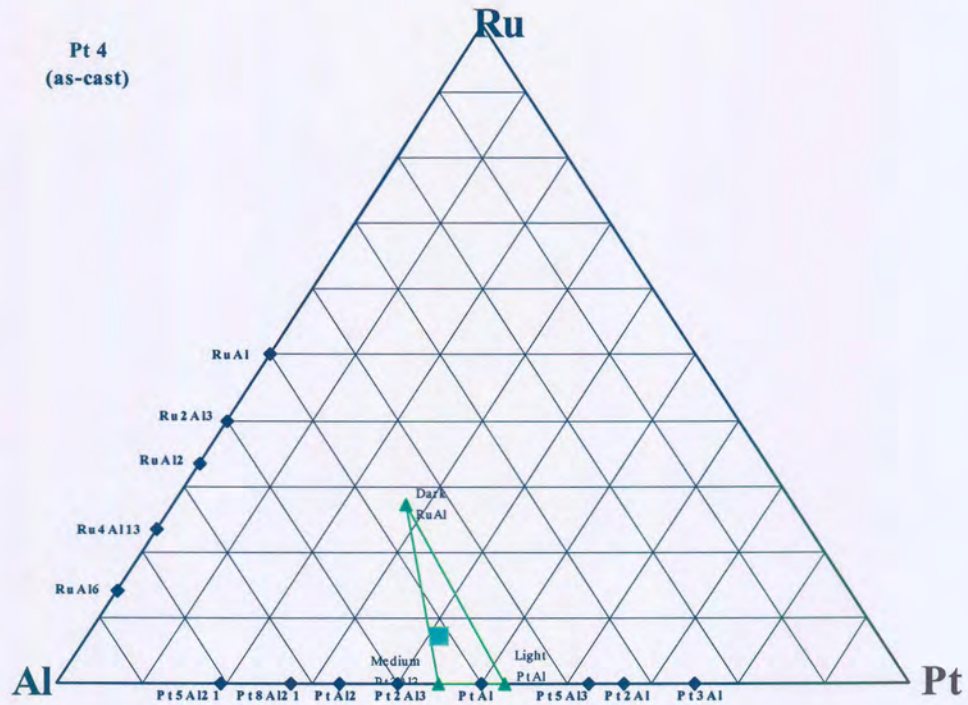
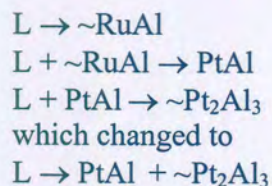


Figure 4.9. A ternary plot of the overall and phase compositions in the PAR 4 alloy.

The RuAl phase solidified as primary dendrites in the liquid. \sim RuAl then reacted peritectically with the liquid to form PtAl, which coated the RuAl dendrites. PtAl reacted peritectically with the liquid to form Pt₂Al₃. The peritectic reaction changed to solidify the final liquid eutectically. The change in the reaction was probably due to a change in the relative stabilities of the phases with respect to each other. Since the final liquid was possibly depleted of Ru, the eutectic solidification of liquid proceeded according to the Al-Pt binary, where an eutectic reaction exists between PtAl and Pt₂Al₃.

The proposed solidification sequence is as follows:



(The peritectic reaction $L + \sim\text{RuAl} \rightarrow \text{PtAl}$ was found to be actually the eutectic reaction $L \rightarrow \sim\text{RuAl} + \text{PtAl}$ after studying a 600°C (4 weeks) heat-treated sample.)

The overall analysis of this sample is on the RuAl liquid surface, which indicates that RuAl phase stretches to \sim 10 at. % from the Al-Pt binary.

4.2.5 PAR5 - Al₅₀:Pt₂₅:Ru₂₅ alloy

The PAR5 alloy was extremely brittle and it disintegrated into small pieces without a strong external force.

The BSE microstructure images in Figure 4.10 show a dark dendritic phase in a light matrix. The light matrix consists of two very fine light phases (Figure 4.10 b).

The phase compositions determined by EDS analyses are listed in Table 4.6 and have been plotted on a ternary projection in Figure 4.11.

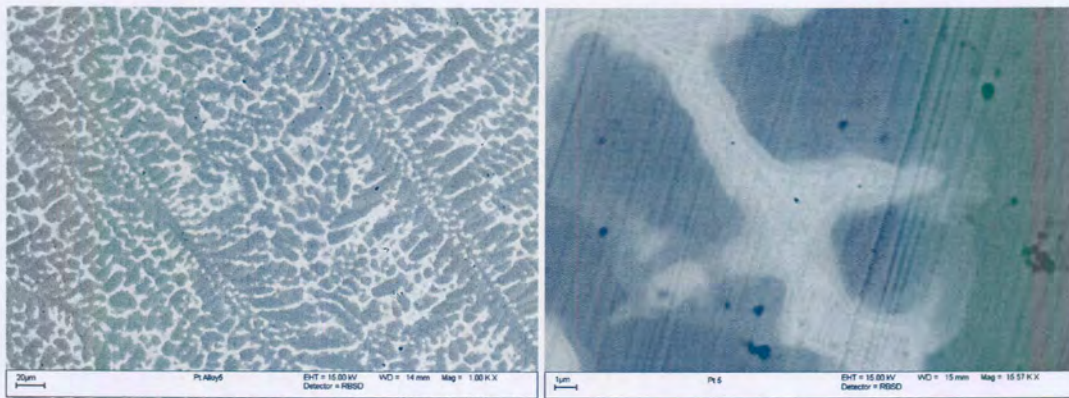


Figure 4.10. BSE image on the right showing dark ~RuAl dendrites in a light two-phase matrix. The light matrix consists of PtAl and Pt₅Al₃, which is the very light phase.

Table 4.6. Summary of phase and composition analysis for the PAR 5 alloy.

Sample	Condition	Phase Description	Composition			Proposed phase(s)	No of analyses
			Al	Pt	Ru		
PAR5	Arc-melted	Overall	43.6 ± 0.9	26.5 ± 0.8	29.9 ± 1.3		5
		Dark	45.0 ± 0.9	16.9 ± 0.4	38.1 ± 0.9	~RuAl	7
		Light	46.8 ± 0.9	51.6 ± 2.4	1.6 ± 2.3	PtAl +	7
		Very Light	43.3 ± 0.5	49.3 ± 0.4	7.4 ± 0.2	Pt ₅ Al ₃	

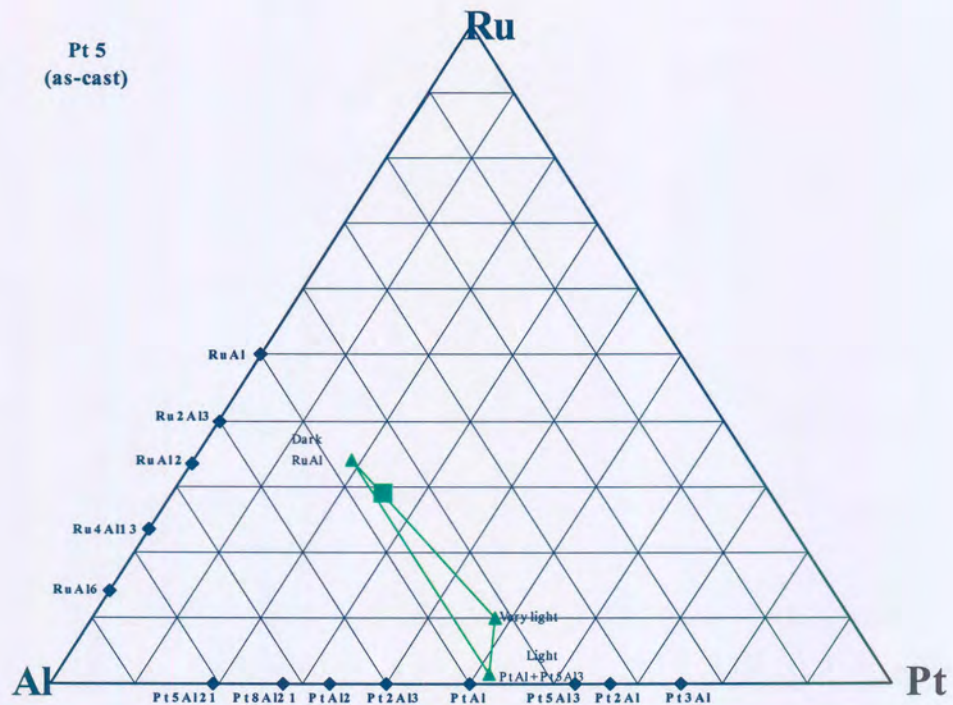
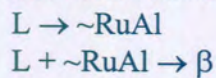


Figure 4.11. A ternary plot of the overall and phase compositions in the PAR 5 alloy.

The liquid solidified as primary \sim RuAl dendrites, and showed some coring on the edges. The remainder of the liquid probably solidified as β phase, which decomposed in the solid state (below 1533 K) to two phases – PtAl and Pt_5Al_3 . These two phases were too fine to analyse accurately individually.

The solidification can be summarised as follow:



β decomposed in the solid-state:



4.2.6 PAR6 - $Al_{25}:Pt_{55}:Ru_{20}$ alloy

The PAR6 alloy was the benchmarking alloy of this study, as it has the same composition as the lowest Pt-content sample of a series of Pt-Al-Ru alloys studied by Biggs [2001Big1]. The results are in good agreement. Unlike most of the other alloys, this alloy was ductile.

The BSE microstructure (Figure 4.12) shows big long dark needles in a light matrix, with some finer dark needles and irregular-shaped ‘blobs’ in the areas between the big long needles. The big long needles appear in a fan-like structure, and dissect through each other.

The phase compositions determined by EDS analyses are listed in Table 4.7 and have been plotted on a ternary projection in Figure 4.13.

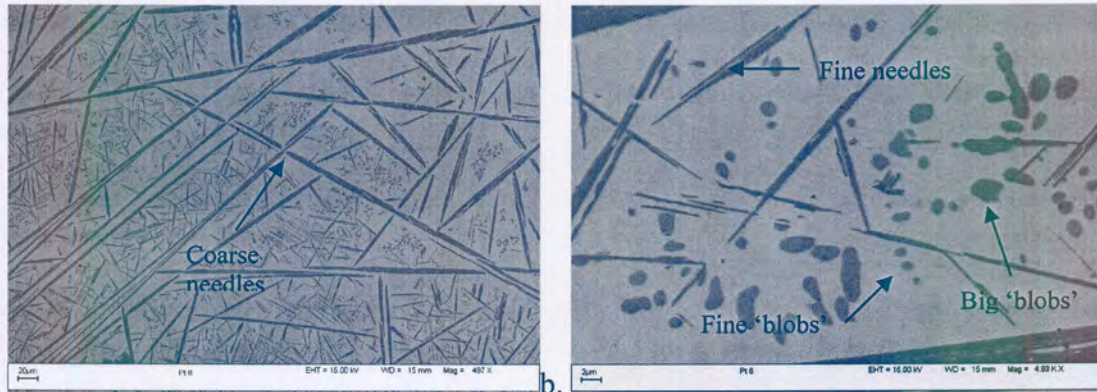


Figure 4.12. (a) The BSE image of PAR 6. (a) shows the long dark (Ru) needles in the light $\sim\text{Pt}_3\text{Al}$ matrix, with a finer dark phase present between the long needles. (b) shows that the fine (Pt) blob-like phase, and the finer (Ru) needles which formed in the ternary eutectic.

Table 4.7. Summary of phase and composition analysis for the PAR 6 alloy.

Sample	Condition	Phase Description	Composition			Proposed phase	No of analysis
			Al	Pt	Ru		
PAR6	Arc-melted	Overall	21.4 ± 0.7	51.7 ± 0.5	26.2 ±		5
		Light Matrix	28.6 ± 0.8	69.5 ± 0.8	1.9 ± 0.5	$\sim\text{Pt}_3\text{Al}$	7
		Dark needles (big and fine) and big blobs	1.8 ± 0.6	17.8 ± 1.1	80.4 ± 1.6	(Ru)	7
		Dark fine blobs	29.0 ± 1.2	68.7 ± 1.7	2.3 ± 1.1	(Pt)	7

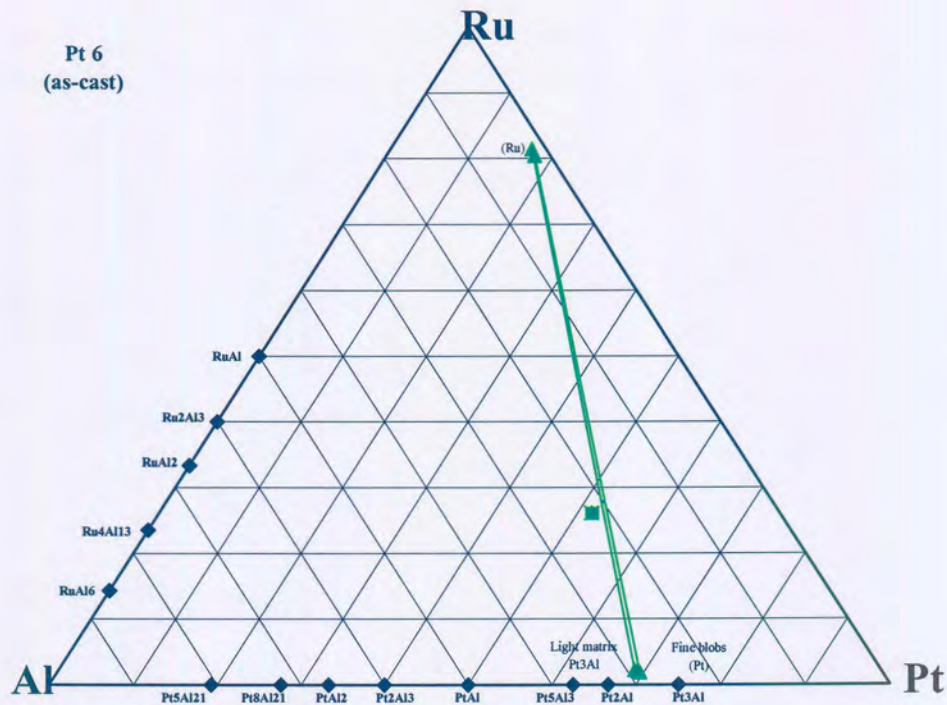


Figure 4.13. A ternary plot of the overall and phase compositions in the PAR 6 alloy.

The PAR 6 alloy solidified by primary (Ru) needles growing in the liquid. The needles probably only thickened after their formation, since it appears as if they are pinched where they have grown through each other. This was probably followed by a eutectic reaction from the liquid, forming (Ru) and \sim Pt₃Al, the light matrix. The binary eutectic was followed by a ternary eutectic, forming (Ru), \sim Pt₃Al and (Pt).

Coarser and finer needles appear in the microstructure. Both needles have a similar morphology. The big needles are primary (Ru), while the fine needles are (Ru) formed from the ternary eutectic reaction. The cross-section of the needles is irregular and appears 'blob'-like, with the larger 'blobs' corresponding to (Ru). The finer 'blobs' are (Pt) which formed in the ternary eutectic reaction. These are indicated in Figure 4.12 b.

The ternary eutectic has not been reported by Biggs [2001Big1].

The proposed solidification sequence can be summarised as:

- L → (Ru)
- L → (Ru) + \sim Pt₃Al
- L → (Ru) + \sim Pt₃Al + (Pt)

4.2.7 PAR7 - Al₇₃:Pt₂₂:Ru₅ alloy

The as-cast alloy was extremely brittle and broke into pieces even during repeated arc-melting to homogenise the sample. It could, therefore, only be partially melted together. The as-cast alloy was very porous, which made it difficult to prepare a smooth surface metallographically.

The BSE microstructure (Figure 4.14 a) shows light dendrites in a darker matrix. The dendrites are not homogeneous (Figure 4.14 b), another phase can be observed in the light dendrites.

The phase compositions determined by EDS analyses are listed in Table 4.8 and have been plotted on a ternary projection in Figure 4.15.

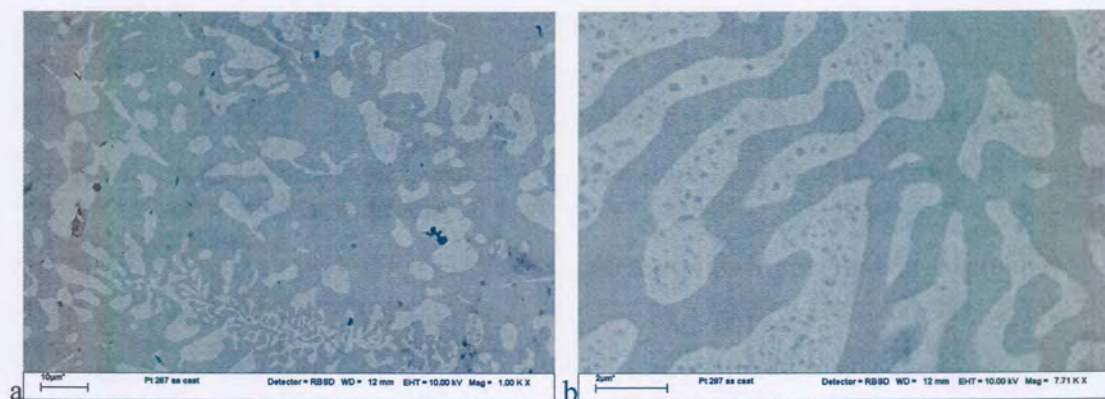


Figure 4.14. The BSE images of PAR 7. (a) shows white PtAl₂ dendrites in a darker X matrix. (b) shows precipitates of X in the PtAl₂ dendrites.

Table 4.8. Summary of phase and composition analysis for the PAR 7 alloy.

Sample	Condition	Phase Description	Composition			Proposed phase(s)	No of analyses
			Al	Pt	Ru		
PAR 7	Arc-melted	Overall	70.8 ± 0.4	21.6 ± 0.4	7.6 ± 0.6		5
		Light	67.9 ± 1	32.1 ± 1	0	PtAl ₂	5
		Dark	72.1 ± 1.2	18.4 ± 1.2	9.5 ± 2.2	X	8

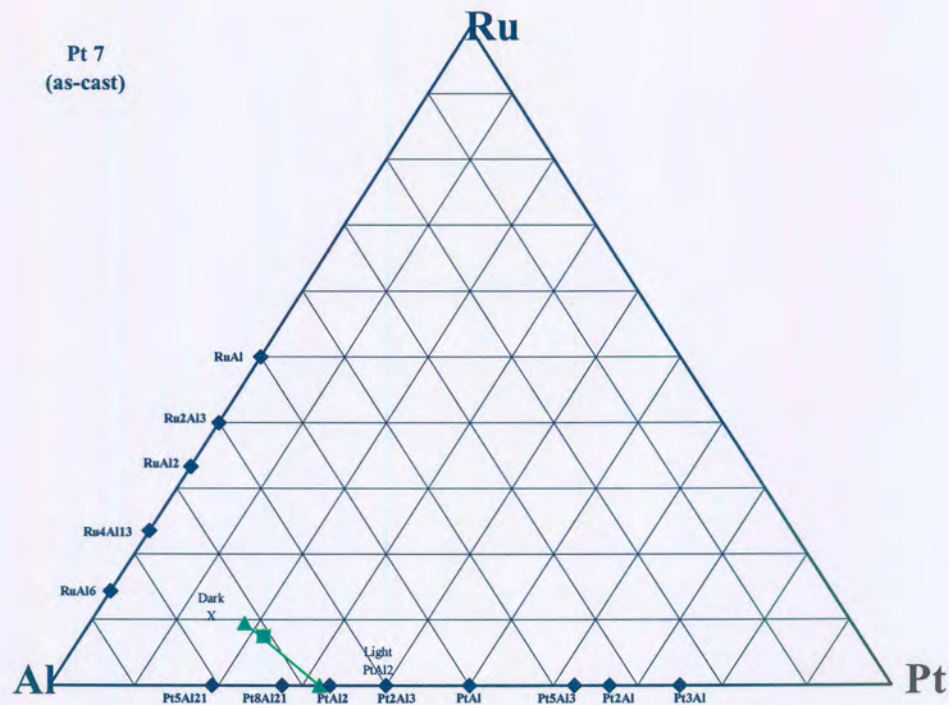
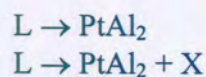


Figure 4.15. A ternary plot of the overall and phase compositions in the PAR 7 alloy.

The PAR 7 alloy solidified forming primary $PtAl_2$ dendrites in the liquid. The final volume of the liquid solidified eutectically, forming $PtAl_2$ and X. The fine phase present in the primary $PtAl_2$ dendrites are the X phase. This can either be due to the precipitation of the X phase because of a sloping solvus, or because the dendrites were probably wetted by the liquid, and small liquid ‘pockets’ remained in the dendrites, which then solidified as X phase.

The proposed solidification sequence is as follows:



4.2.8 PAR 8 - $Al_{71}:Pt_7:Ru_{22}$ alloy

The PAR 8 alloy was brittle and porous.

The BSE image (Figure 4.16 a) shows dark dendrites in a medium matrix. An irregular very light phase is present in the matrix (Figure 4.16 b).

The phase compositions determined by EDS analyses are listed in Table 4.9 and have been plotted on a ternary projection in Figure 4.17.

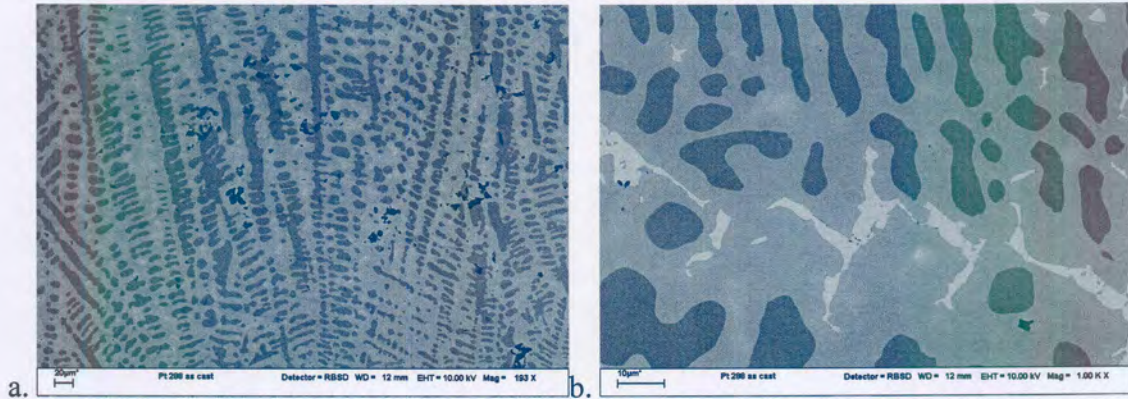


Figure 4.16. BSE images of PAR 8. (a) shows dark $\sim\text{RuAl}$ dendrites in a medium grey X phase. A very light phase $\sim\text{PtAl}_2$ is present in the medium grey phase. (b) shows the microstructure in more detail.

Table 4.9. Summary of phase and composition analysis for the PAR 8 alloy.

Sample	Condition	Phase Description	Composition			Proposed phase(s)	No of analyses
			Al	Pt	Ru		
PAR 8	Arc-melted	Overall	62.0 ± 0.5	6.2 ± 0.4	31.8 ± 0.7		5
		Medium	67.0 ± 0.6	10.4 ± 0.3	22.6 ± 0.7	X	7
		Dark	56.2 ± 0.8	0	41.2 ± 0.8	$\sim\text{RuAl}$	7
		Very light	61.7 ± 1	30.4 ± 1.2	7.9 ± 1.1	$\sim\text{PtAl}_2$	7

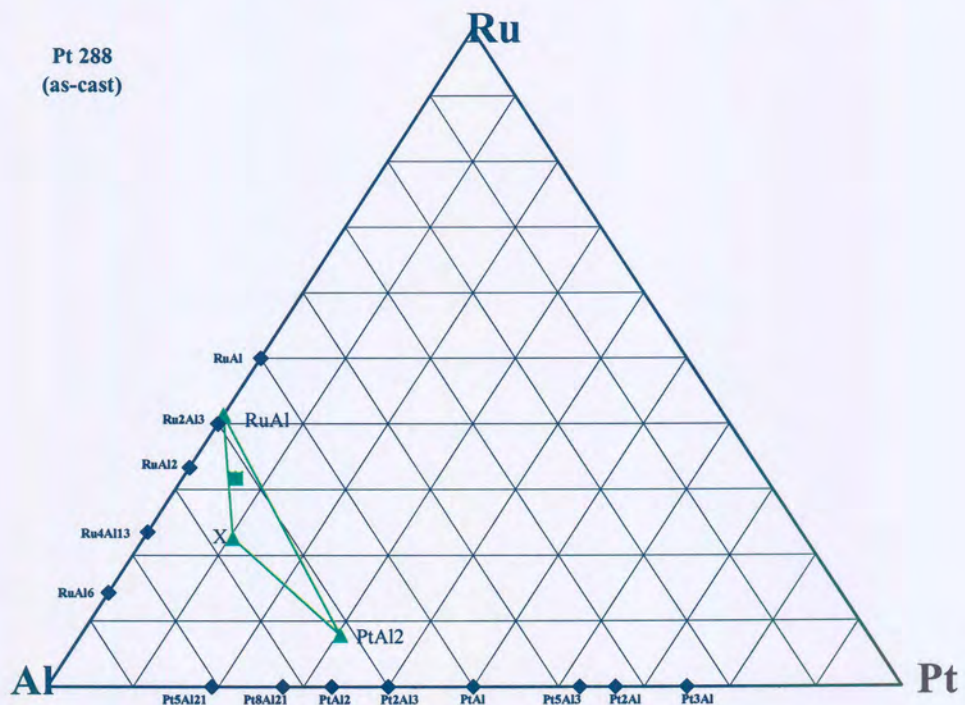
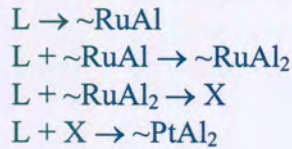


Figure 4.17. A ternary plot of the overall and phase compositions in the PAR 8 alloy.

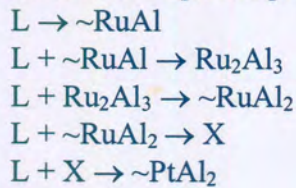
Primary $\sim\text{RuAl}$ dendrites solidified from the liquid. The $\sim\text{RuAl}$ reacted peritectically with the liquid to form $\sim\text{RuAl}_2$, which subsequently reacted with the liquid to form X, a ternary phase. The final liquid reacted with X to form $\sim\text{PtAl}_2$, the white phase.

From the EDS analysis it seemed that the final peritectic reaction consumed all the $\sim\text{RuAl}_2$ phase, as it was not detected.

The proposed solidification sequence is as follows:



However, when comparing the proposed solidification sequence with the proposed liquidus surface projection, Ru_2Al_3 should have formed. It was thus assumed that a small amount Ru_2Al_3 did form, but that it was consumed in the subsequent peritectic reaction. The solidification sequence probably was as follows:



4.2.9 PAR 9 - $\text{Al}_{59}:\text{Pt}_{33}:\text{Ru}_8$ alloy

The PAR 9 alloy was brittle.

Only two phases were observed in the BSE microstructure (Figure 4.18). The primary dendrite phase shows coring.

The phase compositions determined by EDS analyses are listed in Table 4.10 and have been plotted on a ternary projection in Figure 4.19.

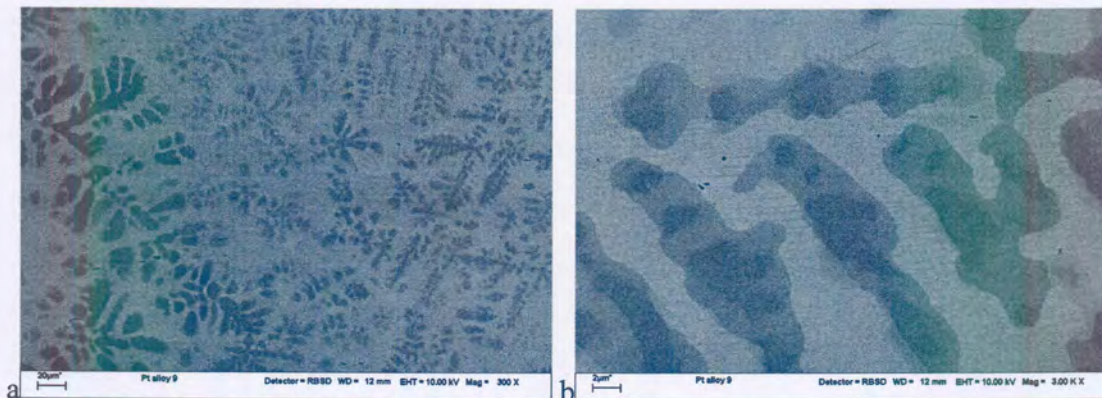


Figure 4.18. BSE microstructure of PAR 9. (a) shows the dendritic structure. (b) shows the coring of the dark grey \sim RuAl phase.

Table 4.10. Summary of phase and composition analysis for the PAR 9 alloy.

Sample	Condition	Phase Description	Composition			Proposed phase(s)	No of analyses
			Al	Pt	Ru		
PAR9	Arc-melted	Overall	55.4 ± 1.2	32.5 ± 0.6	12.1 ± 1		5
		Light	60.4 ± 0.2	39.6 ± 0.2	0	Pt_2Al_3	6
		Dark	47.6 ± 0.7	20.6 ± 0.4	31.8 ± 0.9	\sim RuAl	5

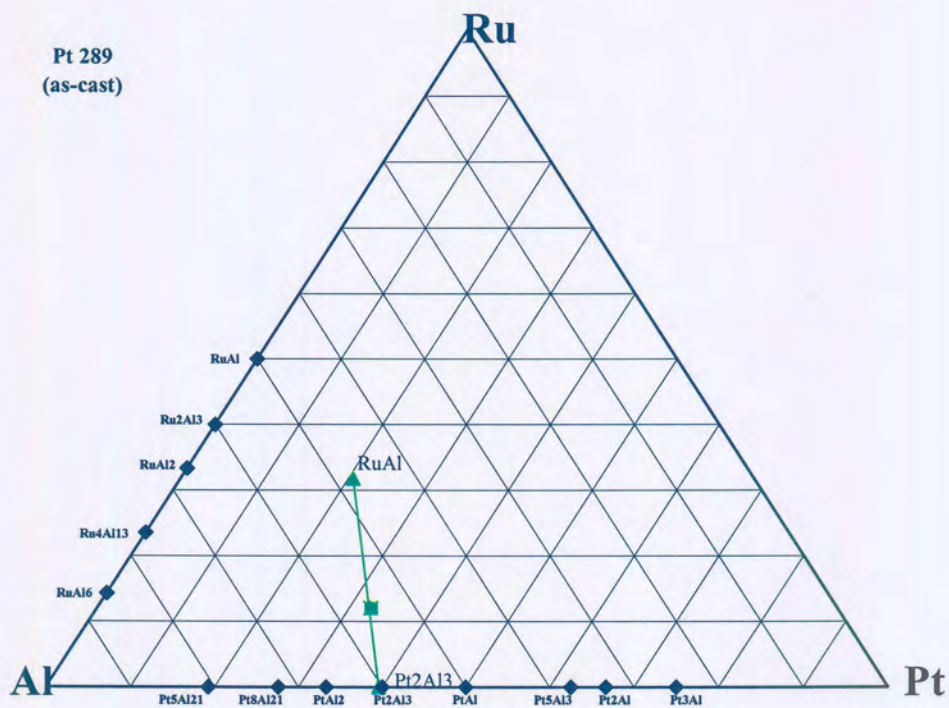
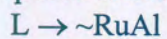


Figure 4.19. A ternary plot of the overall and phase compositions in the PAR 9 alloy.

The liquid solidified forming primary \sim RuAl dendrites. The dendrites showed coring. The final liquid reacted peritectically with the liquid to form Pt_2Al_3 .

The proposed solidification sequence is as follows:



4.2.10 PAR10 - Al₃₄:Pt₄₀:Ru₂₆ alloy

The PAR 10 alloy was ductile.

The low magnification BSE image of the as-cast microstructure (Figure 4.20 a) shows long, directional dark 'feather-like' dendrites in a light matrix. In some areas it looked as if there were 'blotches' clouding the clear dendrite image. In these blotchy areas the dark dendrites were coated with a lighter phase as can be seen in Figure 4.20 (b). In the areas between the dendrites a fine 'eutectic' structure was observed.

The phase compositions determined by EDS analyses are listed in Table 4.11 and have been plotted on a ternary projection in Figure 4.21.

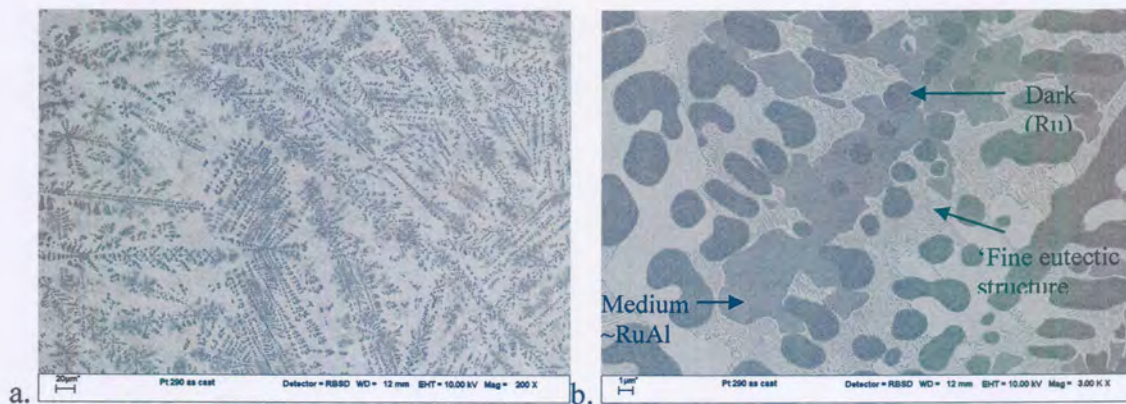


Figure 4.20. BSE images of PAR10. (a) shows the 'feather-like' dendrite solidification structure, with some areas which appear 'cloudy'. In the close up, (b), the dark (Ru) needles, coated by a medium phase, ~RuAl in a light (Pt₅Al₃ + PtAl) matrix. Between the dendrites, a fine eutectic structure is visible.

Table 4.11. Summary of phase and composition analysis for the PAR 10 alloy.

Sample	Condition	Phase Description	Composition			Proposed phase(s)	No of analyses
			Al	Pt	Ru		
PAR 10	Arc-melted	Overall	28.0 ± 0.6	32.6 ± 0.5	39.5 ± 1		5
		Light matrix	40.5 ± 3.6	59.5 ± 3.6	0	(PtAl + Pt ₅ Al ₃)	3
		Dark	3.4 ± 0.3	3.4 ± 0.3	93.3 ± 0.6	(Ru)	11
		Medium	42.3 ± 0.7	21.3 ± 0.6	36.4 ± 0.8	~RuAl	5

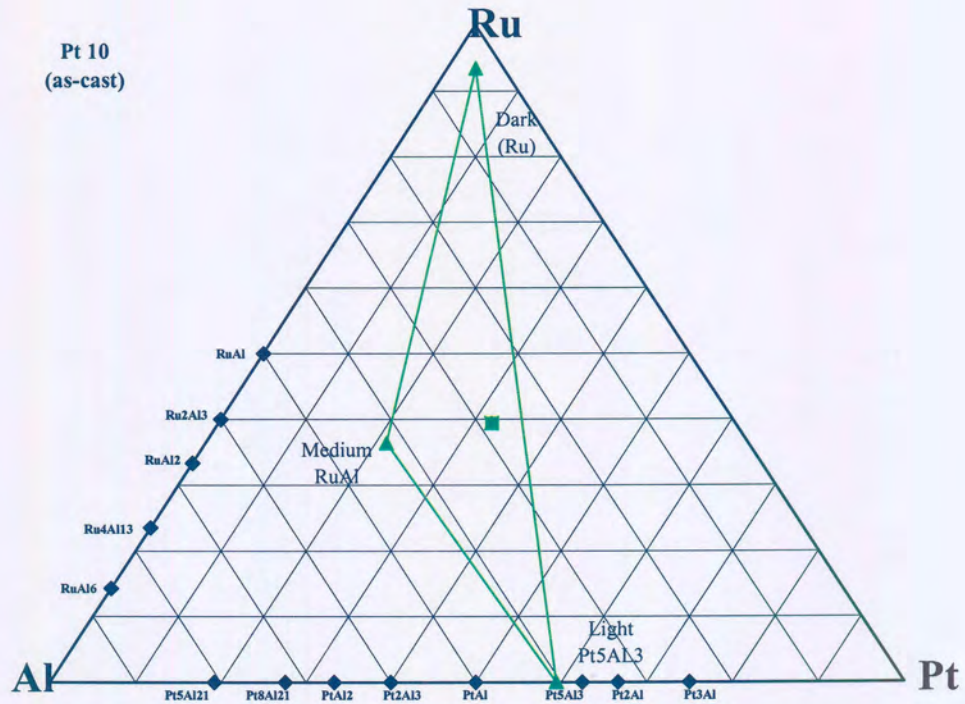
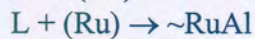
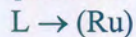


Figure 4.21 A ternary plot of the overall and phase compositions in the PAR 10 alloy.

(Ru) solidified as the primary phase with needles growing in the liquid, before it reacted with the liquid to form \sim RuAl. The \sim RuAl reacted with the remaining liquid to form β . The reaction transformed to a eutectic reaction due to more favourable thermodynamic conditions. β decomposed in the solid state to Pt_5Al_3 and PtAl, as it is unstable below 1533 K. More Pt_5Al_3 than PtAl was observed, as the composition was far to the platinum side of the β phase.

The proposed solidification sequence is as follows:



β decomposed by solid state reaction:



4.2.11 PAR 11 - Al₄₂:Pt₅₂:Ru₆ alloy

PAR11 did not show any brittleness.

The BSE microstructure (Figure 4.22) shows a dark dendrite, coated by a lighter phase, in a light matrix. At a higher magnification (Figure 4.22 b), both the dark and medium phases show the presence of another phase, very finely dispersed, in it.

The phase compositions determined by EDS analyses are listed in Table 4.12 and have been plotted on a ternary projection in Figure 4.23.

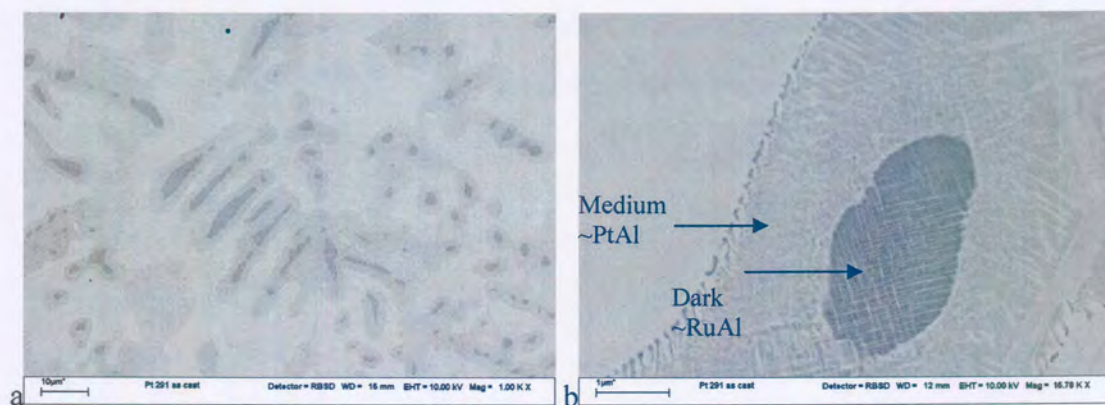


Figure 4.22. BSE images of PAR 11. (a) shows the dendritic structure of the alloy. (b) clearly shows the presence of a fine phase in the dark dendrite phase as well as the area surrounding the dark dendrite.

Table 4.12. Summary of phase and composition analysis for the PAR 11 alloy.

Sample	Condition	Phase Description	Composition			Proposed phase(s)	No of analyses
			Al	Pt	Ru		
PAR 11	Arc-melted	Overall	39.7 ± 0.8	50.1 ± 0.9	10.2 ± 1.1		9
		Light matrix	37.6 ± 0.4	62.4 ± 0.4	0	Pt ₅ Al ₃	4
		Dark *	42.4 ± 0.7	23.5 ± 0.8	34.1 ± 0.9	~RuAl	7
		Medium *	49.9 ± 0.9	44.4 ± 3.3	12.6 ± 2.8	~PtAl	7

* bulk phase composition, as a finely dispersed second phase is present in the bulk phase, the fine phase was too fine to analyse with EDS.

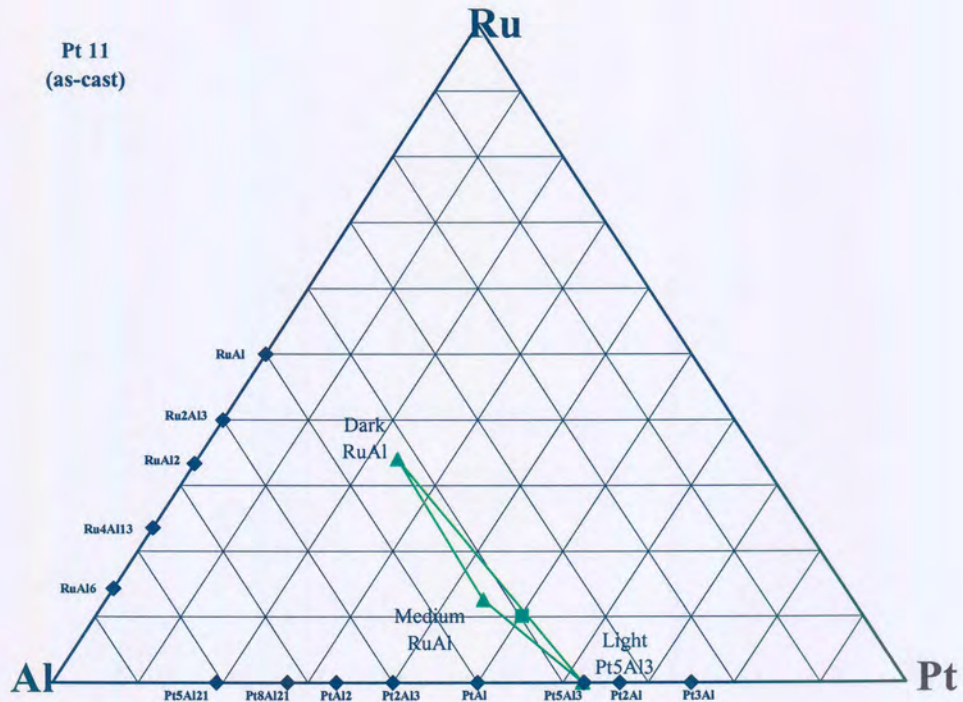


Figure 4.23. A ternary plot of the overall and phase compositions in the PAR 11 alloy.

The liquid solidified as primary \sim RuAl dendrites (these dark dendrites were very fine and their size on the limit of the spatial resolution of EDS). The dendrites were coated with β phase when the liquid reacted peritectically with the \sim RuAl to form β . The final of the liquid then solidified as Pt_5Al_3 through a peritectic reaction between the liquid and β . The β -phase decomposed at lower temperatures to Pt_5Al_3 and PtAl.

There is also a fine phase present in the dark \sim RuAl dendrites. Although it was too fine to analyse accurately with EDS, it is proposed that it is Pt_5Al_3 . It probably appeared in the \sim RuAl phase due to a solid-state precipitation of Pt_5Al_3 because of a sloping solvus.

The proposed solidification sequence is:



A solid-state transformation is observed after the solidification:



4.2.12 PAR 12 - Al₃₃:Pt₅₉:Ru₈ alloy

PAR 12 was a small and dense button-melt sample. It was ductile, but showed some porosity in the microstructure.

The BSE images (Figure 4.24) show fine dark primary needles formed in a light matrix. The microstructure appeared similar to the PAR 6, but the needles in PAR 12 were finer and also did not show the distinct fan-like structure of PAR 6. Where the sample preparation has cut through a needle, it showed that these were thin flat needles (Figure 4.24 b), and not round and blob-like as the needles in PAR 6.

The phase compositions determined by EDS analyses are listed in Table 4.13 and have been plotted on a ternary projection in Figure 4.25.

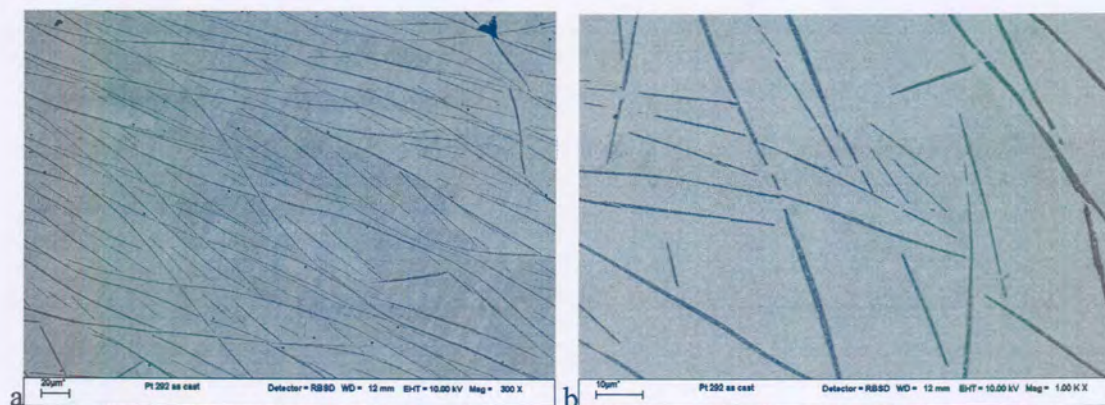


Figure 4.24. BSE images of PAR 12. (a) shows long thin and small fine (Ru) needles in a light Pt₃Al matrix. (b) shows the microstructure at a higher magnification.

Table 4.13. Summary of phase and composition analysis for the PAR 12 alloy.

Sample	Condition	Phase Description	Composition			Proposed phase(s)	No of analyses
			Al	Pt	Ru		
PAR12	Arc-melted	Overall	29.9 ± 0.6	54.3 ± 0.7	15.8 ± 0.6		5
		Light matrix	34.9 ± 0.4	65.1 ± 0.4	0	Pt ₃ Al	9
		Dark needles	0	10.2 ± 2.3	89.8 ± 2.3	(Ru)	7

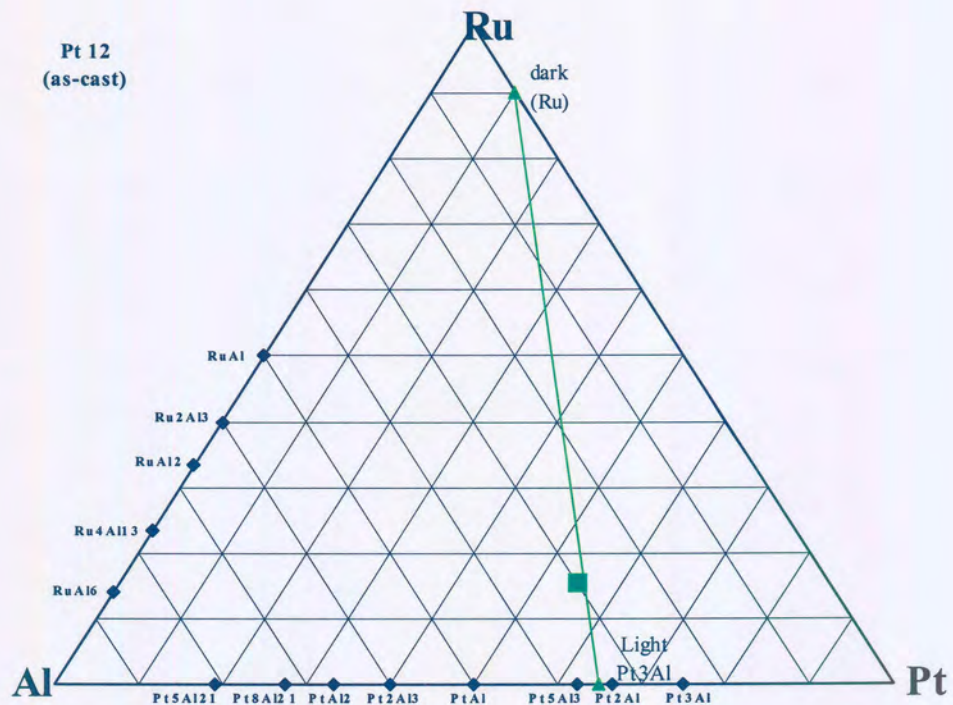
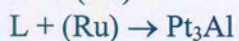
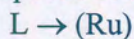


Figure 4.25. A ternary plot of the overall and phase compositions in the PAR 12 alloy.

Fine dark primary (Ru) needles formed from the liquid, before reacting with the liquid to form Pt_3Al by a peritectic reaction. The needles were finer than the ones observed in the as-cast PAR6 alloy, and also did not show the distinct fan-like structure of the PAR6 needles.

The proposed solidification sequence is as follows:



4.2.13 The PAR 13- $Al_{85}:Pt_{10}:Ru_5$ alloy

The alloy was brittle and cracked easily.

The BSE microstructure (Figure 4.26 a and b) shows light primary dendrites in a dark matrix. On the edge of the dendrites a fine lighter phase is observed (Figure 4.24 c), which formed peritectically. Between the dendrites, an eutectic structure formed (Figure 4.24 d).

The phase compositions determined by EDS analyses are listed in Table 4.14 and have been plotted on a ternary projection in Figure 4.25.

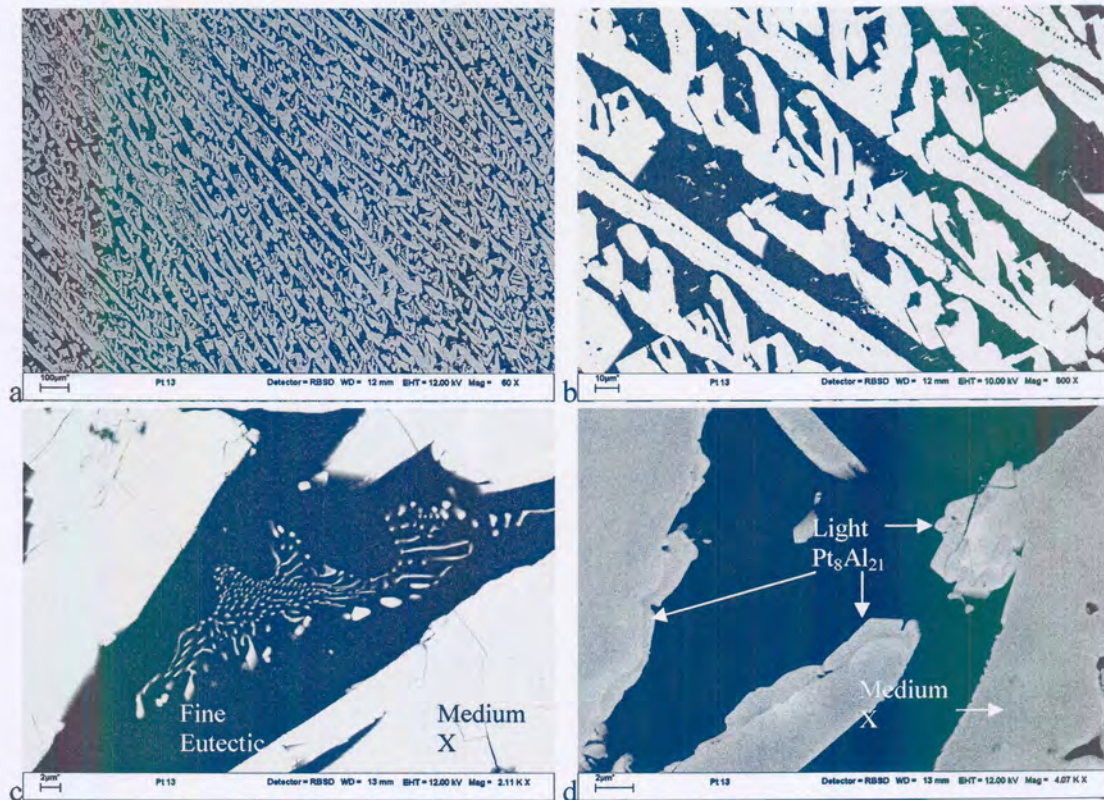


Figure 4.26. BSE images of PAR 13. (a) and (b) show the general microstructure. In (c) the ternary eutectic structure between the primary X dendrites can be seen. (d) shows the presence of another phase (lighter than dendrites) on the edges of the X dendrites.

Table 4.14. Summary of phase and composition analysis for the PAR 13 alloy.

Sample	Condition	Phase Description	Composition			Proposed phase(s)	No of analyses
			Al	Pt	Ru		
PAR13	Arc-melted	Overall	87.6 ± 0.4	8.5 ± 0.4	4.0 ± 0.4		5
		Medium	73.4 ± 0.4	17.1 ± 0.8	9.5 ± 0.7	X	5
		Light	76.8 ± 0.7	24.2 ± 0.8	0	Pt ₈ Al ₂₁	5
		Dark	100	0	0	(Al)	5

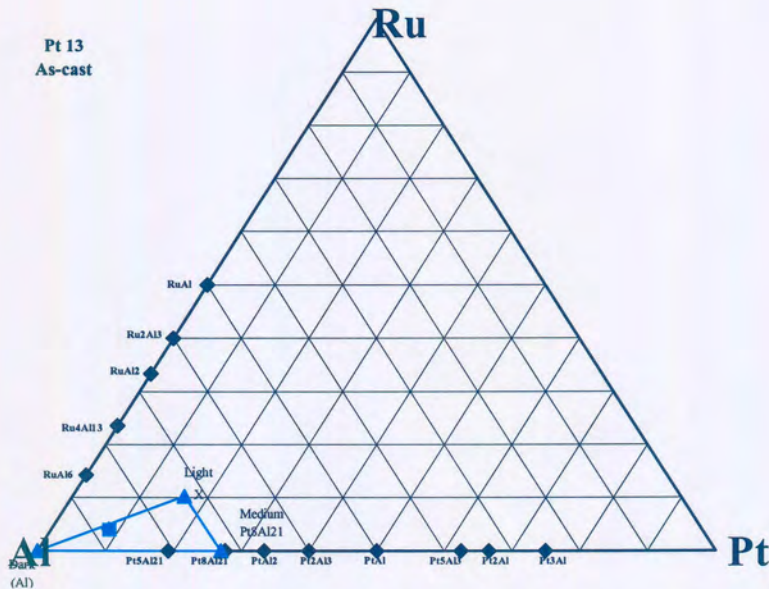
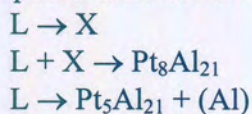


Figure 4.27 A ternary plot of the overall and phase compositions in the PAR 13 alloy.

The microstructure shows light primary X faceted crystals in a dark (Al) matrix. On the edge of the crystals, Pt_8Al_{21} , formed peritectically. The final liquid solidified eutectically, forming Pt_5Al_{21} and (Al).

The proposed solidification sequence is:



Another reaction probably occurred between the last two reactions, as there should be continuity of the phases between the different steps of the proposed solidification sequence. However, it has not been observed.

4.2.14 The PAR14- $Al_{66}:Pt_{13}:Ru_{21}$ alloy

The sample was brittle and fractured easily.

The BSE microstructure reveals three distinct phases (Figure 4.28). Dark dendrites are coated by a medium phase in a light matrix.

The phase compositions determined by EDS analyses are listed in Table 4.15 and have been plotted on a ternary projection in Figure 4.29.

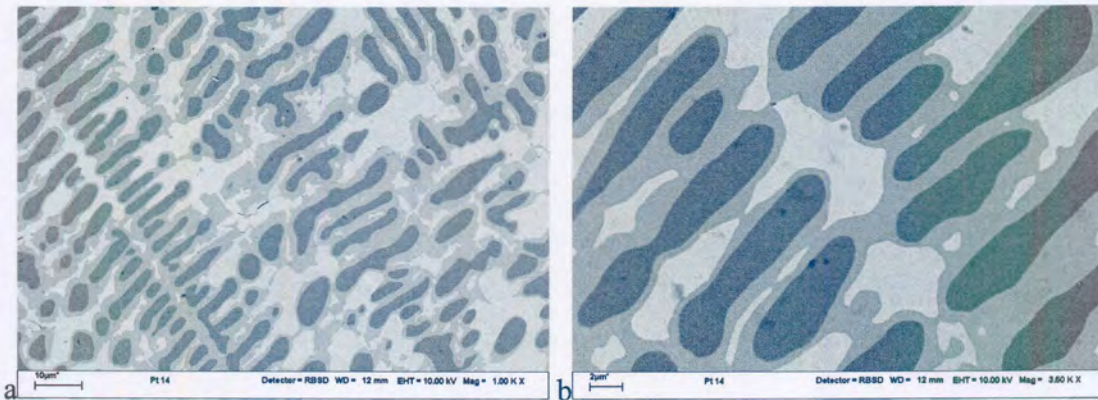


Figure 4.28. BSE images of PAR 14. (a) shows the dark RuAl_2 dendrites surrounded by a medium X phase in a light $\sim\text{PtAl}_2$ matrix. (b) shows a higher magnification of the microstructure.

Table 4.15. Summary of phase and composition analysis for the PAR 14 alloy.

Sample	Condition	Phase Description	Composition			Proposed phase(s)	No of analyses
			Al	Pt	Ru		
PAR14	Arc-melted	Overall	64.0 ± 0.4	13.6 ± 0.4	22.4 ± 0.2		5
		Light	57.8 ± 0.6	32.4 ± 1.1	9.8 ± 0.9	$\sim\text{PtAl}_2$	7
		Medium	69.7 ± 0.5	13.9 ± 0.7	16.4 ± 1.0	X	7
		Dark	63.9 ± 0.5	0	36.1 ± 0.5	RuAl_2	7

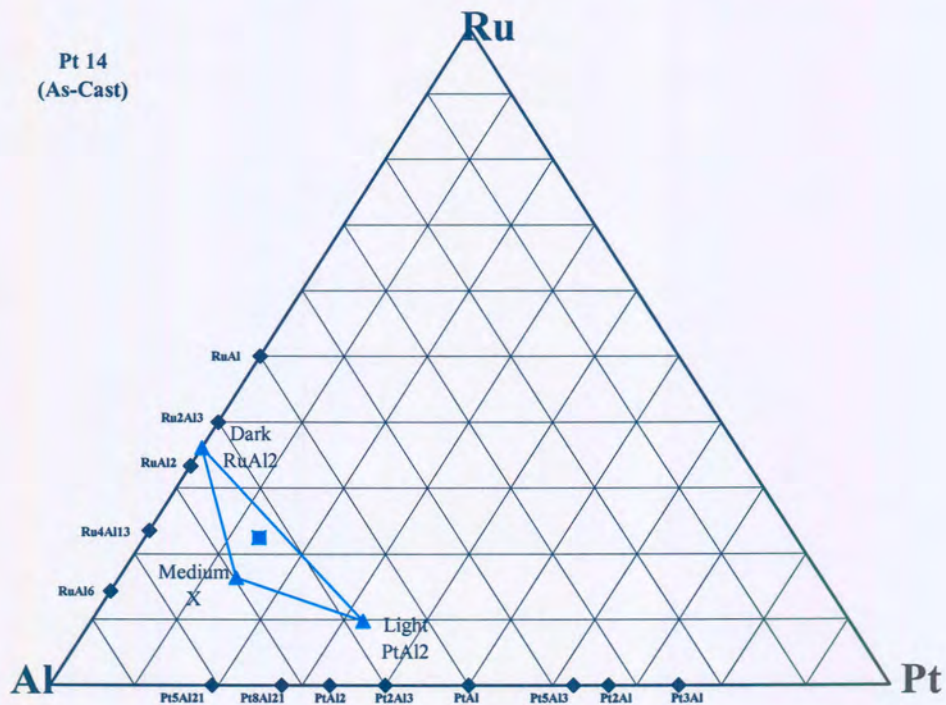
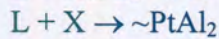


Figure 4.29. A ternary plot of the overall and phase compositions in the PAR 14 alloy.

The primary dendrites of RuAl_2 formed in the liquid. The liquid then reacted with the RuAl_2 peritectically and formed X, which coated the primary dendrites. This was followed by another peritectic reaction where $\sim\text{PtAl}_2$ formed from the liquid and X

The proposed solidification sequence is:



4.2.15 The PAR 15- $\text{Al}_{47}\text{Pt}_{51}\text{Ru}_2$ alloy

The PAR 15 alloy did not show any brittleness.

The BSE images show 'island', with a two-phase structure in them, in a matrix that also shows a finer structure (Figures 4.30 a and b). The two fine phases differ in appearance (Figures 4.30 c and d).

The phase compositions determined by EDS analyses are listed in Table 4.16 and have been plotted on a ternary projection in Figure 4.31.

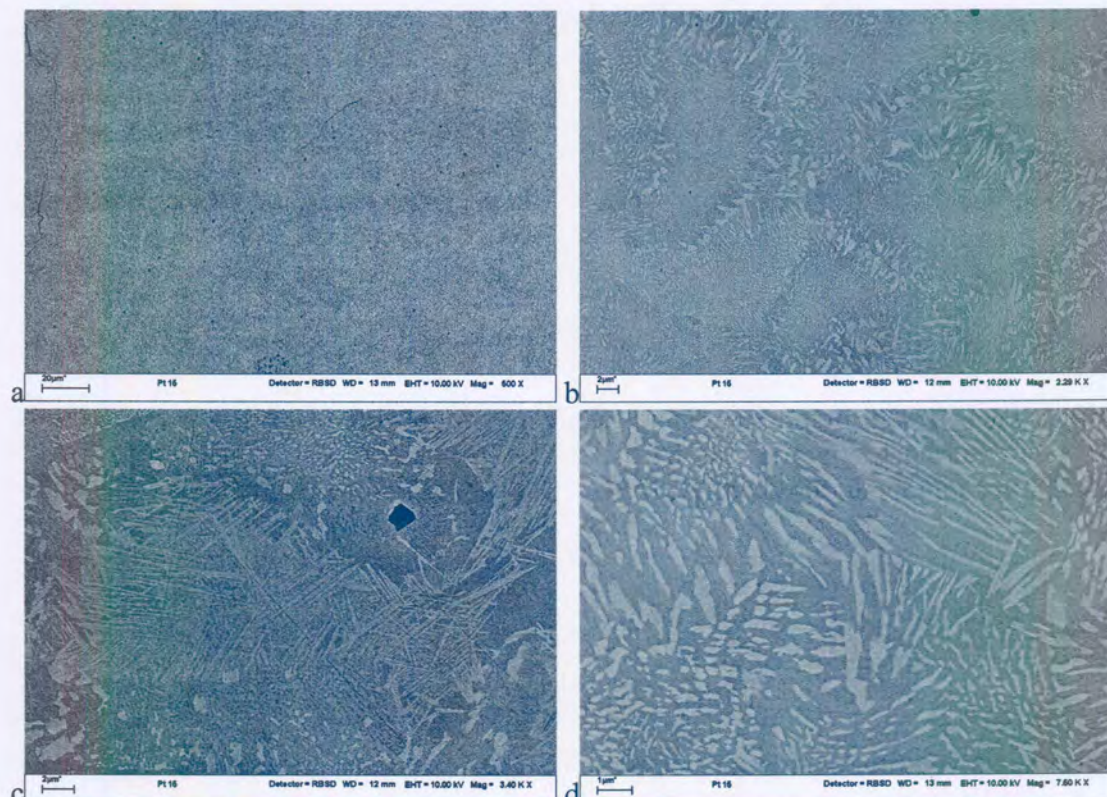


Figure 4.30. (a) shows the overall microstructure of PAR 15. (b) shows the 'grain'-like structure. (c) shows the solid state decomposition of a primary β grain while (d) shows the difference in decomposition microstructures.

Table 4.16. Summary of phase and composition analysis for the PAR 15 alloy.

Sample	Condition	Phase Description	Composition			Proposed phase(s)	No of analyses
			Al	Pt	Ru		
PAR15	Arc-melted	Overall	42.0 ± 0.3	55.7 ± 0.8	2.3 ± 0.7		5
		Light	35.0 ± 0.4	61.9 ± 0.6	3.1 ± 0.5	~Pt ₅ Al ₃	5
		Dark	45.2 ± 0.2	52.1 ± 0.7	2.7 ± 0.6	~PtAl	5

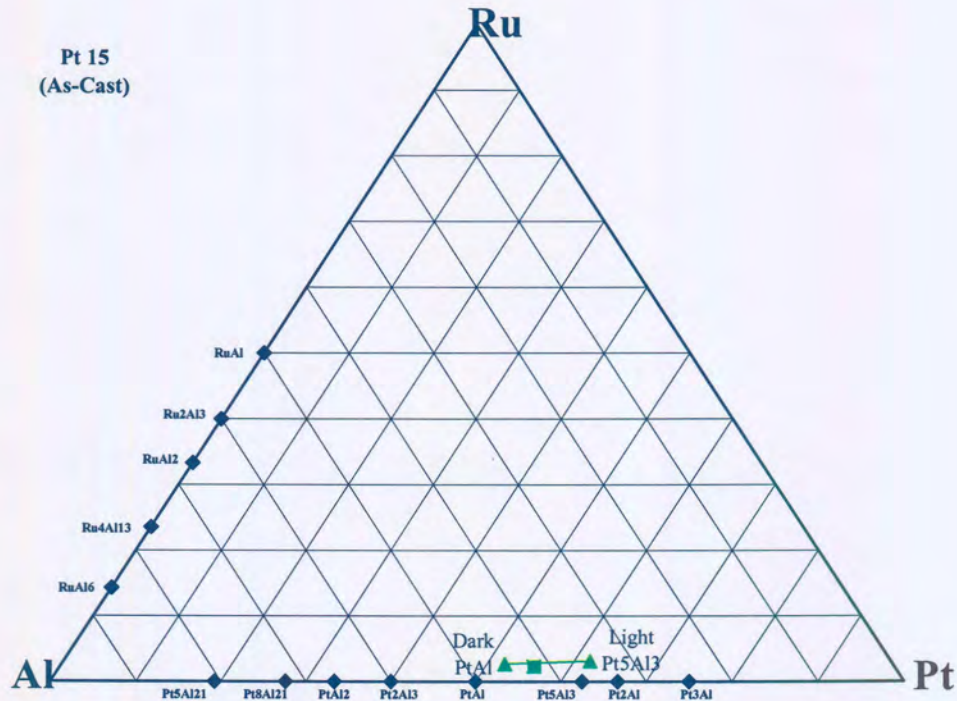
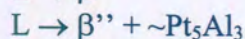


Figure 4.31. A ternary plot of the overall and phase compositions in the PAR 15 alloy.

Primary discrete β phase 'islands' formed in the liquid. The reaction then changed to a eutectic reaction where β and $\sim\text{Pt}_5\text{Al}_3$ formed from the liquid. The β phase decomposed below 1533 K to $\sim\text{PtAl}$ and $\sim\text{Pt}_5\text{Al}_3$. Inside the 'islands' it was only β phase decomposing; in the matrix as $\sim\text{Pt}_5\text{Al}_3$ was already present before the β decomposed, resulting in two different microstructures of $\sim\text{PtAl}$ and $\sim\text{Pt}_5\text{Al}_3$ in the primary 'islands' and in the eutectic mixture. This is illustrated schematically in Figure 4.32.

The proposed solidification sequence is:



(β' is the primary β phase which formed from the liquid, β'' is the eutectically formed β phase)

The β phase then decomposes



The development of the solidification microstructure is illustrated in Figure 4.32. Primary β particles form from the liquid (shown as β'). The remainder of the liquid solidifies eutectically, leaving the β' in a β'' and $\sim\text{Pt}_5\text{Al}_3$ matrix. The β phase then decomposes to $\sim\text{PtAl}$ and $\sim\text{Pt}_5\text{Al}_3$, as described above.

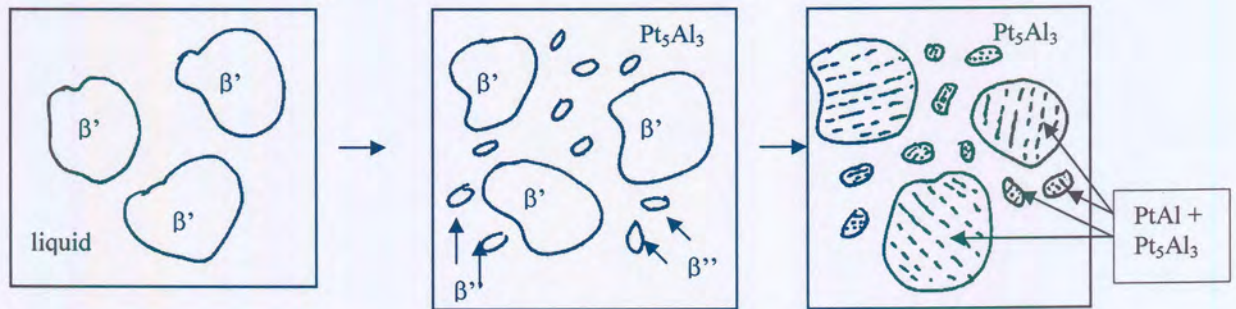


Figure 4.32. Schematic development of the solidification microstructure of the PAR15 alloy.

4.2.16 The PAR 16- $\text{Al}_{74}:\text{Pt}_8:\text{Ru}_{18}$ alloy

The PAR 16 alloy was very brittle. Some porosity was visible.

The BSE microstructures (Figures 4.33) show a medium grey dendrite phase that is coated by a black phase. The coated dendrites are surrounded by a light grey phase, which shows some coring. Finally there are small particles of a very light phase present in a light cored area.

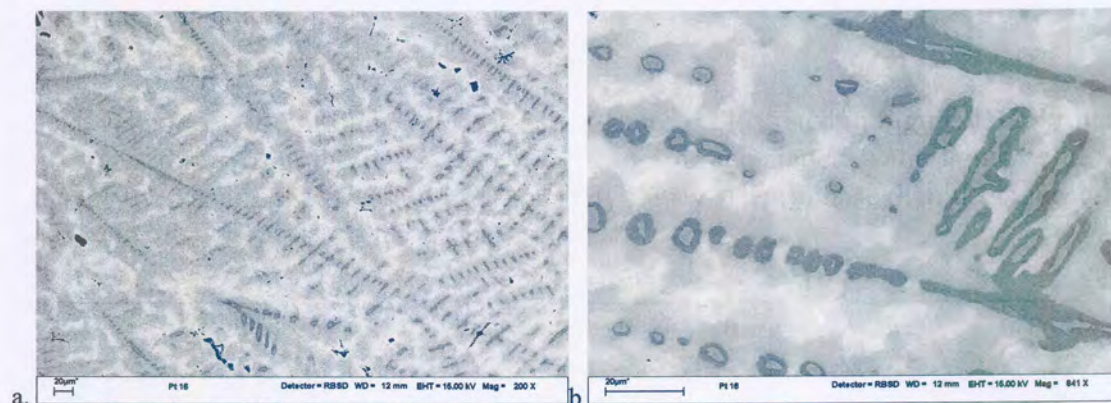


Figure 4.33. (a) shows the overall microstructure of PAR 16. (b) shows the medium primary $RuAl_2$ dendrites coated by the black Ru_4Al_{13} phase. Small, very light areas of $PtAl_2$ can be seen in the cored X phase.

The phase compositions determined by EDS analyses are listed in Table 4.17 and have been plotted on a ternary projection in Figure 4.34.

Table 4.17. Summary of phase and composition analysis for the PAR 16 alloy.

Sample	Condition	Phase Description	Composition			Proposed phase(s)	No of analyses
			Al	Pt	Ru		
PAR16	Arc-melted	Overall	71.9 ± 0.4	8.9 ± 0.3	19.2 ± 0.3		5
		Medium Grey (dendrite core)	63.9 ± 0.3	0.5 ± 0.2	35.6 ± 0.3	$RuAl_2$	5
		Dark	75.3 ± 0.2	0.5 ± 0.2	25.2 ± 0.2	Ru_4Al_{13}	5
		Cored phase	71.5 ± 1.6	15.2 ± 1.3	13.3 ± 2.5	X	5
		Very light	65.4 ± 0.9	34.6 ± 0.9	0	$PtAl_2$	5

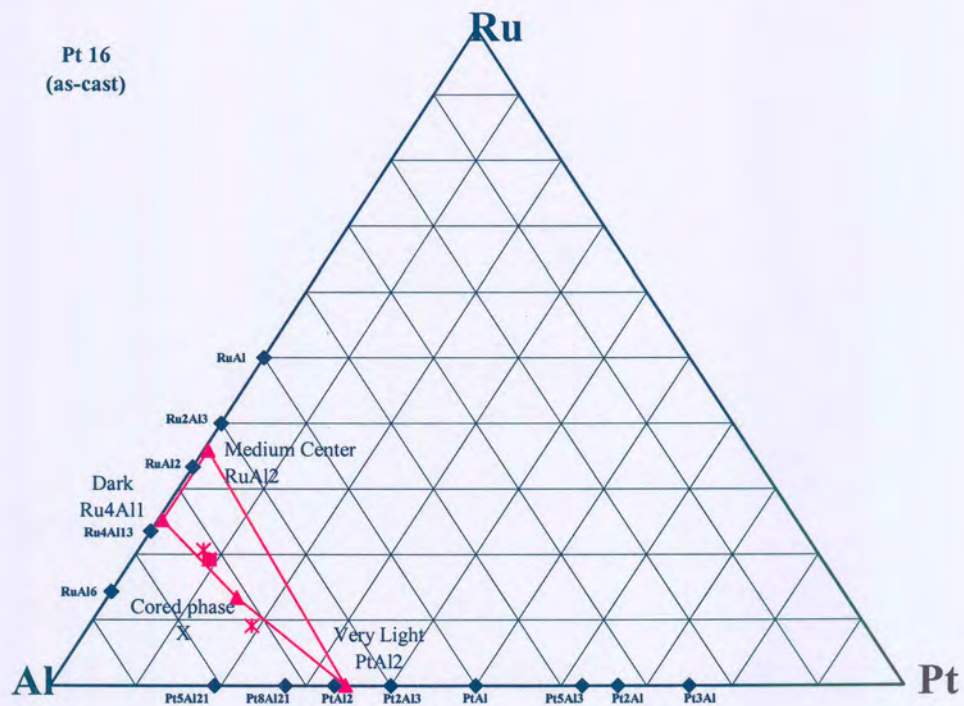
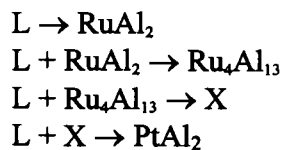


Figure 4.34. A ternary plot of the overall and phase compositions in the PAR 16 alloy.

Primary $RuAl_2$ dendrites formed in the liquid. Through a cascade of peritectic reactions, the primary dendrites were coated by Ru_4Al_{13} , then by a very cored X phase and finally by $PtAl_2$.

The proposed solidification sequence is:



4.3 XRD results

The initial attempt to identify and confirm the phases suggested by the EDS analyses proved to be no simple task. This was due to the fact that only some of the binary phases are included in the ICDD [2002ICD] and ICSD [2002ICS], which contain the standard diffraction data for phases. The diffraction data are normally only for the pure phases and solid solution phases are not considered. Furthermore, when there is third element solid solubility of an element in a binary phase, the diffraction patterns shifts.

These complications lead to a separate, but related XRD project on the binary phases of this study, thus the work presented in this section is still ongoing at the CSIR-NML. In most cases, the pure binary phases would have to be evaluated before the effect of the third element can be considered. It has also been found that the analyses of the corresponding heat-treated samples were easier to interpret than the as-cast samples, as the heat-treated phases are closer to equilibrium conditions. Unfortunately, only the 600°C heat treated samples of the first six alloys were available at the time of this study.

Two new ternary phases were suggested in the EDS analyses. It is considered that the one phase is a high temperature phase that decomposed. The other phase was present in a number of samples. The high temperature phase is preliminary called phase T with a suggested composition of $\text{Ru}_{18}\text{Pt}_{28}\text{Al}_{64}$. Since the phase decomposed, it was not detected by XRD and no prototype could be suggested. The second ternary phase, called phase X here, was matched through a search-and-match procedure to be similar to $\text{IrAl}_{2.75}$ and/or $\text{RhAl}_{2.63}$. It is proposed that the composition is $\text{Ru}_{12}\text{Pt}_{15}\text{Al}_{73}$, that the phase has a primitive cubic structure and that the lattice parameter is 0.7712 nm.

In some cases the peak overlaps made the phase identification complicated. In sample PAR4, RuAl and PtAl_2 were found in the EDS analysis. However, the main reflections in the diffraction patterns for the two phases overlap almost completely, as both phases are cubic, with the PtAl_2 lattice parameter about twice the size of the RuAl lattice parameter. By looking at the (311) reflection, which is the second strongest reflection in the PtAl_2 pattern and absent in the RuAl pattern, it could be determined with XRD that it was in fact RuAl and not PtAl_2 in the sample, thus confirming the EDS results. Similarly, in sample PAR3, the RuAl and RuAl_2 patterns also overlap. Although the former is cubic and the latter orthorhombic, the identification of the RuAl_2 was difficult: it was a minor phase and its major reflections were overlapping with the RuAl phase. Again, the presence of the (311) reflection in the RuAl_2 and absence in the RuAl phase was used as a signature in identification. In sample PAR8, the RuAl phase have not been identified in the XRD spectrum, as it is not the major phase and the main reflections overlap with the RuAl_2 reflections.

Three crystal structures have been reported for the Pt₃Al phase. The cubic L1₂ structure is not included in the ICDD or ICSD, and was also not found in any sample in this study. Sample PAR6 only contained the low temperature DOc structure. Pt₃AL was also found in sample PAR12, where it preferred orientation. It could not be determined which Pt₃Al structure formed in PAR12, as both structures gave a very good R² value through the grain refinement procedure. It could also be that both forms are present.

The PtAl phase is not included in the ICDD. The PdAl phase was used as a prototype. However, the PdAl phase has a high temperature and low temperature polymorph. The high temperature polymorph agrees with the β phase that has been suggested in the Al-Pt binary system, and the lattice parameter calculated through the refinement program was in good agreement with the experimental lattice parameter. The presence of the β phase in the samples indicated that the decomposition was not complete, probably the cooling rate was too slow to quench the phase in, but too fast to allow complete decomposition as initially suspected in the EDS analysis.

In some cases where there are many phases in the alloy, all the phases (especially when they were minor or trace phases) could not be identified by XRD. For example, in sample PAR3, the X phase could not be detected in the XRD spectrum. However, from the EDS analysis it is known that there was only a minor amount of X phase in the sample. The X phase was also only found in some regions and not throughout the sample's microstructure.

No phases have yet been confirmed satisfactorily in sample PAR11. The difficulty is probably due to the high percentage of third element in the binary structures.

The lattice parameters are influenced by the presence of the third element in the binary. Since the samples were not at equilibrium, no attempt could be made to calculate the relationship between the lattice parameter and the solid solutions of the third element.

The XRD results are listed in Table 4.18. For each alloy, the phases suggested by EDS analyses are listed. The crystal detail for each phase, as reported in the literature, was compared with the XRD results. The ICDD numbers have been listed only where a phase had been identified by XRD. Only where the lattice parameters have been calculated with the refinement program, have values been listed. Details on specific phases are provided in the footnotes. The XRD analysis of sample PAR 4 is attached in Appendix B.

Although not all the phases could be identified by XRD at this stage and while some minor discrepancies still remain, it was found that EDS and XRD are complementary to each other in this work. Where XRD data existed in the ICDD, the techniques were in good agreement. XRD proves to be a powerful technique to identify the phases in a metal alloy sample. Furthermore, where EDS could only pick up the composition of the phase, and not distinguish between phases with similar compositions, XRD revealed the presence of different prototypes on some phases. In some cases where the high temperature binary phase was thought to have decomposed completely, evidence of the high temperature phases was still found.

Sample PAR	EDS proposed phase	Space Group	Proto-type	Reported lattice parameter [nm]			Reference	Prototype used	Prototype ICDD number	Calculated lattice parameter [nm]			R ²	n	Notes
				a	b	c				a	b	c			
9	RuAl	Pm-3m	CsCl	0.295			1966Eds								
	Pt ₂ Al ₃	P3m1	Ni ₂ Al ₃	0.4208		0.5172	1963Fer	Pd ₂ Al ₃	06-0654	0.4229		0.5153		11	
	PtAl ₂	Fm3m	CaF ₂	0.5926			1937Zin	PtAl ₂	03-1006	0.5942				8	11
10	(Ru)	P6 ₃ /mmc	Mg	0.27059		0.42819		(Ru)	06-0663	0.2711		0.4305	0.9995	7	
	RuAl	Pm-3m	CsCl	0.295			1966Eds								
	β	Pm-3m	CsCl	0.3125			1978Bah								8
	PtAl	P213	FeSi	0.4866			1963Fer								6
	Pt ₅ Al ₃	Pbam	Rh ₅ Ge ₃	0.514	1.07	0.395	1964Huc								
11	RuAl	Pm-3m	CsCl	0.295			1966Eds								
	β	Pm-3m	CsCl	0.3125			1978Bah								8
	PtAl	P213	FeSi	0.4866			1963Fer								6
	Pt ₅ Al ₃	Pbam	Rh ₅ Ge ₃	0.514	1.07	0.395	1964Huc								9
12	(Ru)	P6 ₃ /mmc	Mg	0.27059		0.42819		(Ru)	06-0663	0.2689		0.4335	0.9994	5	
	Pt ₃ Al	P4/mbm	GaPt3(LT)	0.5448		0.7814		Pt ₃ Al	48-1815						10
		I4/mcm		0.3830		0.3890			29-0070						
13	X							Ir Al _{2.75}	50-1335						
	Pt ₈ Al ₂₁	I41/a	1.29595			1.06731	1966Eds								
	Pt ₅ Al ₂₁	(cI416)		1.923			1964Huc								
	(Al)	Fm-3m		0.4049				(Al)	04-0787	0.4045			0.9995	4	
14	RuAl ₂	Fddd	Si ₂ Ti	0.8015	0.4715	0.878	1963Sch	RuAl ₂	18-0057	0.7999	0.4714	0.8784	0.9993		
	X							Ir Al _{2.75}	50-1335	0.7712			0.9990		1
	PtAl ₂	Fm3m	CaF ₂	0.5926			1937Zin	PtAl ₂	03-1006	0.5914			0.9990		
15	β	Pm-3m	CsCl	0.3125			1978Bah								8
	PtAl	P213	FeSi	0.4866			1963Fer	PdAl	34-0564	0.4860			0.9993		6
	Pt ₅ Al ₃	Pbam	Rh ₅ Ge ₃	0.514	1.07	0.395	1964Huc								9
16	RuAl ₂	Fddd	Si ₂ Ti	0.8015	0.4715	0.878	1963Sch	RuAl ₂	18-0057						
	Ru ₄ Al ₁₃	C2/m		1.5862	0.8188	1.1736	1965Eds								12
	X							IrAl _{2.75}	50-1335	0.7732			0.9990		
	PtAl ₂	Fm3m	CaF ₂	0.5926			1937Zin	PtAl ₂	03-1006						

Notes

R² – Coefficient of determination (confidence level)

N – number of peaks in diffraction pattern assigned used to identify the phase.

1. Proposed new ternary phase X with composition $\sim\text{Ru}_{12}\text{Pt}_{15}\text{Al}_{73}$ with primitive cubic structure and $a = 0.7712$ nm. Similar to $\text{IrAl}_{2.75}$ and $\text{RhAl}_{2.63}$. Trace amounts only in PAR3, which was not detected by XRD.
2. Only Pearson symbol reported in the literature.
3. > 10 at. % Pt in RuAl_6 , structure too distorted in the non-equilibrium condition.
4. High temperature ternary phase T, decomposed at lower temperatures. Estimated composition $\sim\text{Ru}_{18}\text{Pt}_{28}\text{Al}_{64}$.
5. Ru_2Al_3 proposed in solidification reactions, decomposed and not observed in EDS or XRD.
6. PtAl not in ICDD. Found that $\text{PdAl-}\mu$ from Al-Pd system is very similar. PdAl in ICDD: 34-0564 and $a=0.4867$ nm.
7. Pt_2Al_3 not in ICDD. Pd_2Al_3 is very similar. Pd_2Al_3 in ICDD: 06-0654 and $a=0.4221$ nm and $c=0.5155$ nm.
8. β not in ICDD, only reported by [1978Bah]. Found that β in Al-Pd system is very similar, also stable at high temperatures only. $\text{PdAl-}\beta$ in ICDD: 06-0626 and $a=0.3049$ nm.
9. Pt_5Al_3 not in ICDD, could not match up with prototype or any other similar phase and could not identify the pattern. Structure is orthorhombic, so presence of the third element shifts peaks in different directions. Need equilibrium pure binary sample.
10. Different prototypes of Pt_3Al exist. $L1_2$ (cubic, $a = 0.3876$ nm) is high temperature, DOc' (tetragonal, $a = 0.3830$ nm and $c = 0.3890$ nm) is stable $\sim 600 - 1200$ K, DOc (tetragonal, $a = 0.5448$ nm and $c = 0.7814$ nm) stable below 600 K. $L1_2$ not in ICDD, DOc' in ICDD 29-0070 and DOc in ICDD 48-1815. In PAR 6, only DOc was found, in PAR12 DOc' and/or DOc were found, could not distinguish as both gave good R^2 . No trace of $L1_2$ in the as-cast samples.
11. Not observed in EDS analysis
12. $\text{Ru}_4\text{Al}_{13}$ in ICDD, but pattern only recorded up to $40^\circ 2$ theta. Could not identify.

4.4 Solidification projection.

The phase analyses of the sixteen alloys are summarised in Figure 4.35.

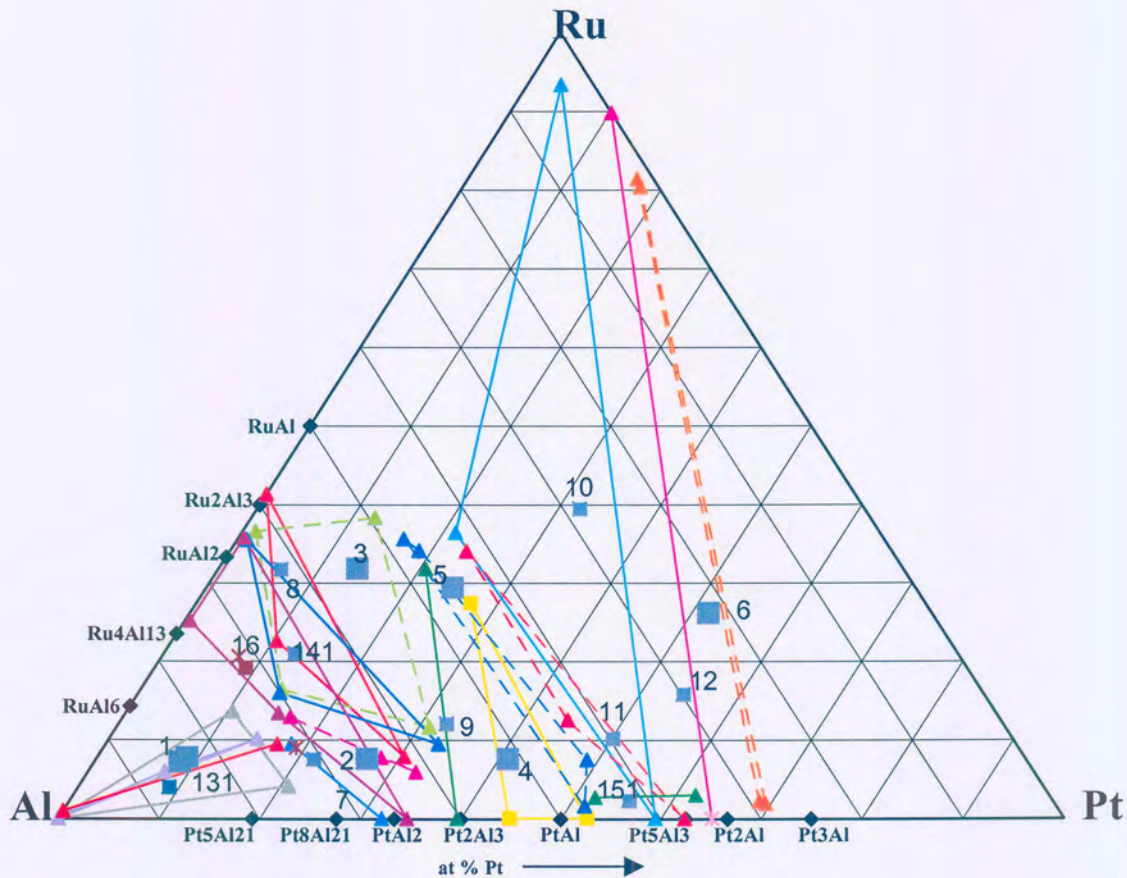


Figure 4.35. Summary of results for ternary Al-Pt-Ru alloys (square = overall composition, triangle = phase composition).

From the analyses of alloys, the following results were obtained:

- The liquidus surface is dominated by RuAl; it occurred to within 10 at. % of the Al-Pt binary.
- (Ru) also has a large liquidus surface. This is an important factor to consider when making alloys that are just outside of the region of the alloys targeted for commercialisation.

- RuAl was found to contain at least 20 at. % platinum
- PtAl₂ exhibited up to 11 at. % solubility for ruthenium.
- RuAl₂ exhibited up to 10 at. % solubility for platinum.
- Ru₄Al₁₃ and RuAl₆ were difficult to analyse, since they were found together on a fine scale.
- RuAl₆ showed solubility of at least 10 at. % platinum.
- Most of the other phases showed limited solubilities for the ternary element, less than 2 at. %: Ru₄Al₁₃, Pt₂Al₃, Pt₅Al₃, Pt₅Al₂₁ and PtAl.
- A ternary phase X, with a composition \sim Ru₁₂Pt₁₅Al₇₃, was found to be present. Initial XRD analysis showed that the X phase probably has a primitive cubic structure and is similar to \sim RhAl_{2.63} and \sim IrAl_{2.75}. The lattice parameter is 0.7712 nm.
- A high-temperature ternary phase T, with composition of \sim Ru₁₈Pt₂₈Al₆₄, exists.
- Ru₂Al₃, T and β decomposed through solid-state reactions:

$$\begin{aligned} \text{Ru}_2\text{Al}_3 &\rightarrow \sim\text{RuAl} + \sim\text{RuAl}_2 \\ \text{T} &\rightarrow \text{X} + \sim\text{PtAl}_2 \\ \beta &\rightarrow \sim\text{PtAl} + \text{Pt}_5\text{Al}_3 \end{aligned}$$
- \sim RuAl was involved in a number of subsequent reactions in different alloys:
 - peritectic formation of \sim PtAl,
 - peritectic formation of \sim PtAl₂
 - peritectic formation of β phase of the Al-Pt binary.
- There was good agreement between the experimental EDS and XRD results, despite the lack of phases present in the ICDD. In many cases, the structures of prototypes could be used through a grain refinement process to identify the binary phases.

4.4.1 Liquidus surface projection

The proposed liquidus surface projection is presented in Figure 4.36. The overall compositions of the alloys have been superimposed on the liquidus surface projection in Figure 4.37. The solidification reaction sequence for the Al-Pt-Ru systems, starting at the platinum corner, is summarised in Table 4.16.

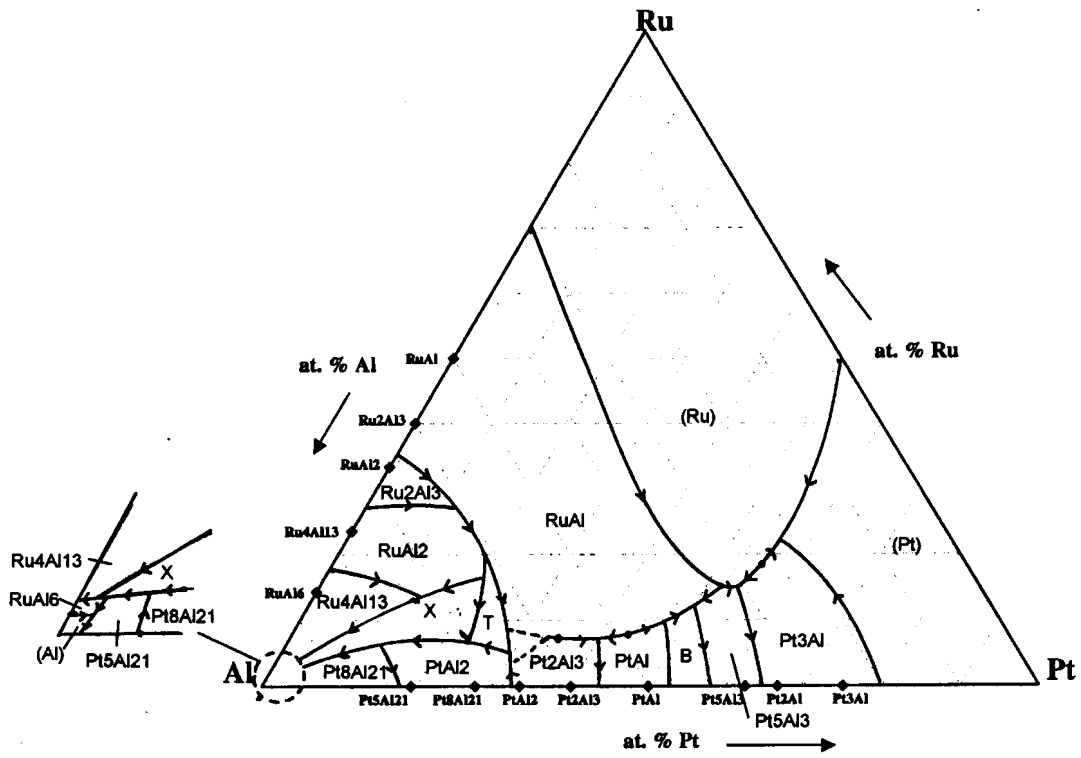


Figure 4.36. Proposed experimental liquidus surface projection.

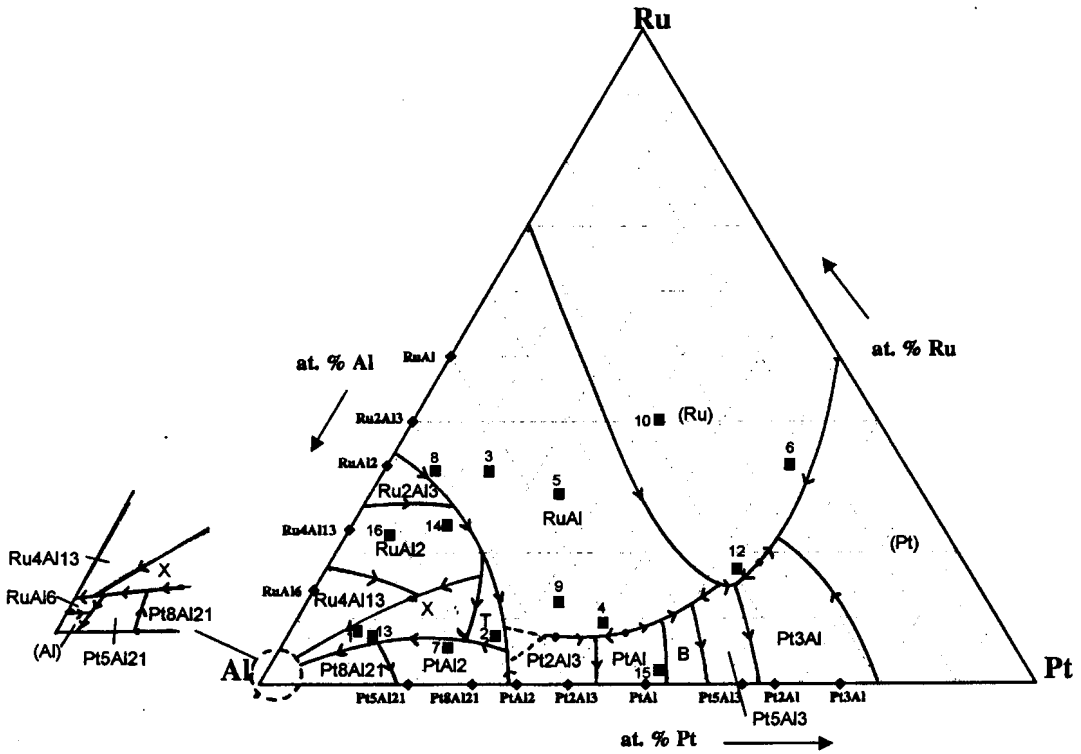


Figure 4.37. Overall alloy compositions on the liquidus surface projection.

The primary phase of each of the alloys indicated on which liquidus surface it lay. The solidification sequence was then used to determine the rest of the liquidus surface. Where there was a reaction between more than one phase and the liquid, it means that the liquidus surfaces of the phases must be adjacent. The liquidus surface projection is consistent with the solidification sequence of the alloys.

Two ternary phases appear on the liquidus surface projection. The ternary phase T is only stable at higher temperatures, as it decomposed on cooling. The ternary phase X is stable to lower temperatures.

4.4.2 Solidification reaction sequence

The solidification reactions are shown in Figure 4.37, and are listed in Table 4.19.

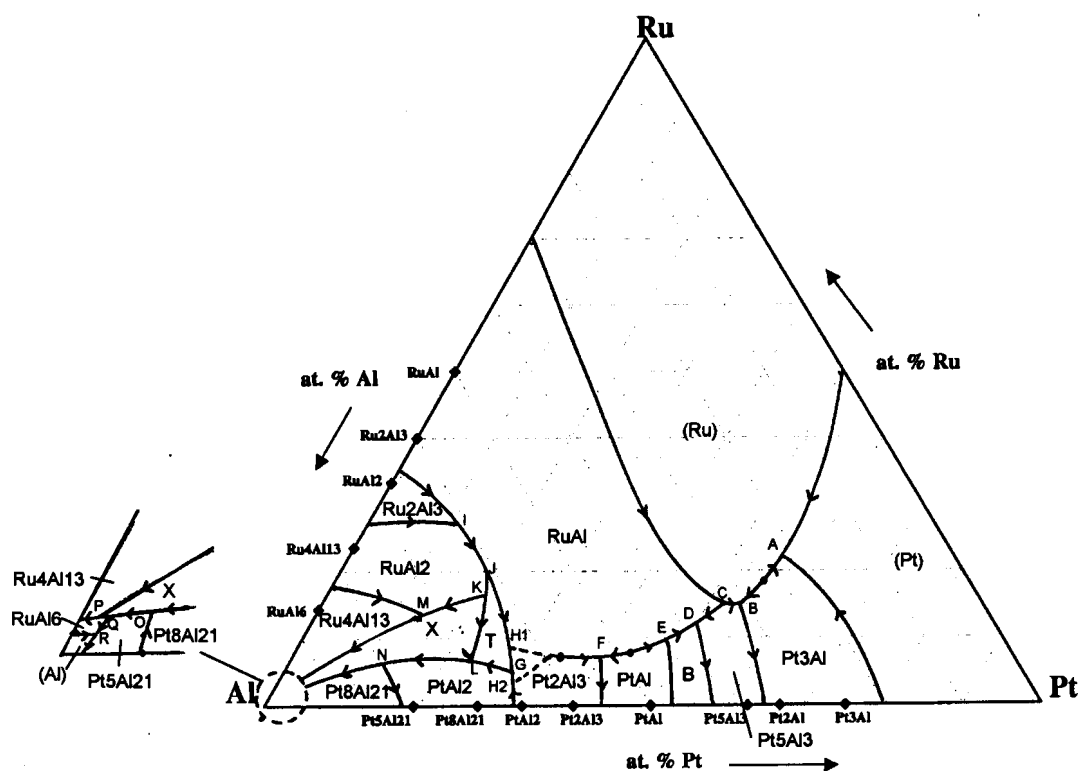


Figure 4.38. Experimental liquidus surface projection for the Al-Pt-Ru system, showing the solidification reactions.

Table 4.19. Solidification reactions for Al-Pt-Ru.

Equation number	Reaction
A	$L \rightarrow (Ru) + (Pt) + \sim Pt_3Al$
B	$L + (Ru) \rightarrow Pt_5Al_3 + \sim Pt_3Al$
C	$L + (Ru) + \sim RuAl \rightarrow \sim Pt_5Al_3$
D	$L + \sim RuAl \rightarrow \beta + \sim Pt_5Al_3$
E *	$(\uparrow) L + \sim PtAl \rightarrow \sim RuAl + \beta$ $(\downarrow) L + \sim PtAl + \sim RuAl \rightarrow \beta$
F	$L + \sim RuAl \rightarrow \sim PtAl + Pt_2Al_3$
G *	$L + Pt_2Al_3 \rightarrow \sim PtAl_2 + \sim Ru_{18}Pt_{28}Al_{64}$
H1 *	$L + \sim RuAl \rightarrow \sim Ru_{18}Pt_{28}Al_{64} + Pt_2Al_3$
G *	$L + \sim RuAl \rightarrow \sim PtAl_2 + \sim Ru_{18}Pt_{28}Al_{64}$
H2 *	$L + Pt_2Al_3 \rightarrow \sim RuAl + \sim PtAl_2$
I	$L + Ru_2Al_3 \rightarrow \sim RuAl + \sim RuAl_2$
J	$L + \sim RuAl + \sim RuAl_2 \rightarrow \sim Ru_{18}Pt_{28}Al_{64}$
K	$L + \sim Ru_{18}Pt_{28}Al_{64} + \sim RuAl_2 \rightarrow \sim Ru_{12}Pt_{15}Al_{73}$
L	$L + \sim Ru_{18}Pt_{28}Al_{64} \rightarrow \sim Ru_{12}Pt_{15}Al_{73} + \sim PtAl_2$
M	$L + \sim RuAl_2 \rightarrow \sim Ru_{12}Pt_{15}Al_{73} + \sim Ru_4Al_{13}$
N	$L + \sim PtAl_2 + \sim Ru_{12}Pt_{15}Al_{73} \rightarrow \sim Pt_8Al_{21}$
O	$L + \sim Pt_8Al_{21} \rightarrow \sim Ru_{12}Pt_{15}Al_{73} + \sim Pt_5Al_{21}$
Q	$L + \sim Ru_{12}Pt_{15}Al_{73} + \sim Pt_5Al_{21} \rightarrow \sim RuAl_6$
P £	$L + \sim Ru_{12}Pt_{15}Al_{73} \rightarrow \sim Ru_4Al_{13} + \sim RuAl_6$
R	$L + \sim RuAl_6 \rightarrow \sim Pt_5Al_{21} + (Al)$

* Not enough experimental data available to conclude in which direction this reaction proceeds.

£ Exit reaction must be peritectic to be consistent with the Al-Ru binary.

* not enough experimental data are available to determine conclusively which direction this reaction goes.

4.5 Conclusions

Sixteen alloy samples were studied with SEM/EDS and XRD. The results from the two techniques were in good agreement. The solidification sequences and a liquidus surface projection have been proposed.

Chapter 5

Phase Diagrams with the CALPHAD Method

5.1 Introduction

Materials science investigates the structure, properties, preparation and processing of materials. These investigations are increasingly supported by models based on concepts of chemistry, physics and crystallography as modern society is constantly looking for new and innovative materials to enable and support new technologies.

If one considers that 86 of the about 100 elements known to man (excluding the inert gases and transuranic elements) combine to as many as 7.7×10^{25} systems (binary, ternary, quaternary up to the 86-element system), it is not surprising that as computational power became available and was developed, many modelling methods have been adopted to predict phase diagrams, material structures, material properties and processing conditions by computational methods.

One of these methods, based on the 19th century work of Gibbs, is the CALPHAD (CALculation of PHase Diagrams) method, a completely general, extendable and theoretically meaningful technique. With this technique, experimental data is used to derive the Gibbs energy of an element or phase as a function of temperature, pressure and composition. From the Gibbs energies, the thermodynamic properties of a system can be derived and the equilibrium phase diagram can be predicted, since a phase diagram is a graphical representation of the loci of thermodynamic variables when equilibrium (lowest energy state) among the phases of a system is established under a given set of conditions [1996Pel].

A brief overview of the development of computational methods is given, as well as the software available. However, as the Thermo-Calc [1985Sun] software was used in this study, most of the emphasis will be placed on it.

5.2 History

Gibbs's famous study in 1876 provided the theoretical background for the thermodynamic examination of complex, chemically reacting systems. In 1908, Van Laar applied the Gibbs energy concepts to phase equilibria. Then, in the 1930s, Hume-Rothery [1934Hum] developed an alternative approach based on band-structures. When it became evident that his concepts could not be applied to industrially-relevant materials such as steels, nickel-based alloys and the emerging titanium and uranium alloys, interest focused on the thermodynamic approach again, especially those of Meijering and Hillert in Europe and Kaufman in America. Meijering [1957Mei] calculated a phase diagram for Ni-Cr-Cu, giving a quantitative description to all topological features of the phase diagram. This was pioneering work, as the mere interpolation of the binary systems would have yielded an erroneous diagram. Meijering had to extrapolate a lattice stability value (the relative Gibbs energy for a crystal structure of the pure element) for fcc Cr as this could not be obtained directly from experiment - it is interesting to note that these early results from Meijering have only been marginally improved over the years!

The thermodynamic approach showed that the lattice stabilities were not only related to the solubility limits, electron concentrations (or electron per atom ratios) and electrochemical (valence) factors from Hume-Rothery's band-structure theory, but that they also depend on the properties and interaction of the co-existing phases as well as on the temperature. Kaufman and Hume-Rothery had extensive discussions to try and clarify the conflict in different value sets of lattice stabilities. Not only was there the Hume-Rothery approach, with Jones and Mott [1936Mot] taking the electron per atom ratio model further, but also Engel [1949Eng] and Brewer [1963Bre] developed a method which correlates the structure of metals with the number of s and p valence electrons in the system. Their proposed lattice stabilities, based on spectroscopic data, differed as much as an order of magnitude in some cases with experimental values. In the next development, lattice stabilities were also obtained from electron energy calculations. The lack of agreement in these fundamental values delayed the more general acceptance of the CALPHAD technique. Pettifor [1972Pet], by following a Jones-type analysis, related band-structure to the density-of-state (DOS) in transition metals. These density functional calculations have confirmed the existence of wave mechanical oscillatory energy difference functions between lattices in a crystal, which is difficult to handle in an extrapolation technique like CALPHAD. Another factor that contributes to the discrepancies in theory and CALPHAD lattice stability values is that in the CALPHAD technique, positive melting temperatures are assigned to the metastable phases, while they are theoretically predicted to be mechanically unstable at absolute zero.

At the same time, two other modelling methods were developed to predict alloy properties. Already in 1949, Kikuchi [1951Kik] introduced the cluster variation model (CVM), but further development only started in the 1970s as the method requires substantial computing power. CVM is based on the mutual interactions of all the atoms, which are described in sets of clusters. The tetrahedron is the smallest cluster in a three-dimensional lattice and can thus reflect a great variety of atomic interactions. CVM is very powerful in treating order/disorder phenomena. Miedema [1988deB] developed a semi-empirical technique to predict the enthalpy of formation and interaction parameters for binary and some ternary alloys.

Despite the differences that existed, Larry Kaufman went ahead with his vision in 1970 and used the name 'CALPHAD' for a technique where one may calculate an improved phase diagram after assessing the thermodynamic properties of all the phases that may form from a set of components (elements, ions, compounds). This method is based on the axiom that complete Gibbs energy versus composition curves can be constructed for all the structures exhibited by the elements right across the complete alloy system. This involves the extrapolation of G/x (where x is the composition) curves for many phases into regions where they are metastable or unstable. The relative Gibbs energy for various crystal structures of the pure elements (lattice stabilities) in the system must, therefore, be established. Kaufman drafted a bilateral agreement to generate official meetings between the American and French experts, and he extended this invitation to representatives from the UK, Sweden and Germany. This was the birth of the CALPHAD meetings. The objectives defined by Kaufman and Ansara in 1973 are today still the CALPHAD objectives:

We believe that substantial progress can be made in a short period of time if we would arrange to work together for one week at one of our facilities to define problems, disband, carry out some individual activities, and meet again for a week at a second facility to compare results and chart future activities. (2003: www.calphad.org)

In 1977, the first CALPHAD – Computer Coupling of Phase Diagrams and Thermochemistry journal was published. Since 2000, the journal also accepts *ab initio* contributions.

5.3 Current Status

The CALPHAD technique has clearly come of age and it now allows for the calculation of complex phase equilibria equations. A number of commercial software packages are available. These include Thermo-Calc, FactSage, MTDATA, PANDAT, MALT and Exterm. An edition of the Calphad journal was dedicated to detailed overviews of these commercial packages (CALPHAD, Vol. 26, No. 2, 2002). Another popular program was the Lukas program (BINGS and TINGS programmes), developed by Hans-Leo Lukas at the Max Planck Institut fur Metallforschung in Stuttgart [1977Luk], Germany, but this program has not been commercialised. The CALPHAD technique is used extensively in alloy development, as well as hardmetals (carbides), aqueous solutions, chemical vapour deposition and corrosion applications. It is also possible to apply the CALPHAD technique to model polymer solutions, though this is a relatively new application and suitable models are still in an early stage of development. Extensive databases have been developed for general as well as specific applications, with the most significant being the Science Group ThermoData Europe (SGTE) consortium's databases (www.sgte.org). Databases for alloy-specific applications, e.g. Ni-based superalloys, Al-alloys, solder and steels, have been developed by the relevant industry sectors. These databases are the result of CALPHAD optimisations.

Some of the software includes a module for the optimisation of the Gibbs energy functions, e.g. the Parrot module [1984Jan] in Thermo-Calc. Many databases have been developed for various commercial alloy systems. Conversion programs are also available to transport data from one system to another, although the current trend is to present data in the SGTE format, which can be used by all the programs.

The success of the CALPHAD technique is underwritten by the many application programming interfaces which are being developed to use the results from the equilibrium CALPHAD calculations in third party software programs like MatLab®. Major successes have been the combination of thermodynamics and kinetics to simulate diffusion transformations, e.g. DICTRA in Thermo-Calc and JMatPro, a software program developed by ThermoTech in the UK [2001Li], which uses thermodynamic and kinetic databases to predict material structures and mechanical properties. The Phase Field method is a new method under development, where the microstructures of alloys are simulated through equilibrium calculations based on the CALPHAD method. A commercial application program, MICRESS, has been released by ACCESS e.V. Solidification, solid-state transformations, grain growth and recrystallisation can be studied.

Evaluating recent literature, it is clear that the different modelling techniques are getting closer to each other and increasingly often data are extrapolated between the different methods. Thermochemical and first principle (*ab initio*) values are becoming more comparable. It seems that most of the discrepancies which still exist are associated with cases where the postulated metastable allotrope is mechanically unstable to shear and will spontaneously collapse at 0 K [1988Pet]. Miedema's semi-empirical method is frequently used to generate enthalpies of formation for the assessments of systems where no experimental data are available. The CALPHAD thermodynamic assessments also have been successfully performed using a CVM approach to describe the lattices [1990Sun].

One of the major obstacles in the marriage of the different thermodynamic modelling techniques, however, still remains the extrapolation of sets of data between the CALPHAD technique and *ab initio* modelled systems, as the data are incompatible and the conversions

are complex. This limits the use of data from one technique to another to the use of individual values for constituents, substances and phases.

5.4 CALPHAD Methodology

The CALPHAD technique fits experimental data on the phase equilibria, thermochemical information on the separate phases and physical information of the elements, constituents and phases through a mathematical regression process to Gibbs energy curves. One of the most significant advantages of this methodology is that, because a total Gibbs energy is calculated, all the associated functions (heat capacities, enthalpy, activity, chemical potential, etc.) and characteristics of phase equilibria (phase diagrams, potential diagrams, Scheill diagrams, etc.) can be derived.

The standard methodology of a CALPHAD type assessment is illustrated in Figure 5.1. The procedure defines three different stages: first the literature is critically evaluated and models are proposed for the different phases in the system. Secondly, the Gibbs energies are calculated and re-calculated, in an iterative process, continuously comparing the calculated result with the experimental data, until the final stage, where a workable description is obtained such that it satisfies the application requirements. These stages will be discussed in broad terms to provide an understanding of the principles involved. For more detailed information, the reader is referred to the optimiser program's manual, 'CALPHAD - A comprehensive Guide' by Saunders and Miodownik [1998Sau] and some general and practical optimisation guidelines by Kumar and Wollants [2001Kum].

A thorough literature review of the experimental data of the alloy system to be assessed is essential. Data that can be used for an assessment includes experimental phase diagram data and thermodynamic data. Experimental phase diagram data can be invariant reactions, phase compositions and composition ranges, liquidus temperatures and crystal structure information. Thermodynamic data can be experimental, calculated with *ab initio* methods or predicted by empirical models. Enthalpies of formation, activity data, chemical potentials, differential thermal analysis (DTA) and differential scanning calorimetry (DSC) results, etc. can be used. *Ab initio* methods have proved to be successful in providing data for cases where there are no data available. Predictions, like Miedema's semi-empirical model, are useful to estimate enthalpies of formation, especially when the necessary experiments cannot be performed due to adverse conditions necessary, for example, very high temperatures or very reactive compounds.

The data must be evaluated for accuracy, reliability and consistency. Different types of data have different accuracies associated with them. For instance, composition analysis can be performed by analytical chemistry, microprobe analysis or X-ray energy dispersive analysis (EDS) with or without standards, in the scanning electron microscope. Chemical analysis using a primary method will produce much more accurate results than standardless EDS analysis. Thermodynamic data from DTA are affected by whether a heating or cooling cycle has been used for the calculations. It is thus important to not just rely on review articles, but to scrutinise the original publications to objectively evaluate the data. According to the accuracy, reliability and consistency of the data, relative weights are assigned to the data during the CALPHAD optimisation. Unreliable and inconsistent data should not be included in the optimisation.

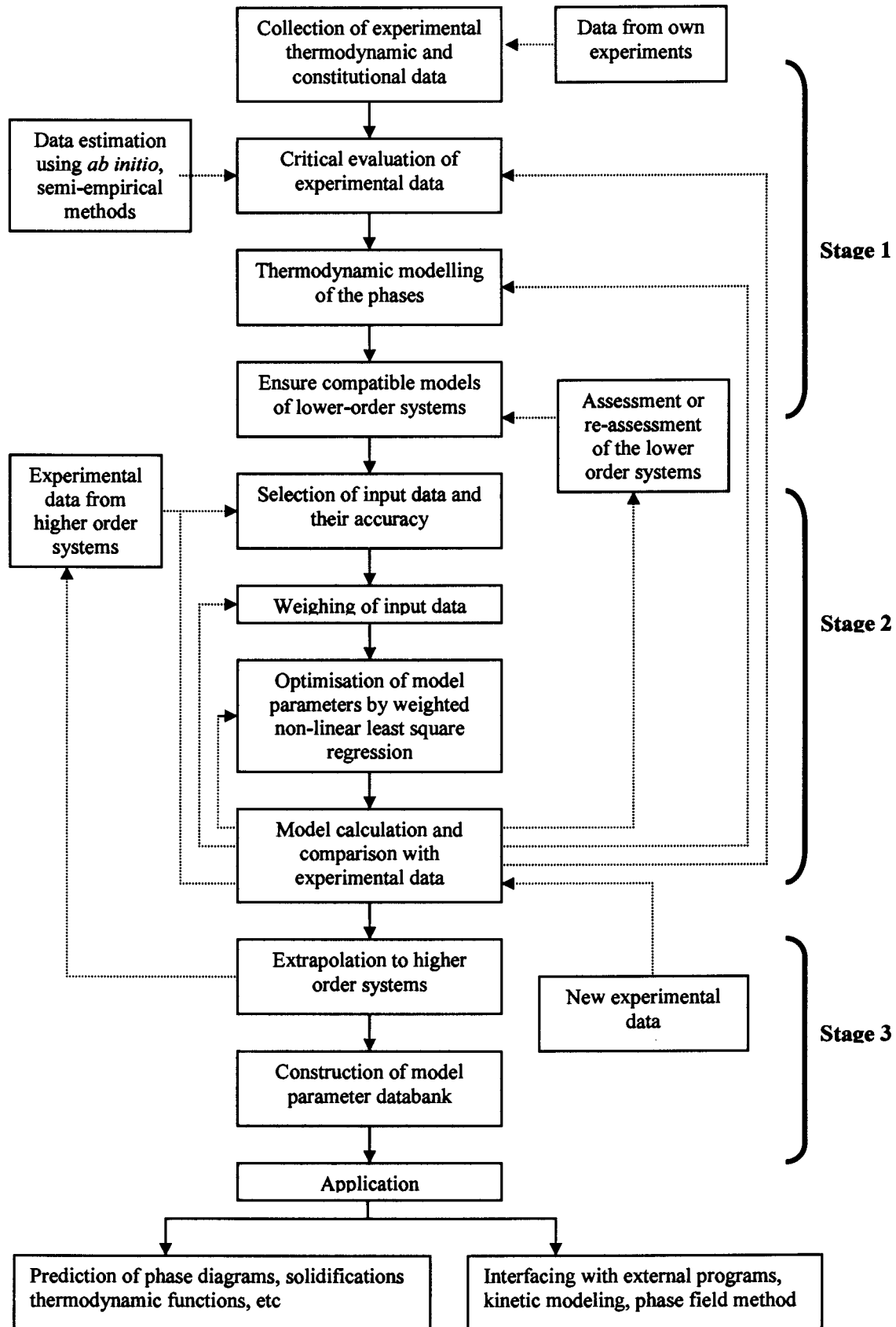


Figure 5.1. Flowchart of the CALPHAD method, adapted from [2001Kum].

The data can be compiled as a set of equilibrium data-points in the system. Each data-point is such that there are zero degrees of freedom in the phase rule

$$F = C - P + 2$$

where F is the degrees of freedom, C is the number of components and P is the number of phases.

A measurement error associated with the equilibrium data-point must be determined. Each equilibrium data-point contains dependent and independent quantities. The dependent quantity of each data-point must fulfil the phase rule, since it will be calculated in the optimisation. Thus it is important, when extracting data from, for example phase diagrams, that care is taken as to whether the composition or temperature is set as the dependent quantity. This is illustrated in Figure 5.2. For a steep slope on a phase diagram, a larger error is associated with the temperature than with the composition, so the composition should be the dependent value, as it has a smaller error in comparison the error associated to the temperature value, so that the smallest value contributes with the sum of squares in the optimisation.

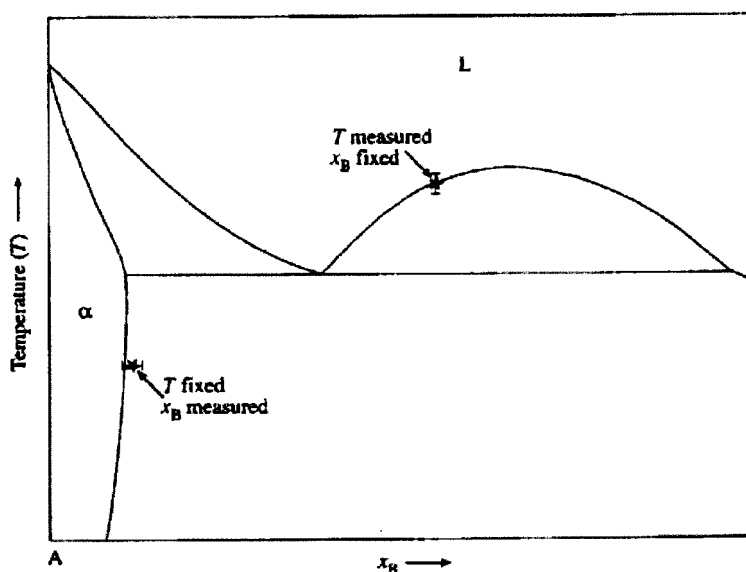


Figure 5.2. Phase diagram showing regions where only composition can be reliably measured at a given temperature and vice versa [2001Kum].

A reference state must be established for each element or component. This is generally taken to be the crystal structure in which the element exists at standard temperature and pressure. For consistency, and to allow extrapolations between different calculated systems, the reference state as prescribed in the SGTE database is usually referred to.

An important factor in the calculation of the Gibbs energy curves for a phase or system is the selection of the models that are used to describe the phases. Although the models are not strictly based on the crystal structures, some consideration should be given to the crystal structure and the model must have some physical meaning in describing the phase as for example a stoichiometric compound, an ordered phase or as a solid solution phase. Homogeneity ranges in a phase are normally due to defects (either anti-site atoms - atoms occupying the 'wrong site' - or vacancies) in the ideal structure of the phase. In most cases, the types of defect are not known and then a general approach can be applied adding the defects

on an additional lattice. However, care must be taken to select a suitable, simple and robust model, especially if the data are needed for extrapolation into higher order systems, as complex models are difficult to handle by the software and can lead to problems when extrapolated. Where possible, the model must follow ‘standardisation’ to ensure consistency, for instance the order/disorder transformations and structure relations of bcc-A2/B2 and fcc-A1/L1₂. Although there are good references available in the literature for some specific models [2001HilC, 1999Dup], models are constantly refined and changed as knowledge and understanding of the phase and its behaviour increases.

The assessments in this study were performed with the Parrot module [1984Jan] in the Thermo-Calc software [1985Sun]. Parrot is a program for the evaluation of thermodynamic model parameters from experimental observations of quantities describing a set of equilibrium states of the system. The model parameters are estimated by a weighted non-linear least squares optimisation of thermochemical and constitutional data.

5.5 CALPHAD Thermodynamics

5.5.1 Some basic principles

The CALPHAD method is based on Gibbs free energy functions. The state of a system can always be described in terms of the Gibbs free energy, since a system always tries to minimise its energy by minimising its enthalpy while maximising its entropy at constant pressure. Thus, the Gibbs energy is the most fundamental way to describe a system in terms of its energy status.

The Gibbs energy is always given related to some reference, since for many elements more than one structure is stable, depending on the temperature and pressure. In the CALPHAD method, the state of the element that is stable at 101 325 Pa and 298 K is usually selected as the reference state.

Data must be kept consistent, that is, refer to the same reference states and have the same mathematical polynomial formalisms, in order to allow interchanging data with other data as well as to extrapolate data from various assessments to higher order systems. This study complies to the format of the Science Group Thermodata Europe (SGTE). All reference data for elements in this work is from Dinsdale [1991Din], who published a unified database under the auspices of SGTE.

5.5.2 Thermodynamics of Pure Elements

The Gibbs free energy $G_{[P,T]}$ of a pure element is given by the equation

$$G_{[P,T]} = H_{[P,T]} - TS_{[P,T]} \quad (5.1)$$

where $H_{[P,T]}$ and $TS_{[P,T]}$, respectively, are the enthalpy and entropy as a function of temperature and pressure. These data are obtained from the SGTE database [1991Din]. The SGTE format for a pure element i , at constant atmospheric pressure, is

$$GHSE_{i,T} = G_{m[T]} - H_m^{SER}(298.15K) = a + bT + cT \ln(T) + \sum d_n T^n \quad (5.2)$$

$$(\Sigma d_n T^n = dT^2 + eT^3 + fT^{-1} + gT^7 + hT^{-9}) \quad (5.3)$$

The left-hand side of the equation is defined as the Gibbs energy relative to a standard element reference state (SER) where H_m^{SER} is the enthalpy of the element in its defined reference state at 298.15 K; a , b , c and d_n are coefficients and n represents a set of integers, typically taking the values of 2, 3, -1, 7 and -9. The terms T^7 and T^9 have been introduced to remove the possibility of phases becoming incorrectly stable at high or low temperatures, respectively. The equation can be expanded to include terms to describe pressure and magnetic dependence. These effects are not relevant to the elements (Al, Pt and Ru) in this study.

The first and second derivatives of GHSER with respect to temperature are related to the absolute entropy and heat capacity of the element at the same temperature. This means experimentally determined heat capacity values can be used directly and the coefficients will be related to c , d , e , f , g and h .

This convention is convenient since all the data in a database, stored relevant to the SGTE reference state, are inter-consistent and can be combined to calculate chemical and metallurgical equilibria.

5.5.3 Thermodynamics of solutions

In CALPHAD, a solution phase is defined as any phase in which there is a range of solubility of more than one component. On atomistic scale, solutions consist of a mixture of different species, in the simplest case atoms. Solutions can be classified as substitutional solutions, sublattices, ionic, aqueous or polymers/organic molecules, and for the first four, specialised models have already been developed. The models for substitutional solutions and sublattices will be discussed in detail since they are relevant to metallic alloy systems. Although metallic alloy systems are referred to as solid solutions in physical metallurgy, the general terminology 'solution' will be used here as more than just metallic alloy systems can be described as 'solutions' in CALPHAD models described below.

The format for solutions is the same as the SGTE format used for pure elements (Equations 5.2 and 5.3). However, in most cases only the terms $a + b T$ are used. The term $T \ln T$ is usually only used in cases where heat capacity data are available, which depicts the use of this term to ensure the correct derivation of the heat capacity from the Gibbs energy.

For all solution phases, the Gibbs energy is given by the general formula

$$G = G^{ref} + G^{id} + G^{xs} \quad (5.4)$$

where G^{ref} is the contribution of the pure compounds of the phase to the Gibbs energy, G^{id} is the ideal mixing contribution and G^{xs} is the contribution due to non-ideal mixing, also known as the Gibbs excess energy of mixing. G^{ref} for a system with N pure elements is obtained from

$$G^{ref} = \sum_{i=1}^N G_i^{ref} \quad (5.5)$$

where ${}^0G_i^{ref}$ is the Gibbs energy of i for the reference state obtained from the SGTE database.

5.5.3.1 Substitutional Solutions

A random substitutional approach is used for phases such as the gas phase or simple metallic liquid and solid solution phases where components can mix on any spatial position which is available in the phase. For instance, in a simple bcc phase of two bcc components, any of the components can occupy any of the atomic sites that define the cubic structure. In a gas and liquid, the crystallographic structure is lost, but otherwise positional occupation of the various components relies on the random substitution rather than any preferential occupation of a site by any particular component. Randomness can only be assumed as long as the species, atoms or molecules are sufficiently similar in size, shape, electronegativity, etc.

In evaluating simple mixtures, **ideal solutions** follow Raoult's law, i.e. the activity of an element i in the solution is equal to its mole fraction at all compositions as the bond strength between A and B are so similar that A and B are randomly distributed. Gases tend to follow ideal behaviour. However, in real A-B solutions, the interaction between A and B is different from that between A and A or B and B. Due to these attractive or repulsive forces, there will not be a random distribution of the compounds in the solution. The Gibbs energy of an ideal solution is

$$G_m = \sum x_i G_i^\circ + RT \sum x_i \log_e x_i \quad (5.6)$$

where G_i° defines the Gibbs energy of the phase containing the pure component i . x_i is the mole fraction of component i . Ideal solutions do not have an excess energy contribution associated with them.

Some solutions exhibit random mixing, but the net heat absorbed or released is not zero ($H^M \neq 0$). This is called a **regular solution**. For a regular solution, an excess energy is needed and this is described with the excess energy G^{xs} term.

The excess energy G^{xs} can be expressed as $x_A x_B L_{AB}$, where L_{AB} is the interaction parameter as defined by Hildebrand [1929Hil]. The physical meaning of L_{AB} can be described as follows: When one considers the magnitude and sign of the interactions between the components in the phase that will have an influence on the total energy, but assumes that it is composition independent and further assumes that the total energy arises from only nearest-neighbour bond energies, the total energy becomes

$$E_o = \omega_{AA} E_{AA} + \omega_{BB} E_{BB} + \omega_{AB} E_{AB} \quad (5.7)$$

where ω_{AA} , ω_{BB} , ω_{AB} , E_{AA} , E_{BB} and E_{AB} are the number of bonds and their energies associated with the formation of different bond types AA, BB and AB respectively. Assuming the reference states of pure A and B and that the bond energies are temperature dependent, it is then deduced that

$$G_m = \sum x_i G_i^\circ + RT \sum x_i \log x_i + \sum \sum x_i x_j L_{ij} \quad (5.8)$$

with L_{ij} the temperature dependent interaction parameter between species i and j . For an ideal solution, the last term falls away as $x_i x_j$ becomes zero for pure i as well as pure j (Equation 5.6).

Since the regular solution model is composition independent, Kaufman and Bernstein developed the model further to include composition dependence and proposed the **subregular model**. In this model, interaction energies are considered to change linearly with composition and the Gibbs excess energy can be expressed as

$$G_{mix}^{xs} = x_i x_j (L_{ij}^i x_i + L_{ij}^j x_j) \quad (5.9)$$

The subregular model can be expanded to more complex composition dependencies in terms of a power series. The Redlich-Kister expansion is the most commonly-used expansion and the Gibbs energy for a substitutional solution can then be rewritten as

$$G_m = \sum x_i G_i^\circ + RT \sum x_i \log x_i + \sum_i \sum_{j>i} x_i x_j \sum_v (x_i - x_j)^v L_{i,j}^v \quad (5.10)$$

where the temperature dependence of the interaction parameter can be described as

$$L_{i,j;i} = y_i' y_j' [a_0 + b_0 T + c_0 T \ln T (a_1 + b_1 T) (y_i' - y_j')] \quad (5.11)$$

The index v denotes the regularity of the solution, L^0 is designated for the regular solution, L^1 is referred to as the subregular solution parameter and L^2 the subsubregular solution parameter.

Equation 5.10 is usually used to describe metallic systems for substitutional phases and to describe a disordered solution such as liquid, fcc, bcc and hcp.

5.5.3.2 Sublattice Model / Compound Energy Formalism

The above-mentioned models fall short in accurately extrapolating to higher solute contents or extending the description to higher order alloy systems for phases which display some form of order. As the CALPHAD approach sometimes needs to evaluate or estimate unknown, unstable and/or metastable phases and stoichiometric compounds, a sublattice model (SL), also designated the Compound Energy Formalism (CEF), has been developed [1970Hil, 1945Tem, 1981Sun]. This model can be envisaged as interlocking sublattices on which the various components can mix. Although the model does not define any crystal structure, internal parameter relationships can be defined with respect to different crystal structures, such as the order-disorder transformation. This is now one of the most commonly-used methods to describe solution and compound phases because it is flexible and can account for a variety of different phase types (e.g. interstitial phases, intermetallics, σ , μ). In simplified form, this model can also describes stoichiometric line compound phases where each sublattice is occupied by a single type of atom, and substitutional solution phases which contain only one sublattice. To be in line with modern literature on sublattice modelling, the term 'Compound Energy Formalism' (CEF), will be used.

The physical meaning of the sublattice model for the system $(A,B)_1(C,D)_1$ has been schematically described by Saunders and Miodownik [1998Sau] with a composition space and reference energy surface, as illustrated in Figure 5.3.

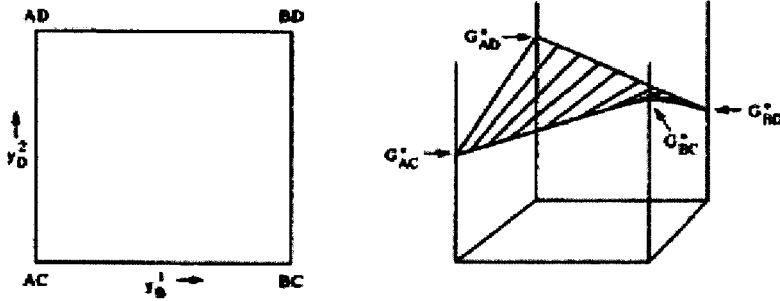


Figure 5.3. Composition space and reference energy surface for $(A,B)_1(C,D)_1$ [1998Sau].

All possible compositions in the system are encompassed by the composition space AC-AD-BD-BC. These four compounds at the corners of the composition space are the so-called 'end-members'.

The reference energy surface can be represented by the equation

$$G^{ref} = y_A^I y_C^I G_{A:C}^0 + y_A^I y_D^I G_{A:D}^0 + y_B^I y_C^I G_{B:C}^0 + y_B^I y_D^I G_{B:D}^0 \quad (5.12)$$

The Gibbs energies of the compounds AC, BC, AD and BD control the interactions A-C, A-D, B-C and B-D respectively. Mixing on the sublattices controls A-B and B-D interactions and the simplest form of interaction is a regular solution format such that

$$G^{xs} = y_A^I y_B^I L_{A,B,*}^0 + y_C^I y_D^I L_{C,D}^0 \quad (5.13)$$

where $L_{A,B,*}^0$ and $L_{C,D}^0$ denote regular solution parameters for mixing on the sublattices irrespective of the site occupation of the other sublattice and '*' denotes that the sublattice is independent of the constituent on that sublattice. Equation 5.13 is composition independent. However, the interactions can be composition dependent and the excess energy is then described with a subregular model (Equations 5.10 and 5.11).

According to the sublattice model developed by Sundman and Jönsson [1981Sun], an intermetallic phase can be described as

$$(A_{y_A} B_{y_B} \dots)_p (C_{y_C} D_{y_D} \dots)_q \dots \quad (5.14)$$

where the species A, B... can be atoms or vacancies. p and q are the number of sites, y_i^I and y_j^I are the respective site fractions of species i and j in their respective sub-sublattices, designated by ' and ". Each sublattice (s) has the condition $\sum_i y_i^s = 1$. When $p + q + \dots = 1$, the thermodynamic quantities are referred to as one mole of sites.

The Gibbs energy of mixing for a sublattice phase is

$$G_m = G^{ref} + G^{id} + G^{xs} \quad (5.15)$$

The components of Equation 5.15 are expanded as follows [1981Sun]:

$$G^{ref} = y'_A y'_C G_{A:C}^\circ + y'_A y'_D G_{A:D}^\circ + y'_B y'_C G_{B:C}^\circ + y'_B y'_D G_{B:D}^\circ \quad (5.16)$$

$$G^{id} = RT[p(y'_A \ln y'_A + y'_B \ln y'_B) + q(y'_C \ln y'_C + y'_D \ln y'_D)] \quad (5.17)$$

$$G^{xs} = y'_A y'_B [y'_C L_{A,B:C} + y'_D L_{A,B:D}] + y'_C y'_D [y'_A L_{A:C,D} + y'_B L_{B:C,D}] + y'_A y'_B y'_C y'_D L_{A,B:C,D} \quad (5.18)$$

$G_{A:B}^\circ$, $G_{A:D}^\circ$, $G_{B:C}^\circ$ and $G_{B:D}^\circ$ represent the Gibbs energy of formation of the stoichiometric compounds $A_p C_q$, $A_p D_q$, $B_p C_q$ and $B_p D_q$, which might be stable, metastable or even unstable in the system. y'_i is the site fraction of element i on sublattice s . In Equation 5.18, L is the interaction parameter and expressed as a function of temperature $L = a + b*T$.

For the special case where order-disorder relationships exist between phases in a system, the Gibbs energy can be described as [1998Ans]:

$$G_m = G_m^{dis}(x_i) + \Delta G^{ord*}(y'_i y''_i) - \Delta G^{ord*}(x_i, x_i) \quad (5.19)$$

where $G_m^{dis}(x_i)$ is the molar Gibbs energy contribution from the disordered state and $\Delta G_m^{ord}(y'_i; y''_i)$ is the ordering energy contribution, equal to zero in the disordered state and $\Delta G^{ord*}(x_i, x_i)$ represents the extraneous excess energy contribution from the ordered parameters when the phase becomes disordered.

The power of the sublattice model lies in the fact that many of the other models, like the substitutional solution model, are simplifications of the SL/CEF. On the other hand, the model can be specifically applied to a complex ordered crystal structure, like sigma phase, or used to describe order-disorder relations between similar phases, like the γ/γ' in Ni-based super alloys. Some of the applications of the CEF are listed in Table 5.1.

Table 5.1. Applications of the compound energy formalism.

Phase	Description
Stoichiometric Compound	$(A)_a(B)_b$
Interstitial Solutions	$(Fe, Ni)_p(C, N, Va)_q$
Substitutional Solutions	$(A_{x1}, B_{x2}, C_{x3}, \dots)$
Ordered Phase (ie Ni_3Al -L1 ₂)	$(Al, Ni)_{0.25}(Al, Ni)_{0.25}(Al, Ni)_{0.25}(Al, Ni)_{0.25}$
Ordered Phase (e.g. Ru_2Al_3)	$(Al)_3(Al, Ru)_2(Ru, Va)$
Salt Mixtures	$(A^+, B^+)_a(C^-, D^-)_b$
III-V compounds	$(A^{III}, B^{III})_a(C^V D^V)_b$
Liquid Ionic solution	$(Al^{+3})_p(O^{-2}, SiO_4^{-4})_q$

A number of custom two-, three- and four-sublattice models have been developed to describe additional parameter relations in certain order-disorder transformations. These models ensure consistency and data compatibility in the descriptions from different researchers and allow the

data to be extrapolated to higher order systems without adjusting the phase descriptions. The application of the CEF to fcc and B2 ordering will be discussed as in the Al-Pt-Ru system.

Hillert [2001Hil] recently published a comprehensive review article on the compound energy formalism. It was accompanied by an applications article by Frisk and Selleby [2001Fri], which will give the reader more insight into CEF modelling.

5.5.3.2.1 CEF applied to B2/A2 order/disorder transformation

The disordered form of the B2 phase (CsCl-type) is the A2 phase (W-type). Figure 5.4 presents schematic diagrams of both structures. The B2 phase can be seen as two interpenetrating primitive cubic sublattices and in the completely ordered crystals (ideal case) the positions of the first sublattice, α , are occupied by atoms of kind A and the other sublattice, β , by atoms of kind B. In the A2 structure, all the sites are equivalent and the structure is called disordered. Disorder reactions have been experimentally observed as first or second order.

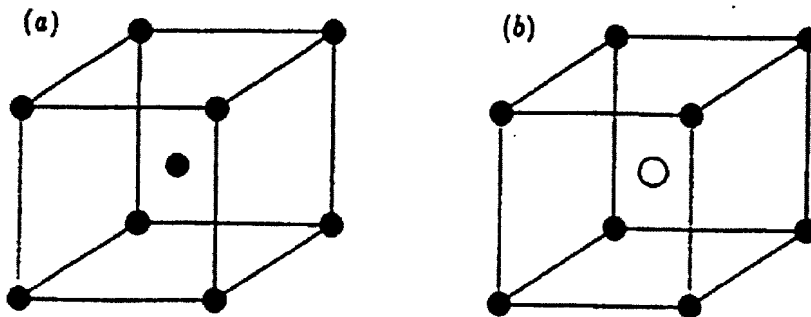


Figure 5.4. Schematic crystallographic structure of the A2 and B2 phases. (a). A2, the disordered structure, where all the sites are equivalent. (b) B2, the ordered structure where the occupation of the site in the centre of the cube is different to the one on the corner.

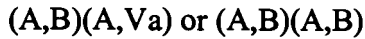
Phases with the B2 structure are generally formed around the equiatomic composition in binary systems and are often characterised by a considerable homogeneity range. In many cases, they remain ordered to high temperatures, and normally melt congruently. The deviations from the stoichiometric composition AB are possible by formation of statistically distributed point defects (so-called constitutional defects). Four basic kind of defects can occur in a crystal of the CsCl type (interstitial positions are not considered)

- (i) A atoms on the β sublattice;
- (ii) B atoms on the α sublattice;
- (iii) vacancies on the α sublattice or
- (iv) vacancies on the β sublattice.

The first two defects are called the anti-structure atoms. Traditionally, the B2 phases are divided into two groups according to the predominant defect mechanisms, the first group is dominated by anti-structure atoms (also called substitutional type) while the second group is dominated by vacancies on the α sublattices with A atoms on the β sublattice. The latter is called the triple defect, as two vacancies are needed to balance one anti-structure atom on the

other lattice. In only some B2 structures the defect mechanisms have been identified. In the modelling of the B2 phases, these defect structures have to be considered. This could be quite troublesome when the defect mechanism is not known and assumptions must be made. This has also lead to the use of different models to describe the B2 phase. Problems arose when different models were used and higher order systems had to be extrapolated.

Two CEF models have been used in the past to describe the B2 phase, where for a simple binary case, it can be described as



Due to the different defects assumed, the models are incompatible and complex and cumbersome conversions are required to make the models equivalent.

A modification of the traditional two-sublattice model has been introduced by Dupin and Ansara [1999Dup]. It is called the Modified Sublattice Model (MSL) and considers all defects simultaneously in a symmetrical description of the B2 phase



This description is mathematically equivalent to the previous models. The mathematical conversion between the different models has been reported by Dupin and Ansara [1999Dup]. In the light of this modified model, Hillert and Selleby [2001Hil2] then suggested to treat all defects rather as point defects, as this simplifies the usage of the MSL model.

The MSL model introduces some constraints that must be met. As both lattices are identical, the Gibbs energy contribution of the ordered state is given by

$$G_{Al:Ru:Va}^{B2} = G_{Ru:Al:Va}^{B2} \quad (5.21)$$

$$G_{Al,Ru:Ru:Va}^{B2} = G_{Ru:Al,Ru:Va}^{B2} \quad (5.22)$$

In the case of the MSL the disordered state of the B2 phase is described by the bcc-A2 phase. However, when the MSL is used in an optimisation, certain parameters are not free and should not be optimised [1999Dup].

5.5.3.2.2 CEF applied to fcc ordering

The Pt₃Al phase is an ordered structure (L1₂) of the disordered fcc phase (A1), the latter in which the atoms are randomly distributed on the lattice. The Pt₃Al phase shows both long-range and short range order (*lro* and *sro* respectively).

A four sublattice compound energy formalism (4SL CEF) has been successfully used by Sundman *et al.* [1998Sun] to describe the order-disorder relationship in the L1₂, L1₀ and fcc-A1 phases in the Au-Cu system, where they introduced the concept of reciprocal parameters to describe the short range order. Kusoffsky *et al.* [2002Kus] described the general principles of the CEF applied to fcc ordering.

In order to model the disordered fcc phase (A1) and the ordered fcc phases (L1₀ and L1₂) phase with a single model, it is necessary to consider four sublattices. Thus according to 4SL CEF, the fcc phases for the case Al-Pt can be described with the following model

$$(\text{Al,Pt})_{0.25}(\text{Al,Pt})_{0.25}(\text{Al,Pt})_{0.25}(\text{Al,Pt})_{0.25} \quad (5.23)$$

Physically, the sublattices describe the four corners of a tetrahedron in a unit cell, which are illustrated in Figure 5.5. Due to the crystallographic symmetry of the unit cell, the sublattices must be identical, implying that all nearest neighbours of an atom are on a different sublattice. With 0.25 sites for each sublattice, the requirement of 1 mole of atoms in the model is met. For the disordered structure (fcc_A1), all the sublattices are equivalent, which reduces this model to an equivalent (Al,Pt) substitutional model. When two sublattices have the same fractions, but are different to the other two which also have the same fractions, it describes the PtAl phase (L1₀ structure). When three sublattices have the same fractions and the fourth sublattice a different fraction, the above model describes the Al₃Pt and Pt₃Al phases (L1₂ structure). Not all four phases are necessarily stable in a system. PtAl₃ and Pt₂Al₂ are unstable in the Al-Pt system, i.e. they don't exist in any stable form in the Al-Pt system.

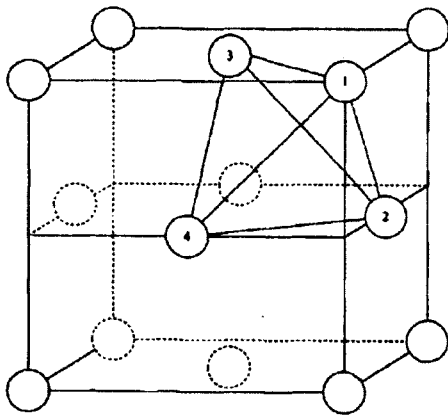


Figure 5.5. The face-centred cubic (fcc) structure. The numbers indicate the four sublattices for ordering.

From the model, the following relationships hold

$$\sum_i y_i^s = 1 \quad (5.24)$$

$$x_i = 0.25 \sum_s y_i^s \quad (5.25)$$

with y_i^s the site fraction of each element i on each sublattice s and x_i the molar fraction of i .

The Gibbs energy expression describing the fcc phases is

$$G_m = \sum_i \sum_j \sum_k \sum_l y_i^{(1)} y_j^{(2)} y_k^{(3)} y_l^{(4)} {}^oG_{ijkl} + 0.25RT \sum y_i^{(s)} \ln(y_i^{(s)}) + {}^E G_m \quad (5.26)$$

where the first term describes the mechanical mixing of all the stoichiometric compounds defined by the model, with ${}^oG_{ijkl}$ being the Gibbs energy of the stoichiometric compound $ijkl$ relative to the pure elements in the fcc state. The second term is the random mixing of all elements in each sublattice. The excess term ${}^E G_m$ includes the first two interactions according to the CEF model and is defined as

$$\begin{aligned}
 {}^E G_m = & \sum_{i_1} \sum_{i_2} \sum_j \sum_k \sum_l y_{i_1}^{(r)} y_{i_2}^{(r)} y_j^{(s)} y_k^{(t)} y_l^{(u)} L_{i_1, i_2; j; k; l} + \dots + \\
 & \sum_{i_1} \sum_{i_2} \sum_{j_1} \sum_{j_2} \sum_k \sum_l y_{i_1}^{(r)} y_{i_2}^{(r)} y_{j_1}^{(s)} y_{j_2}^{(s)} y_k^{(t)} y_l^{(u)} L_{i_1, i_2; j_1, j_2; k; l} + \dots
 \end{aligned} \tag{5.27}$$

The comma "," separates interacting constituents on the same sublattice and the column ":" separates the sublattices. The first summation describes the regular interaction parameters, $L_{i_1, i_2; j; k; l}$, which represents interactions between i_1 and i_2 on sublattice r , when the other sublattices, s , u and t , are occupied by constituents j , k and l . This is the next nearest neighbour interactions.

The second summation is called the reciprocal parameters. It represents the interaction on two sublattices, r and s , simultaneously while the other two sublattices, t and u , are occupied by constituents k and l respectively. This describes the nearest neighbour interactions, thus introducing a component to describe *sro* in the model. As all the sublattices are equivalent, symmetry relations can be applied to reduce the number of independent parameters.

The 4SL-CEF described above is mathematically equivalent to the two-sublattice CEF (2SL-CEF, first introduced by Ansara *et al.* [198Ans] for the Al-Ni system, as $(Al, Ni)_{0.25}(Al, Ni)_{0.75}$ describing fcc-Al and Ni_3Al simultaneously. The 2SL-CEF has been widely used to describe the order-disorder relation in fcc phases. However, the 4SL-CEF can describe all the related fcc phases, resulting in a simpler description for multi-component systems where many of the fcc phases are stable.

5.6 CALPHAD Optimisations

The optimisation is based on the calculation of the local equilibria for the data-points used with the set of parameters. This is done through a least-squares method. The success of the optimisation depends on a number of factors, which, if not considered, can result in a set of parameters which give totally wrong results when the calculation is completed, even though a minimum set of parameters have been obtained.

The success of an optimisation depends on:

1. the selected models,
2. the selected experimental data,
3. the number of model parameters,
4. starting values for the model parameters, and
5. the order in which the parameters are optimised.

The main difficulty in starting an optimisation, after selecting the models, parameters and experimental data, is to supply starting values for all the model parameters that are optimised. Often parameters of a similar system can be used as starting values. However, the optimisation can fail to calculate a corresponding value for the data-points with the given set of starting values.

Thus, it is generally best to start with a minimum set of data and first calculate only the liquid phase and the end members, e.g. fcc or hcp, of the system. It is also important to include thermodynamic data-points as they can be explicitly calculated from the Gibbs energy model,

unlike phase diagram data that are implicit and have to be calculated through solving non-linear equations. Once acceptable descriptions for these have been obtained, the phases can be introduced one by one. The results should regularly be evaluated against the experimental data by calculating the phase diagram for the phases that have been assessed.

The optimisation programs report a standard deviation for each parameter being optimised, and its meaning should be considered throughout the optimisation, since it is a measure of the significance of the parameter. A large standard deviation implies that the parameter is badly determined and should not be included in the optimisation. In such cases, a fixed value can be assigned to the parameter or the model should be changed.

5.7 Prediction of higher order systems

The usual strategy for assessment of a multi-component system is shown in Figure 5.6. First, the thermodynamic descriptions of the constituent binary systems are derived. Thermodynamic extrapolation methods are then used to extend the thermodynamic functions of the binaries into ternary and higher order systems. The results of the experiments are compared to the extrapolation, and if necessary, interaction functions are added to the thermodynamic description of the higher order system.

The coefficients of these higher-order system interaction functions are, similar to the binary case, calculated using experimental data and the CALPHAD method. In principle, this strategy is followed until all 2, 3, ... n constituent systems of an n-component system have been assessed. However, in most cases, no corrections or very minor corrections are necessary for reasonable prediction of quaternary or higher component systems, as true quaternary phases are rarely found in metallic systems.

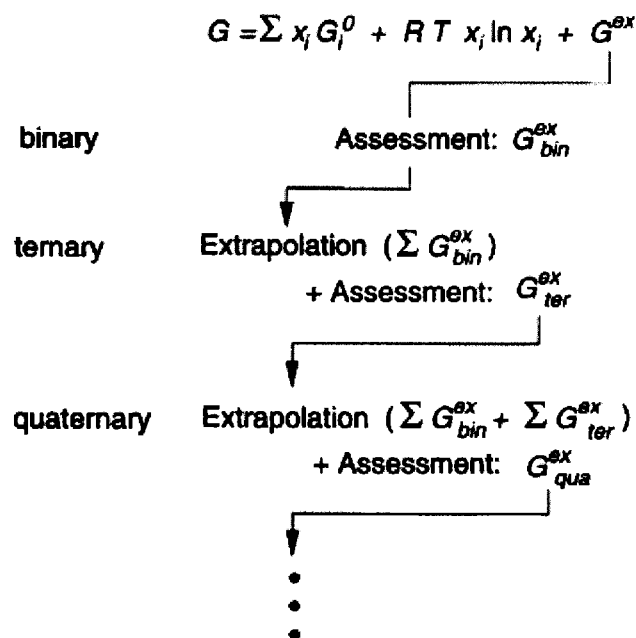


Figure 5.6. Extrapolation to higher order systems [1997Kat].

The results of such extrapolations can also be used to design critical experiments, saving the time and experimental cost to evaluate the complete system.

5.8 Conclusions

It has been shown above that computational methods can play an important role in materials science. Although the models used are simplified in comparison to real crystal structures, good approximations can be made of real systems. For some specialised cases, such as where order/disorder relationships exist between similar types of phases, specialised models have been successfully developed to address the relationships and simplify the calculations.

The CALPHAD method can be used to build databases that can predict the phase and property diagrams for a system. Where there is not enough data yet for accurate predictions, computational thermodynamics is a useful tool to critically design experiments.

Chapter 6

Results and Discussion of the Assessments

The Al-Ru, Al-Pt and Al-Pt-Ru phase diagrams were assessed with the CALPHAD method, using the Parrot module [1984Jan] in Thermo-Calc [1985Sun]. This chapter describes the models used in the assessments, the experimental data used and reports the modelled sets of parameters for the phases in each system. The Pt-Ru system has not been optimised. Instead, the existing description has been taken from Spencer's [1998Spe] noble alloy database, which is only an extrapolation of the elemental data.

As no textbook is available on the finer subtleties of optimisation, the optimisations are discussed in detail. The reasons for certain decisions are provided, as in many cases, model parameters are fixed by the user and not optimised. The reader is referred to the Thermo-Calc user's guide for information on the format of the data.

6.1 The Models

The success of an optimisation is based on the selection of sound models to describe the phase. Although the phase descriptions in the CALPHAD method are not strictly based on the crystallography of the phases, the crystallography can provide insight in how to model the phase. Certain phases, like the intermetallic B2 phase, are important in many related alloy systems and should be modelled to be consistent with previous descriptions to allow future combination of phase diagrams for extrapolation to higher order systems.

The models used in this study are listed in Tables 6.1 and 6.2 for the Al-Ru and Al-Pt systems respectively. A phase is called 'stoichiometric' when it is a line compound. Where the phase model was selected after a similar phase already modelled, it is referenced. Furthermore, in the phases where there are defects on the sublattices, instead of a separate set of parameters, only an enthalpy term was added in the calculation to compensate for the defect. Vacancies are indicated as Va.

Table 6.1. Thermodynamic models of the intermetallic phases in Al-Ru.

Phase	Model description	Model prototype	Reference	Comments
RuAl ₆	(Al) ₆ (Ru)	MnAl ₆		Stoichiometric
Ru ₄ Al ₁₃	(Al) _{0.6275} (Ru) _{0.235} (Al, Va) _{0.1375}	Fe ₄ Al ₁₃		Sublattice
RuAl ₂	(Al) ₂ (Ru)(Al, Ru, Va)			Sublattice
Ru ₂ Al ₃	(Al) ₃ (Al, Ru) ₂ (Ru, Va)	Ni ₂ Al ₃		Sublattice
RuAl	(Al, Ru, Va) _{0.5} (Al, Ru, Va) _{0.5} (Va) ₃ (Al, Ru)(Al, Va)	NiAl-B2* CoTi-B2**	[1997Ans] [2001Dav]	MSL Sublattice

Table 6.2 Thermodynamic models of the intermetallic phases in Al-Pt.

Phase	Model description	Model prototype	Reference	Comments
Pt ₅ Al ₂₁	(Al) ₂₁ (Pt) ₅			Stoichiometric
Pt ₈ Al ₂₁	(Al) ₂₁ (Pt) ₈			Stoichiometric
PtAl ₂	(Al) ₂ (Pt)			Stoichiometric
Pt ₂ Al ₃	(Al) ₃ (Pt) ₂			Stoichiometric
PtAl	(Al)(Pt)			Stoichiometric
β	(Al) _{0.48} (Pt) _{0.52}			Stoichiometric
Pt ₅ Al ₃	(Al) ₃ (Pt) ₅			Stoichiometric
Pt ₂ Al	(Al)(Pt) ₂			Stoichiometric
Pt ₃ Al	(Al,Pt) _{0.25} (Al,Pt) _{0.25} (Al,Pt) _{0.25} (Al,Pt) _{0.25} (Va)	AuCu ₃	[1998Sun]	4SL CEF

The RuAl₆ phase is the only stoichiometric phase (line compound) in the Al-Ru system and the model is the simplified sublattice model for stoichiometric phases. Ru₄Al₁₃ and RuAl₂ both have a composition range over which they are stable, but no data are available on the defects resulting in the composition ranges. Ru₄Al₁₃ has been divided into 3 sublattices and modelled after the Fe₄Al₁₃ phase [COST507], as the structure has been compared to Fe₄Al₁₃ by Edshammer [1965Eds]. For RuAl₂, a sublattice has been added to accommodate the defects, only Va and Al atoms have been considered as defects as the phase width is more to the Al side of stoichiometry. Ru₂Al₃ is similar to the ordered Ni₂Al₃ and the description of Ansara *et al.* [1997Ans] was adopted. RuAl is a B2 phase with a very high degree of ordering throughout the temperature range that the phase is stable. Both vacancies and aluminium atoms have been suggested as defect mechanisms for this phase. In the sublattice description, the defect lattice contains Al and Va. The modified sublattice model (MSL) is completely symmetrical and the defects are only treated in selecting the model parameters which have to be calculated.

All the phases in the Al-Pt system, except for Pt₃Al, have been modelled as stoichiometric line-compound phases. According to the literature, the β phase is of the B2 type and has a composition range. The β phase has been simplified to a line compound, as no experimental or thermodynamic data are available. If data becomes available in future, the model can be changed without major impact on the overall set of parameters calculated for the system. The Pt₃Al phase has been described using the four-sublattice compound energy formalism (4SL CEF), suggested by Sundman [1998Sun] to treat the order-disorder relation in fcc structures (Al and L₁₂). To simplify the calculation, a functional approach is used for the 4SL CEF.

When the phases are modelled with different sublattices, the ratio of the sublattices can either be the stoichiometric ratios, or they can be defined as fractions so that the total number of sites adds up to one, so that the description describes one mole of atoms. In the first case, the parameters are then expressed as J/mole, while the latter is defined as J/mole of atoms. It is good practice to use only one of these methods, as mixing of the

methods can lead to confusion in the unit of the Gibbs energy for a phase. For example, the phase description for RuAl₆ can be (modified syntax)

```
ent-phase RUAL6 , 2 6 1 AL ; RU ; N N
G(RUAL6,AL:RU;0)=-156000+7*T+6*GHSERAL+GHSERRU ;
```

or

```
ent-phase RUAL6 , 2 0.8571 0.1429 AL ; RU ; N N
G(RUAL6,AL:RU;0)=-22286+T+0.8571*GHSERAL+0.1471*GHSERRU ;
```

where the first set gives the results in J/mole and the second set the results in J/mole of atoms, as the description is referring to one mole of atoms only. In this calculation of the Al-Ru system, both these descriptions had been used, while all sublattices were normalised to one mole in the Al-Pt system.

The Al-Pt-Ru phase diagram has only been extrapolated from the binaries; no ternary elements have been added to any of the intermetallic phases. A ternary assessment will only be possible when some thermodynamic data becomes available for the system. Ternary parameters would then probably have to be added to the liquid and fcc/L₁₂ phases in the system. The optimisation of the ternary system falls outside the scope of this study.

The thermodynamic database for Al-Pt-Ru is listed in Appendix C, providing detailed descriptions of the phases.

6.2 Some basic concepts

The best approach to an optimisation with the Parrot module is to create a set-up file containing all the phase information, with variables for the model parameters that will be calculated. This is a text file with a .TCM extension and it is run with the 'macro' command in Thermo-Calc. Extra information can be entered into this file for future reference, model changes can be indicated allowing the user to keep track of the input and major phase compositions can be set to assist in the calculations.

To assist in the calculation of the ordered RuAl-B2 phase, a command setting the major composition was included, thus having Al on the first sublattice and Ru on the second. Only model parameters for the enthalpy contribution were set in the RuAl-B2 phase, the entropy contribution is described by the disordered bcc-A2 phase.

Experimental data are summarised in the POP file. The data are entered in 'equilibrium' sets. Each condition has its own data-set associated with it, and an example for the eutectic reaction $L \rightarrow (Ru) + RuAl$ at 2193 K and 70 at% Ru is provided here.

```

CREATE 1 1
SET-LABEL AINV
CHANGE-STATUS PHASE LIQUID HCP B2=FIX 0
SET-CONDITION P=1e5 T=2193:2
EXPERIMENT X(LIQUID,RU)=0.7:0.05
EXPERIMENT ORD≥0.9
SET-ALT-COND X(HCP,RU)=0.96
SET-ALT-COND X(B2,RU)=0.505

```

The conditions of the fixed phases, pressure and temperature fix the equilibrium. The 'experiment' is not an independent condition.

The ordering of the RuAl-B2 phase is important and a function

$$\text{ORD} = (Y(\text{B2}, \text{Al}\#1) - Y(\text{B2}, \text{Al}\#2))^2$$

was included in all the datasets containing the RuAl-B2 phase to ensure the RuAl-B2 phase is always ordered; this was met when $\text{ORD} \geq 0.7$. The physical meaning of this is that the difference of the fraction of Al atoms on the first and Al atoms on the second lattice is calculated and when this is equal to one, the structure is fully ordered (only Al atoms on the one sublattice, and only Ru atoms on the second sublattice).

ALT conditions were added for when the optimisation is done in ALT mode. The ALT mode is discussed below.

Additional datasets were also added where negative driving forces were set to ensure the stability of a phase to lower temperatures. The Thermo-Calc POP files containing the datasets used in the optimisations are listed in Appendix D.

6.3 Assessment procedures

6.3.1 Al-Ru

The phase (Al) shows virtually no solubility for Ru, and on the phase diagram, (Al) forms through the eutectic reaction $L \rightarrow (\text{Al}) + \text{RuAl}_6$ at < 0.01 at % Ru and 923 K, only 3 degrees lower than the melting point of pure Al. This implies that the slope of the liquidus must be negative at the temperature axis. So, as a first step, to ensure that the slope of the liquidus was correct at the melting point of the Al-fcc phase, only the liquid, Al-fcc and Ru-hcp phases were optimised. A metastable eutectic reaction was created for this purpose. This also ensured that the slope on the Ru-side is correct, though this would not have been a problem due to the high melting temperature of Ru and the fact that the eutectic $L \rightarrow (\text{Ru}) + \text{RuAl}$ occurs at 2193 K and 70 at. % Ru, about 414 K lower than the melting temperature of Ru.

However, when there is virtually no solubility of ruthenium in the (Al) solid phase, the slope of the liquidus surface is dependent on the enthalpy of melting. This means that the parameter cannot be effectively optimised and arbitrary values can be selected and fixed for the fcc phase. For fcc-A1, the interaction parameter $L_{Al,Ru}^0$ was set to $-10\,000 - 10 \cdot T$ from experience with other systems [2000Sun].

Once an acceptable liquidus slope was calculated, the RuAl-B2 phase, using the modified sublattice (MSL) formalism description, was included in the optimisation as this is the only phase with experimental thermodynamic data. This also gave the liquid phase a reference point. The bcc-A2 phase had to be introduced with the RuAl-B2 phase, as the bcc-A2 phase describes the disordered Gibbs energy contribution of the RuAl-B2 phase. The model parameters for the bcc-A2 interactions, where mixing with vacancies occurs (L_{Al,v_a}^0 and L_{Ru,v_a}^0), were set to a high positive value ($80 \cdot T$) as this prevents the stabilisation of the bcc-A2 phase due to excess vacancies in the RuAl-B2 phase.

The ALT mode in Parrot was used to determine the first model parameters, as the parameters initially were set to zero. The optimisation was continued in the normal mode once the ALT mode converged. The ALT mode is based on a 'reversal' of the normal model: the difference in chemical potential for each phase is calculated as the 'experimental information' and the program adjusts the model parameters to make the chemical potentials of all the phases the same, usually resulting in model parameters which can be successfully used as starting values in the normal mode. When the ALT mode is going to be used, extra information, such as the compositions of all the phases partaking in the equilibrium, should be included in the POP file.

An alternative to the ALT mode is to select starting values for model parameters from similar systems previously optimised. In a second optimisation, prompted at a later stage due to a model change, this approach was followed. There are many examples of the B2 phase, and the most well-known is probably the NiAl-B2 phase. However, the parameters from NiAl-B2 phase [1999Dup] could not be used, as NiAl-B2 has its phase extension to the Ni-rich side while RuAl-B2 has its phase width to the Al-rich side. TiCo-B2 has a similar phase shape as RuAl-B2, and the data from Davydov *et al.* [2001Dav] was used as a first estimation. In the initial optimisation, it was necessary to relax the ordering requirement to 0.7 until better model parameters were obtained.

The other phases, except for the Ru_2Al_3 phase, were introduced simultaneously. The liquid parameters were fixed while introducing the other phases into the calculation. These phases were introduced as stoichiometric congruent melting phases instead of the cascade of peritectic reactions by which they form in the phase diagram. This was done as congruent melting equilibria are easier to calculate than peritectic reactions. Once the phases were forming at the correct composition ranges in the calculated phase diagram, the peritectic reactions were introduced and the weights on the metastable congruent melting data were set to zero. The phase widths for Ru_4Al_{13} and $RuAl_2$ were only introduced after satisfactory results were obtained for the peritectic reactions.

Finally, the Ru_2Al_3 phase was introduced in a similar fashion as the above phases. The solid-state decomposition dataset was included at the end.

To ensure stability of the thermodynamic parameters of the intermetallic phases, a condition forcing the entropy of formation to be negative was set. The coefficients of the B2 and A2 phases were tested for interdependence and the entropy contribution of the ordered B2 phase is described by the disordered A2 phase. The interdependence testing was done by calculating the solubility range of the B2 phase as a function of the $L(\text{bcc-A2,Al,Ru})$ parameter. When the $L(\text{bcc-A2,Al,Ru})$ parameter is made more negative, the solubility range for B2 becomes wider, whereas when the $G(\text{B2,Al:Ru}) = G(\text{B2,Ru,Al})$ is made more negative, the solubility range becomes more narrow. Thus the parameters for the bcc-A2 phase could be fixed to give a reasonable solubility range for the B2 phase and the B2 parameters were optimised to adjust the solubility range.

The parameters were fixed through a rounding process. The parameter with the largest standard deviation was fixed with the number of significant numbers determined by the exponent of the standard deviation. The set of parameters was optimised again to ensure that the total sum of squares of error does not increase. This was repeated until only one value was left.

As the B2 phase can be described by either the MSL or the SL model, a second assessment was performed to obtain model parameters for the B2 phase using the SL model. The mathematical conversion model proposed for converting between MSL and SL parameters is not valid for the Al-Ru system as the bcc-A2 phase is unstable in this system, forcing some constraints on the MSL parameters [1999Dup].

For the SL optimisation, all the parameters calculated in the MSL optimisation were fixed. The description of the B2 phase was changed to the sublattice format. Only these parameters were optimised during the second assessment. The values from the TiCo-B2 phase [2001Dav] were used as starting values.

6.3.2 Al-Pt

The optimisation of Al-Pt was a re-assessment, as Wu and Jin [2000Wu] assessed the Al-Pt system. The re-assessment was considered to be necessary as their assessment did not describe the ordering in the Pt_3Al phase, and they also excluded the β and Pt_2Al phases from their optimisation due to a lack of experimental data on the phases. To be compatible with the latest order-disorder modelling of systems with a γ/γ' relation, the disordered fcc-Al and ordered Pt_3Al should be described using one Gibbs energy function. Furthermore, based on new experimental data [2000Big1, and this work], which were not available previously, the Pt_2Al and β phases have been confirmed and should thus be included.

The values reported by [2000Wu] were used as initial input values to the re-assessment. When their results were reproduced, the description for the fcc phases were changed to

the four-sublattice compound energy formalism (4SL CEF). In the 4SL CEF, the ordered Pt_3Al ($L1_2$ type fcc phase) and disordered fcc-A1 phases are described with one Gibbs energy function. The physical meaning of the 4SL CEF has been described in Chapter 5. In the Al-Pt system, only the fcc-A1 and Pt_3Al - $L1_2$ phases are stable, the PtAl_3 - $L1_2$ and Pt_2Al_2 - $L1_0$ phases are unstable. Pt_3Al forms congruently. Metastable congruent melting equilibria were introduced for the unstable phases, and a condition was set to suppress the phases in the diagram.

The Pt_2Al and β phases were also introduced initially by a metastable congruent melting as described in the Al-Ru system. The metastable conditions were removed and the peritectic reactions were introduced. The solid-state decomposition of the β phase was added in the final step. Although the literature [1986McA] suggests that the β phase has a B2 structure, it was decided not to model β as a B2 phase for a number of reasons. Firstly, the B2 phase descriptions are usually symmetrical around the 50:50 at. % compositions, thus a B2 phase description will have to be too far off the stoichiometry composition, suggesting excess defect formation in the phase. No data were available to confirm or contradict this. Secondly, because the β phase decomposes through a solid-state reaction at 1250 K, structural studies are extremely difficult. Thirdly, the PtAl phase is stable at 50:50 at. % in the system, with the Pt_2Al_2 phase from the 4SL CEF unstable at this same composition. Adding another phase at this composition would have complicated the optimisation too much. Also, the β phase (suggested to be the B2 structure) and RuAl-B2 phase are not continuous in the ternary system, so they can be modelled separately as simpler systems. It is usually better to model phases which are not continuous separately when a binary will be extrapolated to higher order systems.

6.3.3 Al-Pt-Ru

The Al-Pt-Ru phase diagram was predicted by extrapolation only from the three binary systems after the binary optimisations had been performed. However, thermodynamic parameters for the metastable descriptions of hcp-Pt, bcc-Pt and fcc-Ru were added from the SGTE database since all the metastable forms relevant to the system must be included in the description. Only the MSL B2 description version of the calculated Al-Ru system was used in the extrapolation.

Pt and Ru were added to the B2 and $L1_2$ phases respectively to stabilise these phases in the ternary system. B2 and $L1_2$ are both ordered phases and are described with one Gibbs energy function for the ordered and disordered forms of the phases, using the MSL model and 4SL CEF respectively. The inclusion of the third element to the disordered solutions (bcc and fcc respectively) requires the inclusion of the third element in the ordered phase as well. However, no parameters were included in the ordered descriptions for the third elements. No ternary interaction parameters were included for any phase in the system.

6.4 Results and discussion

6.4.1 Al-Ru

The calculated model parameters for the Al-Ru system are listed in Table 6.3. The calculated phase diagram is shown in Fig 6.1. The calculated phase diagram is compared with experimental data in Figure 6.2 and the invariant temperatures and compositions are compared in Table 6.4.

Table 6.3 Calculated thermodynamic parameters for the Al-Ru system [J/mol]

Liquid	Disordered Solution Phase: (Al,Ru) ${}^0G_{Al}^{liq}(T) - H_{Al}^{0, fcc-A1}(298.15) : [1991Din]$ ${}^0G_{Ru}^{liq}(T) - H_{Ru}^{0, hcp-A3}(298.15) : [1991Din]$ ${}^0L_{(Al,Ru)}^{Liq} = -73000 - 14T$ ${}^1L_{(Al,Ru)}^{Liq} = -56000$
(Al) (fcc-A1)	Disordered Solution Phase: (Al,Ru)(Va) ${}^0G_{Al}^{fcc-A1}(T) - H_{Al}^{0, fcc-A1}(298.15) : [1991Din]$ ${}^0G_{Ru}^{fcc-A1}(T) - H_{Ru}^{0, fcc-A1}(298.15) : [1991Din]$ ${}^0L_{(Al,Ru)}^{fcc-A1} = -10000 - 10T$
(Ru) (hcp-A3)	Disordered Solution Phase: (Al, Ru)(Va) _{0.5} ${}^0G_{Ru}^{hcp-A3}(T) - H_{Ru}^{0, hcp-A3}(298.15) : [1991Din]$ ${}^0G_{Al}^{hcp-A3}(T) - H_{Al}^{0, hcp-A3}(298.15) : [1991Din]$ ${}^0L_{(Al,Ru)}^{hcp-A3} = -105000 + 30T$
bcc-A2	Disordered Solution Phase: (Al, Ru, Va)(Va) ₃ ${}^0G_{Al}^{bcc-A2}(T) - H_{Al}^{0, bcc-A2}(298.15) : [1991Din]$ ${}^0G_{Ru}^{bcc-A2}(T) - H_{Ru}^{0, bcc-A2}(298.15) : 26500 - 6.2 * T + GHSERRU [1991Din]$ ${}^0L_{Al,Ru:Va}^{bcc-A2} = -176000 + 32 * T$ ${}^0L_{Al,Va:Va}^{bcc-A2} = 120 * T$ ${}^0L_{Ru,Va:Va}^{bcc-A2} = 120 * T$
RuAl₆	Stoichiometric Phase: (Al) ₆ (Ru) $fG_{Al:Ru}^{RuAl_6} = 6 {}^0G_{Al}^{fcc-A1} + {}^0G_{Ru}^{hcp-A3} - 156000 + 7 * T$
Ru₄Al₁₃	Sublattice Solution Phase: (Al) _{0.6275} (Ru) _{0.235} (Al, Va) _{0.1375} $fG_{Al:Ru:Al}^{Ru_4Al_{13}} = 0.765 {}^0G_{Al}^{fcc-A1} + 0.235 {}^0G_{Ru}^{hcp-A3} - 35100 + 1.65 * T$ $fG_{Al:Ru:Va}^{Ru_4Al_{13}} = 0.6275 {}^0G_{Al}^{fcc-A1} + 0.235 {}^0G_{Ru}^{hcp-A3} - 35100 + 1.65 * T$
RuAl₂	Sublattice Solution Phase: (Al) ₂ (Ru)(Al, Ru, Va)



$$\begin{aligned} f G_{Al:Ru:Va}^{RuAl_2} &= 2^0 G_{Al}^{fcc-A1} + {}^0 G_{Ru}^{hcp-A3} - 136500 + 8 * T \\ f G_{Al:Ru:Al}^{RuAl_2} &= 3^0 G_{Al}^{fcc-A1} + {}^0 G_{Ru}^{hcp-A3} - 138000 + 8 * T \\ f G_{Al:Ru:Ru}^{RuAl_2} &= 2^0 G_{Al}^{fcc-A1} + 2^0 G_{Ru}^{hcp-A3} - 138000 + 8 * T \end{aligned}$$

Ru₂Al₃

Sublattice Solution Phase : (Al)₃(Al,Ru)₂(Ru,Va)

$$\begin{aligned} f G_{Al:Al:Va}^{Ru_2Al_3} &= 5^0 G_{Al}^{bcc-A2} \\ f G_{Al:Al:Ru}^{Ru_2Al_3} &= 5^0 G_{Al}^{bcc-A2} + {}^0 G_{Ru}^{bcc-A2} \\ f G_{Al:Ru:Va}^{Ru_2Al_3} &= 3^0 G_{Al}^{bcc-A2} + 2^0 G_{Ru}^{bcc-A2} - 312630 + 30.5 * T \\ f G_{Al:Ru:Ru}^{Ru_2Al_3} &= 3^0 G_{Al}^{bcc-A2} + 3^0 G_{Ru}^{bcc-A2} - 312630 + 30.5 * T \end{aligned}$$

RuAl (B2)

Sublattice Solution Phase: (Al,Ru)(Al,Va)

$$\begin{aligned} f G_{Al:Al}^{B2} &= 2^0 G_{Al}^{bcc-A2} \\ f G_{Al:Va}^{B2} &= {}^0 G_{Al}^{bcc-A2} + 60000 \\ f G_{Ru:Va}^{B2} &= {}^0 G_{Ru}^{bcc-A2} + 60000 \\ f G_{Ru:Al}^{B2} &= {}^0 G_{Ru}^{bcc-A2} + {}^0 G_{Al}^{bcc-A2} - 138700 + 15.5 * T \\ {}^0 L_{Al:Al:Va}^{B2} &= 49100 - 22.4 * T \\ {}^0 L_{Ru:Al:Va}^{B2} &= -51770 + 20 * T \\ {}^0 L_{Al,Ru:Al}^{B2} &= -30000 \\ {}^0 L_{Al,Ru:Va}^{B2} &= -30000 \end{aligned}$$

Modified Sublattice Model: (Al,Ru,Va)_{0.5}(Al,Ru,Va)_{0.5}(Va)₃

$$\begin{aligned} f G_{Al:Al:Va}^{B2} &= 0 \\ f G_{Ru:Ru:Va}^{B2} &= 0 \\ f G_{Va:Va:Va}^{B2} &= 0 \\ f G_{Al:Ru:Va}^{B2} &= f G_{Ru:Al:Va}^{B2} = -87600 \\ {}^0 L_{Al,Ru:Al:Va}^{B2} &= {}^0 L_{Al:Al,Ru:Va}^{B2} = -73000 \end{aligned}$$

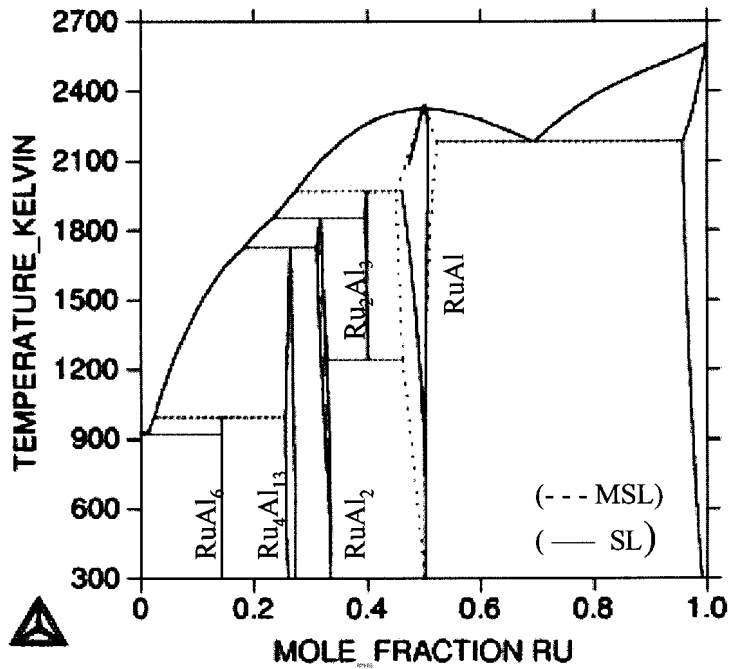


Figure 6.1 The calculated Al-Ru phase diagram showing RuAl-B2 calculated using the SL (—) and MSL (---) models.

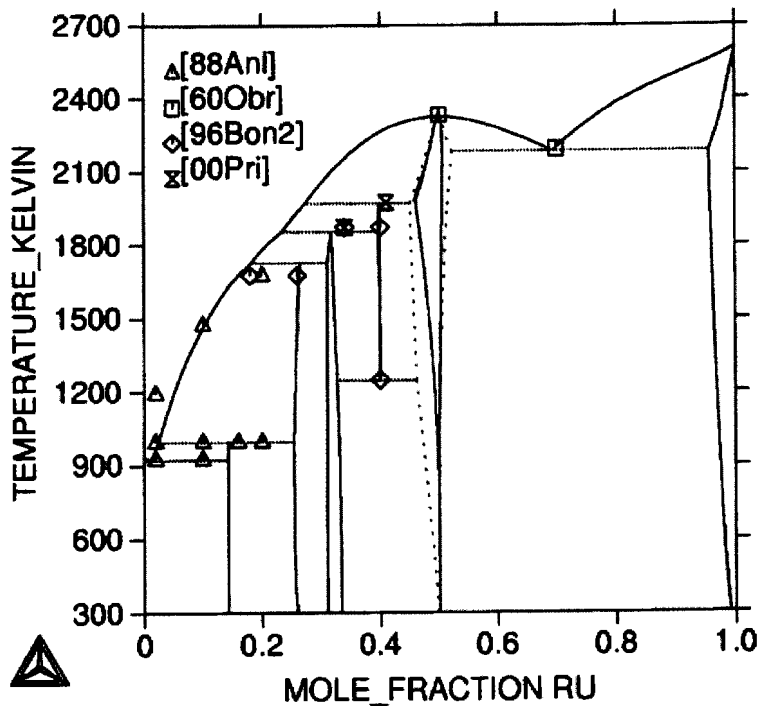


Figure 6.2 Comparison between the calculated Al-Ru phase diagram and experimental data from the literature (as listed in Table 6.4)

The calculated temperatures for the invariant reactions are in good agreement with the experimental temperatures, except for the peritectic formation of the Ru₄Al₁₃ phase, which is about 50 K too high. This is probably due to the modifications to the invariant temperatures for the RuAl₂ and Ru₂Al₃ phases by Prins and Cornish [2000Pri] to correct the liquidus slope from the diagram of Boniface and Cornish [1996Bon2].

The homogeneity ranges of the Ru₄Al₁₃ and RuAl₂ phases are acceptable in comparison with the experimental data. Ru₂Al₃ appears as a stoichiometric compound with no homogeneity range. The optimisation was simplified due to the lack of data for this phase and no interaction on any of the sublattices was taken into account, so effectively no defects were considered. The phase appears in the correct composition and temperature ranges and the description is considered satisfactory for the purpose of this work.

The two descriptions for the RuAl-B2 phase compare well, with the MLS description giving a better agreement to experimental data for the composition range. Both descriptions have a very limited extension to the Ru-rich side and correctly have the composition range to the Al-rich side.

Table 6.4 Calculated and Experimental invariant temperatures and compositions for the Al-Ru system.

Reaction (at. %Ru)	Reaction Temperature [K]	Reference
L ↔ (Al) + RuAl ₆ 0.1 0 14.8 0.1 0 14.3	923 922	[1988An1] This work
L + Ru ₄ Al ₁₃ ↔ RuAl ₆ 1.5 25 14.3 2.5 25.4 14.3	996 997	[1988An1] This work
L + RuAl ₂ ↔ Ru ₄ Al ₁₃ 17.6 33.6 25.8 18.1 31.1 26.7	1676 1725	[1988An1] This work
L + Ru ₂ Al ₃ ↔ RuAl ₂ 26 36 33.4 23 36.1 33.9 23.4 39.6 31.8	1733 1873 1854	[1996Bon1] [2000Pri]* This work
L + RuAl ↔ Ru ₂ Al ₃ 33.5 42.5 42 27 42 41 35 45.9 39.9	1873 1973 1978	[1996Bon1] [2000Pri]* This work
Ru ₂ Al ₃ ↔ RuAl + RuAl ₂ 395 46 35.9 40 49.5 32.9	1249 1243	[1996Bon1] This work
L ↔ RuAl 50 50 50 50	2333 2342	[1960Obr] This work
L ↔ RuAl + (Ru) 70 51 96 69.7 50.7 95.7	2193 2189	[1960Obr] This work

* indicates values which was used for the optimisation.

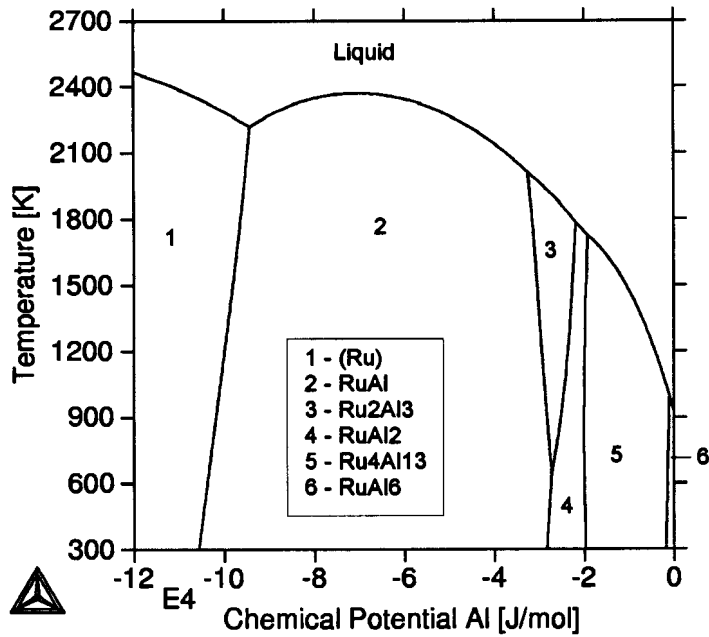


Figure 6.3. Phase diagram of temperature against chemical potential of Al.

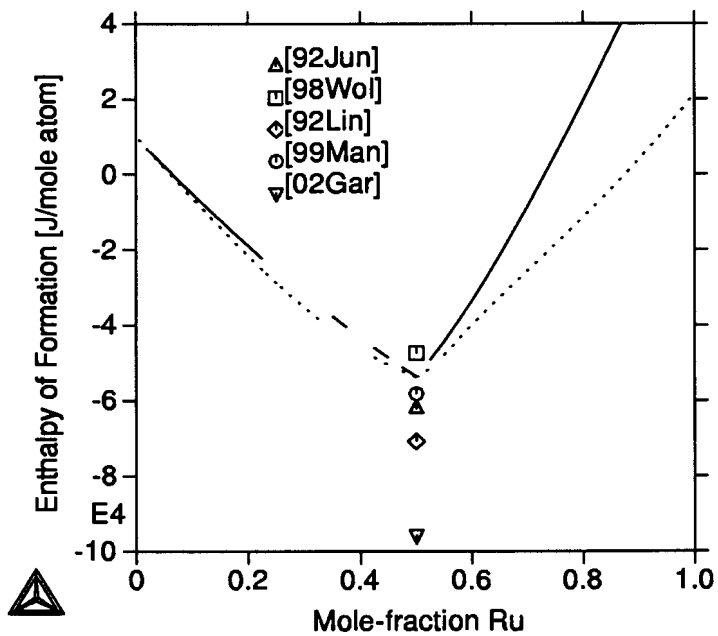


Figure 6.4. Comparison of calculated enthalpy of formation for the SL (—) and MSL (---) RuAl-B2 models with experimental results [1992Jun] and *ab initio* [1992Lin, 1998Wol, 1999Man, 2002Gar] predictions.

In Figure 6.3, the phase diagram is plotted as a function of the chemical potential of the Al instead of composition. The slope of the curves is equal to dG/dT , which represents the entropy. The diagram shows that no phase has an excessive entropy contribution, which is important as most of the thermodynamic data that was used in the optimisation was obtained by Miedema's semi-empirical method. In Figure 6.4 the enthalpy of formation for the sublattice and MSL descriptions of the RuAl-B2 phase is compared to experimental and ab initio values from the literature. The enthalpy of formation is in good agreement with the experimental value from Jung and Kleppa [1992Jun]. As expected, the MSL description resulted in a more symmetrical curve for the enthalpy of formation. For the sublattice description, the curve on the Ru-rich side of the 50:50 at. % composition indicates that the phase becomes more unstable at the higher Ru contents, which is in agreement with the non-symmetrical model.

6.4.2 Al-Pt

The calculated model parameters for the Al-Pt system are listed in Table 6.5. The optimised/calculated phase diagram is shown in Figure 6.5. The optimised phase diagram is compared with experimental data from the literature in Figure 6.6 and the invariant temperatures and compositions are compared in Table 6.6. The reactions for the PtAl, β and liquid phases are enlarged in Figure 6.7, as these are nearly indistinguishable on the full binary diagram.

The calculated compositions and temperatures for the invariant reactions for the intermetallic phases are in general good agreement with the experimentally reported compositions and temperatures. However, there are some areas in less good agreement, and in most cases it is due to the models being used.

The congruent formation of the Pt₃Al phase and $L \rightarrow \text{Pt}_3\text{Al} + (\text{Pt})$ eutectic reactions are not in very good agreement with the experimental diagram, both reactions are shifted to lower platinum compositions in the calculated system. The 4SL CEF model is such that the formation composition of Pt₃Al is fixed at 75 at. %, while it has been reported in the literature to form congruently at 73.2 at. %. This off-stoichiometry formation cannot be described with the model, and had subsequently an influence on the temperature as well as the enthalpy of formation for the Pt₃Al phase. The symmetry and fixed compositions of the 4SL CEF model made it also impossible to move the eutectic reaction to lower Pt-contents. Furthermore, the phase area of the (Pt) solid solution is too narrow, especially at lower temperatures, but the phase area for the Pt₃Al phase is acceptable. However, the Pt₃Al phase is ordered throughout its phase area and the unstable PtAl₃ (L₁₂) and Pt₂Al₂ (L₁₀) phases, which are introduced through the 4SL CEF, are not stable at any composition or temperature in the phase diagram, which is correct.

Since the β -phase has been modelled as a line compound, with the stoichiometric composition fixed to the experimentally reported formation composition of 52 at% Pt, there are some discrepancies in the comparison of the calculated and experimentally reported compositions and temperatures. The formation composition and temperature are in good agreement with the value reported in literature, but the decomposition

composition is incorrect. The literature suggests the β -phase as an irregular phase area (see the Al-Pt phase diagram, Chapter 2, Figure 2.1), with the decomposition at higher platinum contents than the formation platinum content. This affected the calculated results for the reactions involving the β -phase. The calculated eutectic temperature for the $L \rightarrow \beta + \text{Pt}_5\text{Al}_3$ is ~ 50 K too high. This can also be due to the estimate of the enthalpy of formation for the β phase. The phase area is enlarged in Figure 6.7.

The Pt_5Al_3 phase forms experimentally through a peritectic reaction $L + \text{Pt}_3\text{Al} \rightarrow \text{Pt}_5\text{Al}_3$, which is very close to the liquid, it seems very close to a congruent melting reaction. The calculated Pt_5Al_3 phase forms congruently at 1750 K and 62.5 at. % Pt. This introduced an extra eutectic reaction $L \rightarrow \text{Pt}_5\text{Al}_3 + \text{Pt}_3\text{Al}$ at 1720 K and 67.1 at. % Pt, which is not observed in the experimental diagram.

On the Al-side of the phase diagram the (Al) shows a too high solubility for platinum. This is again due to the use of the 4SL CEF to describe the fcc phases. This also shifted the eutectic reaction $L \rightarrow (\text{Al}) + \text{Pt}_5\text{Al}_{21}$ to a too high Pt-content. As a result of the too high platinum solubility and the shift of the eutectic reaction, the liquidus is also too far too the right in comparison to results reported in the literature. However, the calculated results were accepted since the work is not aimed at studying Al-based alloys.

Table 6.5. The calculated model parameters for Al-Pt [J/mole of atoms].

Liquid	Disordered Solution Phase: (Al,Pt) ${}^0G_{\text{Al}}^{\text{liq}}(T) - H_{\text{Al}}^{0,\text{fcc}-\text{Al}}(298.15) : [1991\text{Din}]$ ${}^0G_{\text{Pt}}^{\text{liq}}(T) - H_{\text{Pt}}^{0,\text{hcp}-\text{Al}_3}(298.15) : [1991\text{Din}]$ ${}^0L_{(\text{Al},\text{Pt})}^{\text{Liq}} = -352540 + 114.8 * T$ ${}^1L_{(\text{Al},\text{Pt})}^{\text{Liq}} = 68570 - 53 * T$
fcc-Al	Disordered Solution Phase: (Al,Pt)(Va) ${}^0G_{\text{Al}}^{\text{fcc}-\text{Al}}(T) - H_{\text{Al}}^{0,\text{fcc}-\text{Al}}(298.15) : [1991\text{Din}]$ ${}^0G_{\text{Pt}}^{\text{fcc}-\text{Al}}(T) - H_{\text{Pt}}^{0,\text{fcc}-\text{Al}}(298.15) : [1991\text{Din}]$ ${}^0L_{(\text{Al},\text{Pt})}^{\text{fcc}-\text{Al}} = \text{ULDO} + \text{DGO} + 1.5 * \text{USRO}$ ${}^1L_{(\text{Al},\text{Pt})}^{\text{fcc}-\text{Al}} = \text{ULD1} + \text{DG1}$ ${}^2L_{(\text{Al},\text{Pt})}^{\text{fcc}-\text{Al}} = \text{ULD2} + \text{DG2} - 1.5 * \text{USRO}$
$\text{Pt}_5\text{Al}_{21}$	Stoichiometric Phase: (Al) _{0.8077} (Pt) _{0.1923} ${}^fG_{\text{Al:Pt}}^{\text{Pt}_5\text{Al}_{21}} = 0.8077 {}^0G_{\text{Al}}^{\text{fcc}-\text{Al}} + 0.1923 {}^0G_{\text{Pt}}^{\text{fcc}-\text{Al}} - 56870 + 14.8 * T$
$\text{Pt}_8\text{Al}_{21}$	Stoichiometric Phase: (Al) _{0.7242} (Pt) _{0.2759} ${}^fG_{\text{Al:Pt}}^{\text{Pt}_8\text{Al}_{21}} = 0.7242 {}^0G_{\text{Al}}^{\text{fcc}-\text{Al}} + 0.2759 {}^0G_{\text{Pt}}^{\text{fcc}-\text{Al}} - 81805 + 23.2 * T$
PtAl_2	Stoichiometric Phase: (Al) _{0.666} (Pt) _{0.334} ${}^fG_{\text{Al:Pt}}^{\text{PtAl}_2} = 0.666 {}^0G_{\text{Al}}^{\text{fcc}-\text{Al}} + 0.334 {}^0G_{\text{Pt}}^{\text{fcc}-\text{Al}} - 87371 + 22.1 * T$
Pt_2Al_3	Stoichiometric Phase: (Al) _{0.6} (Pt) _{0.4}



PtAl	${}^f G_{Al:Pt}^{Pt_2Al_3} = 0.6 {}^0 G_{Al}^{fcc-Al} + 0.4 {}^0 G_{Pt}^{fcc-Al} - 89885 + 21.5 * T$ Stoichiometric Phase: (Al) _{0.5} (Pt) _{0.5} ${}^f G_{Al:Pt}^{PtAl} = 0.5 {}^0 G_{Al}^{fcc-Al} + 0.5 {}^0 G_{Pt}^{fcc-Al} - 94071 + 24.1 * T$
Beta	Stoichiometric Phase: (Al) _{0.48} (Pt) _{0.52} ${}^f G_{Al:Pt}^{\beta} = 0.48 {}^0 G_{Al}^{fcc-Al} + 0.52 {}^0 G_{Pt}^{fcc-Al} - 92959 + 24.1 * T$
Pt₅Al₃	Stoichiometric Phase: (Al) _{0.375} (Pt) _{0.625} ${}^f G_{Al:Pt}^{Pt_5Al_3} = 0.375 {}^0 G_{Al}^{fcc-Al} + 0.625 {}^0 G_{Pt}^{fcc-Al} - 87260 + 24 * T$
Pt₂Al	Stoichiometric Phase: (Al) _{0.334} (Pt) _{0.666} ${}^f G_{Al:Pt}^{Pt_2Al} = 0.334 {}^0 G_{Al}^{fcc-Al} + 0.666 {}^0 G_{Pt}^{fcc-Al} - 85325 + 24.9 * T$
L1₂ (Pt₃Al)	4SL-CEF: (Al,Pt) _{0.25} (Al,Pt) _{0.25} (Al,Pt) _{0.25} (Al,Pt) _{0.25} ${}^f G_{Al:Al:Al:Pt}^{L1_2} = {}^f G_{Al:Al:Pt:Al}^{L1_2} = {}^f G_{Al:Pt:Al:Al}^{L1_2} = {}^f G_{Pt:Al:Al:Al}^{L1_2} = UPTAL3$ ${}^f G_{Al:Al:Pt:Pt}^{L1_2} = {}^f G_{Al:Pt:Pt:Al}^{L1_2} = {}^f G_{Pt:Pt:Al:Al}^{L1_2} = {}^f G_{Pt:Al:Al:Pt}^{L1_2} = UPTAL$ ${}^f G_{Al:Pt:Pt:Pt}^{L1_2} = {}^f G_{Pt:Al:Pt:Pt}^{L1_2} = {}^f G_{Pt:Pt:Al:Pt}^{L1_2} = {}^f G_{Pt:Pt:Pt:Al}^{L1_2} = UPT3AL$ $L_{Al,Pt:*,*}^{L1_2} = L_{*,Al,Pt:*,*}^{L1_2} = L_{*,*:Al,Pt,*}^{L1_2} = L_{*,*:*:Al,Pt}^{L1_2} = ULO$ $L_{Al,Pt:Al,Pt:*,*}^{L1_2} = L_{*,Al,Pt:Al,Pt,*}^{L1_2} = L_{*,*:Al,Pt:Al,Pt}^{L1_2} = L_{*,*:*:Al,Pt}^{L1_2} = L_{Al,Pt:*,*}^{L1_2} = USRO$
UAB	$= -13595 + 8.3 * T$
UPTAL	$= 3 * UAB - 3913$
UPTAL3	$= 4 * UAB$
UPT3AL	$= 3 * UAB$
USRO	$= UAB$
ULO	$= 1412.8 + 5.7 * T$
ULD0	$= -110531 - 22.9 * T$
ULD1	$= -25094$
ULD2	$= 21475$
DGO	$= UPTAL3 + 1.5 * UPTAL + UPT3AL$
DG1	$= 2 * UPTAL3 - 2 * UPT3AL$
DG2	$= UPTAL3 - 1.5 * UPTAL + UPT3AL$

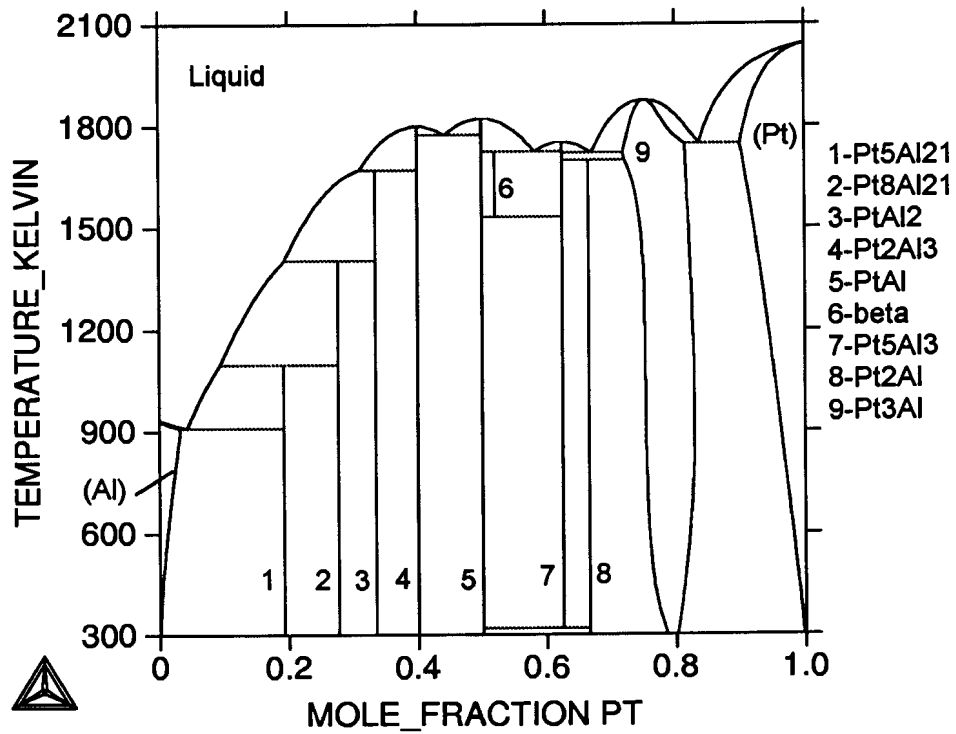


Figure 6.5. The calculated Al-Pt phase diagram.

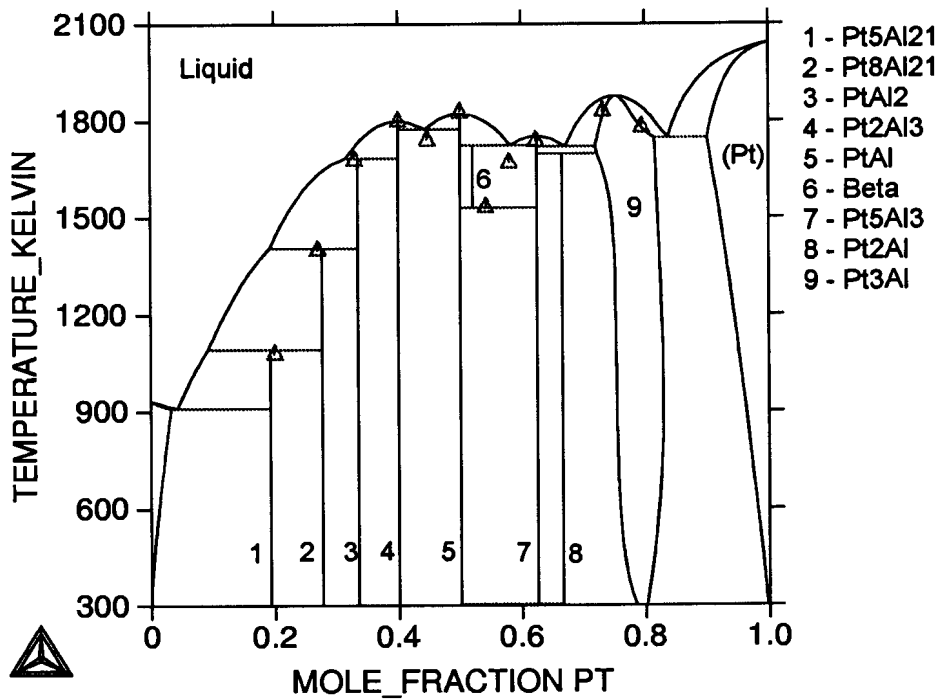


Figure 6.6. The calculated Al-Pt phase diagram compared with experimental invariant data points from the literature [1986McA].

Table 6.6. Experimental and calculated invariant temperatures and compositions for the Al-Pt system.

Reaction and Compositions (at. % Pt)					Reaction Temperature [K]	Reference
L	↔	Pt ₃ Al	+	(Pt)	1780	[1986McA]
79.5		76.4		85.7	1748 ¹	This work
83.7		81.1		99		
PtAl	+	L	↔	β	1783	[1986McA]
50.0		53.7		51.5	1725 ²	This work
50.0		58		52.0		
L	↔	Pt ₂ Al ₃	+	PtAl	1741	[1986McA]
44.47		40.0		50.0	1770	This work
46.7		40.0		50		
L	+	Pt ₃ Al	↔	Pt ₅ Al ₃	1738	[1986McA]
62.3		67.3		62.5		Not included ³
Pt ₅ Al ₃	+	Pt ₃ Al	↔	Pt ₂ Al	1703	[1986McA]
62.7		67.0		67.5	1701	This work
62.5		72		66.5		
L	+	Pt ₂ Al ₃	↔	PtAl ₂	1679	[1986McA]
31.8		40.0		33.3	1671	This work
40		40.0		33.3		
L	↔	β	+	Pt ₅ Al ₃	1670	[1986McA]
55.7		57.9		66.5	1723 ⁴	This work
58		52.0		62.5		
β	↔	PtAl		Pt ₅ Al ₃	1533	[1986McA]
54.2		50.0		61.5	1533	This work
52.0		50.0		62.5		
L	+	PtAl ₂	↔	Pt ₈ Al ₂₁	1400	[1986McA]
18.8		32.6		27.5	1404	This work
30		33.3		27.5		
L	+	Pt ₈ Al ₂₁	↔	Pt ₅ Al ₂₁	1079	[1986McA]
3.1		27.5		19.2	1097	This work
9		27.5		19.2		
L	↔	(Al)	+	Pt ₅ Al ₂₁	930	[1986McA]
0.4		0.0		19.2	910	This work
4		3		19.2		
L	↔	Pt ₃ Al			1829 ¹	[1986McA]
73.2		73.2			1877	This work
75.3		75.3				
L	↔	PtAl			1827	[1986McA]
50.0		50.0			1827	This work
50.0		50.0				
L	↔	Pt ₂ Al ₃			1800	[1986McA]
40.0		40.0			1800	This work
40.0		40.0				
L	↔	Pt ₅ Al ₃			1800	This work ³
62.5		62.5				

¹ Pt₃Al phase at too high at. % Pt due to symmetry of 4SL CEF. See text for discussion.

² β phase modelled as line compound, simplification and assumed stoichiometry influences equilibria.

³ Pt₅Al₃ in calculated diagram forms congruently and not by peritectic reaction [1986McA]. See text for discussion.

⁴ 50 K too high, due to β phase model and congruent formation of Pt₅Al₃.

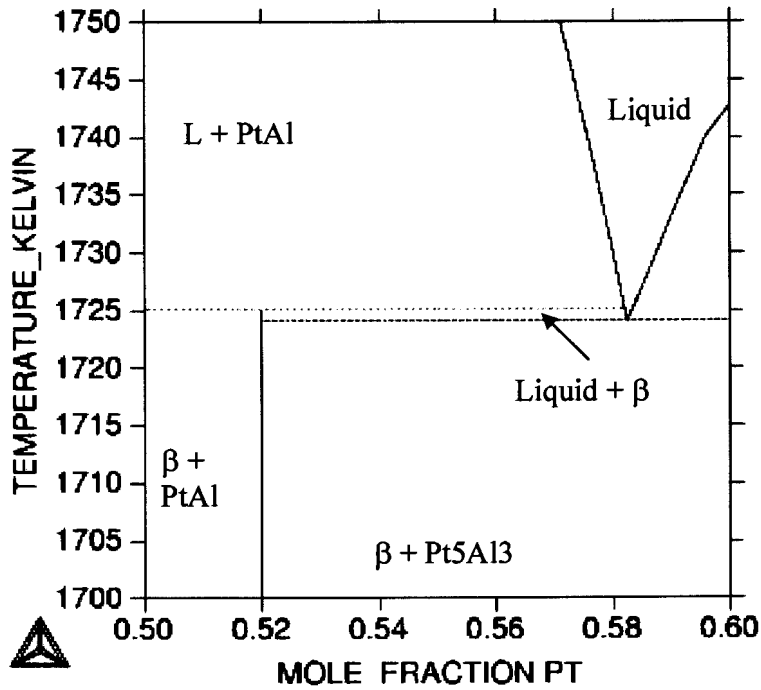


Figure 6.7. Enlargement on the Al-Pt binary system to show the reactions for the PtAl, β and liquid phases

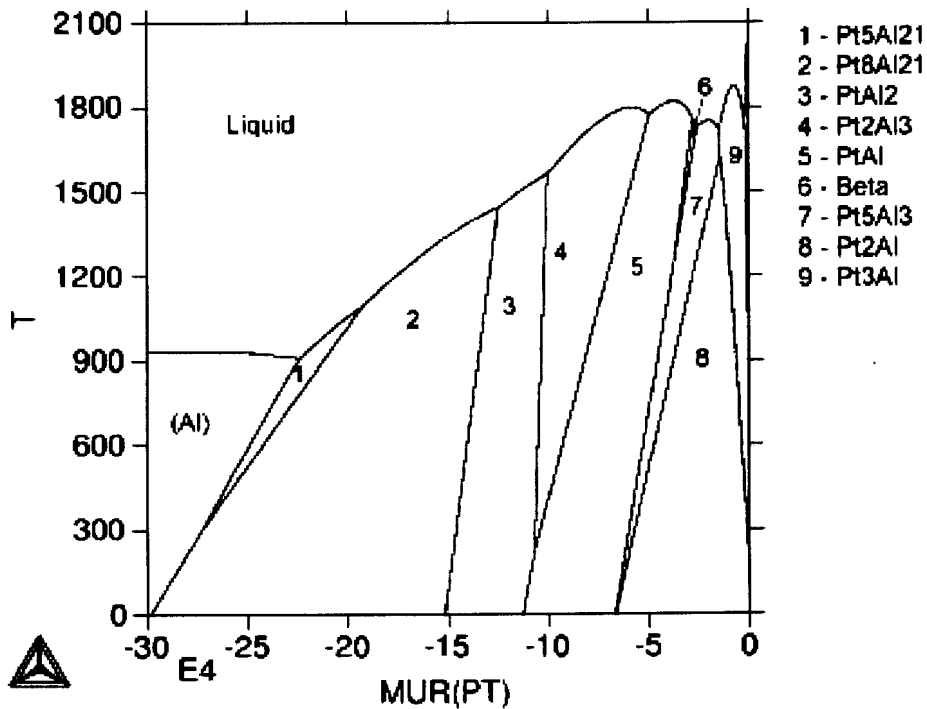


Figure 6.8 The Al-Pt phase diagram of temperature against chemical potential of Pt.

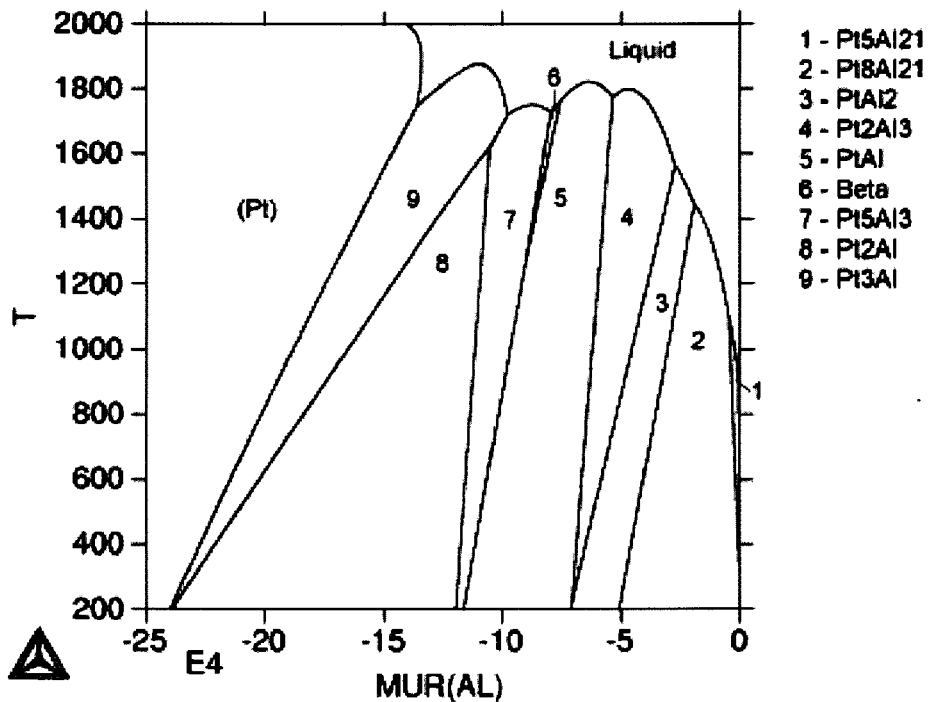


Figure 6.9. The Al-Pt phase diagram of temperature against chemical potential of Al.

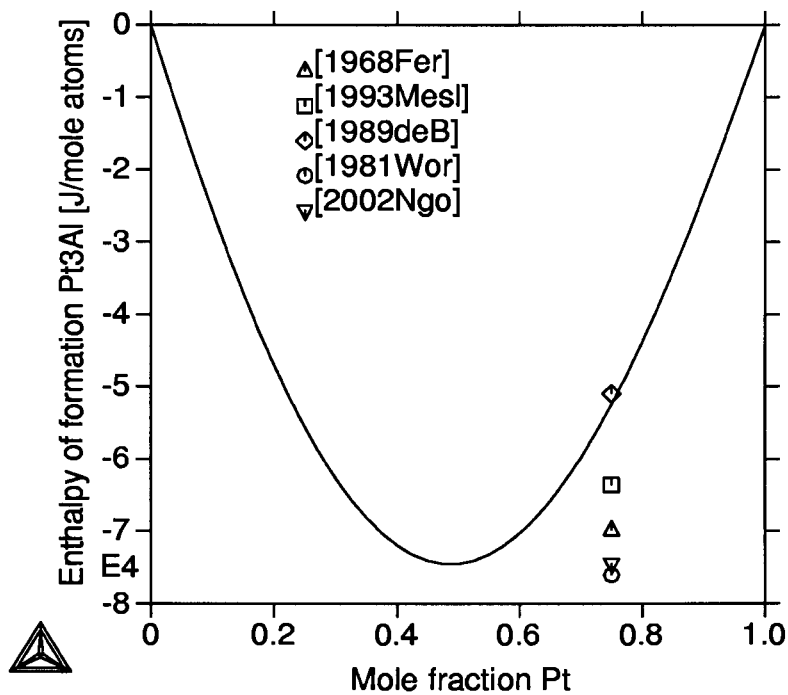


Figure 6.10. Comparison of calculated enthalpy of formation for Pt_3Al (L_{12}) phase with experimental results [1968Fer, 1981Wor, 1993Mes], Miedema estimations [1989deB] and *ab initio* predictions [2002Ngo].

Figures 6.8 and 6.9 show the phase diagram as a function of the chemical potential instead of the composition. The slope of the curves is equal to dG/dT , which is the entropy of the phases. It does not show any excessive entropy contributions for any of the phases in the system, since the slopes are all more or less similar. The decomposition of the β phase (phase number 6) is shown, as well as the solid-state formation of the Pt_2Al phase (phase number 8).

Table 6.7. Experimental and calculated enthalpies of formation for the Al-Pt system.

Phase	ΔH_f [J/mole atoms]	Method	Reference
Pt_5Al_{21}	-57 320	Solute solvent drop calorimetry	[1968Fer]
	-56 827	Calculated	This work
Pt_8Al_{21}	-71 130	Solute solvent drop calorimetry	[1968Fer]
	-81 751	Calculated	This work
Pt Al ₂	-84 000	Solute solvent drop calorimetry	[1968Fer]
	-87 325	Calculated	This work
Pt_2Al_3	-94 980	Solute solvent drop calorimetry	[1968Fer]
	-79 000	Miedema semi-empirical method	[1988deB]
	-96 500	Direct Synthesis Calorimetry	[1993Mes]
	-89 839	Calculated	This work
PtAl	-100 420	Solute solvent drop calorimetry	[1968Fer]
	-100 000	Direct Synthesis Calorimetry	[1991Jun]
	-82 000	Miedema semi-empirical method	[1988deB]
	-67 440	<i>Ab initio</i>	[2002Ngo]
	-94 025	Calculated	This work
β	-91 300	Calorimetry*	[1968Fer]
	-92 913	Calculated	This work
Pt_5Al_3	-90 730	Miedema semi-empirical method	[1988deB]
	-87 213	Calculated	This work
Pt_2Al	-88 280	Miedema semi-empirical method	[1988deB]
	-85 278	Calculated	This work
Pt_3Al	-69 870	Solution Calorimetry	[1968Fer]
	-63 600	Direct Synthesis Calorimetry	[1993Mes]
	-50 990	Miedema semi-empirical method	[1988deB]
	-76 000**	Electrochemical	[1981Wor]
	-74 380	<i>Ab initio</i>	[2002Ngo]
	-51 668	Calculated	This work

* estimated from the curve fitted to the enthalpies of formation experimentally determined by Ferro *et. al.* [1968Fer].

** estimated from the Gibbs free energy of mixing $\Delta G_m = -76\,640 + 7.48 \cdot T$ [1981Wor].

The calculated enthalpies of formation are compared to the experimental values in Table 6.7. They are all within the 10% error of Ferro's [1968Fer] experimental results, except for Pt_3Al , which is much lower, indicating the predicted phase is more stable than the experimental phase. This can also be affected by the fact the Pt_3Al forms at 73.2 at. % Pt

and not the expected stoichiometric 75 at % Pt of the perfect crystal structure, and the modelling could not fit the composition to 73.2 at. % Pt for the congruent melting. The enthalpy of formation for the Pt₃Al phase is compared with the experimental and *ab initio* predicted values in Figure 6.10.

Although there are some differences between the calculated and experimental Al-Pt phase diagrams, these are in areas where limited experimental data are available. In some cases the experimental diagram is based on the results on only one report. The limited data forced the need for simplified models, especially for the β phase. Thus the data appear to be not in good agreement, however, it is due to the simplified model. Considering the assumptions and limited data, the calculated phase diagram is in general excellent agreement with the experimental phase diagram.

6.4.3 Al-Pt-Ru

The predicted liquidus surface projection is shown in Figures 6.10 and 6.11. The solidification reactions are listed in Table 6.9. The reaction types were identified by projecting the surface on a temperature against liquid composition diagram (Figure 6.12). Ternary eutectic reactions were recognised by the meeting of three lines, forming a local minimum. A true ternary peritectic was identified by one of the line above the reaction, and two below [1965Wes].

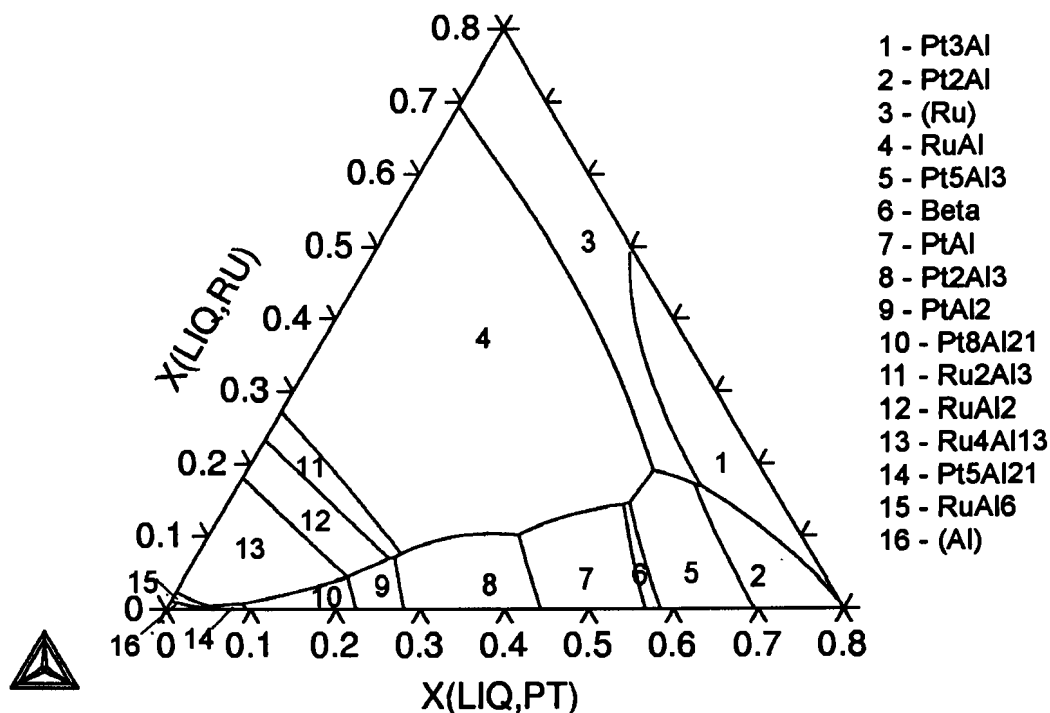


Figure 6.11. Liquidus surface projection for Al-Pt-Ru, indicating liquidus surface areas for the phases.

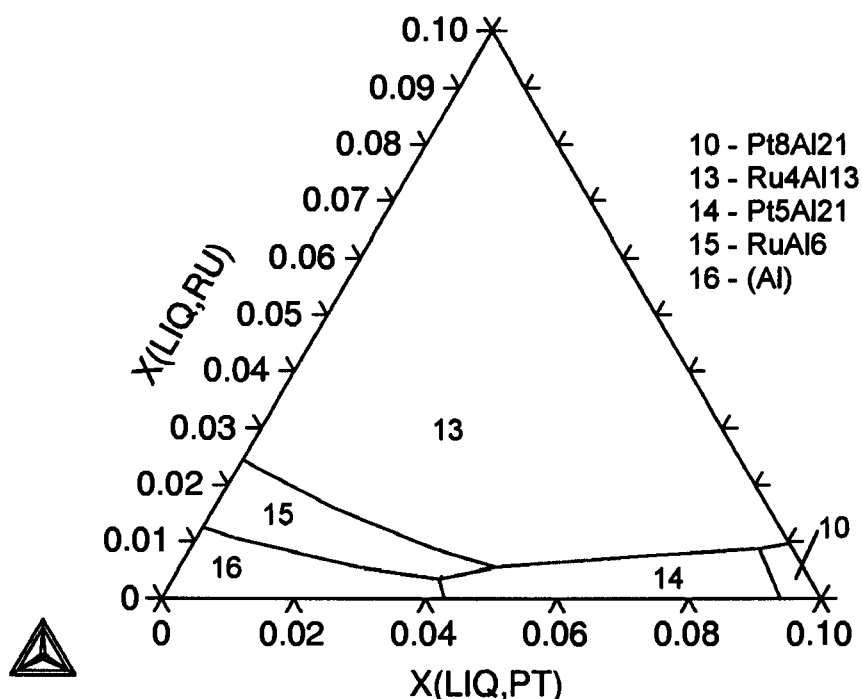


Figure 6.12. Enlargement of the Al-corner of the Al-Pt-Ru liquidus projection (Figure 6.10).

The solidification projection is only presented up to 80 at. % Pt. Although the ThermoCalc software calculated individual equilibrium values above this composition, it was not possible to map the liquidus projection for the area above 80 at. %. This is probably due to the 4SL CEF description of the Pt_3Al phase, as this phase is too stable in this projection, giving a too large phase surface on the liquidus projection. The extrapolation gives about 10 at% Ru in Pt_3Al , while experimental work [2001Big1, 2001Big2, 2001Hil1] showed a limited solubility of ruthenium in Pt_3Al . No attempts have been made to correct this at this stage. No thermodynamic data are yet available for the Al-Pt-Ru system, and an optimisation without thermodynamic data to give the liquid a reference point, would be meaningless.

Very little has been published to date on ternary extrapolations and ternary optimisations using the 4SL-CEF. Kuskoffsky [2002Kus1, 2002Kus2] evaluated the use of ternary parameters in the 4SL-CEF, and calculated the Ag-Au-Cu ternary. It was noted that care had to be taken with the reciprocal parameters. In the case of Ag-Au-Cu, data on the bonding energies of nearest neighbours and next-nearest neighbours were available to allow successful use of the 4SL-CEF.

Reactions 1 and 2 in Table 6.8 include the formation of Pt_2Al . This is an artefact of the modelling, again probably due to the use of 4SL-CEF. In the binary, Pt_2Al forms by a solid-state eutectoid reaction, $Pt_5Al_3 + Pt_3Al \rightarrow Pt_2Al$. Pt_2Al should, therefore, not form

from the liquid as it does in this extrapolation. However, it is possible that the presence of a third element in a binary structure can change the reaction in the ternary. In this case the extrapolation stabilised the Pt₂Al phase too much.

Table 6.8. Solidification sequence for Al-Pt-Ru.

Equation number	Reaction	Temperature [K]
1	$L + Pt_3Al \rightarrow (Ru) + Pt_2Al$	1445
2	$L \rightarrow (Ru) + Pt_5Al_3 + Pt_2Al$	1443
3	$L \rightarrow RuAl + Pt_5Al_3 + (Ru)$	1435
4	$L + \beta \rightarrow RuAl + Pt_5Al_3$	1485
5	$L + PtAl \rightarrow RuAl + \beta$	1500
6	$L \rightarrow RuAl + Pt_2Al_3 + PtAl$	1620
7	$L + RuAl \rightarrow Ru_2Al_3 + Pt_2Al_3$	1525
8	$L + Pt_2Al_3 \rightarrow Ru_2Al_3 + PtAl_2$	1507
9	$L + Ru_2Al_3 \rightarrow RuAl_2 + PtAl_2$	1500
10	$L + PtAl_2 \rightarrow Ru_4Al_{13} + Pt_8Al_{21}$	1415
11	$L + RuAl_2 \rightarrow Ru_4Al_{13} + Pt_8Al_{21}$	1408
12	$L + Pt_8Al_{21} \rightarrow Ru_4Al_{13} + Pt_5Al_{21}$	1080
13	$L + Ru_4Al_{13} \rightarrow RuAl_6 + Pt_5Al_{21}$	945
14	$L \rightarrow (Al) + RuAl_6 + Pt_5Al_{21}$	900

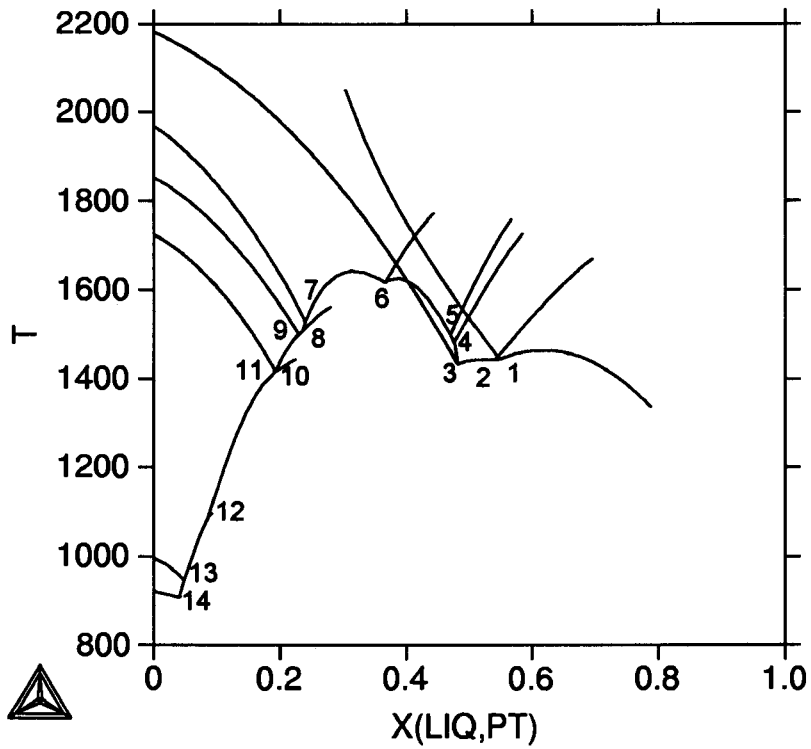


Figure 6.13. Projection of temperature against composition to identify the reaction types.

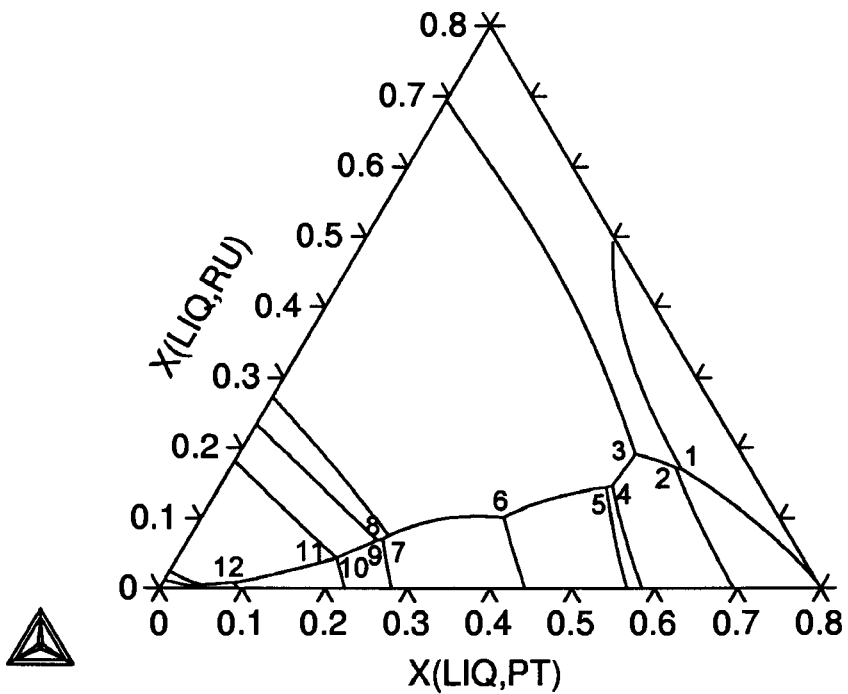


Figure 6.14. Solidification reactions, as listed in Table 6.8.

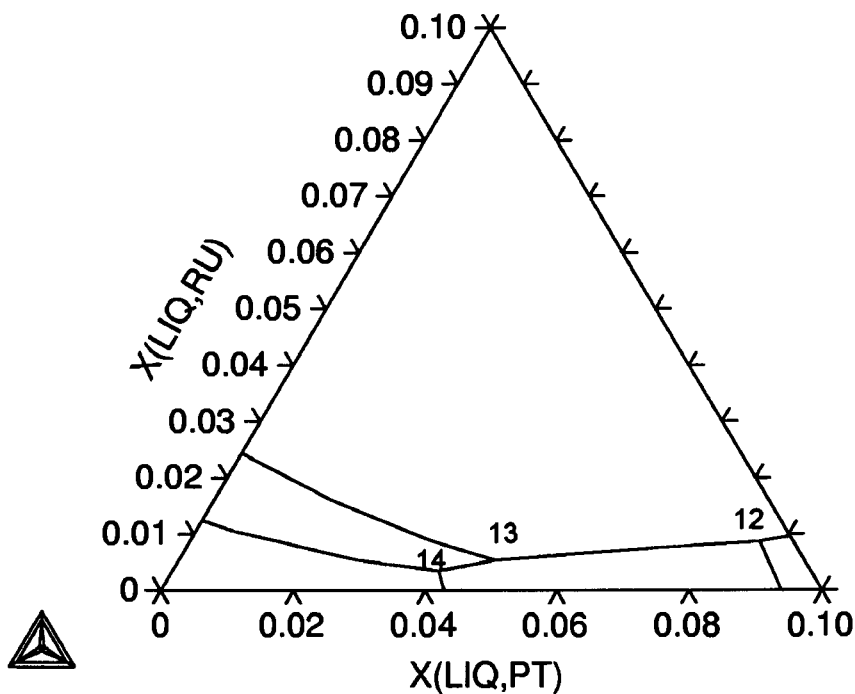


Figure 6.15. Solidification reactions, as listed in Table 6.8 (enlargement of Al-corner in Figure 6.13)

6.5 Conclusions

Stable Gibbs energy functions have been calculated for the phases in the Al-Ru and Al-Pt phase diagrams. Two models have been used to describe the ordered RuAl-B2 phase in the Al-Ru system. The results from MSL model were in better agreement with results from the literature. Although there were some areas of lesser agreement in the calculated Al-Pt system, they can be contributed to the 4SL CEF that has been used, as well as a lack on experimental data for the β -phase, which necessitated the stoichiometric treatment of the phase.

The ternary Al-Pt-Ru phase diagram was extrapolated from the calculated binary phase diagrams. The extrapolated diagram is in good agreement with the experimental diagram. The major differences arised from the fact that two new ternary phases were found in the experimental study. Since an extrapolation was based on the Gibbs energy functions for already entered phases, the software could not predict these new phases.

The good agreement between the experimental and calculated liquidus surface projections proves that thermodynamic modeling is powerful technique in the development of new alloy systems.

Chapter 7

Comparison of Experimental and Computational Results

7.1 Introduction

The results of the experimental determined Al-Pt-Ru liquidus surface projection and solidification reaction scheme are compared to the predicted liquidus projection and solidification reaction sequence. The agreements and discrepancies are discussed.

7.2 Results and discussion

Figures 7.1 and 7.2 show the experimental and predicted liquidus surface projections respectively. The results are in good agreement except for the Pt_3Al liquid surfaces, which is more stable in the predicted diagram than in the experimental diagram. The predicted phase diagram does not include the two ternary phases, X and T, which were found in the experimental investigation.

The solidification reactions are compared in Tables 7.1 and 7.2. There are some inconsistencies when comparing the experimentally deduced solidification sequence and the sequence predicted from the calculated Al-Pt-Ru system.

In the experimental solidification sequence, not enough data were available to determine the solidification direction of some of the reactions (direction of liquidus slope) listed in Table 7.1. However for most reactions the direction of decreasing temperature could be deduced. For the reaction at E, the data were not enough to decide which reaction is more probable. Both possible reactions are listed.

In the predicted system, the $\sim Pt_3Al$ phase area is too large, implying the calculated Gibbs energy function is too stable relative to the function for the (Pt). The predicted solidification reactions 1 and 2 in Table 7.2 show the Pt_2Al phase forming from a liquid reaction. In the Al-Pt binary system, Pt_2Al forms from the solid state through a peritectoid reaction. Although it is possible that the presence of a third element in a binary phase can change the behaviour of the phase, e.g. stabilise it to higher temperatures, the results from the extrapolation is not in agreement with the experimental results. The experimental results did not show Pt_2Al forming during solidification.

Reactions C and D from the experimental solidification sequence compare with reactions 3 and 4 in the predicted solidification sequence, although the reaction types differ. This could be either due to not enough experimental data or due to the extrapolation from pure binary phases without taking into account the possible effect of a third element on the Gibbs energy functions of the binary phases.

The ternary extrapolation also does not include the two ternary phases, as the extrapolation is based on phases already entered in the data file. Thus the rest of the solidification sequence cannot be compared beyond reactions 4 and D.

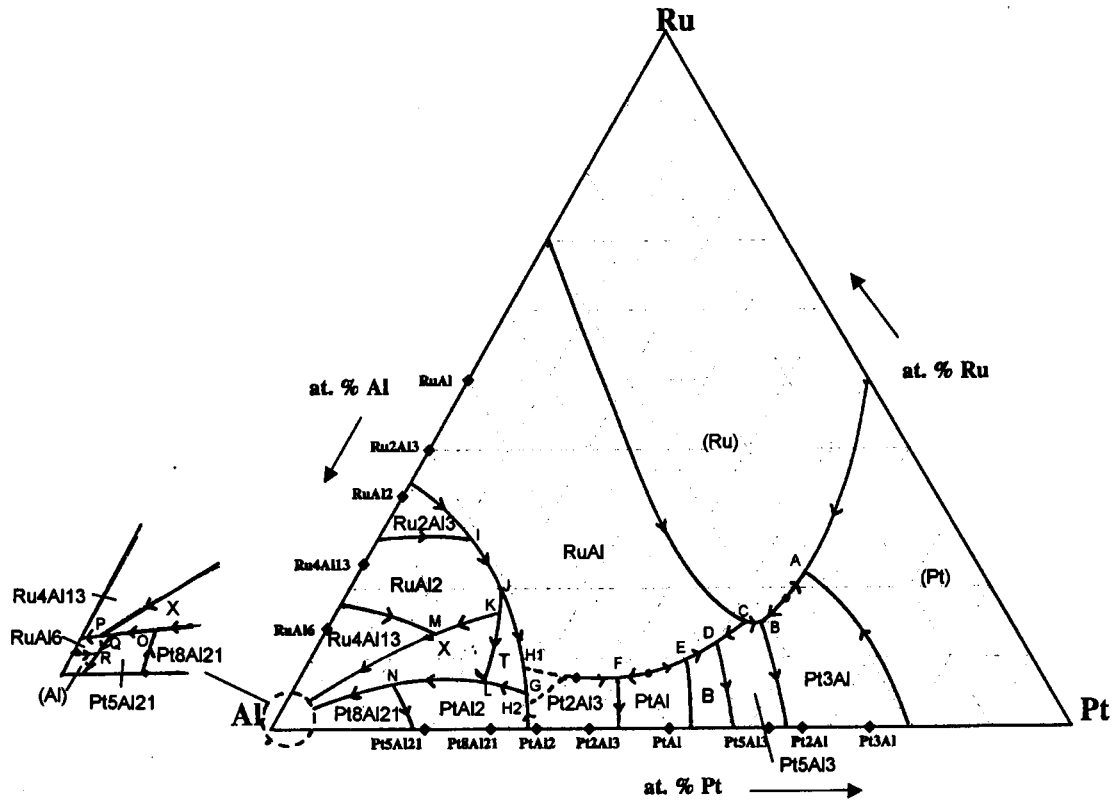


Figure 7.1. Experimental liquidus surface projection, showing the solidification reactions (A-R).

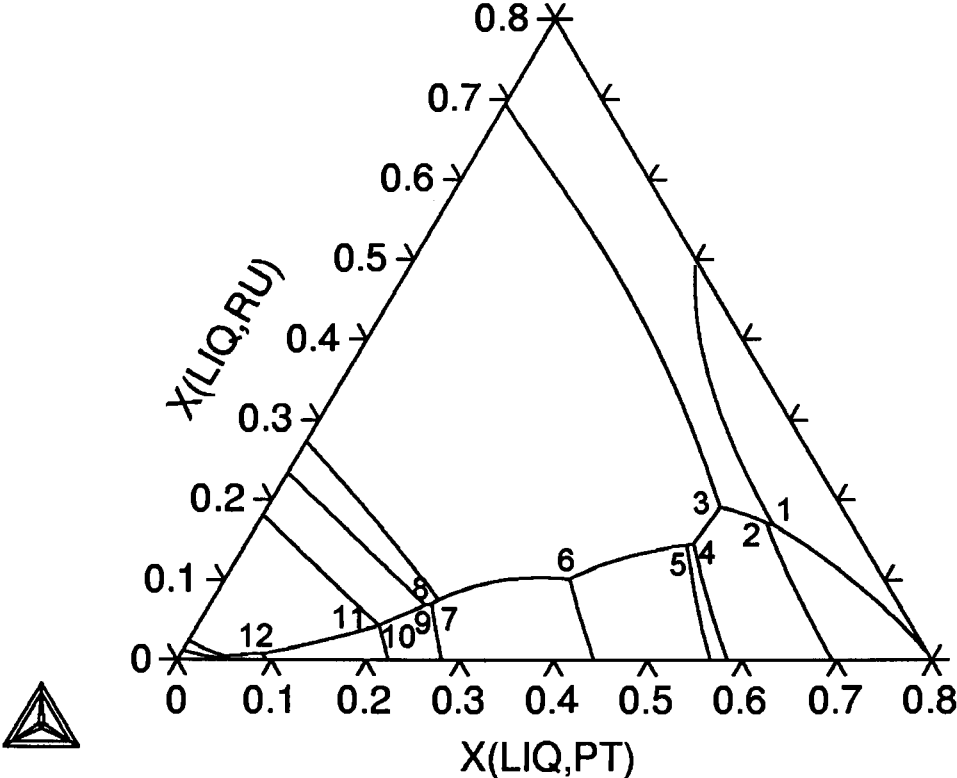


Figure 7.2. Predicted liquidus surface projection, showing the solidification reactions (1-12).

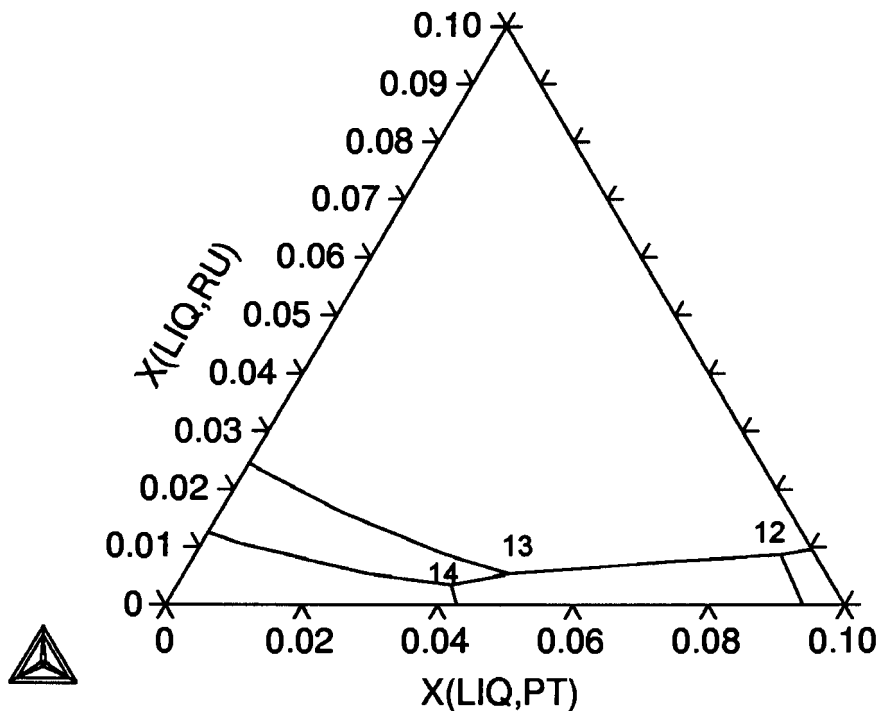


Figure 7.3 Predicted liquidus surface projection for the Al-corner, showing the solidification reactions (1-12) (enlargement of the Al-corner from Figure 7.2).

7.3 Conclusions

Although there are some discrepancies, the general comparison is excellent. The comparison of the experimentally determined and calculated prediction shows that predicting phase diagrams through computational methods is a useful tool for the metallurgist. The discrepancies in the comparison are mainly due to the absence of the two new ternary phases in the extrapolated phase diagram. To include these the ternary lattice stabilities will have to be calculated through an optimisation procedure, which fell outside the scope of this study.

In the continuation of the project, which this study was part of, this predicted ternary phase diagram will be used to select experimental points for further investigation in order to obtain maximum results from them.

Table 7.1. Experimental solidification reactions for Al-Pt-Ru (indicated in Figure 7.1).

Equation number	Reaction
A	$L \rightarrow (Ru) + (Pt) + \sim Pt_3Al$
B	$L + (Ru) \rightarrow Pt_5Al_3 + \sim Pt_3Al$
C	$L + (Ru) + \sim RuAl \rightarrow \sim Pt_5Al_3$
D	$L + \sim RuAl \rightarrow \beta + \sim Pt_5Al_3$
E *	$(\uparrow) L + \sim PtAl \rightarrow \sim RuAl + \beta$ $(\downarrow) L + \sim PtAl + \sim RuAl \rightarrow \beta$
F	$L + \sim RuAl \rightarrow \sim PtAl + Pt_2Al_3$
G*	$L + Pt_2Al_3 \rightarrow \sim PtAl_2 + \sim Ru_{18}Pt_{28}Al_{64}$
H1*	$L + \sim RuAl \rightarrow \sim Ru_{18}Pt_{28}Al_{64} + Pt_2Al_3$
G*	$L + \sim RuAl \rightarrow \sim PtAl_2 + \sim Ru_{18}Pt_{28}Al_{64}$
H2*	$L + Pt_2Al_3 \rightarrow \sim RuAl + \sim PtAl_2$
I	$L + Ru_2Al_3 \rightarrow \sim RuAl + \sim RuAl_2$
J	$L + \sim RuAl + \sim RuAl_2 \rightarrow \sim Ru_{18}Pt_{28}Al_{64}$
K	$L + \sim Ru_{18}Pt_{28}Al_{64} + \sim RuAl_2 \rightarrow \sim Ru_{12}Pt_{15}Al_{73}$
L	$L + \sim Ru_{18}Pt_{28}Al_{64} \rightarrow \sim Ru_{12}Pt_{15}Al_{73} + \sim PtAl_2$
M	$L + \sim RuAl_2 \rightarrow \sim Ru_{12}Pt_{15}Al_{73} + \sim Ru_4Al_{13}$
N	$L + \sim PtAl_2 + \sim Ru_{12}Pt_{15}Al_{73} \rightarrow \sim Pt_8Al_{21}$
O	$L + \sim Pt_8Al_{21} \rightarrow \sim Ru_{12}Pt_{15}Al_{73} + \sim Pt_5Al_{21}$
Q	$L + \sim Ru_{12}Pt_{15}Al_{73} + \sim Pt_5Al_{21} \rightarrow \sim RuAl_6$
P**	$L + \sim Ru_{12}Pt_{15}Al_{73} \rightarrow \sim Ru_4Al_{13} + \sim RuAl_6$
R	$L + \sim RuAl_6 \rightarrow \sim Pt_5Al_{21} + (Al)$

* Not enough experimental data available to conclude in which direction this reaction proceeds.

** Exit reaction must be peritectic to be consistent with the Al-Ru binary.

Table 7.2. Predicted solidification reactions for the calculated Al-Pt-Ru system.

Equation number	Reaction
1	$L + Pt_3Al \rightarrow (Ru) + Pt_2Al$
2	$L \rightarrow (Ru) + Pt_5Al_3 + Pt_2Al$
3	$L \rightarrow RuAl + Pt_5Al_3 + (Ru)$
4	$L + \beta \rightarrow RuAl + Pt_5Al_3$
5	$L + PtAl \rightarrow RuAl + \beta$
6	$L \rightarrow RuAl + Pt_2Al_3 + PtAl$
7	$L + RuAl \rightarrow Ru_2Al_3 + Pt_2Al_3$
8	$L + Pt_2Al_3 \rightarrow Ru_2Al_3 + PtAl_2$
9	$L + Ru_2Al_3 \rightarrow RuAl_2 + PtAl_2$
10	$L + PtAl_2 \rightarrow Ru_4Al_{13} + Pt_8Al_{21}$
11	$L + RuAl_2 \rightarrow Ru_4Al_{13} + Pt_8Al_{21}$
12	$L + Pt_8Al_{21} \rightarrow Ru_4Al_{13} + Pt_5Al_{21}$
13	$L + Ru_4Al_{13} \rightarrow RuAl_6 + Pt_5Al_{21}$
14	$L \rightarrow (Al) + RuAl_6 + Pt_5Al_{21}$

Conclusions and recommendations

Conclusions

The Al-Pt-Ru phase diagram was investigated experimentally and a liquidus surface projection is proposed. The experimental results were compared to a predicted liquidus surface projection using the CALPHAD method.

The following conclusions may be drawn from the experimental results:

- The liquidus surface is dominated by the RuAl phase; it occurred to within 10 at. % of the Al-Pt binary.
- (Ru) also has a large liquidus surface. This is an important factor to consider when making alloys that are just outside of the region of the alloys targeted for commercialisation.
- RuAl was found to contain at least 20 at. % platinum
- PtAl₂ exhibited up to 11 at. % solubility for ruthenium.
- RuAl₂ exhibited up to 10 at. % solubility for platinum.
- Ru₄Al₁₃ and RuAl₆ were difficult to analyse, since they were found together on a fine scale.
- RuAl₆ showed solubility of at least 10 at. % platinum.
- Most of the other phases showed limited solubilities for the ternary element, less than 2 at. %: Ru₄Al₁₃, Pt₂Al₃, Pt₅Al₃, Pt₅Al₂₁ and PtAl.
- A ternary phase X, with a composition \sim Ru₁₂Pt₁₅Al₇₃, was found to be present. Initial XRD analysis showed that the X phase probably has a primitive cubic structure and is similar to \sim RhAl_{2.63} and \sim IrAl_{2.75}. The lattice parameter is 0.7712 nm.
- A high-temperature ternary phase T, with composition of \sim Ru₁₈Pt₂₈Al₆₄, exists.
- Ru₂Al₃, T and β decomposed through solid-state reactions:

$$\begin{aligned} \text{Ru}_2\text{Al}_3 &\rightarrow \sim\text{RuAl} + \sim\text{RuAl}_2 \\ \text{T} &\rightarrow \text{X} + \sim\text{PtAl}_2 \\ \beta &\rightarrow \sim\text{PtAl} + \text{Pt}_5\text{Al}_3 \end{aligned}$$
- \sim RuAl was involved in a number of subsequent reactions in different alloys:
 - o peritectic formation of \sim PtAl,
 - o peritectic formation of \sim PtAl₂
 - o peritectic formation of β phase of the Al-Pt binary.
- There was good agreement between the experimental EDS and XRD results, despite the lack of data on some of the phases present in the ICDD. In many cases, the

structures of prototypes could be used through a grain refinement process to identify the binary phases.

The binary phase diagrams were calculated with the Thermo-Calc software, using the CALPHAD method. The calculated binaries are in excellent agreement with the experimentally reported phase diagrams in the literature. Furthermore, a liquidus surface projection has also been predicted from extrapolating the ternary system from the calculated binaries. The predicted results are in good agreement with the experimental results, thus showing that computational thermodynamics is a powerful tool in alloy development. Thermo-Calc did not provide any evidence for the ternary phases, which is not surprising.

Recommendations:

- Thermal analysis should be conducted on some of the samples to obtain reaction temperature and thermodynamic values (enthalpy of formation) for phases in the system, as these are required for the further optimisation of the ternary system. DTA, DSC, TG and calorimetry should be considered.
- Samples should be heat treated, as this will bring them to equilibrium conditions. This would assist in the XRD analyses (some heat treatments were done at 600°C, although 1000°C would be more relevant for the future applications of Pt-based alloys. Analysis of the samples after heat treatments is in progress and is part of a continuing project.).
- *Ab initio* predictions could be useful in predicting the enthalpies of formation for some of the binary phases, and the new ternary phases. More *ab initio* calculations on the polymorphs of the L1₂ phase would be valuable information for the CALPHAD modeling of this part of the Al-Pt phase diagram.
- XRD work should be conducted on especially the binary Al-Pt system, as very little standard data is available (this is planned as part of the current continuing project).
- TEM studies of samples containing the ternary phases would be needed to confirm the crystal structures.
- The calculated ternary phase diagram should be optimised. The ternary phases must be included. However, this is subject to first obtaining some thermodynamic values of the phases and suggesting crystal structure models for the new ternary phases. The optimisation will also solve the current discrepancies in phase stabilities with the experimental results.
- Re-optimisation of the Al-Pt system. A change in the use of the 4 SL CEF has been proposed after this work was submitted. The metastable phase diagram for the fcc ordered and disordered phases must first be optimised using *ab initio* calculated enthalpies of formation. Once an acceptable description for the fcc phases has been obtained, the complete system should be optimised in such a way that the metastable phases are not stable in the optimised system. The revised optimisation and use of the model will be published in the CALPHAD journal.

References

1934Hum	W. Hume-Rothery, <i>Phil. Trans. Roy. Soc.</i> , A244 (1934) 1.
1936Mot	N.F. Mott and H. Jones, <i>The Theory of the Properties of Metals and Alloys</i> (Oxford, UK, Oxford University Press, 1963), Chapter V.
1937Zin	E. Zintl, A. Harder and W. Haucke, <i>Z. Phys. Chem.</i> , B35 (1937) 354.
1949Eng	N. Engel, <i>Kemisk Maandesblad</i> , 30 (1949)
1951Kik	R. Kikichu, <i>Phys. Rev.</i> , 81 (1951) 988.
1957Mei	J.L. Meijering, <i>Acta. Met.</i> , 5 (1957) 257.
1960Obr	W. Obrowski, <i>Metallwissenschaft und Technik</i> (Berlin), 17 (1960) 108-112.
1962Bro	W. Bronger and W. Klemm, <i>Z. Anorg. Allg. Chem.</i> , 319 (1962) 58.
1963Bre	L. Brewer, <i>Electronic Structure and Alloy Chemistry of the Transition Metals</i> , ed. P.A. Beck (New York, NY: Interscience Publishers, Inc. 1963).
1963Fer	R. Ferro and R. Capelli, <i>Rend. Acad. Naz. Lincei.</i> , 34 (1963) 659.
1963Mag	A. Magneli, L. Edshammer and T. Dagerhamm, Final Technical Report No. 1 under Contract No DA-91-591-EUC-2734 (AD 426927) (1963) 44-50.
1963Sch	O. Schwomma, H. Nowotny, A. Wittmann, <i>Monatshefte für Chemie</i> , 94 (1963) 924-926.
1964Com	J. J. Comer, <i>Acta Cryst.</i> , 17 (1964) 444-445.
1964Huc	R. Huch and W. Klemm, <i>Z. Anorg. Allg. Chem.</i> , 329 (1964) 123-135.
1965Eds	L. Edshammer, <i>Acta Chem. Scand.</i> , 19 (1965) 2124-2130.
1965Wes	D.R.F. West, "Ternary Equilibrium Diagrams", (Macmillan and Co Ltd, London, 1965) 78.
1966Eds	L. Edshammer, <i>Acta Chem. Scand.</i> , 20 (1966) 427-431.
1968Eds	L. Edshammer, <i>Acta Chem. Scand.</i> , 22 (1968) 2374-2375.
1968Fer	R. Ferro, R. Gapelli, A. Borsese and G. Centineo, <i>Ren. Della Classe di Sci. Fis. Mat e Nat</i> , VIII (1968) 10-15.
1970Dar	A. S. Darling, G. L. Selman and R. Rushforth, <i>Platinum Met. Rev.</i> , 14 (1970) 124-130.
1970Kau	L. Kaufman and H. Bernstein, <i>Computer Calculation of Phase Diagrams</i> , (New York, NY: Academic Press, 1970)
1972Cha	G.A. Chadwick, <i>Metallography of Phase Transformations</i> (Butterworths, London, 1972).
1972Pet	D.G. Pettifor, 'Theory of the crystal structures of transition metals at absolute zero', <i>Metallurgical Chemistry</i> , ed. O. Kubaschewski (London, UK: HMSO 1972) 191.
1973Var	A.N. Varich and R. B. Lyukevich, <i>Russ. Metall.</i> , 1 (1973) 73-75.
1975Cha1	T. Chattopadhyay and K. Schubert, <i>J. Less-Common Met.</i> , 41 (1975) 19-32.
1975Cha2	D. Chatterij, R.C. Decries and J.F. Fleisher, <i>J. Less-Common Met.</i> , 42 (1975) 187-198.
1975Ton	A.M. Tonejc, A. Tonejc and A. Bonafacic, <i>J. Mater. Sci.</i> , 9 (1974) 523-526.
1976Cha	T. Chattopadhyay and K. Schubert, <i>J. Less-Common Met.</i> , 45 (1976) 79-83.
1976Gue	P. Guex and P. Feschotte, <i>J. Less-Common Metals</i> , 46 (1976) 101-116.
1976Neu	J.P. Neumann, Y.A. Chang and C.M. Lee, <i>Acta Metall.</i> , 24 (1976) 593-604.
1977Luk	H. Lukas, E-T. Hening and B. Zimmermann, <i>CALPHAD</i> , 9 (1977) 225.
1978Bah	S. Bahn and H. Kudielka, <i>Z. Metallkde.</i> , 69 (1978) 333-334.
1978Sch	K. Schubert, <i>Z. Krist.</i> , 70 (1978) 3113-321.
1979Cha	T. Chattopadhyay and P. Mamachandrarao, <i>Mater. Sci. Eng.</i> , 38 (1979) 7-17.
1979Sch	H.J. Schaller, <i>Z. Metallkde.</i> , 70 (1979) 318.
1979Wop	W. Wopersnow and Ch.J. Raub, <i>Metallwissenschaft</i> (Berlin). 33 (1979) 736-740.
1980Pia	G. Piatti and G. Pellegrini, <i>J. Mater. Sci.</i> , 15 (1980) 2403-2408.
1981Sun	B. Sundman and J. Agren, <i>J. Phys. Chem. Solids</i> , 42 (1981) 292-301.



1981Wor	W. L. Worrel and T. A. Ramanarayanan, <i>Chemical Metallurgy - A Tribute to Carl Wagner</i> (TMS-AIME, Warrendale, PA, 1980) 69-74.
1982Cha	Z.A. Chaudhury, G.V.S. Sastry and C. Suryanarayana, <i>Z. Metallkde</i> , 73 (1982) 201-206.
1982Eil	M. Ellner, U. Kattner and B. Predel, <i>J. Less-Common Metal.</i> , 87 (1982) 305-325.
1984Jan	B. Jansson, "Evaluation of Parameters in Thermodynamic Models Using Different Types of Experimental Data Simultaneously" Tricta-Mac-0234 (Royal Institute of Technology, Stockholm, Sweden, 1984).
1985Sun	B. Sundman, B. Janson and J.-O. Andersson, <i>CALPHAD</i> , 9 (1985) 153-190.
1985Vil	P. Villars and L.D. Calvert, 'Pearson's handbook of crystallographic data for intermetallic phases' Vol 2, ASM (1985).
1986McA	A.J. McAlister and D.J. Kahan, <i>Bull. Alloy Phase Diagr.</i> , 7 (1986) 47-51.
1987Fle	R.L. Fleischer, <i>J. Mat. Sci.</i> , 22 (1987) 2281-2288.
1987Oya	Y. Oya, Y. Mishima and T. Suzuki, <i>Z. Metallkde</i> , 78 (1987) 485-490.
1988Anl	S.M. Anlage, P. Nash, R. Ramachandran and R.B. Schwarz, <i>J. Less-Common Met.</i> , 163 (1988) 237-247.
1988Ans	I. Ansara, B. Sundman and B. Williams, <i>Acta Met.</i> 36 (1988) 977-989.
1988deB	F.R. De Boer, R. Boom, W.C.M. Maartens, A.R. Miedema and A.K. Niessen, <i>Cohesion in Metals: Cohesion and Structure Vol 1.</i> (Elsevier Science, Amsterdam, 1988).
1988Pet	D.G. Pettifor, quoted in [1998Sau].
1990Mas	T.B. Massalksi, Binary Alloy Phase Diagrams (ASM International, 1990).
1990Sun	B. Sundman and T. Mohri, <i>Z. Metallkde</i> , 81 (1990) 251.
1991Din	A.T. Dinsdale, <i>CALPHAD</i> , 15 (1991) 319-425.
1991Fle	R.L. Fleischer, R.D. Field and C.L. Briant, <i>Met. Trans. A</i> , 22A (1991) 404-414.
1991Jun	W-G. Jung and O.J. Kleppa and L. Topor, <i>J. Alloys and Compounds.</i> , 176 (1991) 309-318.
1991Tom	A. Tomer, Structure of Metals through Optical Microscopy (ASM International, 1991).
1992Jun	W-G. Jung and O.J. Kleppa, <i>Met. Trans. B</i> , 23B (1992) 53-56.
1992Lin	W. Lin, Jian-hua Xu and A.J. Freeman, <i>J. Mater. Res.</i> 7 (1992) 592-604.
1992Pet	D.G. Pettifor, <i>Electron Theory in Alloy Design</i> ed. D.G. Pettifor and A.H. Cottrell (London, UK: Institute of Materials, 1992) Chapter 4.
1993Fle	R.L. Fleischer, <i>Acta Metall. Mater.</i> , 41 (1993) 863-869.
1993Mes	S.V. Meschel and O.J. Kleppa, <i>J. Alloys and Compounds</i> , 197 (1993) 75-81.
1994Bon	T.D. Boniface, M.Sc. Dissertation, University of the Witwatersrand, Johannesburg, 1994.
1994Ste	H. De V. Steyn, I.M. Wolff and R. Coetzee, Spark-Plug Electrodes Containing Intermetallic Phases and Spark-Plug Electrodes Containing Same, S.A. Patent 94/10180, 22 December 1994.
1995Smi	E.G. Smith and C.I. Lang, <i>Scripta Met. et Mater.</i> , 33 (1995) 1225-1229.
1996Bon1	T.D. Boniface and L.A. Cornish, <i>J. Alloys and Compounds</i> , 233 (1996) 241-245.
1996Bon2	T.D. Boniface and L.A. Cornish, <i>J. Alloys and Compounds</i> , 233 (1996) 275-279.
1996Cor	M.B. Cortie and T.D. Boniface, <i>J. Mat. Syn. and Proc.</i> 4 (1996) 413-428.
1996McE	J.J. McEwan and T. Biggs, 13 th International Corrosion Congress, Melbourne, Australia, 25-29 November 1996, ACA Inc., Victoria, Paper 096.
1996Pel	A. D. Pelton, <i>Physical Metallurgy, Vol. 1</i> , ed. R. W. Cahn and P. Haasen (Elsevier Science, Amsterdam, 1996) Chapter 6.
1996Spe	P.J. Spencer, Noble Metal Database, Spencer Group Inc. 1996.
1996Wol	I.M. Wolff, <i>Met and Mat. Trans. A</i> (1996) 27A , 3688-3699.
1997Ans	I. Ansara, N. Dupin, H. L. Lukas and B. Sundman, <i>J Alloys and Compounds</i> , 247 (1997) pp 20-30.
1997Bro	W. Bronger, K. Wrzesien and P. Muller, <i>Solid State Ionics</i> , 101-103 (1997) 633-640.
1997Hor	I.J. Horner, L.A. Cornish and M.J. Witcomb, <i>J. Alloys and Compounds</i> , 256 (1997) 221-227.
1997Kat	U. R. Kattner, <i>JOM</i> , 49 (1997) 14-19.

1997Oka	H. Okamoto, <i>J. Phase Equil.</i> 18 (1997) 105.
1997Wol	I.M. Wolff, G. Sauthoff, L.A. Cornish, H. DeV. Steyn and R. Coetzee, <i>Structural Intermetallics 1997</i> , Ed. M.V. Nathal <i>et al.</i> , The Minerals, Metals and Materials Society, Champion, PA, USA, September 1997, 815-823.
1998And	S.A. Anderson and C.I. Lang, <i>Scripta Met. et Mater.</i> , 38 (1998) 493-497.
1998Wol	I.M. Wolf, private communication, (1998).
1998Ans	COST 507: Thermochemical Database for Light Metal Alloys, ed. I. Ansara, A.T. Dinsdale and M.H. Rand (1998).
1998Sau	N. Saunders and A.P. Miodownik, " <i>CALPHAD - A comprehensive guide</i> ", ed RW Cahn, Pergamon (1998).
1998Sun	B. Sundman, S.G. Fries and W.A. Oates, <i>CALPHAD</i> , 22 (1998) 335-354.
1999Dup	N. Dupin and I. Ansara, <i>Z. Metallkde</i> , 90 (1999) pp76-85.
1999Hil	P.J. Hill, L.A. Cornish and M.J. Witcomb, <i>J. Alloys and Compounds</i> , 291 . (1999) 130-144.
1999Hu	
1999Man	D. Nguyen-Manh and D.G. Pettifor, <i>Intermetallics</i> , 7 (1999) 1095-1106.
1999Oat	W.A. Oates, F. Zhang, S-L. Chen and Y. A. Chang, <i>CALPHAD</i> , 23 (1999) pp 181-188.
2000Com	D.N. Compton, L.A. Cornish and M.J. Witcomb, <i>Proc. Microsc. Soc. South Afr.</i> , Grahamstown, 30 (2000) 14.
2000Fai	G.B. Fairbank, C.J. Humphreys, A. Kelly and C.N. Jones, <i>Intermetallics</i> , 8 (2000) 1091-1100.
2000Hay	J. Haynes, K.L. More, B.A. Pint, I.G. Wright, K. Cooley and Y. Zhang, <i>High Temperature Corrosion and Protection of Materials</i> 5 (2000).
2000Hil	M. Hillert, " <i>The science of alloys for the 21st Century: A Hume-Rothery Symposium Celebration</i> ", (2000), ed P.E.A. Turchi <i>et al.</i> , TMS.
2000Hoh	J. Hohls, L.A. Cornish, P. Ellis and M.J. Witcomb, <i>J. Alloys and Compounds</i> , 308 (2000) 205-215.
2000Raj	F.A. Rajabalee, 'Wincell 1.1: A Window package of DOS routines for unit cell refinements', Bordeaux, France, updated March 2000.
2000Pri	S.N. Prins and L.A. Cornish, <i>CALPHAD XIX Conference Proceedings and Abstracts</i> , 2000, 84.
2000Sun	B. Sundman private communication, (2000).
2000Wu	K. Wu and Z. Jin, <i>Journal of Phase Equilibria</i> , 21 (2000) 221-226.
2001Big1	T. Biggs, P.J. Hill, L.A. Cornish. M.J. Witcomb, <i>J. Phase Equilibria</i> , 22 (2001) 214-218.
2001Big2	T. Biggs, PhD Thesis, University of Witwatersrand, Johannesburg, South Africa, 2001
2001Com1	D.N. Compton, L.A. Cornish and M.J. Witcomb, <i>J. Alloys and Compounds</i> , 317-318 (2001) 372-378.
2001Com2	D.N. Compton, L.A. Cornish and M.J. Witcomb, <i>Proceedings of the Microscopy Society of America, Microscopy and Analysis 2001</i> , Vol. 7, Supplement 2, 1248-1249. Long Beach USA, 5-9 August 2001.
2001Dav	A.V. Davydov, U.R. Kattner, D. Josell, J.E. Blendell, R.M. Waterstrat, A.J Shapiro and W.J. Boettinger, <i>Met. Mater. Trans A</i> , 32A (2001) 2175-2186.
2001Fri	K. Frisk and M. Selleby, <i>J. Alloys and Compounds</i> , 320 (2001) 177-188.
2001Hil1	P.J. Hill, PhD Thesis, University of Witwatersrand, Johannesburg, South Africa, 2001
2001Hil2	M. Hillert and M. Selleby, <i>J. Alloys and Compounds</i> , 320 (2001) 161-176.
2001Hil3	M. Hiller and M. Selleby, <i>J. Alloys and Compounds</i> , 329 (2001) 208-213.
2001ICD	International Center for Diffraction Data (ICDD), 'Powder Diffraction File', Pennsylvania, USA, 2001
2001Kum	K.C. Hari Kumar and P. Wollants, <i>J. Alloys and Compounds</i> , 320 (2001) 189-198.
2001Lab	J.L. Labar, A. Kovacs and P.B. Barna, <i>J. Applied Physics</i> , 90 (2001) 6545-6547.
2001Li	X. Li, A. P. Miodownik, N. Saunders, <i>J. Phase Equilibria</i> , 22 (2001) 247.



2001Sun	B. Sundman private communication, (2001).
2001Wil	R.J. Wilder, The Hydrogen Fuel Cell Institute, www.h2fuelcells.org (2002).
2002Bru	H. Brunner, 'Platinum-based Industries of the future', CSIR Workshop September 2002 (www.csir.co.za/platinum)
2002Gar	P. Gargano, H. Mosca, G. Bozolla and R.D. Noebe, Submitted to <i>Scripta Met.</i>
2002Cor	L.A. Cornish, J. Hohls, P.J. Hill, S.N. Prins, R. Suss and D.N. Compton, 34 th International Conference on Mining and Metallurgy, 545-550, Bor Lake, Yugoslavia, 30 September – 3 October 2002.
2002Eco	The Economist, 14 Sept 2002, 80-81
2002ICS	Inorganic Crystal Structure Database (ICSD) Fachinformationszentrum Karlsruhe, Germany, 2002.
2002Joh	Johnson Matthey 'Platinum 2002' ISSN 0268-7305.
2002Kus1	A. Kusoffsky, N. Dupin and B. Sundman, <i>CALPHAD</i> , 25 (2002) 549-565.
2002Kus2	A. Kusoffsky, Ph. D Thesis, Royal Institute of Technology, Sweden, Stockholm, 2002.
2002Ngo	P. Ngoepe, private communication, 2002.
2002Pri	S.N. Prins and L.A. Cornish, Phases Formed on Solidification in the Al-Pt-Ru System, 15 th International Congress on Electron Microscopy, Volume 1, 695-696, (Paper No. 619) 1-6 September 2002, Durban, South Africa.

Appendices

Appendix A Papers and Presentations

Appendix B XRD refinement example

Appendix C Al-Pt-Ru Database (SGTE format)

Appendix D Thermo-Calc Binary and ternary TDB and POP files (on CD)

Appendix E XRD spectra in .wmf format (on CD)

Appendix A

Papers and Conference Presentations

(Only copies of the abstracts and papers that are available have been attached in this section)

Papers and Conference Presentations related to this study:

- 1. A reassessment of the Al-Pt binary system**
S.N. Prins, L.A. Cornish, W.E. Stumpf and B. Sundman
Proceedings of CALPHAD XXXI Conference, 5-10 May 2002, Stockholm, Sweden.
- 2. Phases formed on solidification in the Al-Pt-Ru system**
S.N. Prins and L.A. Cornish
15th International Conference on Electron Microscopy, Volume 1, 695-696 (Paper No. 619).
1-6 Sept 2002, Durban, South Africa
- 3. The Development of Platinum-based Alloys and their Thermodynamic Database**
L.A. Cornish, J. Hohls, P.J. Hill, S.N. Prins, R. Süß and D.N. Compton
34th International Conference on Mining and Metallurgy, 545-550, Bor Lake, Yugoslavia,
30 September – 3 October 2002.
- 4. Thermodynamic Assessment of the Al-Ru System**
S.N. Prins, L.A. Cornish, W.E. Stumpf and B. Sundman
CALPHAD, 27 (2003) 79-90
- 5. Development of Platinum-based Alloys for High Temperature Applications**
L.A. Cornish, S.N. Prins, R. Süß and D.N. Compton
Oral presentation at the 7th Materials Modeling Meeting. 6 March 2003, Pietersburg, South
Africa. (2003: <http://mmc.unorth.ac.za>).
- 6. Case Study: Comparison of experimentally determined and CALPHAD-method
predicted liquidus surfaces of the Al-Pt-Ru system.**
S.N. Prins and L.A. Cornish
Oral presentation at the 7th Materials Modeling Meeting. 6 March 2003, Pietersburg, South
Africa. (2003: <http://mmc.unorth.ac.za>).
- 7. Thermodynamic Assessment of the Al-Pt-Ru system.**
S.N. Prins, B. Sundman, L.A. Cornish and W.E. Stumpf
Accepted as oral presentation to the CALPHAD XXXII Conference, 25-30 May 2003,
Quebec, Canada.
- 8. Thermodynamic Re-assessment of the Al-Pt System.**
S.N. Prins, L.A. Cornish and B. Sundman
Submitted to CALPHAD Journal.
- 9. Solidification of Al-Pt-Ru alloys (title to be confirmed)**
S.N. Prins, L.A. Cornish, W.E. Stumpf and P.S. Boucher
To be submitted to Journal of Alloys and Compounds.

10. **XRD study of phases in an investigation of the Al-Pt-Ru system**
S.N. Prins, P.S. Boucher and L.A. Cornish
21st European Crystallographic Meeting, 24-29 August 2003, Durban, South Africa.

Other publications and conference contributions submitted during this period, but not directly related to the thesis:

1. **High Al-content Ternary Phases in Al-Cr-Ni**
Lesley Cornish, Sara Prins, Daven Compton and Michael Witcomb
Proceedings CALPHAD XXX, May 2001, York, UK.
2. **Comparing Quantitative and Semi-Quantitative Energy Dispersive X-ray Spectroscopy**
S.N. Prins
Oral presentation and paper in proceedings, Metrology Workshop, August 2002, Roodevallei, Pretoria, South Africa (2003: <http://www.nla.org.za/workshops>).
3. **ILZRO Zinc Alloy Development Project**
J.M. Benson, S.N. Prins and D. Hope
15th International Congress on Electron Microscopy, Volume 1, 1 - 6 September 2002, Durban, South Africa.
4. **Thermodynamic Assessments of the Pt-Cr and Cr-Ru Systems with an Extrapolation into the Pt-Cr-Ru System.**
U. Glatzel and S.N. Prins
Accepted as a poster contribution to the CALPHAD XXXII Conference, 25-30 May 2003, Quebec, Canada.
5. **The study of the Al-Pt-Ru system at 600°C**
S.N. Prins and L.A. Cornish
Submitted to the Microscopy and Microanalysis 2003 Conference, 3- 7 August 2003, San Antonio, Texas.
6. **A Metrology Approach to Uncertainty in Quantitative EDS Analyses.**
S.N. Prins, L.H. Adlem and M.E. Lee
Submitted to the Microscopy and Microanalysis 2003 Conference, 3- August 2003, San Antonio, Texas, USA.

Additionally, two confidential reports were submitted at Mintek

1. **Experimental and Thermo-Calc work on the development of Pt-based superalloys 2nd Report**
L.A. Cornish, R. Suss, L. Glaner, D. Compton and S. N. Prins
Mintek Report C3466M, 16 September 2002
2. **Experimental and Thermo-Calc work on the development of Pt-based superalloys 3rd Report**
R. Suss, L. Glaner, D. Compton, L.A. Cornish and S. N. Prins
Mintek Report C3536M, 6 February 2003

A reassessment of the Al-Pt binary system

S. Prins^{1,2}, L.A. Cornish³, W. Stumpf², B. Sundman⁴

¹CSIR-NML, P.O. Box 395, Pretoria, 0001, South Africa;

²Department of Metallurgical Engineering and Materials Science, University of Pretoria, Pretoria, 0002, South Africa;

³Physical Metallurgy Division, Mintek, Private Bag X3015, Randburg, 2125, South Africa

⁴Department of Materials Science and Engineering, Royal Institute of Technology, S-10044 Stockholm, Sweden

The Al-Pt system is important as it is similar to the Al-Ni system and also showing a γ/γ' (Pt)/Pt₃Al phase relation. This phase relation in the Al-Pt system has been earmarked as the basis of potential high temperature alloys, replacing the Ni-based superalloys in applications where the Ni-based superalloys have reached their upper temperature limits [01Hil1].

A current study investigating the Al-Cr-Pt-Ru alloy system has lead to this reassessment of the Al-Pt binary system as in the CALPHAD assessment by Wu and Jin [00Wu], modelling of the L12 Pt₃Al phase does not accommodate the ordering of the L12 phase, as reported by Mishima *et al.* [86Mis] and Bronger *et al.* [97Bro]. A low temperature martensitic transformation for the Pt₃Al has also been reported [86Mis] and experimental observations of ternary Al-Pt-X alloys indicated that the ternary additions either stabilise the high temperature or the low temperature form of Pt₃Al (L1₂ and DO_c respectively) [01Hil2]. The previous assessment [00Wu] also did not include the β phase since there are some discrepancies about its existence [90Mas]. However, experimental analysis of some ternary alloys indicated a phase which is probably β .

The current reassessment allows for the ordering of the Pt₃Al phase and the Pt₂Al and β phases has been included and the phase diagram is in good agreement with experimental observations.

The assistance of the PDI and DACST is gratefully acknowledged.

References

- [01Hil1] P.J. Hill, L.A. Cornish, P. Ellis and M.J. Witcomb, *J. Alloy Comp.* 322 (2001) 166.
- [01Hil2] P.J. Hill, Y. Yamabe-Mitarai, H. Murakami, L.A. Cornish, M.J. Witcomb, I.M. Wolff and H. Harada, 3rd International Symposium on Structural Intermetallics, TMS (2001 - rescheduled for April 2002) 527-533.
- [00Wu] K. Wu and Z. Jon, *J. Phase Equilibria*, 21 (2000) 221.
- [97Bro] W. Bronger, K. Wresien and P. Muller, *Solid State Ionics* 101-103 (1997) 663.
- [90Mas] T.B. Massalski, *Binary Alloy Phase Diagrams*, ASM Publishers (1990).
- [86Mis] Y. Mishima, Y. Oya and T. Suzuki, *Proceedings of the International Conference on Martensitic Transformations*, Japan Institute of Metals (1986) 1009.

PHASES FORMED ON SOLIDIFICATION IN THE Al-Pt-Ru SYSTEM

S.N. Prins^{1,2} and L.A. Cornish³

¹CSIR-NML, P.O. Box 395, Pretoria, 0001, South Africa;

²Department of Metallurgical Engineering and Materials Science, University of Pretoria, Pretoria, 0002, South Africa;

³Physical Metallurgy Division, Mintek, Private Bag 3, Randburg, 2125, South Africa

Two-phase high Pt content alloys have been shown to exhibit a structure similar to that of γ/γ' (Ni)/ $\sim\text{Ni}_3\text{Al}$ in the Ni-based superalloys [1] and very good properties have been obtained, even at high temperatures [2]. High Pt content alloys in the Al-Pt-Ru system were studied after heat treatment at 1350°C to allow the two-phase structure to be optimised at the envisaged application temperature [3]. This work is part of a larger investigation in which the component phase diagrams of the Al-Cr-Pt-Ru system will be studied in detail, so that the phase relationships and phase compositions can serve as an input to Thermo-CalcTM. The solidification reactions were required, thus the alloys were studied in the as-cast condition.

Six alloy samples were manufactured by arc-melting the elements and were studied in the as-cast condition using a LEO 1525 FE-SEM with an Oxford Inca EDS. At least five analyses were made on each phase or area.

The highest Pt content alloy had a very similar structure to an alloy studied by Biggs *et al.* [3]. There were (Ru) needles in a eutectic comprising (Ru) needles and small (Pt) dendrites in a $\sim\text{Pt}_3\text{Al}$ matrix. Figure 1 shows a ternary eutectic which was not reported before [3].

Results from three alloys indicated that the $\sim\text{RuAl}$ phase was found to contain at least 20 at.% Pt. The $\sim\text{PtAl}_2$ phase exhibited up to 11 at.% solubility for ruthenium. The $\sim\text{Ru}_4\text{Al}_{13}$ and $\sim\text{RuAl}_6$ phases were difficult to analyse accurately, since they were found together on a fine scale (Figure 2), but they both showed solubility of at least 10 at.% platinum. Most of the other phases showed a more limited solubility; $\sim\text{RuAl}_2$, $\sim\text{Pt}_2\text{Al}_3$ and $\sim\text{PtAl}$ contained only about 2 at.% of the third component.

The liquidus surface was dominated by the $\sim\text{RuAl}$ phase, which stretched to within 10 at.% of the Al-Pt binary system, and then by the (Ru) phase. This is not surprising since both of these phases have very high melting points and they often dominate the phase diagram in related systems [4]. The $\sim\text{RuAl}$ phase was involved in a number of subsequent reactions in the different alloys. It was involved in at least three peritectic reactions, forming $\sim\text{PtAl}$, $\sim\text{PtAl}_2$ and a phase which was too fine to be analysed accurately, although it appears to have a composition close to the β phase of Al-Pt [5]. It was also involved in the ternary invariant reaction:

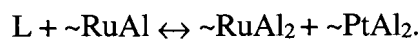


Figure 3 shows the remnants of $\sim\text{RuAl}$ dendrites, appearing as fine particles, after the peritectic formation of $\sim\text{Pt}_2\text{Al}$. This reaction was followed by an eutectic reaction forming $\sim\text{Pt}_2\text{Al}$ and $\sim\text{Ru}_4\text{Al}_{13}$. Figure 4 shows $\sim\text{RuAl}$ dendrites surrounded by a thin two-phase

region (probably produced by subsequent solid state precipitation at much lower temperatures), then a $\sim\text{RuAl}_2 + \sim\text{PtAl}_2$ eutectic. The binary eutectic reaction forming $\sim\text{PtAl}$ and $\sim\text{Pt}_2\text{Al}_3$ was also observed, very close to the Al-Pt binary. The other reactions were mainly peritectic in nature and tended to form more aluminium-rich phases. This is consistent with the Al-Ru and Al-Pt phase diagrams.

More alloys are being manufactured and the alloys are also being studied using XRD so that the phases can be confirmed.

The assistance of DACST and the PDI is gratefully acknowledged.

References

1. Hill, P.J., Cornish, L.A., Ellis, P., Witcomb, M.J. (2001) *J. Alloys Comp.* 322, 166 .
2. Hill, P.J., Yamabe-Mitarai, Y., and Wolff, I.M. (2001) *Scr. Mater.* 44, 43.
3. Biggs, T., Hill, P.J., Cornish, L.A., Witcomb, M.J. (2001) *J. Phase Equil.* 22, 214.
4. Cornish, L.A., Witcomb, M.J., Hill, P.J, Horner, I.J. (1999) *S. Afr. J. Sci.* 95, 517.
5. Massalski, T.B. (1990) *Binary Alloy Phase Diagrams*, ASM Publishers.

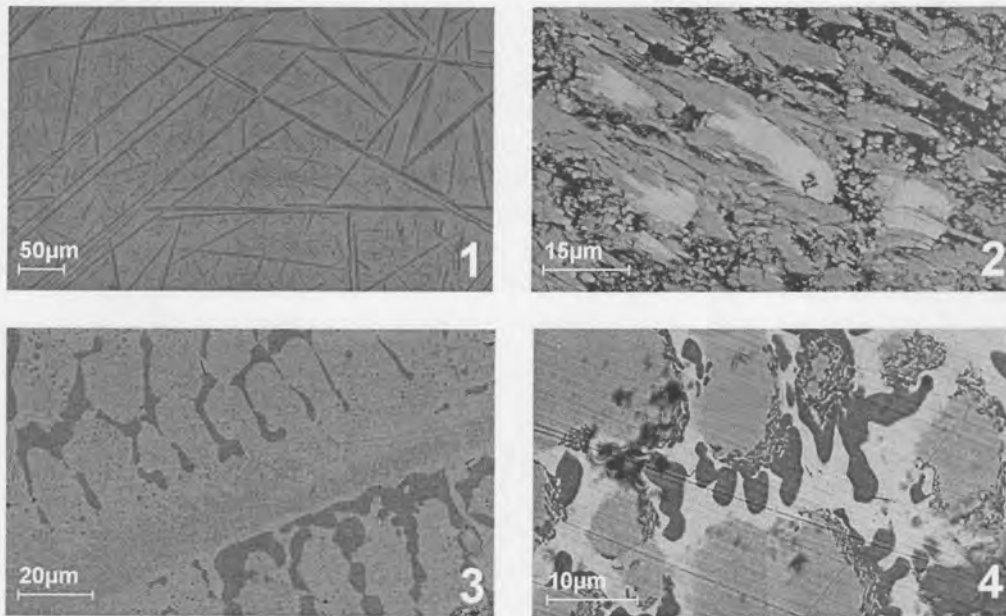


Figure 1. BSE image of $\text{Al}_{21}:\text{Pt}_{52}:\text{Ru}_{27}$ showing primary (Ru) needles in a ternary eutectic comprising (Ru) (smaller needles) + (Pt). **Figure 2.** BSE image of $\text{Al}_{84}:\text{Pt}_{8.5}:\text{Ru}_{7.5}$ showing $\sim\text{Pt}_5\text{Al}_{21}$ within a fine mixture of $\sim\text{Ru}_4\text{Al}_{13}$ and $\sim\text{RuAl}_6$. **Figure 3.** BSE image of $\text{Al}_{65}:\text{Pt}_{27}:\text{Ru}_8$ showing remnant dendrites of $\sim\text{RuAl}$ (dark particles) within $\sim\text{Pt}_2\text{Al}$ dendrites (light), surrounded by $\sim\text{Pt}_2\text{Al} + \sim\text{Ru}_4\text{Al}_{13}$ eutectic. **Figure 4.** BSE image of $\text{Al}_{54}:\text{Pt}_{14}:\text{Ru}_{32}$ showing $\sim\text{RuAl}$ dendrites (medium) within $\sim\text{Ru}_4\text{Al}_{13}$ (dark) + $\sim\text{PtAl}_2$ eutectic (light). There are regions of solid state precipitation at the dendrite edges.



seems very small scatter in

σ_{C2}
900 K
0.914
0.849
0.767
0.709
0.673
0.583
0.506
0.434
0.361

described above explain the
on of the ZnTe-CdTe solid
phase sharply in the region

57),379.

r. Trans. JIM,32(1991),169-
and T. Iida; Netsu Sokutei,
and T. Iida; Mater. Trans. JI

THE DEVELOPMENT OF PLATINUM-BASED ALLOYS AND THEIR THERMODYNAMIC DATABASE

Lesley Alison Cornish¹, Jeanette Hohls¹, Patricia Joan Hill¹,
Sara Prins^{2,3}, Rainer Süß¹ and Daven Northumberland Compton¹

¹Physical Metallurgy Division, Mintek, Private Bag 3, Randburg, 2125, South Africa

²CSIR-NML, P.O. Box 395, Pretoria, 0001, South Africa

³Department of Metallurgical Engineering and Materials Science, University of Pretoria,
Pretoria, 0002, South Africa

ABSTRACT

A series of quaternary platinum-based alloys have been demonstrated to exhibit the same two-phase structure as Ni-based superalloys and showed good mechanical properties. The properties of ternary alloys were a good indication that the quaternary alloys, with their better microstructure, will be even better. The quaternary alloy composition has been optimised at Pt₄₂Al₁₁Ru₂Cr₁ for the best microstructure and hardness.

Work has begun on establishing a thermodynamic database for Pt-Al-Ru-Cr alloys, and further work will be done to enhance the mechanical and oxidation properties of the alloys by adding small amounts of other elements to the base composition of Pt₄₂Al₁₁Ru₂Cr₁.

Keywords: platinum-based alloys, thermodynamic database

INTRODUCTION

Nickel-based superalloys have excellent mechanical properties because they have a microstructure comprising many small, strained-coherent, particles in a softer matrix [1987Sim]. The strengthening originates from dislocations being slowed down as they negotiate the small ordered particles. Additionally, there is solid solution strengthening in the (Ni) matrix. Although these alloys are used at relatively high temperatures, coarsening does not occur because the surface energy itself is very small. This is because the particle structure is very closely related to that of the matrix. Both are based on the face centred cubic structure: the matrix has a random fcc structure, and the particles have an L1₂ ordered structure. The lattice misfit between these structures is very small and renders the surface energy negligible [1987Sim].

The Ni-based superalloys have virtually reached their temperature limit for operation in turbine engines. However, there is a need to further increase the operational temperatures of these engines to achieve greater thrust, reduced fuel consumption and lower pollution. Thus, there is interest in developing a whole new suite of similar structured alloys based on a metal with higher melting point which can be used at temperatures of ~1300°C.

Platinum has been selected as the base material for these alloys because of its similarity to Ni in fcc structure and similar chemistry. Thus, similar phases to Ni₃Al could be used to give similar mechanisms as found in the Ni-based superalloys. The important differences are the higher melting point (1769°C for platinum compared to 1455°C for nickel) and improved corrosion resistance. Although platinum-based alloys are unlikely to replace all Ni-based superalloys on account of both higher price and higher density, it is likely that they can be used for the highest application temperature components. Pt₃Al has two forms, and the more desirable high temperature L1₂ form needs to be stabilised.

Experimental Pt-based alloys have been studied. It was found that successful Ni-based superalloy analogues could be manufactured with alloys of the approximate composition Pt₄₂Al₁₁X₁ where X was Cr, Ti and Ru [2001Hil1, 2001Hil2]. The best properties were exhibited by the Pt-Al-Cr and Pt-Al-Ru alloys, although the precipitate volume fraction was not as high as in the Ni-based superalloys. Although much heavier, the Pt-based alloys have the advantages of good mechanical properties and high temperature oxidation resistance [2000Hil1, 2001Sus1]. The ternary alloys have

34th IOC on Mining and Metallurgy, 30 Sept-3 Oct 2002, Hotel "Jezero", Bor Lake, Yugoslavia

mechanical properties which are better than those of the Ni- and Co-based superalloys, higher than conventional solid-solution strengthened Pt-based alloys, and comparable with mechanically alloyed ferritic ODS alloys [2002Sus].

EXPERIMENTAL PROCEDURE

Several alloys were made up in order to ascertain whether the two-phase structure could be achieved in the quaternary system. Compositions were selected based on the results of the ternary Pt-Al-Cr and Pt-Al-Ru systems.

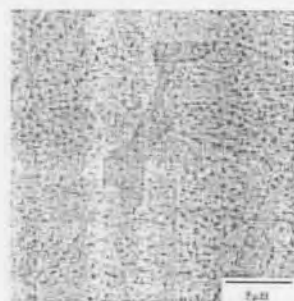
The alloys were prepared by arc-melting the pure elements several times to achieve homogeneity. The samples were then heat treated at 1350°C for 96 hours. The heat-treated samples were then cut in half, mounted and polished. The microstructure was examined using scanning electron microscopy (SEM) and, where possible, the phases were analysed using electron dispersive X-ray spectroscopy (EDS). The hardness of the alloys was measured using a Vickers hardness tester with a 10 kg load.

RESULTS AND DISCUSSION

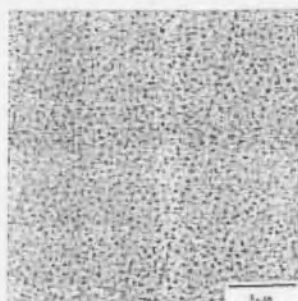
Three alloys were single-phase \sim Pt₃Al, while three had two-phase microstructures. Two of these had large areas of \sim Pt₃Al, together with a mixture of (Pt) and \sim Pt₃Al (Figure 1a). The third (Pt₈₄:Al₁₁:Ru₂:Cr₃) was composed entirely of a fine two-phase mixture, which is the desired microstructure (Figure 1b). The EDS analyses of the overall and phase compositions are given in Table 1. Very fine phases were not analysed.

Table 1. Compositions of the Pt-Al-Ru-Cr alloys after heat treatment at 1350°C for 96 hours.

Alloy Composition	Phase	Phase composition (at.%)			
		Pt	Al	Ru	Cr
Pt ₇₉ :Al ₁₅ :Ru ₂ :Cr ₄	(Pt)	79.7±0.5	8.4±0.5	5.4±0.5	6.5±0.5
	\sim Pt ₃ Al	75.2±0.3	20.5±0.4	0.8±0.2	3.5±0.4
	$\gamma\gamma$	79.3±0.5	10.6±0.6	4.5±0.4	5.6±0.7
Pt ₈₇ :Al ₁₁ :Ru ₂ :Cr ₂	\sim Pt ₃ Al	76.0±0.1	20.9±0.4	0.3±0.3	2.8±0.2
	$\gamma\gamma$	81.2±0.5	11.6±0.1	2.7±0.3	4.5±0.3
Pt ₈₄ :Al ₁₁ :Ru ₂ :Cr ₃	$\gamma\gamma$	83.5±1.3	11.3±0.6	2.4±0.5	2.8±0.4



a) Pt₈₁:Al₁₃:Ru₂:Cr₄



b) Pt₈₄:Al₁₁:Ru₂:Cr₃

Figure 1. SEM micrographs, in back-scattered electron (BSE) mode, of the two types of two-phase alloys. a) With primary \sim Pt₃Al (dark contrast) in a fine mixture of (Pt) and \sim Pt₃Al; b) Fine mixture of (Pt) and \sim Pt₃Al.

 34th IOC on Mining a

The hardness of the three Table 2. The alloys were small cracks on the edges.

Table 2. Vickers hard

Alloy Designation
Pt ₇₉ :Al ₁₅ :Ru ₂ :Cr ₄
Pt ₈₇ :Al ₁₁ :Ru ₂ :Cr ₂
Pt ₈₄ :Al ₁₁ :Ru ₂ :Cr ₃

Table 3. Composition

Alloy Designation
Pt ₈₅ :Al ₁₁ :Ru ₂ :Cr ₂
Pt ₈₄ :Al ₁₁ :Ru ₂ :Cr ₃
Pt ₈₁ :Al ₁₃ :Ru ₂ :Cr ₄
Pt ₈₀ :Al ₁₂ :Ru ₂ :Cr ₂
Pt ₈₁ :Al ₁₂ :Ru ₂ :Cr ₄

More alloys were pro be increased. Table 3 sh 1350°C in argon. Only th were also small areas of pr

The hardness of the alloys The hardness ranged from around the indentations.

Table 4. Vickers hard

Alloy Designation
Pt ₈₅ :Al ₁₁ :Ru ₂ :Cr ₂
Pt ₈₄ :Al ₁₁ :Ru ₂ :Cr ₃
Pt ₈₁ :Al ₁₃ :Ru ₂ :Cr ₄
Pt ₈₀ :Al ₁₂ :Ru ₂ :Cr ₂
Pt ₈₁ :Al ₁₂ :Ru ₂ :Cr ₄
Pt ₇₉ :Al ₁₅ :Ru ₂ :Cr ₄

in an attempt to imp treatment was conducted fo small size of the samples, t improvement. However, microstructure after this h There was no primary \sim Pt



Bor Lake, Yugoslavia

sed superalloys, higher than
parable with mechanically

wo-phase structure could be
on the results of the ternary

several times to achieve
rs. The heat-treated samples
as examined using scanning
re analysed using electron
s measured using a Vickers

ase microstructures. Two of
-Pt₃Al (Figure 1a). The third
xture, which is the desired
re compositions are given in

ment at 1350°C for 96 hours.

Composition (at.%)		
	Ru	Cr
5	5.4±0.5	6.5±0.5
4	0.8±0.2	3.5±0.4
6	4.5±0.4	5.6±0.7
4	0.3±0.3	2.8±0.2
1	2.7±0.3	4.5±0.3
6	2.4±0.5	2.8±0.4

The hardness of the three two-phase heat treated alloys was measured and the results are given in Table 2. The alloys were reasonably ductile, although some of the hardness indentations exhibited small cracks on the edges.

Table 2. Vickers hardness of the two-phase quaternary alloys, using a 10 kg load

Alloy Designation	Hardness (HV ₁₀)
Pt ₇₀ :Al ₁₅ :Ru ₂ :Cr ₁₃	438 ± 11
Pt ₆₁ :Al ₁₁ :Ru ₂ :Cr ₂₆	453 ± 16
Pt ₆₇ :Al ₁₁ :Ru ₂ :Cr ₂₀	472 ± 14

Table 3. Compositions of the Pt-Al-Ru-Cr alloys after heat treatment at 1350°C for 96 hours

Alloy Designation	Phase	Phase composition (at.%)			
		Pt	Al	Ru	Cr
Pt ₇₀ :Al ₁₅ :Ru ₂ :Cr ₁₃	-Pt ₃ Al	76.6±0.4	21.8±0.2	0.0±0.0	1.6±0.3
	γ/γ	85.3±0.3	10.1±0.7	2.2±0.1	2.4±0.3
Pt ₆₁ :Al ₁₁ :Ru ₂ :Cr ₂₆	-Pt ₃ Al	76.0±0.5	22.2±0.2	0.4±0.4	1.4±0.3
	γ/γ	84.9±0.6	10.1±1.4	2.3±1.1	2.7±0.9
Pt ₆₇ :Al ₁₁ :Ru ₂ :Cr ₂₀	-Pt ₃ Al	76.1±0.8	21.4±0.6	0.6±0.6	1.9±0.2
	γ/γ	84.9±0.4	9.5±0.2	2.4±0.3	3.2±0.3
Pt ₆₀ :Al ₁₂ :Ru ₂ :Cr ₂₆	-Pt ₃ Al	75.9±0.7	20.6±0.6	0.8±0.4	2.7±0.4
	γ/γ	81.6±1.0	9.2±1.2	3.9±1.7	5.3±0.7
Pt ₆₁ :Al ₁₁ :Ru ₂ :Cr ₂₆	-Pt ₃ Al	76.3±0.3	20.6±0.1	0.5±0.1	2.6±0.2
	γ/γ	83.0±0.8	9.2±0.4	3.1±0.1	4.7±0.4

More alloys were produced to ascertain if the volume fraction of the -Pt₃Al precipitates could be increased. Table 3 shows the measured compositions after heat treatment for 96 hours at 1350°C in air. Only the Pt₆₁:Al₁₁:Ru₂:Cr₂₆ alloy had a clear fine two-phase mixture, but there were also small areas of primary -Pt₃Al.

The hardness of the alloys was measured after heat treatment and the results are given in Table 4. The hardness ranged from 417 to 430 HV₁₀. The alloys showed good ductility, with no cracking around the indentations.

Table 4. Vickers hardness of the second batch of quaternary alloys, using a 10 kg load.

Alloy Designation	Hardness (HV ₁₀)
Pt ₆₇ :Al ₁₁ :Ru ₂ :Cr ₂₀	430 ± 5
Pt ₆₁ :Al ₁₁ :Ru ₂ :Cr ₂₆	425 ± 21
Pt ₆₇ :Al ₁₁ :Ru ₂ :Cr ₂₀	421 ± 12
Pt ₆₀ :Al ₁₂ :Ru ₂ :Cr ₂₆	419 ± 22
Pt ₆₁ :Al ₁₁ :Ru ₂ :Cr ₂₆	425 ± 10
Pt ₆₇ :Al ₁₁ :Ru ₂ :Cr ₂₆	417 ± 8

In an attempt to improve the microstructure of the second batch of alloys, a second heat treatment was conducted for 96 hours at 1350°C in air. Some oxidation took place, and due to the small size of the samples, this caused loss of aluminium. In all but one of the alloys, there was no improvement. However, alloy Pt₆₁:Al₁₁:Ru₂:Cr₂₆ showed a clear, fine two-phase microstructure after this heat treatment, possibly due to the change in its overall composition. There was no primary -Pt₃Al in evidence, so the overall composition is that of the two-phase



Cr₃
mode, of the two types of two-
a fine mixture of (Pt) and

mixture: 85.2 ± 0.3 at.% Pt, 7.1 ± 0.8 at.% Al, 3.1 ± 0.8 at.% Ru and 4.6 ± 0.1 at.% Cr. Since the overall composition changed, the sample was redesignated as $Pt_{85}:Al_7:Ru_3:Cr_5$.

Figure 2 shows the microstructure of this alloy after the first and second heat treatments, and that of the $Pt_{84}:Al_{11}:Ru_2:Cr_3$ alloy from the first batch. It can be seen that the precipitates in $Pt_{84}:Al_{11}:Ru_2:Cr_3$ are approximately twice as large, but more well-defined than those of $Pt_{85}:Al_7:Ru_3:Cr_5$. The hardnesses were re-measured and are given in Table 7. They range from 396 to 415 HV_{10} , and were less after the second anneal.

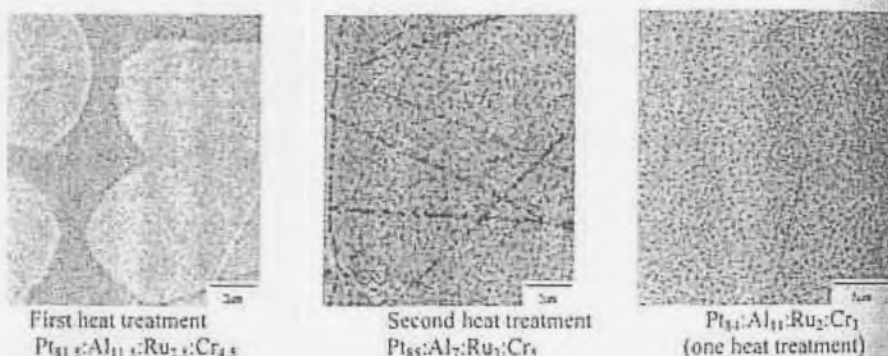


Figure 2. SEM BSE micrographs of alloy $Pt_{81.5}:Al_{11.5}:Ru_{2.5}:Cr_{4.5}$ after one, and two heat treatments, and alloy $Pt_{84}:Al_{11}:Ru_2:Cr_3$ after one heat treatment (Scratches can be seen.)

Table 2.7. Vickers hardness of the second batch of quaternary alloys after the second heat treatment, using a 10 kg load.

Alloy Designation	Hardness (HV_{10})
$Pt_{84}:Al_{11}:Ru_2:Cr_3$	403 ± 20
$Pt_{84}:Al_{11.5}:Ru_2:Cr_{2.5}$	403 ± 14
$Pt_{83}:Al_{11}:Ru_2.5:Cr_{3.5}$	405 ± 8
$Pt_{80.5}:Al_{17.5}:Ru_{2.5}:Cr_{4.5}$	414 ± 9
$Pt_{81.5}:Al_{11.5}:Ru_{2.5}:Cr_{4.5}$	396 ± 6
$Pt_{79.5}:Al_{10.5}:Ru_{4.5}:Cr_{5.5}$	415 ± 10

DISCUSSION

As has been shown before [2001Hil3], it is possible to obtain a (Pt) + γ -Pt₃Al microstructure in the quaternary alloys. The volume fraction of γ -Pt₃Al was estimated, using image analysis, to be approximately 25-30%. The highest hardness was found in the alloy without primary γ -Pt₃Al. In the second batch of quaternary alloys, there was no clear relationship between the hardness and the composition or microstructure. The decrease in hardness after the second heat treatment is likely to be due to the changes in composition due to oxidation.

The best alloy to date is $Pt_{84}:Al_{11}:Ru_2:Cr_3$ it has the required structure, no primary γ -Pt₃Al and reasonable hardness. Other work has already shown that its oxidation resistance is better than the original ternary alloys [2001Sus2].

The other part of the project is the development of a thermodynamic database to facilitate the further development of these Pt alloys, while simultaneously developing the alloys further. This work will build on the information already gleaned from prior work, and will also extend the work to Pt alloys of higher order (i.e. alloys with more components, such as Ni).

The Parrot module is based on that of SGTE [1] the Al-Ru and Pt-Al system phase diagram for Al-Pt [2002Pri1] as Wu and Jin only described one form of this phase are important for

The Al-Ru system will be optimised and will be combined for the systems: Al-Cr-Ru [2002Sus2]. The Pt-Al-Cr also be studied. Results of phase or near single-phase optimisation.

Once the Pt-alloy design additions, added to improve optimisation.

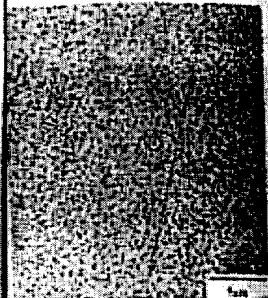
CONCLUSION

It is possible to produce precipitates of similar shape. $Pt_{84}:Al_{11}:Ru_2:Cr_3$ is the optimal Pt-Al-Ru-Cr thermodynamic. The assistance of DACST

REFERENCES

1. B. Sundman, B.
2. C.T. Sims, N.S.
3. Noble Metal Database
4. A.T. Dinsdale, C
5. D.N. Compton, I Volume 6, Supplement 2000.
6. D.N. Compton, I Volume 30, p. 9.
7. P.J. Hill, L.A. Cor Temperature Control 17th-22nd September
8. P. Hill, L.A. Cor Volume 30, p. 17.
9. K. Wu and Z. Jin
10. D.N. Compton, I Vol. 7, Supplement California, USA.
11. P.J. Hill, Y. Yam and H. Harada, Rese Sept 2001.

4.6±0.1 at.% Cr. Since the second heat treatments, and seen that the precipitates in well-defined than those of Table 7. They range from 396



Pt₈₄Al₁₁Ru₂Cr₃
(one heat treatment)

after one, and two heat treatments (Scratches can be seen.)

alloys after the second heat

Hardness (HV ₁₀)
403 ± 20
403 ± 14
405 ± 8
414 ± 9
396 ± 6
415 ± 10

in a (Pt) + ~Pt₃Al microstructure, using image analysis, to be alloy without primary ~Pt₃Al. In ship between the hardness and the second heat treatment is likely to

structure, no primary ~Pt₃Al oxidation resistance is better than

dynamic database to facilitate the developing the alloys further. This work, and will also extend the work on Ni).

The Parrot module in Thermo-Calc™ [1985Sun] that is being used to optimise the database is based on that of SGTE [1991Din] and Spencer's database [1998Spe]. The intermetallic phases in the Al-Ru and Pt-Al systems are not included in the current SGTE database. Although a calculated phase diagram for Al-Pt has been published by Wu and Jin [2000Wu], this was re-calculated [2002Pri1] as Wu and Jin's description did not exhibit any ordering in the Pt₃Al phase. They also only described one form of the Pt₃Al phase, and since both the cubic and tetragonal structures of this phase are important for this work, they must both be included.

The Al-Ru system has also been optimised by the group [2002Pri1]. Next, each ternary system will be optimised individually (already started for Al-Cr-Ru), and then once finalised, they will be combined for the quaternary. Experimental work has already commenced on the ternary systems: Al-Cr-Ru [2000Com1, 2000Com2, 2001Com], Pt-Al-Ru [2002Pri2] and Pt-Cr-Ru [2002Sus2]. The Pt-Al-Cr system will also be studied. Additionally, more quaternary alloys will also be studied. Results from the phase diagram work, together with enthalpies from the single-phase or near single-phase compositions from Leeds, UK will be input to Thermo-Calc™ for optimisation.

Once the Pt-alloy database has been optimised against some quaternary alloys, other small additions, added to improve the properties (as in nickel-based superalloys), will be included in the optimisation.

CONCLUSION

It is possible to produce a fine two-phase γ/γ' structure in the Pt-Al-Ru-Cr system, with precipitates of similar shape to those in the nickel-based superalloy systems. The composition of Pt₈₄Al₁₁Ru₂Cr₃ is the optimum composition because it has no primary phase. Development of the Pt-Al-Ru-Cr thermodynamic database has commenced. The assistance of DACST and the PDI is gratefully acknowledged.

REFERENCES

1. B. Sundman, B. Jansson and J.O. Andersson, CALPHAD, 9 (1985) 153.
2. C.T. Sims, N.S. Stoloff, and W.C. Hagel, Superalloys II, Wiley Interscience, USA, 1987.
3. Noble Metal Database, The Spencer Group, 1995.
4. A.T. Dinsdale, Calphad, 17 (1991) 319.
5. D.N. Compton, L.A. Cornish and M.J. Witcomb, Microscopy and Microanalysis 2000, Volume 6, Supplement 2, 370-371, Philadelphia, Pennsylvania, USA, 13th-17th August 2000.
6. D.N. Compton, L.A. Cornish and M.J. Witcomb, Proc. Microsc. Soc. South Afr., Volume 30, p. 9, Grahamstown, 6th-8th December 2000.
7. P.J. Hill, L.A. Cornish and M.J. Witcomb, International Symposium on High Temperature Corrosion and Protection 2000, Rusutsu Resort Hotel, 185-190, Japan, 17th-22nd September 2000.
8. P. Hill, L.A. Cornish, M.J. Witcomb and P. Ellis, Proc. Microsc. Soc. South Afr., Volume 30, p. 13, Grahamstown, 6th-8th December 2000.
9. K. Wu and Z. Jon, J. Phase Equilibria, 21 (2000) 221.
10. D.N. Compton, L.A. Cornish and M.J. Witcomb Microscopy and Microanalysis 2001, Vol. 7, Supplement 2, 1248-1249. Pub. Springer-Verlag, NY, Inc., Long Beach, California, USA, 5th-9th August 2001.
11. P.J. Hill, Y. Yamabe-Mitarai, H. Murakami, L.A. Cornish, M.J. Witcomb, I.M. Wolff and H. Harada, TMS, 527-533. Snow King Resort, Jackson Hole, Wyoming, USA, Sept 2001. Rescheduled for 28th April - 1st May 2002.



Pergamon

PII: S0364-5916(03)00033-6

DOI: 10.1016/S0364-5916(03)00033-6

Thermodynamic Assessment of the Al-Ru System

S.N. Prins^{1,2}, L.A. Cornish^{3,4}, W.E. Stumpf², B. Sundman⁵

¹CSIR-NML, PO Box 395, Pretoria, 0001, South Africa

²Department of Materials Science and Metallurgical Engineering, University of Pretoria, Pretoria, 0001, South Africa

³School of Process and Materials Engineering, University of the Witwatersrand, Private Bag 3, WITS, 2050, South Africa

⁴now at: Physical Metallurgy Division, Mintek, Private Bag X3015, Randburg, 2125, South Africa

⁵Division of Computational Thermodynamics, Department of Materials Science and Engineering, Royal Institute of Technology, SE-100 44 Stockholm, Sweden
Corresponding author's email: sprins@csir.co.za

(Received November 28, 2002)

Abstract. The CALPHAD technique was used to calculate the Al-Ru binary phase diagram. The RuAl (B2) phase was described with the sublattice model (SL), also designated Compound Energy Formalism (CEF), as well as the Modified Sublattice Formalism (MSL), which describes the order disorder transformation with one Gibbs energy function. The RuAl₆ phase was described as a stoichiometric phase and the remaining intermetallic phases (Ru₄Al₁₃, RuAl₂ and Ru₂Al₃) were modelled with the sublattice model. The solubility of Ru in (Al) was considered negligible. Good agreement was obtained between the calculated and the experimental phase diagrams. © 2003 Published by Elsevier Science Ltd.

Introduction

The RuAl compound has an unusual combination of properties which have been exploited in high temperature and high wear environments such as spark plugs [1994Ste]. Fleischer and co-workers [1991Fle] first reported the excellent room temperature toughness, compared to other intermetallic compounds, and recommended its potential for structural applications because of its high melting point and good oxidation resistance. The improved toughness is due to five independent slip systems in the crystal.

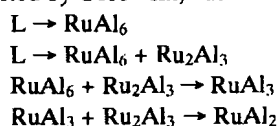
The excellent corrosion resistance of RuAl in hot, concentrated mineral acids was first reported by Wopersnow and Raub [1979Wop], and more recently, McEwan and Biggs [1996McE] demonstrated its capability as a coating in a range of aqueous media. They recognised that it has potential in corrosion-resistant coatings and electrochemical applications. The electrical conductivity of RuAl is high, almost metallic in value, and it exhibits good work function attributes [1995Smi]. This, and the good thermal conductivity [1998And] also renders the material suitable for spark-plug electrodes [1997Wol].

Although RuAl is difficult to manufacture by melting because of its high melting point, it can be manufactured by powder processing techniques, especially by reactive powder processing [1996Cor], or reactive hot isostatic processing (RHIP) [1996Wol].

Experimental Data

Phase Diagram Data

The crystal data for the phases of the Al-Ru system are listed in Table 1. Obrowski [1960Obr] reported the first phase diagram for the Al-Ru system and this was based on microscopic, X-ray and thermoanalytical observations. Six intermetallic phases were reported: RuAl₁₂ (although some uncertainty existed of the exact composition), RuAl₆, RuAl₃, RuAl₂, Ru₂Al₃ and RuAl, taking part in eight invariant reactions. The Ru-rich solid solution was reported to dissolve ~4 at. % Al at the eutectic temperature. No solubility of Ru in (Al) was detected and it was also concluded that all the Al-rich intermetallic compounds were line compounds. The RuAl phase was observed to melt at 2333 ± 20 K and the eutectic reaction between RuAl + (Ru) was at 2193 ± 20 K. Reactions were observed at 1573 and 1873 K and these were assigned to eutectic and peritectic reactions respectively. It was concluded, however, that some uncertainty existed of the solid-state reactions between 20 and 40 at. % Ru. Apart from Obrowski, no subsequent workers have reported the existence of RuAl₁₂. Other reactions reported by Obrowski, but not found by other workers were:



Schwomma [1963Sch] undertook X-ray work on a 33.3 at. % Ru sample, and found RuAl₂ and RuAl. The possibility of contamination by silicon and oxygen was, however, raised as a possibility by the author.

Edshammar determined the crystal structure for Ru₄Al₁₃ [1965Eds] (Obrowski's RuAl₃ [1960Obr]), and noted the similarity with Fe₄Al₁₃ because of the twinned prismatic structure and co-ordination numbers, although Ru₄Al₁₃ showed even better agreement with Os₄Al₁₃. He also found that Al atoms were absent from some of the sites which were partially occupied by Al in Fe₄Al₁₃ and Co₄Al₁₃. Ru₄Al₁₃ was, therefore, considered to be the ideal structure of RuAl₃ [1960Obr]. Subsequently with X-ray powder methods, Edshammar reported the crystal structures for five more intermetallic phases: RuAl, Ru₂Al₃, RuAl₂, RuAl_{-2.5} and RuAl₆ [1966Eds, 1968Eds]. The phase RuAl_{-2.5} was observed only in arc-melted samples. There were some additional CsCl-like phases reported around the composition RuAl, but no further details were given. No evidence of the RuAl₁₂ phase was found, and there were other inconsistencies with Obrowski's phase diagram [1960Obr] concerning the Ru₂Al₃ and RuAl₂ phases.

Anlage *et al.* [1988Anl] undertook experiments up to 26 at. % Ru using scanning electron microscopy, X-ray diffraction and thermal analysis (DSC). The RuAl₁₂ phase could not be confirmed, and Edshammar's [1965Eds] notation for the Ru₄Al₁₃ phase was used. It was also reported that both RuAl₆ and Ru₄Al₁₃ melt by peritectic reaction at 996 K and 1676 K respectively, and not congruently as suggested by Obrowski [1960Obr]. Some liquidus temperatures were provided. Problems with homogeneity of the alloys were reported, and also that the peritectic reaction forming RuAl₆ was sluggish. Under rapid solidification conditions, icosahedral phases were reported between 2.4 and 23.5 at. % Ru.

Table 1
The crystal data for the elements and compounds in the Al-Ru system.

Phase	Struktur-bericht	Pearson symbol	Prototype	Reference
Al	A1	<i>cF</i> 4	Cu	
RuAl ₆		<i>oC</i> 28	MnAl ₆	[1968Eds] [1982Cha]
Ru ₄ Al ₁₃		<i>mC</i> 102	Fe ₄ Al ₁₃	[1965Eds]
RuAl ₂	C11α C54	<i>tI</i> 6 <i>oF</i> 24	CaC ₂ TiSi ₂	[1960Obr] [1966Eds]
Ru ₂ Al ₃	D5 ₁₃	<i>hP</i> 5 <i>tI</i> 10	Ni ₂ Al ₃ Os ₂ Al ₃	[1960Obr] [1966Eds]
RuAl	B2	<i>cP</i> 2	CsCl	[1960Obr]
Ru	A3	<i>hP</i> 2	Mg	

Table 2
Experimental, predicted and calculated thermodynamic data.

Phase	ΔH° [J/mole atoms]	Reference
RuAl ₆	-17 930 ± 10%	Estimated using Miedema's method [1998Wol]
	-22 286	Calculated – this work
Ru ₄ Al ₁₃	-30 030 ± 10%	Estimated using Miedema's method [1998Wol]
	-38 535	Calculated –this work
RuAl ₂	-38 260 ± 10%	Estimated using Miedema's method [1998Wol]
	-45 125	Calculated –this work
Ru ₂ Al ₃	-44 040 ± 10%	Estimated using Miedema's method [1998Wol]
	-43 946	Calculated –this work
RuAl	-47 320 ± 10%	Estimated using Miedema's method [1998Wol]
	-62 050 ± 3000	Experimental, calorimetry [1992Jun]
	-70 740	<i>Ab initio</i> [1992Lin]
	-58 150	<i>Ab initio</i> [1999Man]
	-95 510	<i>Ab initio</i> [2002Gar]
	-51 126	Calculated – this work (MSL)
-51 057	Calculated - this work (SL)	

Boniface and Cornish [1996Bon1] confirmed Anlage's results for the high-Al end of the phase diagram. No evidence of the $L \rightarrow Ru_2Al_3 + RuAl_6$ eutectic reaction reported by Obrowski [1960Obr] was found and the presence of RuAl₂ in as-cast samples indicated stability at higher temperatures. The microstructures revealed that there was a peritectic cascade of reactions from the formation of Ru₂Al₃ to the formation of RuAl₆. A slight endothermic peak at 1733 K suggested the formation temperature for RuAl₂ [1996Bon2]. The Ru₂Al₃ phase was found to decompose at ~1223K.

Although Varich and Luykevich [1973Var] found a maximum solubility of Ru in (Al) of 3.23 at.% Ru by rapid solidification techniques, this solubility has not been reported at equilibrium conditions.

Thermodynamic data

The only reported experimental thermodynamic result for the Al-Ru system was determined by Jung and Kleppa [1992Jun] by dropping a mixed 1:1 powder mixture (atomic percent) of the elements into the calorimeter, which showed that RuAl (B2) has a high heat of formation, -124.1 kJ.mol⁻¹.

Miedema's method was used to estimate values for the heats of formation for the intermetallic phases [1998Wol], as no other data were available.

Several *ab initio* results have been reported for the enthalpy of formation of RuAl. However, the data are scattered, probably due to the different assumptions for defect formation in RuAl, which has been indicated to be vacancies [1987Fle] or anti-structure defects [1976Neu].

The thermodynamic data are listed in Table 2.

Thermodynamic modelling

Elements

The pure elements in their stable states at 298.15 K were chosen as the reference states for the system. Thermodynamic descriptions for the stable and metastable states of the pure elements were taken from the SGTE Database [1991Din].

The data [1991Din] are described as

$${}^{\circ}G_i^{\circ} - H_i^{SER} = A_i^{\circ} + B_i^{\circ}T + C_i^{\circ}T \ln T + D_i^{\circ}T^2 + E_i^{\circ}T^{-1} + F_i^{\circ}T^3 + I_i^{\circ}T^7 + J_i^{\circ}T^{-9} \quad (1)$$

where H_i^{SER} (in which 'SER' stands for standard element reference) are the enthalpy values for the elements in their stable forms at 10^5 Pa and 298.15K.

Disordered solution phases: liquid, fcc, hcp and bcc

The solution phases were modelled as substitutional solution phases according to the polynomial Redlich-Kister Model. The Gibbs energy for a solution phase ϕ is expressed as

$$G_m^\phi = x_{Al} {}^\circ G_{Al}^\phi + x_{Ru} {}^\circ G_{Ru}^\phi + RT(x_{Al} \ln x_{Al} + x_{Ru} \ln x_{Ru}) + {}^{xy}G_m^\phi \quad (2)$$

where ${}^\circ G_i^\phi$ is the Gibbs energy of the pure element i with the structure ϕ (Eq. 1) and x_i is the mole fraction of the phase. The excess Gibbs energy is given by

$${}^{xy}G_m^\phi = x_{Al} x_{Ru} \sum_{v=1}^n {}^v L_{Al,Ru}^\phi (x_{Al} - x_{Ru})^v \quad (3)$$

where ${}^v L_{Al,Ru}^\phi$ is the interaction parameter expressed as $a + b^*T$. The a and b parameters are calculated with the CALPHAD method.

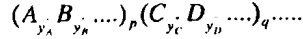
Intermetallic phases

There are five stable intermetallic phases in the Al-Ru binary system (Table 1). The intermetallic phases were modelled with the sublattice model, which is flexible enough to be applied to all of them. For Ru_4Al_{13} , $RuAl_2$, Ru_2Al_3 and $RuAl$ some defects have been introduced on the sublattices to model the solubility range, whereas $RuAl_6$ has been modelled without any solubility range. Furthermore, the $RuAl$ -B2 phase was also modelled with an alternative model, the modified sublattice model (MSL), which can describe both ordered B2 and disordered bcc-A2 with one single Gibbs energy function.

The Gibbs energy of mixing for a sublattice phase is given by

$$G_m = G^{ref} + G^{id} + G^{xs} \quad (4)$$

An intermetallic phase can schematically be described as follows [1981Sun]



where the species A, B... can be atoms or vacancies. p and q are the number of sites, y_i and y_j are the respective site fractions of species i and j in their respective sub-sublattices, designated by ' and ". When $p + q + \dots = 1$, the thermodynamic quantities are referred to as one mole of sites

The components of Eq. 4 are expanded as follows [1981Sun]:

$$G^{ref} = y_A' y_C'' G_{A:C}^\circ + y_A' y_D'' G_{A:D}^\circ + y_B' y_C'' G_{B:C}^\circ + y_B' y_D'' G_{B:D}^\circ \quad (5)$$

$$G^{id} = RT[p(y_A' \ln y_A' + y_B' \ln y_B') + q(y_C'' \ln y_C'' + y_D'' \ln y_D'')] \quad (6)$$

$$G^{xs} = y_A' y_B' [y_C'' L_{A,B:C} + y_D'' L_{A,B:D}] + y_C' y_D' [y_A'' L_{A:C,D} + y_B'' L_{B:C,D}] + y_A' y_B' y_C' y_D' L_{A,B,C,D} \quad (7)$$

$G_{A:B}^\circ$, $G_{A:D}^\circ$, $G_{B:C}^\circ$ and $G_{B:D}^\circ$ represent the Gibbs energy of formation of the stoichiometric compounds $A_p C_q$, $A_p D_q$, $B_p C_q$ and $B_p D_q$, which might be stable, metastable or even unstable in the system. y_i^s is the site fraction of element i on sublattice s . In Eq. 7, L is the interaction parameter and it is expressed as a function of temperature $L = a + b^*T$.

For the pure stoichiometric phase $RuAl_6$, the sublattice model reduces to

$$\Delta_f G^{RuAl_6}(T) = {}^\circ G^{RuAl_6}(T) - 6 {}^\circ G_{Al}^{fcc-A1}(T) - {}^\circ G_{Ru}^{hcp-A3}(T) = a + bT \quad (8)$$

The models for Ru_4Al_{13} , $RuAl_2$ and Ru_2Al_3 were based on models from previous assessments of similar phases in other systems. The Ru_4Al_{13} phase was modelled after the Fe_4Al_{13} phase in the COST507 database, as these phases have been reported to have similar structures [1965Eds]. Several crystal structures have been reported for $RuAl_2$ and Ru_2Al_3 . $RuAl_2$ was finally modelled after the $TiSi_2$ prototype suggested by Edshammer [1966Eds]. In the COST507 database the $TiSi_2$ phase has been described as stoichiometric but to allow for the solubility range, an interstitial sublattice for defects was added since no information is available for the defect structures in $RuAl_2$. This would be filled with vacancies at the ideal stoichiometry and both Al and Ru were allowed to enter this. To ensure compatibility with the Ni-Al system, Ru_2Al_3 was modelled after the reported Ni_2Al_3 prototype [1960Obr]. The model used in this assessment is based on the ordered model for Ni_2Al_3 by Ansara *et al.* [1997Ans].

The RuAl-B2 phase was expressed with the sublattice (SL) model with vacancies (Va) as the main defect, as found by Fleischer [1993Fle]. The model, (Al,Ru)(Al,Va), allows for the phase extension to the Al-rich side rather than the Ru-rich side of the B2 phase. This SL model is different to the more frequently used form, (Al,Ni)(Ni,Va) suggested by Ansara *et al.* [1997Ans], since RuAl decomposes eutectically on the Ru-rich side of the stoichiometric composition.

Applying the MSL formalism, the RuAl-B2 phase was described as suggested by Dupin and Ansara [1999Dup] as $(Al,Ru,Va)_{0.5}(Al,Ru,Va)_{0.5}(Va)_3$, the Gibbs energy is expressed as

$$G_m = G_m^{dis}(x_i) + \Delta G^{ord*}(y_i', y_i'') - \Delta G^{ord*}(x_i, x_i) \quad (9)$$

where $G_m^{dis}(x_i)$ is the molar Gibbs energy contribution from the disordered state (bcc-A2, modelled as a disordered solution phase) and $(\Delta G_m^{ord*}(y_i', y_i'') - \Delta G^{ord*}(x_i, x_i))$ is the ordering energy contribution, equal to zero in the disordered state. Though the value zero is now built in for the ordering energy, some constraints must still be introduced between the thermodynamic parameters of the function. Since the lattices are indistinguishable because of the crystallography, the following constraints in the model parameter must be met

$$G_{Al:Ru:Va}^{MSL,B2} = G_{Ru:Al:Va}^{MSL,B2} \quad (10)$$

$$L_{Al,Ru:Ru}^{MSL,B2} = L_{Ru:Al,Ru}^{MSL,B2} \quad (11)$$

$$L_{Al,Ru:Al}^{MSL,B2} = L_{Al:Al,Ru}^{MSL,B2} \quad (12)$$

The symmetrical MSL model description of RuAl-B2 introduces substitutional vacancies to the bcc-A2 disordered description. To ensure that the vacancy fraction in bcc-A2 is low at all temperatures, a high positive value of $120 \cdot T$ have been assigned to the interaction parameters ${}^0L_{Al,Va:Va}^{bcc-A2}$ and ${}^0L_{Ru,Va:Va}^{bcc-A2}$.

In the SL model description of RuAl-B2, the interaction parameters for the two unstable end-members $G_{Al:Va}^{B2}$ and $G_{Ru:Va}^{B2}$ were fixed to 60 000 J/mole of atoms. This ensures that the unstable B2 structure, where half the sites are empty, does not become stable, as this will represent a simple cubic bcc structure with no ordering.

Optimisation

Some of the high Al-content data of Obrowski [1960Obr] were found to disagree with that of other workers [1966Eds, 1968Eds, 1988Anl, 1996Bon1, 1996Bon2], and only data that were consistent were, therefore, used. The diagram of Boniface and Cornish [1996Bon2] was modified raising the formation temperatures of the $RuAl_2$ and Ru_2Al_3 phases to give a more correct liquidus slope [2000Pri]. The invariant reactions used in the optimisation are listed in Table 3. Higher weights were given to reliable and consistent data. The experimental enthalpy value [1992Jun] was also assigned a higher weight than the enthalpies estimated with the Miedema method.

The calculations were carried out using the PARROT module [1984Jan] in the Thermo-Calc software [1985Sun].

As a first step, to ensure that the slope of the liquidus was correct at the melting point of the fcc phase, only the liquid, Al-fcc and Ru-hcp phases were optimised. A metastable eutectic reaction was created for this purpose. Once an acceptable liquidus slope was calculated, the RuAl-B2 phase, using the MSL description, was included in the optimisation as this was the only phase with experimental thermodynamic data. This gave the liquid phase a reference point.

Since one Gibbs energy function describes both the B2 and bcc-A2 phases in the MSL model, the parameters were selected so that the entropy contribution of the ordered B2 phase was described by the disordered A2 phase. This required that the coefficients of the B2 and A2 phases had to be tested for interdependence. This was done by calculating the solubility range of the B2 phase as a function of the $L_{Al,Ru}^{bcc-A2}$ parameter. When the $L_{Al,Ru}^{bcc-A2}$ parameter is made more negative, the solubility range for B2 becomes wider, whereas when the $G_{Al,Ru}^{MSL,B2} = G_{Ru,Al}^{MSL,B2}$ parameter is made more negative, the solubility range becomes more narrow. Thus the parameters for the bcc-A2 phase were fixed to give a reasonable solubility range for the B2 phase and the RuAl-B2 parameters were used to adjust the solubility range.

The other phases, except for the Ru₂Al₃ phase, were introduced simultaneously. The liquid parameters were fixed while introducing the other phases into the calculation. The other phases were initially modelled to form by congruent melting. The peritectic invariant reactions were only introduced once the phases appeared in their correct composition ranges. Lastly, the Ru₂Al₃ phase was introduced in a similar fashion as the other phases.

All parameters were fixed and the MSL description of the B2 phase was changed to the sublattice format. Only these parameters were optimised during the second assessment.

Table 3
Invariant temperatures and compositions for the Al-Ru system.

Reaction (at. % Ru)	Reaction Temperature [K]	Reference
L ↔ (Al) + RuAl ₆ 0.1 0 14.8 0.1 0 14.3	923 922	[1988Anl] This work
L + Ru ₄ Al ₁₃ ↔ RuAl ₆ 1.5 25 14.3 2.5 25.4 14.3	996 997	[1988Anl] This work
L + RuAl ₂ ↔ Ru ₄ Al ₁₃ 17.6 33.6 25.8 18.1 31.1 26.7	1676 1725	[1988Anl] This work
L + Ru ₂ Al ₃ ↔ RuAl ₂ 26 36 33.4 23 36.1 33.9 23.4 39.6 31.8	1733 1873 1854	[1996Bon1] [2000Pri]* This work
L + RuAl ↔ Ru ₂ Al ₃ 33.5 42.5 42 27 42 41 35 45.9 39.9	1873 1973 1978	[1996Bon1] [2000Pri]* This work (MSL)
Ru ₂ Al ₃ ↔ RuAl + RuAl ₂ 395 46 35.9 40 49.5 32.9	1249 1243	[1996Bon1] This work (MSL)
L ↔ RuAl 50 50 50 50	2333 2342	[1960Obr] This work (MSL)
L ↔ RuAl + (Ru) 70 51 96 69.7 50.7 95.7	2193 2189	[1960Obr] This work (MSL)

*indicates the invariants which have been used in the optimisation

To ensure stability of the thermodynamic parameters of the intermetallic phases, a condition forcing the entropy of formation to be negative was set for all the intermetallic phases.

Results and discussion

Despite the lack of experimental thermodynamic data, the calculated phase diagram, as shown in Figure 1, is in good agreement with the later experimental phase diagrams [1988Anl, 1996Bon2]. The experimental and calculated invariant temperatures and compositions are given in Table 3 and the final set of thermodynamic parameters is listed in Appendix 1. The optimised diagram is compared to the experimental data in Figure 2.

The solubility range of the Ru_2Al_3 phase is too narrow [1996Bon1], but not enough experimental data were available to extend the solubility range in the calculations. However, this phase has been shown to have little extension into the ternary Al-Ru-X (where X = Ni, Cr, Ir, Pt) phase diagrams [1997Hor, 1999Hil, 2000Hoh, 2001Com1, 2002Com2, 2002Pri].

The B2 phase is also slightly narrower than in the experimental phase diagram, although it agrees with experimental findings of a larger solubility range towards the Al-rich side than the Ru-rich side. The MSL description gave a wider phase, and hence a better fit to the experimental RuAl-B2 phase.

The B2 phase remains ordered throughout its stability range, which agrees with the available X-ray data [1963Sch, 1966Eds and 1994Bon] and the disordered bcc-A2 phase is unstable in the Al-Ru system at any composition.

The composition ranges of the Ru_4Al_{13} and $RuAl_2$ phases are satisfactory, as both have been reported from stoichiometric compounds to having a 5 at. % composition range [1965Eds, 1988Anl, 1996Bon2]. The model description for Ru_4Al_{13} is acceptable.

In Figure 3, the phase diagram is represented as a function of the chemical potential instead of composition. It indicates that, though the optimisation was performed with limited thermodynamic data, the entropy contributions in the calculated model parameters do not have excessive entropy contributions. The enthalpy of formation for the B2 phase at 298 K for the SL and MSL optimisations are compared with reported enthalpies of formation in Figure 4.

Conclusions

A consistent set of thermodynamic parameters, taking into account the ordered RuAl-B2 phase, was obtained for the Al-Ru binary system, and the resulting phase diagram agrees with a compiled diagram from experimental data. The results for the SL and MSL descriptions of the B2 phase compare well. The MSL description gave a better fit to the width of the experimental RuAl-B2 phase.

The MSL description is the preferred model to describe the ordered B2 phase with, and the description should be as simple as possible.

Acknowledgements

The financial support of the Department of Trade and Industry, the Department of Arts, Culture, Science and Technology, now the Department of Science and Technology, and the Platinum Development Initiative are gratefully acknowledged.

References

- 1960Obr W. Obrowski, *Metallwissenschaft und Technik* (Berlin), **17** (1960) 108-112.
1963Sch O. Schwomma, H. Nowotny, A. Wittmann, *Monatshfte für Chemie*, **94** (1963) 924-926.
1965Eds L. Edshammar, *Acta Chem. Scand.*, **19** (1965) 2124-2130.
1966Eds L. Edshammar, *Acta Chem. Scand.*, **20** (1966) 427-431.
1968Eds L. Edshammar, *Acta Chem. Scand.*, **22** (1968) 2374-2375.

- 1973Var A.N. Varich and R.B. Luykevich, *Russ. Metall.*, **1** (1973) 73-75.
- 1976Neu J.P. Neumann, Y.A. Chang and C.M. Lee, *Acta Metall.*, **24** (1976) 593-604.
- 1979Wop W. Wopersnow and Ch.J. Raub, *Metallwissenschaft* (Berlin), **33** (1979) 736-740.
- 1981Sun B. Sundman and J. Agren, *J. Phys. Chem. Solids*, **42** (1981) 292-301.
- 1982Cha Z.A. Chaudhury, G.V.S. Sastry and C. Suryanarayana, *Z. Metallkde.*, **73** (1982) 201-206.
- 1984Jan B. Jansson, "Evaluation of Parameters in Thermodynamic Models Using Different Types of Experimental Data Simultaneously" Tricta-Mac-0234 (Royal Institute of Technology, Stockholm, Sweden, 1984).
- 1985Sun B. Sundman, B. Janson and J.-O. Andersson, *CALPHAD*, **9** (1985) 153-190.
- 1987Fle R.L. Fleischer, *J. Mat. Sci.*, **22** (1987) 2281-2288.
- 1988Anl S.M. Anlage, P. Nash, R. Ramachandran and R.B. Schwarz, *J. Less-Common Met.*, **163** (1988) 237-247.
- 1991Din A.T. Dinsdale, *CALPHAD*, **15** (1991) 319-425.
- 1991Fle R.L. Fleischer, R.D. Field and C.L. Briant, *Met. Trans. A*, **22A** (1991) 404-414.
- 1992Jun W-G. Jung and O.J. Kleppa, *Met Trans B*, **23B** (1992) 53-56.
- 1992Lin W. Lin, J. Xu and A.J. Freeman, *J. Mat. Res.*, **7** (1992) 592-604.
- 1993Fle R.L. Fleischer, *Acta Metall. Mater.*, **41** (1993) 863-869.
- 1994Bon T.D. Boniface, M.Sc. Dissertation, University of the Witwatersrand, Johannesburg, 1994.
- 1994Ste H. De V. Steyn, I.M. Wolff and R. Coetzee, Spark-Plug Electrodes Containing Intermetallic Phases and Spark-Plug Electrodes Containing Same, S.A. Patent 94/10180, 22 December 1994.
- 1995Smi E.G. Smith and C.I. Lang, *Scripta Met. et Mater.*, **33** (1995) 1225-1229.
- 1996Bon1 T.D. Boniface and L.A. Cornish, *J. Alloys and Compounds*, **233** (1996) 241-245.
- 1996Bon2 T.D. Boniface and L.A. Cornish, *J. Alloys and Compounds*, **233** (1996) 275-279.
- 1996Cor M.B. Cortie and T.D. Boniface, *J. Mat. Syn. and Proc.* **4** (1996) 413-428.
- 1996McE J.J. McEwan and T. Biggs, 13th International Corrosion Congress, Melbourne, Australia, 25-29 November 1996, ACA Inc., Victoria, Paper 096.
- 1996Wol I.M. Wolff, *Met and Mat. Trans. A* (1996) **27A**, 3688-3699.
- 1997Ans I. Ansara, N. Dupin, H.L. Lukas and B. Sundman, *J. Alloys and Compounds*, **247** (1997) 20-30.
- 1997Hor I.J. Horner, L.A. Cornish and M.J. Witcomb, *J. Alloys and Compounds*, **256** (1997) 221-227.
- 1997Wol I.M. Wolff, G. Sauthoff, L.A. Cornish, H. De V. Steyn and R. Coetzee, Structural Intermetallics 1997, Ed. M.V. Nathal *et al.*, The Minerals, Metals and Materials Society, Champion, PA, USA, September 1997, 815-823.
- 1998And S.A. Anderson and C.I. Lang, *Scripta Met. et Mater.*, **38** (1998) 493-497.
- 1998Wol I.M. Wolf, private communication, (1998).
- 1999Dup N. Dupin and I. Ansara, *Z. Metallkde.*, **90** (1999) 76-85.
- 1999Hil P.J. Hill, L.A. Cornish and M.J. Witcomb, *J. Alloys and Compounds*, **291** (1999) 130-144.
- 1999Man D. Nguyen-Manh and D.G. Pettifor, *Intermetallics*, **7** (1999) 1095-1106.
- 2000Hoh J. Hohls, L.A. Cornish, P. Ellis and M.J. Witcomb, *J. Alloys and Compounds*, **308** (2000) 205-215.
- 2000Pri S.N. Prins and L.A. Cornish, CALPHAD XIX Conference Proceedings, 2000.
- 2001Dav A.V. Davydov, U.R. Kattner, D. Josell, J.E. Blendell, R.M. Waterstrat, A.J. Shapiro and W.J. Boettinger, *Met. Mater. Trans A*, **32A** (2001) 2175-2186.
- 2001Com1 D.N. Compton, L.A. Cornish and M.J. Witcomb, *J. Alloys and Compounds*, **317-318** (2001) 372-378.
- 2001Com2 D.N. Compton, L.A. Cornish and M.J. Witcomb, Proceedings of the Microscopy Society of America, Microscopy and Analysis 2001, Vol. 7, Supplement 2, 1248-1249. Long Beach USA, 5-9 August 2001.
- 2002Gar P. Gargano, H. Mosca, G. Bozolla and R.D. Noebe, Submitted to *Scripta Met.*
- 2002Pri S.N. Prins and L.A. Cornish, Phases Formed on Solidification in the Al-Pt-Ru System, 15th International Congress on Electron Microscopy, Volume 1, 695-696, (Paper No. 619) 1-6 September 2002, Durban, South Africa.

Appendix I

Thermodynamic parameters for the Al-Ru system [J/mol]

The temperature range is $298.15 \leq T \leq 6000$, unless specified otherwise.
Parameters which are not listed are equal to zero.

Liquid Disordered Solution Phase: (Al,Ru)

$${}^0G_{Al}^{liq}(T) - H_{Al}^{0, fcc-A1}(298.15) : [1991Din]$$

$${}^0G_{Ru}^{liq}(T) - H_{Ru}^{0, hcp-A3}(298.15) : [1991Din]$$

$${}^0L_{(Al,Ru)}^{liq} = -73000 - 14T$$

$${}^1L_{(Al,Ru)}^{liq} = -56000$$

(Al) (fcc-A1) Disordered Solution Phase: (Al,Ru)(Va)

$${}^0G_{Al}^{fcc-A1}(T) - H_{Al}^{0, fcc-A1}(298.15) : [1991Din]$$

$${}^0G_{Ru}^{fcc-A1}(T) - H_{Ru}^{0, fcc-A1}(298.15) : [1991Din]$$

$${}^0L_{(Al,Ru)}^{fcc-A1} = -10000 - 10T$$

(Ru) (hcp-A3) Disordered Solution Phase: (Al, Ru)(Va)_{0.5}

$${}^0G_{Ru}^{hcp-A3}(T) - H_{Ru}^{0, hcp-A3}(298.15) : [1991Din]$$

$${}^0G_{Al}^{hcp-A3}(T) - H_{Al}^{0, hcp-A3}(298.15) : [1991Din]$$

$${}^0L_{(Al,Ru)}^{hcp-A3} = -105000 + 30T$$

bcc-A2 Disordered Solution Phase: (Al, Ru, Va)(Va)₃

$${}^0G_{Al}^{bcc-A2}(T) - H_{Al}^{0, bcc-A2}(298.15) : [1991Din]$$

$${}^0G_{Ru}^{bcc-A2}(T) - H_{Ru}^{0, bcc-A2}(298.15) : [1991Din]$$

$${}^0L_{Al,Ru:Vu}^{bcc-A2} = -176000 + 32 * T$$

$${}^0L_{Al,Va:Vu}^{bcc-A2} = 120 * T$$

$${}^0L_{Ru,Va:Vu}^{bcc-A2} = 120 * T$$

RuAl₆ Stoichiometric Phase: (Al)₆(Ru)

$${}^fG_{Al:Ru}^{RuAl_6} = 6{}^0G_{Al}^{fcc-A1} + {}^0G_{Ru}^{hcp-A3} - 156000 + 7 * T$$

Ru₄Al₁₃ Sublattice Solution Phase: (Al)_{0.6275}(Ru)_{0.235}(Al, Va)_{0.1375}

$${}^fG_{Al:Ru:Al}^{Ru_4Al_{13}} = 0.765{}^0G_{Al}^{fcc-A1} + 0.235{}^0G_{Ru}^{hcp-A3} - 35100 + 1.65 * T$$

$${}^fG_{Al:Ru:Va}^{Ru_4Al_{13}} = 0.6275{}^0G_{Al}^{fcc-A1} + 0.235{}^0G_{Ru}^{hcp-A3} - 35100 + 1.65 * T$$

RuAl₂ Sublattice Solution Phase: (Al)₂(Ru)(Al, Ru, Va)

$${}^fG_{Al:Ru:Va}^{RuAl_2} = 2{}^0G_{Al}^{fcc-A1} + {}^0G_{Ru}^{hcp-A3} - 136500 + 8 * T$$

$${}^fG_{Al:Ru:Al}^{RuAl_2} = 3{}^0G_{Al}^{fcc-A1} + {}^0G_{Ru}^{hcp-A3} - 138000 + 8 * T$$

$${}^fG_{Al:Ru:Ru}^{RuAl_2} = 2{}^0G_{Al}^{fcc-A1} + 2{}^0G_{Ru}^{hcp-A3} - 138000 + 8 * T$$

Ru₂Al₃Sublattice Solution Phase : (Al)₃(Al,Ru)₂(Ru,Va)

$$\begin{aligned} f G_{Al:Al:Va}^{Ru_2Al_3} &= 5^0 G_{Al}^{bcc-A2} \\ f G_{Al:Al:Ru}^{Ru_2Al_3} &= 5^0 G_{Al}^{bcc-A2} + {}^0 G_{Ru}^{bcc-A2} \\ f G_{Al:Ru:Va}^{Ru_2Al_3} &= 3^0 G_{Al}^{bcc-A2} + 2^0 G_{Ru}^{bcc-A2} - 312630 + 30.5 * T \\ f G_{Al:Ru:Ru}^{Ru_2Al_3} &= 3^0 G_{Al}^{bcc-A2} + 3^0 G_{Ru}^{bcc-A2} - 312630 + 30.5 * T \end{aligned}$$

RuAl (B2)

Sublattice Solution Phase: (Al,Ru)(Al,Va)

$$\begin{aligned} f G_{Al:Al}^{B2} &= 2^0 G_{Al}^{bcc-A2} \\ f G_{Al:Va}^{B2} &= {}^0 G_{Al}^{bcc-A2} + 60000 \\ f G_{Ru:Va}^{B2} &= {}^0 G_{Ru}^{bcc-A2} + 60000 \\ f G_{Ru:Al}^{B2} &= {}^0 G_{Ru}^{bcc-A2} + {}^0 G_{Al}^{bcc-A2} - 138700 + 15.5 * T \\ {}^0 L_{Al:Al:Va}^{B2} &= 49100 - 22.4 * T \\ {}^0 L_{Ru:Al:Va}^{B2} &= -51770 + 20 * T \\ {}^0 L_{Al:Ru:Al}^{B2} &= -30000 \\ {}^0 L_{Al:Ru:Va}^{B2} &= -30000 \end{aligned}$$

Modified Sublattice Model: (Al,Ru,Va)_{0.5}(Al,Ru,Va)_{0.5}(Va)₃

$$\begin{aligned} f G_{Al:Ru:Va}^{MSL,B2} &= f G_{Ru:Al:Va}^{MSL,B2} = -87600 \\ {}^0 L_{Al:Ru:Al:Va}^{MSL,B2} &= {}^0 L_{Al:Al:Ru:Va}^{MSL,B2} = -73000 \end{aligned}$$

THERMODYNAMIC ASSESSMENT OF Al-Ru SYSTEM

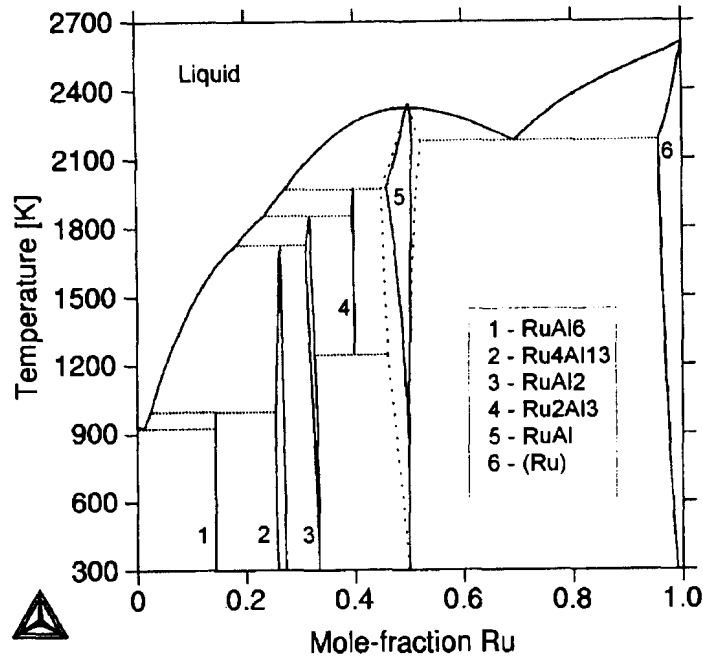


Figure 1. The calculated Al-Ru phase diagram showing B2 calculated using the SL (—) and MSL (---) models.

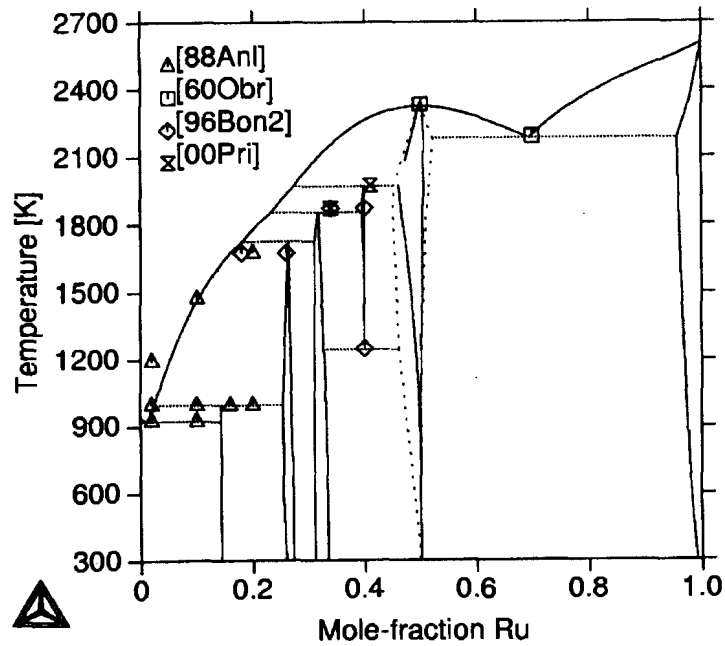


Figure 2. Comparison between the calculated phase diagram and experimental data.

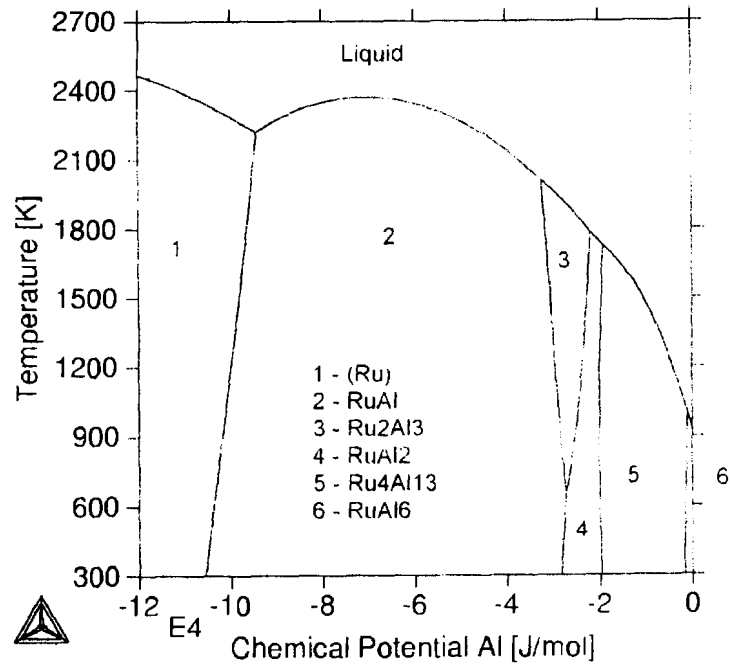


Figure 3. The phase diagram plotted as a function of chemical potential.

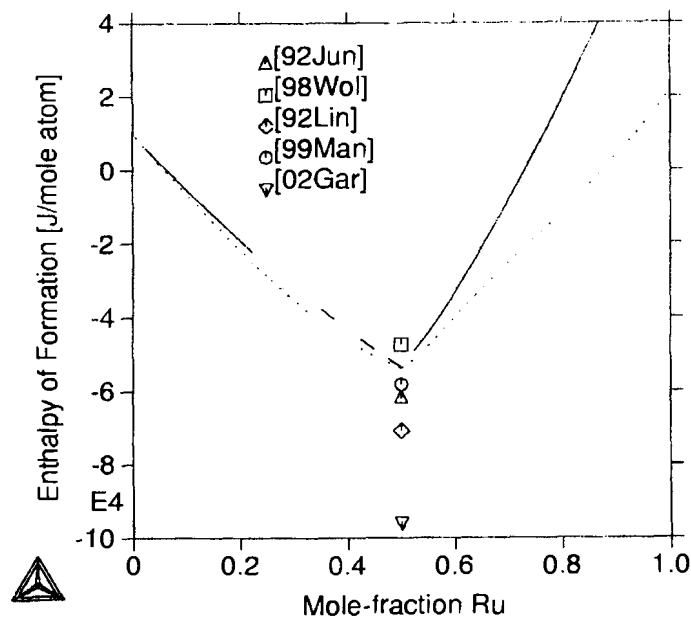


Figure 4. Comparison of the enthalpy of formation at 298 K for the SL (—) and MSL(---) RuAl-B2 descriptions with experimental [1992Jun], Miedema estimations [1998Wol] and *ab initio* [1992Lin, 1999Man, 2002Gar] values.



Case Study: Comparison of experimentally determined and CALPHAD-method predicted liquidus surfaces of the Al-Pt-Ru system.

SN Prins^{1,2} and LA Cornish³

¹CSIR-NML, PO Box 395, Pretoria, 0001

²Department of Materials Science and Metallurgical Engineering, University of Pretoria, Pretoria, 0001

³Physical Metallurgy Division, Mintek, Private Bag X3015, Randburg, 2125

The Al-Pt-Ru ternary system has been studied experimentally. Sixteen samples were prepared by arc-melting. The samples were studied in the as-cast condition. The microstructures and compositions were analysed using scanning electron microscopy and energy dispersive X-ray spectroscopy, and the phases were confirmed by XRD. The solidification sequences of the alloys were derived from the as-cast microstructures and a liquidus surface projection was proposed. [2003Pri3]

Using the CALPHAD method, the Al-Ru and the Al- Pt systems have been calculated with the Parrot module in the Thermo-Calc software [2003Pri1, 2003Pri2]. The Pt-Ru system was calculated by Spencer [1996Spe]. The ternary system was extrapolated from these calculated binary systems to predict the liquidus surface projection. No ternary interaction parameters have been introduced and calculated for these predictions.

The experimental and calculated liquidus surface projections are in good agreement. The major differences arise from the fact that two new ternary phases were found in the experimental study. Since an extrapolation is based on the Gibbs energy functions for already entered phases, the software could not predict these new phases.

The good agreement between the experimental and calculated liquidus surface projections proves that thermodynamic modeling is powerful technique in the development of new alloy systems.

References

- [1996Spe] P. Spencer, Noble Alloy Database, The Spencer Group (1996).
- [2003Pri1] S.N. Prins, L.A. Cornish, W.E. Stumpf and B. Sundman, accepted by *CALPHAD*.
- [2003Pri2] S.N. Prins, L.A. Cornish, W.E. Stumpf and B. Sundman, submitted to *CALPHAD*.
- [2003Pri3] S.N. Prins, L.A. Cornish, P.R.S.J. Boucher and W.E. Stumpf, submitted to *J. Alloys and Compounds*.

Thermodynamic Assessment of the Al-Pt-Ru System

S.N. Prins^{1,2}, B. Sundman³, L.A. Cornish⁴ and W.E. Stumpf²

¹CSIR-NML, PO Box 395, Pretoria, 0001, South Africa

²Department of Materials Science and Metallurgical Engineering, University of Pretoria, Pretoria, 0001, South Africa

³Division of Computational Thermodynamics, Department of Materials Science and Engineering, Royal Institute of Technology, SE-100 44 Stockholm, Sweden

⁴Physical Metallurgy Division, Mintek, Private Bag X3015, Randburg, 2125, South Africa

The Al-Pt-Ru system has been studied experimentally as part of a project to characterise and develop Pt-based superalloys [2002Pri2, 2003Pri2]. Pt-based superalloys have the potential to substitute Ni-based superalloys for high-temperature components in turbine engines, as they have a higher melting point and better corrosion resistance. The second part of the project involves building a thermodynamic database for Pt-based alloys.

The Al-Pt-Ru ternary system has been optimised using the CALPHAD method. The ordered RuAl-B2 phase contains ~20 at. % Pt [2003Pri2] and has been modelled with the modified sublattice model (MSL) where the disorder contribution is given by the bcc-A2 phase. The ordered Pt₃Al-L1₂ phase comprises ~3 at. % Ru [2001Big] and has been modelled with the four sublattice compound energy formalism (4SL CEF), which describes the Gibbs energy of the ordered L1₂ and disordered fcc-A1 phases with one energy function. The 4SL CEF allows for mixing on two sublattices, which gives a thermodynamic description for both short and long range order. The other Al-Pt and Al-Ru intermetallic phases were extrapolated from the optimised Al-Pt [2002Pri1] and Al-Ru [2003Pri1] binaries, without the addition of ternary parameters. Two new ternary phases have been found in the Al-Pt-Ru system, and these have been included in the assessment.

The calculations were done with the Thermo-Calc software. The calculated liquidus surface is in good agreement with the experimental results.

The financial assistance of the Department of Science and Technology and the PDI is gratefully acknowledged.

References

- [2001Big] T. Biggs, P.J. Hill, L.A. Cornish and M.J. Witcomb, *J. Phase Equilibria*, **22** (2001) 214-218.
- [2002Pri1] S.N. Prins, L.A. Cornish, W.E. Stumpf and B. Sundman, CALPHAD XXXI, 5-10 May 2002, Stockholm, Sweden
- [2002Pri2] S.N. Prins and L.A. Cornish, 15th International Conference on Electron Microscopy, Volume 1, 695-696 (Paper No. 619). 1-6 Sept 2002, Durban, South Africa.
- [2003Pri1] S.N. Prins, L.A. Cornish, W.E. Stumpf and B. Sundman, accepted by *CALPHAD*.
- [2003Pri2] S.N. Prins, L.A. Cornish and W.E. Stumpf, submitted to *J. Alloys and Compounds*.

Reassessment of the Aluminum-Platinum Binary System

S.N. Prins^{1,2}, L.A. Cornish³, W.E. Stumpf², B. Sundman⁴

¹CSIR-NML, PO Box 395, Pretoria, 0001, South Africa

²Department of Materials Science and Metallurgical Engineering, University of Pretoria, Pretoria, 0001, South Africa

⁴Division of Computational Thermodynamics, Department of Materials Science and Engineering, Royal Institute of Technology, SE-100 44 Stockholm, Sweden
Corresponding author's email: sprins@csir.co.za

Abstract. The Al-Pt binary system was assessed using the CALPHAD method. The four-sublattice compound energy formalism (4SL CEF) was used to describe the order-disorder relation between the Pt₃Al-L1₂ and (Pt)-fcc phases. The model successfully describes both the long-range and the short-range order observed in PtAl₃-L1₂ phase in this system. The optimization included the solution phases and the Pt₅Al₂₁, Pt₈Al₂₁, PtAl₂, Pt₃Al₅, PtAl, β , Pt₅Al₃, PtAl₂ and PtAl₃ intermetallic phases. The low temperature polymorph of the Pt₃Al phase has not been included in this optimisation.

Introduction

Platinum based alloys are studied as potential alloys to replaced Ni-based superalloys (NBSA) in ultra-high temperature applications. The Pt-Al system exhibits the same γ/γ' relation as Ni-Al, which is the basis of the NBSA. The Pt-Al system is of further interest as Pt is used increasingly in the coating technology to increase the heat and corrosion resistance of NBSA turbine blades, since Pt promotes the formation of stable alumina oxide layers.

The Al-Pt system has been assessed using the CALPHAD method by Wu and Jin [2000Wu], but their assessment did not consider the ordering in the system. They have also not included the PtAl₂ or β phases, due to a lack of experimental data. A study of Pt-Al-X ternaries (X=Ru, Ti, Cr, Ni) confirmed the presence of the Pt₂Al phase [2001Big]. Experimental work on Pt-Al-Ru ternary confirmed the presence of the β phase in the Al-Pt binary [2002Pri].

These experimental observations, and the need to include the ordering of the L1₂ phase, prompted the reassessment of the Al-Pt binary system.

Experimental

Phase diagram data

McAlister and Kahan [McA1986] have reported nine stable intermetallic phases in the Al-Pt system, with two of the phases showing high and low temperature polymorphs (Figure 1). Six metastable phases have also been reported [1986McA, 2001Lab].

Pt₅Al₂₁, Pt₈Al₂₁, Pt₂Al₃ and PtAl are stoichiometric phases, while PtAl₂, Pt₅Al₃, Pt₂Al and Pt₃Al exist with a solubility range. A β phase exists at high temperatures and decomposes below 1533 K. The phase data for the stable phases are listed in Table 1. The existence of the β phase were not confirmed beyond doubt, but rather

Table 1.

The crystal data for the stable elements and phases in the Al-Pt system.

Phase	Composition (at. % Pt)		Pearson symbol	Space Group	Strukturbericht	Prototype	Reference
(Al)	0		<i>cF4</i>	Fm3m	A1	Cu	
Pt ₅ Al ₂₁	19.2		<i>c**</i>				[1964Huc] [1980Pia]
Pt ₈ Al ₂₁	27		<i>tI116</i>	I4 _{1α}			[1968Eds] [1982Eil]
PtAl ₂	31.5	33.5	<i>cF12</i>	Fm3m	C1	CaF ₂	[1937Zin] [1963Fer] [1982Eil]
Pt ₂ Al ₃	40		<i>hP5</i>	P3m1			[1978Bah]
PtAl	50		<i>cP8</i>	P2 ₁₃	B20	FeSi	[1957Sch] [1963Fer] [1975Chs2]
	50.4	51.8					
β	52	56	<i>cP2</i>	Pm3m	B2	CsCl	[1975Cha] [1978Bha]
Pt ₅ Al ₃	61.5	63	<i>oP16</i>	Pbam		Ge ₃ Rh ₅	[1964Huc]
Pt ₂ Al	66	67	<i>oP12</i>	Pnma	C23	PbCl ₂	[1975Cha1]
Pt ₂ Al (LT)	66	67	<i>oP24</i>	Pmma		GaPt ₂ (LT)	[1976Cha]
Pt ₃ Al	67.3	77.7	<i>cP4</i>	Pm3m	L1 ₂	AuCu ₃	[1962Bro] [1964Huc] [1963Mag]
Pt ₃ Al (LT)	73.5	100	<i>tP16</i>	P4/mbm	DO _c '	GaPt ₃ (LT)	[1975Cha1]
(Pt)	83.8	100	<i>cF4</i>	Fm3m	A1	Cu	

deduced from thermal arrest data. However, recent experimental results in the Al-Pt-Ru ternary system confirmed the presence of the β phase in the Al-Pt system.

There are discrepancies on the L12-DOc' transformation temperature of the Pt₃Al phase.

Thermochemical data

Ferro [1968] determined the enthalpies of formation by solution calorimetry. Worrel [1981] used an electrochemical cell technique to determine the Gibbs energy of mixing. Enthalpies of formation have been predicted using Miedema's method [1989deB]. The enthalpies of formation for PtAl and Pt₃Al have been predicted using *ab initio* methods [2002Ngo]. The thermodynamic data are listed in Table 2.

Thermodynamic Models

The pure elements

The pure elements in their stable states at 298.15K were chosen as the reference states for the system (standard element reference SER). The Gibbs energies as a function of temperature for the stable elements were taken from the SGTE database [1991Din].

The liquid phase

The liquid phase was modeled as a substitutional solution phase according to the polynomial Redlich-Kister model. The Gibbs energy for a solution phase is given by

$$G_m = \sum_i x_i^0 G_i + RT \sum_i x_i \ln(x_i) + {}^E G_m \quad (1)$$

Experimental, predicted and calculated enthalpies of formation for the stable phases in the Al-Pt system.

Phase	ΔH_f [J/mole atoms]	Method	Reference
Pt ₅ Al ₂₁	-57 320	Solute solvent drop calorimetry	[1968Fer]
	-56 827	Calculated	This work
Pt ₈ Al ₂₁	-71 130	Solute solvent drop calorimetry	[1968Fer]
	-81 751	Calculated	This work
PtAl ₂	-84 000	Solute solvent drop calorimetry	[1968Fer]
	-87 325	Calculated	This work
Pt ₂ Al ₃	-94 980	Solute solvent drop calorimetry	[1968Fer]
	-79 000	Miedema semi-empirical method	[1989deB]
	-96 500	Direct Synthesis Calorimetry	[1993Mes]
	-89 839	Calculated	This work
PtAl	-100 420	Solute solvent drop calorimetry	[1968Fer]
	-100 000	Direct Synthesis Calorimetry	[1991Jun]
	-82 000	Miedema semi-empirical method	[1989deB]
	-67 440	<i>Ab initio</i>	[2002Ngo]
	-94 025	Calculated	This work
β	-91 300*	Calorimetry	[1968Fer]
	-92 913	Calculated	This work
Pt ₅ Al ₃	-90 730	Miedema semi-empirical method	[1989deB]
	-87 213	Calculated	This work
Pt ₂ Al	-88 280	Miedema semi-empirical method	[1989deB]
	-85 278	Calculated	This work
Pt ₃ Al	-69 870	Solution Calorimetry	[1968Fer]
	-63 600	Direct Synthesis Calorimetry	[1993Mes]
	-50 990	Miedema semi-empirical method	[1989deB]
	-76 000**	Electrochemical	[1981Wor]
	-74 380	<i>Ab initio</i>	[2002Ngo]
	-51 668	Calculated	This work

* estimated from the curve fitted to the enthalpies of formation experimentally determined by Ferro *et. al.* [1986Fer].

** deduced from $G = -76\,460 + 7.48 \cdot T$ [1981Wor]

where x_i is the mole fraction of the element i and 0G_i is the Gibbs energy of the element i in the liquid phase relative to its reference state. The second term is the ideal entropy of mixing, while the third term is excess Gibbs energy, which can be expressed as

$$G_m = x_{Al} x_{Pt} L_{AlPt} \quad (2)$$

L_{AlPt} is the so-called interaction parameter and the composition dependence is expressed as a Redlich-Kister polynomial

$$L_{AlPt} = \sum_{\nu=0} (x_{Al} - x_{Pt})^{\nu} L_{AlPt}^{\nu} \quad (3)$$

where L_{AlPt}^{ν} are obtained from the optimization and may or may not be temperature dependent.

The fcc phases

The four-sublattice compound energy formalism (4SL CEF) [1998Sun] was used to model the fcc phases. The model is based on the four sublattices describing the four corners of a tetrahedron in an fcc unit cell, with all the nearest neighbours of an atom are on a different sublattice. The model can describe the fcc-A1, L1₂ and L1₀ phases, depending of the positions of the atoms on the tetrahedron. Not all the structures need to be stable in the alloy system [2001Kus].

The 4SL CEF describes the Gibbs energy of the A1, L1₂ and L1₀ structures with one function, which includes an ordered and a disordered energy contribution

$$G_m = G_m^{dis}(x_i) + \Delta G_m^{ord}(y_i^s)$$

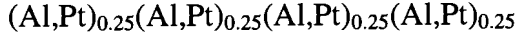
where G_m is the molar Gibbs energy of the phase, G_m^{4sl} is the molar ordering energy. The ordering energy, expressed as

$$\Delta G_m^{ord} = G_m^{4sl}(y_i^s) - G_m^{4sl}(y_i^s = x_i)$$

is zero when the phase is disordered.

The Pt₃Al phase is an ordered structure (L₁₂) of the disordered fcc phase (A1), the latter in which the atoms are randomly distributed on the lattice. The associated other two ordered phases in this system, PtAl₃ (L₁₂) and PtAl (L₁₀), are unstable. The Pt₃Al phase shows both long-range and short-range order (lro and sro respectively).

According to the 4SL CEF, the following model can be used to describe the fcc phases in this system



Physically, the sublattices describe the four corners of a tetrahedron in a unit cell. Due to the crystallographic symmetry of the unit cell, the sublattices must be identical, implying that all nearest neighbours of an atom is on a different sublattice. With 0.25 sites for each sublattice, the requirement of 1 mole of atoms in the model is met. For the disordered structure (fcc_A1), all the sublattices are equivalent, which reduces this model to an equivalent (Al,Pt) substitutional model. When two sublattices have the same fractions, but different to the other two, which also have the same fractions, the model describes the PtAl phase (L₁₀ structure). When three sublattices have the same fractions and the fourth sublattice a different fraction, the above model describes the Al₃Pt and Pt₃Al phases (L₁₂ structure).

From the model, the following relationships hold

$$\sum_i y_i^s = 1 \quad (4)$$

$$x_i = 0.25 \sum_s y_i^s \quad (5)$$

with y_i^s the site fraction of each element i on each sublattice s and x_i the molar fraction of i .

The Gibbs energy expression describing the fcc phases of the 4SL CEF is

$$G_m = \sum_i \sum_j \sum_k \sum_l y_i^{(1)} y_j^{(2)} y_k^{(3)} y_l^{(4)} {}^o G_{ijkl} + 0.25 RT \sum_i y_i^{(s)} \ln(y_i^{(s)}) + {}^E G_m \quad (6)$$

where the first term describes the mechanical mixing of all the stoichiometric compounds defined by the model, with ${}^o G_{ijkl}$ the Gibbs energy of the stoichiometric compound $ijkl$ relative to the pure elements in the fcc state. The second term is the random mixing of all elements in each sublattice. The excess term ${}^E G_m$ includes the first two interactions according to the CEF and is defined as

$${}^E G_m = \sum_{i_1} \sum_{i_2} \sum_j \sum_k \sum_l y_{i_1}^{(r)} y_{i_2}^{(r)} y_j^{(s)} y_k^{(t)} y_l^{(u)} L_{i_1, i_2; j, k, l} + \dots + \sum_{i_1} \sum_{i_2} \sum_{j_1} \sum_{j_2} \sum_k \sum_l y_{i_1}^{(r)} y_{i_2}^{(r)} y_{j_1}^{(s)} y_{j_2}^{(s)} y_k^{(t)} y_l^{(u)} L_{i_1, i_2; j_1, j_2; k, l} + \dots \quad (7)$$

The comma "," separate interacting constituents on the same sublattice, with ":" separating the sublattices. The first summation describes the regular interaction parameters, $L_{i_1, i_2; j, k, l}$, which represents interactions between i_1 and i_2 on sublattice r , when the other sublattices, s , u and t , are occupied by constituents j , k and l . This is the next nearest neighbour interactions.

The second summation is called the reciprocal parameters. They represent interaction on two sublattices, r and s , simultaneously while the other two sublattices, t and u , are occupied by constituents k and l respectively. This describes the nearest neighbour interactions, thus introduces a component to describe sro in the model.

As all the sublattices are equivalent, symmetry relations were applied to reduce the number of independent parameters.

The intermetallic phases

The intermetallic compounds $Pt_{21}Al_5$, $Pt_{21}Al_8$, $PtAl_2$, Pt_2Al_3 , $PtAl$, Pt_5Al_3 and Pt_2Al were treated as stoichiometric compounds. The β phase was assumed to be stoichiometric, since very little experimental information was available. The β phase was treated as $Pt_{52}Al_{48}$.

The Gibbs energy per formula unit Pt_mAl_n is expressed as

$${}^oG_m^{Pt_mAl_n} = m {}^oG_{Pt}^{fcc-Al} + n {}^oG_{Al}^{fcc-Al} + \Delta G_f^{Pt_mAl_n} \quad (8)$$

where $\Delta G_f^{Pt_mAl_n}$ is the Gibbs energy of formation per mole of formula unit Pt_mAl_n and is given by the expression

$$\Delta G_f^{Pt_mAl_n} = a + b * T \quad (9)$$

The parameters a and b were evaluated in the present work.

Optimisation

The optimization was carried out with the Parrot module [1984Jan] of the Thermo-Calc software [1985Sun]. With this module the Gibbs energy functions can be derived by fitting experimental data through a least square method. Different types of experimental data can be used and the weights can be assigned to the data based on the uncertainties associated with the original data.

In the initial optimization, the values from Wu and Jin [2000Wu] were used to calculate a basic set of data. The Pt_3Al phase was excluded. Once their phase diagram was reproduced, the fcc description was modified to the 4SL CEF formal. The ordered phases were introduced using the same Gibbs energy function as the disordered fcc. The results from Kuskofsky et al [2002Kus] were used to estimate starting values for the parameters. Conditions were set to ensure that $PtAl_3$ and Pt_2Al_2 , which are experimentally unstable in this system, were unstable in the thermodynamic description as well.

Both the Pt_2Al and β phases were introduced as a stoichiometric compounds. For the β phase, an initial metastable congruent melting formation was set. This could not be done for the Pt_2Al phase, since it forms in the solid state. The metastable congruent melting for the β phase was removed and the peritectic formation included. The decomposition of the β phase was introduced in the final set of optimisations.

Results and Discussion

A self-consistent thermodynamic description has been obtained for the Al-Pt system. The 4SL CEF has been successfully applied in describing the order disorder transformation between the fcc and Pt_3Al . The calculated model parameters for the Al-Pt system are listed in Appendix I.

The calculated phase diagram is shown in Figure 1 and compared to the experimental data in Figure 2. The invariant temperatures and compositions are compared in Table 3. The calculated enthalpies of formation are compared to experimental, empirical and *ab initio* values in Table 2. The calculated enthalpy of formation for the Pt_3Al phase is compared with reported enthalpies of formation in Figure 4.

The calculated phase diagram is in good agreement with the experimental phase diagram of McAlister and Kahan [1986McA].

The calculated temperatures for the invariant reactions and compositions for the intermetallic phases are in good agreement with the experimental temperatures. The calculated eutectic temperature for the $L \rightarrow \beta + Pt_5Al_3$ is ~ 50 degrees too high. This is not a well-defined area in the phase diagram from McAlister [1986McA], and could also be due to the estimation of the enthalpy of formation for the β phase.

The congruent formation of the Pt_3Al phase and $L \rightarrow Pt_3Al + (Pt)$ eutectic reactions are not in very good agreement with the experimental diagram. The 4SL CEF model is of such that the formation composition of Pt_3Al is at 75 at. %, while it has been found to form congruently at 73.2 at. %. This off-stoichiometry formation cannot be reached with the model, and had an influence on the temperature as well as the enthalpy of formation



for the Pt₃Al phase. The symmetry of the β phase is not possible to move the eutectic reaction to a lower Pt-contents.

Although the phase area of the (Pt) solid solution is too narrow, especially at lower temperatures, the phase area for the Pt₃Al phase is acceptable. The Pt₃Al phase is ordered throughout its phase area and the unstable PtAl₃ and Pt₂Al₂ phases, which are introduced through the 4SL CEF, are not stable at any composition or temperature in the phase diagram, which is correct.

The calculated solubility of Pt in (Al) is too high.

Table 3.
Experimental and calculated invariant compositions and temperatures for the Al-Pt system.


Reaction and Compositions (at. % Pt)	Reaction Temperature [K]	Reference
L ↔ Pt ₃ Al + (Pt) 79.5 76.4 85.7 83.7 99	1780 1748	[1986McA] This work
PtAl + L ↔ β 50.0 53.7 51.5 50.0 52.0	1783 1783	[1986McA] This work
L ↔ Pt ₂ Al ₃ + PtAl 44.47 40.0 50.0 46.7 40.0 50	1741 1773	[1986McA] This work
L + Pt ₃ Al ↔ Pt ₅ Al ₃ 62.3 67.3 62.5 62.5	1738 1720	[1986McA] This work
Pt ₅ Al ₃ + Pt ₃ Al ↔ Pt ₂ Al 62.7 67.0 67.5 62.5	1703 1701	[1986McA] This work
L + Pt ₂ Al ₃ ↔ PtAl ₂ 31.8 40.0 33.3 40.0 33.3	1679 1671	[1986McA] This work
L ↔ β + Pt ₅ Al ₃ 55.7 57.9 66.5 52.0 62.5	1670 1724	[1986McA] This work
β ↔ PtAl + Pt ₅ Al ₃ 54.2 50.0 61.5 52.0 50.0 62.5	1533 1533	[1986McA] This work
L + PtAl ₂ ↔ Pt ₈ Al ₂₁ 18.8 32.6 27.5 33.3 27.5	1400 1404	[1986McA] This work
L + Pt ₈ Al ₂₁ ↔ Pt ₅ Al ₂₁ 3.1 27.5 19.2 27.5 19.2	1079 1097	[1986McA] This work
L ↔ (Al) + Pt ₅ Al ₂₁ 0.4 0.0 19.2 19.2	930 910	[1986McA] This work
L ↔ Pt ₃ Al 73.2 73.2 75.3 75.3	1829 1877	[1986McA] This work
L ↔ PtAl 50.0 50.0 50.0 50.0	1827 1827	[1986McA] This work
L ↔ Pt ₂ Al ₃ 40.0 40.0 40.0 40.0	1800 1800	[1986McA] This work

A consistent set of thermodynamic parameters, taking into account the order-disorder relation between Pt₃Al-L1₂ and (Pt)-fcc, was obtained for the Al-Pt system. The 4SL CEF successfully described the fcc phases. The calculated phase diagram is in good agreement with the experimental phase diagram.

References

1937Zin	E. Zintl, A. Harder and W. Hauke, <i>Z. Phys. Chem B35</i> (1937) 354-362.
1956Sch	K. Schubert, W. Burkhardt, P. Esslinger, E. Gunzel, H. Meissner, W. Schutt, J. Wegst and M. Wilkens, <i>Naturwissenschaften</i> , 43 (1956) 248-249
1962Bro	W. Bronger and W. Klemm, <i>Z. Anorg. Allg. Chem.</i> , 319 (1962) 58.
1963Fer	R. Ferro and R. Capelli, <i>Rend. Acad. Naz. Lincei.</i> , 34 (1963) 659
1963Mag	A. Magneli, L. Edshammer and T. Dagerhamm, Final Technical Report No. 1 under Contract No DA-91-591-EUC-2734 (AD 426927) (1963) 44-50.
1963Sch	O. Schwomma, H. Nowotny, A. Wittmann, <i>Monatshefte für Chemie</i> , 94 (1963) 924-926.
1964Com	J. J. Comer, <i>Acta Cryst.</i> , 17 (1964) 444-445
1964Huc	R. Huch and W. Klemm, <i>Z. Anorg. Allg. Chem.</i> , 329 (1964) 123-135.
1968Eds	L. Edshamar, <i>Acta Chem. Scand.</i> , 22 (1968) 2374-2375.
1968Fer	R. Ferro, R. Capelli, A. Borsese and G. Centineo, <i>Atti Accad. Naz. Lincei, Classe Sci. Fis. Mat. Nat.</i> , 45 (1968) 54-59.
1970Dar	A. S. Darling, G. L. Selman and R. Rushforth, <i>Platinum Met. Rev.</i> , 14 (1970) 124-130.
1975Cha1	T. Chattopadhyay and K. Schubert, <i>J. Less-Common Met.</i> , 41 (1975) 19-32.
1975Cha2	D. Chatterij, R.C. Decries and J.F. Fleisher, <i>J. Less-Common Met.</i> , 42 (1975) 187-198.
1976Cha	T. Chattopadhyay and K. Schubert, <i>J. Less-Common Met.</i> , 45 (1976) 79-83.
1976Gue	P. Guex and P. Feschotte, <i>J. Less-Common Metals</i> , 46 (1976) 101-116.
1978Bah	S. Bahn and H. Kudielka, <i>Z. Metallkde.</i> , 69 (1978) 333-334.
1978Sch	K. Schubert, <i>Z. Krist.</i> , 70 (1978) 3113-321.
1979Cha	T. Chattopadhyay and P. Mamachandrarao, <i>Mater. Sci. Eng.</i> , 38 (1979) 7-17.
1979Sch	H.J. Schaller, <i>Z. Metallkde</i> , 70 (1979) 318
1980Pia	G. Piatti and G. Pellegrini, <i>J. Mater. Sci.</i> , 15 (1980) 2403-2408.
1981Wor	W. L. Worrel and T. A. Ramanarayanan, <i>Chemical Metallurgy - A Tribute to Carl Wagner</i> (TMS-AIME, Warrendale, PA, 1980) 69-74.
1982Cha	Z.A. Chaudhury, G.V.S. Sastry and C. Suryanarayana, <i>Z. Metallkde</i> , 73 (1982) 201-206.
1982Ell	M. Ellner, U. Kattner and B. Predel, <i>J. Less-Common Metal.</i> , 87 (1982) 305-325.
1985Lee	B.J. Lee and F. Sommer, <i>Z. Metallkde</i> , 76 (1985) 750-754.
1985Vil	P. Villars and L.D. Calvert, 'Pearson's handbook of crystallographic data for intermetallic phases' Vol 2, ASM (1985).
1986McA	A.J. McAlister and D.J. Kahan, <i>Bull. Alloy Phase Diagr.</i> , 7 (1986) 47-51.
1987Oya	Y. Oya, Y. Mishima and T. Suzuki, <i>Z. Metallkde</i> , 78 (1987) 485-490.
1988Ans	I. Ansara, B. Sundman and B. Williams, <i>Acta Met.</i> 36 (1988) 977-989.
1988deB	F.R. De Boer, R. Boom, W.C.M. Maartens, A.R. Miedema and A.K. Niessen, <i>Cohesion in Metals: Cohesion and Structure Vol 1.</i> (Elsevier Science, Amsterdam, 1988).
1990Mas	T.B. Massalksi, <i>Binary Alloy Phase Diagrams</i> (ASM International, 1990).
1991Jun	W. G. Jung and O.J. Kleppa and L. Topor, <i>J. Alloys and Compounds.</i> , 176 (1991) 309-318.
1992Jun	W-G. Jung and O.J. Kleppa, <i>Metallurgical Transactions B</i> , 23B (1992) 53-56.
1992Lin	W. Lin, Jian-hua Xu and A.J. Freeman, <i>J. Mater. Res.</i> 7 (1992) 592-604.
1993Mes	S.V. Meschel and O.J. Kleppa, <i>J. Alloys and Compounds</i> , 197 (1993) 75-81.
1997Ans	I. Ansara, N. Dupin, H. L. Lukas and B. Sundman, <i>J Alloys and Compounds</i> , 247 (1997) pp 20-30.
1997Bro	W. Bronger, K. Wrzesien and P. Muller, <i>Solid State Ionics</i> , 101-103 (1997) 633-640.
1998Sun	B. Sundman, S.G. Fries and W.A. Oates, <i>CALPHAD</i> , 22 (1998) 335-354.
2000Com	D.N. Compton, L.A. Cornish and M.J. Witcomb, <i>Proceedings MSSA, Grahamstown</i> , 30 (2000) 14
2000Fai	G.B. Fairbank, C.J. Humphreys, A. Kelly and C.N. Jones, <i>Intermetallics</i> , 8 (2000) 1091-1100.



2000Hay	J. Haynes, K.L. More, B.  and Y. Zhang, <i>High Temperature Corrosion and Protection of Materials</i> 5 (2000).
2000Wu	K. Wu and Z. Jin, <i>Journal of Phase Equilibria</i> , 21 (2000) 221-226.
2001Big	T. Biggs, PhD Thesis, University of Witwatersrand, Johannesburg, South Africa, 2001
2001Lab	J.L. Labar, A. Kovacs and P.B. Barna, <i>J. Applied Physics</i> , 90 (2001) 6545-6547.
2001Li	X. Li, A. P. Miodownik, N. Saunders, <i>J. Phase Equilibria</i> , 22 , (2001), 247
2002Kus1	A. Kuskoffsky, N. Dupin and B. Sundman, <i>CALPHAD</i> , 25 (2002) 549-565.
2002Kus2	A. Kuskoffsky, Ph. D Thesis, Royal Institute of Technology, Sweden, Stockholm, 2002.
2002Ngo	P. Ngoepe, private communication, 2002.
2002Pri	S.N. Prins, L.A. Cornish, P.R.S.J. Boucher and W.E. Stumpf, submitted to <i>J. Alloys and Compounds</i> .

Appendix I

Thermodynamic parameters for the Al-Pt system [J/mol atoms]

The temperature range is $298.15 \leq T \leq 6000$, unless specified otherwise.
Parameters which are not listed are equal to zero.

Liquid	Disordered Solution Phase: (Al,Pt) ${}^0 G_{Al}^{liq}(T) - H_{Al}^{0, fcc-Al}(298.15) : [1991Din]$ ${}^0 G_{Pt}^{liq}(T) - H_{Pt}^{0, hcp-A3}(298.15) : [1991Din]$ ${}^0 L_{(Al,Pt)}^{Liq} = -352540 + 114.8 * T$ ${}^1 L_{(Al,Pt)}^{Liq} = 68570 - 53 * T$
fcc-A1	Disordered Solution Phase: (Al,Pt)(Va) ${}^0 G_{Al}^{fcc-A1}(T) - H_{Al}^{0, fcc-A1}(298.15) : [1991Din]$ ${}^0 G_{Pt}^{fcc-A1}(T) - H_{Pt}^{0, fcc-A1}(298.15) : [1991Din]$ ${}^0 L_{(Al,Pt)}^{fcc-A1} = ULDO + DGO + 1.5 * USRO$ ${}^1 L_{(Al,Pt)}^{fcc-A1} = ULD1 + DG1$ ${}^2 L_{(Al,Pt)}^{fcc-A1} = ULD2 + DG2 - 1.5 * USRO$
Pt₅Al₂₁	Stoichiometric Phase: (Al) _{0.8077} (Pt) _{0.1923} ${}^f G_{Al:Pt}^{Pt_5Al_{21}} = 0.8077 {}^0 G_{Al}^{fcc-A1} + 0.1923 {}^0 G_{Pt}^{fcc-A1} - 56870 + 14.8 * T$
Pt₈Al₂₁	Stoichiometric Phase: (Al) _{0.7242} (Pt) _{0.2759} ${}^f G_{Al:Pt}^{Pt_8Al_{21}} = 0.7242 {}^0 G_{Al}^{fcc-A1} + 0.2759 {}^0 G_{Pt}^{fcc-A1} - 81805 + 23.2 * T$
PtAl₂	Stoichiometric Phase: (Al) _{0.666} (Pt) _{0.334} ${}^f G_{Al:Pt}^{PtAl_2} = 0.666 {}^0 G_{Al}^{fcc-A1} + 0.334 {}^0 G_{Pt}^{fcc-A1} - 87371 + 22.1 * T$
Pt₂Al₃	Stoichiometric Phase: (Al) _{0.6} (Pt) _{0.4} ${}^f G_{Al:Pt}^{Pt_2Al_3} = 0.6 {}^0 G_{Al}^{fcc-A1} + 0.4 {}^0 G_{Pt}^{fcc-A1} - 89885 + 21.5 * T$
PtAl	Stoichiometric Phase: (Al) _{0.5} (Pt) _{0.5} ${}^f G_{Al:Pt}^{PtAl} = 0.5 {}^0 G_{Al}^{fcc-A1} + 0.5 {}^0 G_{Pt}^{fcc-A1} - 94071 + 24.1 * T$
Beta	Stoichiometric Phase: (Al) _{0.48} (Pt) _{0.52} ${}^f G_{Al:Pt}^{Beta} = 0.48 {}^0 G_{Al}^{fcc-A1} + 0.52 {}^0 G_{Pt}^{fcc-A1} - 92959 + 24.1 * T$
Pt₅Al₃	Stoichiometric Phase: (Al) _{0.375} (Pt) _{0.625} ${}^f G_{Al:Pt}^{Pt_5Al_3} = 0.375 {}^0 G_{Al}^{fcc-A1} + 0.625 {}^0 G_{Pt}^{fcc-A1} - 87260 + 24 * T$
Pt₂Al	Stoichiometric Phase: (Al) _{0.334} (Pt) _{0.666} ${}^f G_{Al:Pt}^{Pt_2Al} = 0.334 {}^0 G_{Al}^{fcc-A1} + 0.666 {}^0 G_{Pt}^{fcc-A1} - 85325 + 24.9 * T$
L1₂ (Pt₃Al)	4SL-CEF: (Al,Pt) _{0.25} (Al,Pt) _{0.25} (Al,Pt) _{0.25} (Al,Pt) _{0.25} ${}^f G_{Al:Al:Al:Pt}^{L1_2} = {}^f G_{Al:Al:Pt:Al}^{L1_2} = {}^f G_{Al:Pt:Al:Al}^{L1_2} = {}^f G_{Pt:Al:Al:Al}^{L1_2} = UPTAL3$



$${}^f G_{Al:Al:Pt:Pt}^{L1_2} = {}^f G_{Al:Al:Pt:Pt}^{L1_2} = UPTAL$$

$${}^f G_{Al:Pt:Pt:Pt}^{L1_2} = {}^f G_{Pt:Al:Pt:Pt}^{L1_2} = {}^f G_{Pt:Pt:Al:Pt}^{L1_2} = {}^f G_{Pt:Pt:Pt:Al}^{L1_2} = UPT3AL$$

$$L_{Al, Pt:*,*}^{L1_2} = L_{*, Al, Pt:*,*}^{L1_2} = L_{*,*, Al, Pt:*}^{L1_2} = L_{*,*,*, Al, Pt}^{L1_2} = ULO$$

$$L_{Al, Pt:Al, Pt:*,*}^{L1_2} = L_{*, Al, Pt:Al, Pt:*}^{L1_2} = L_{*,*, Al, Pt:Al, Pt}^{L1_2} = L_{*, Al, Pt:*, Al, Pt}^{L1_2} = L_{Al, Pt:*, Al, Pt:*}^{L1_2} = USRO$$

UAB	= -13595 + 8.3 * T
UPTAL	= 3 * UAB - 3913
UPTAL3	= 4 * UAB
UPT3AL	= 3 * UAB
USRO	= UAB
ULO	= 1412.8 + 5.7 * T
ULD0	= -110531 - 22.9 * T
ULD1	= -25094
ULD2	= 21475
DGO	= UPTAL3 + 1.5 * UPTAL + UPT3AL
DG1	= 2 * UPTAL3 - 2 * UPT3AL
DG2	= UPTAL3 - 1.5 * UPTAL + UPT3AL

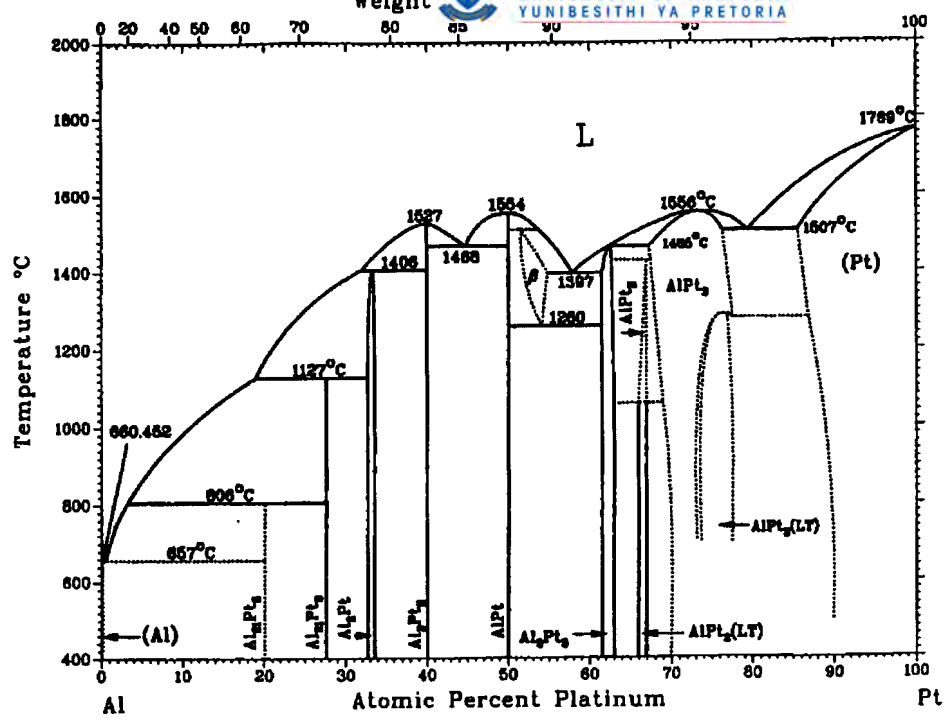


Figure 1. The Al-Pt phase diagram [1990Mas]

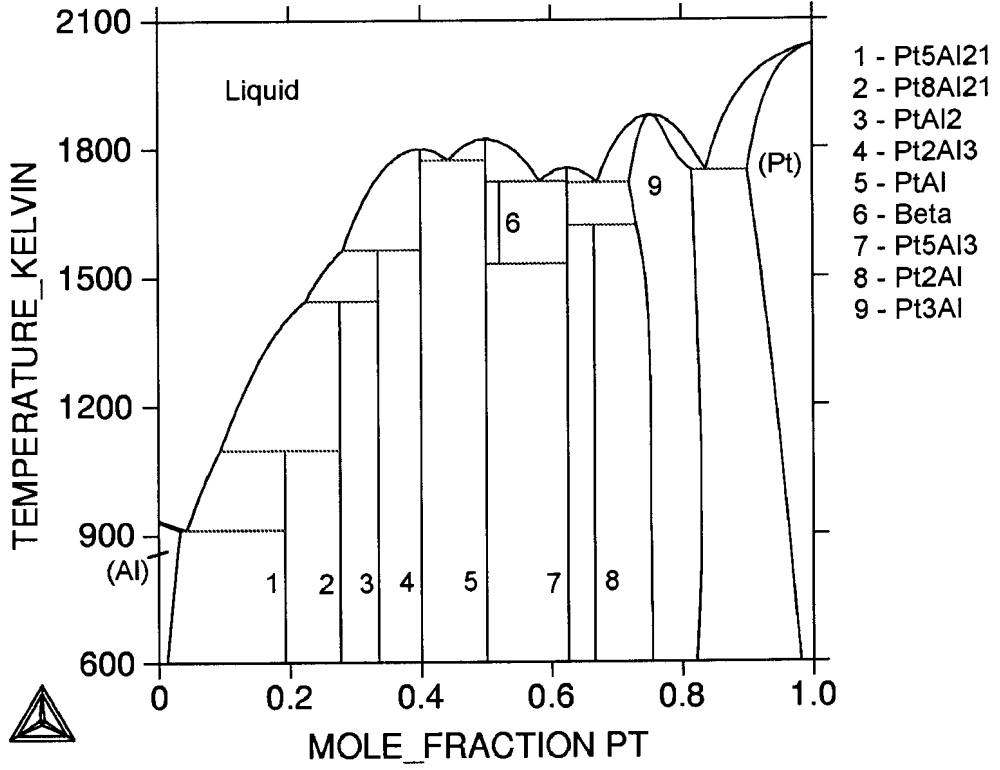


Figure 2. The calculated Al-Pt phase diagram.

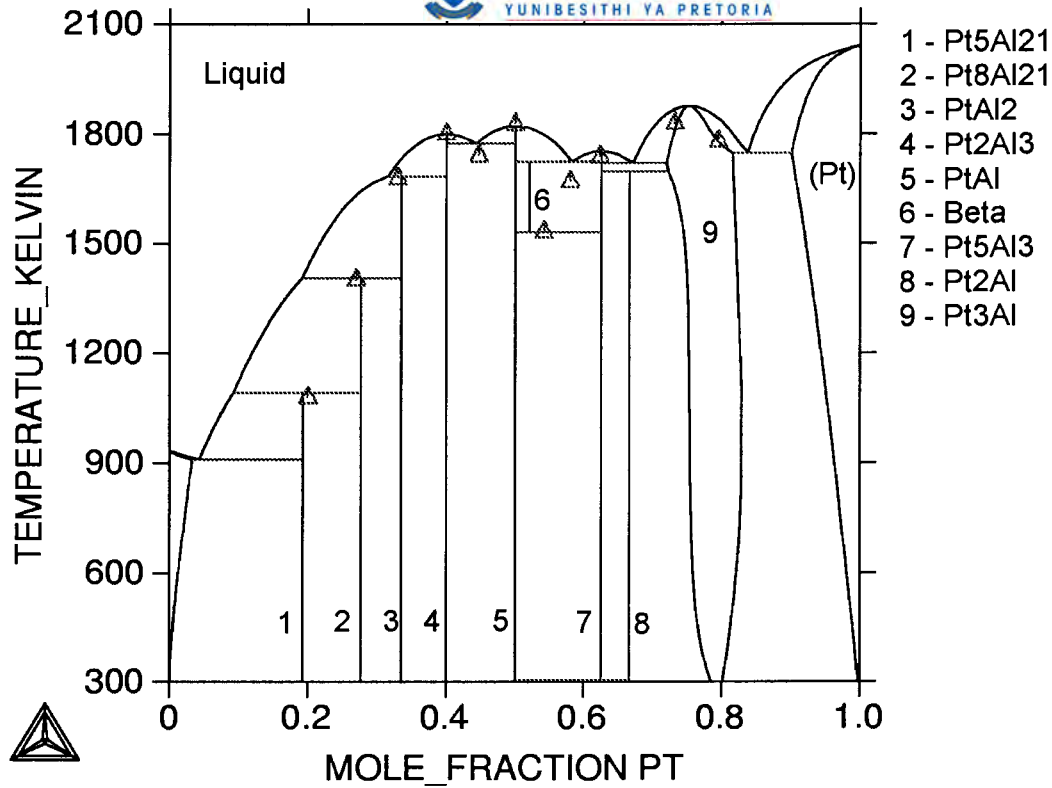


Figure 2. Comparison between the calculated phase diagram and experimental data [1986McA].

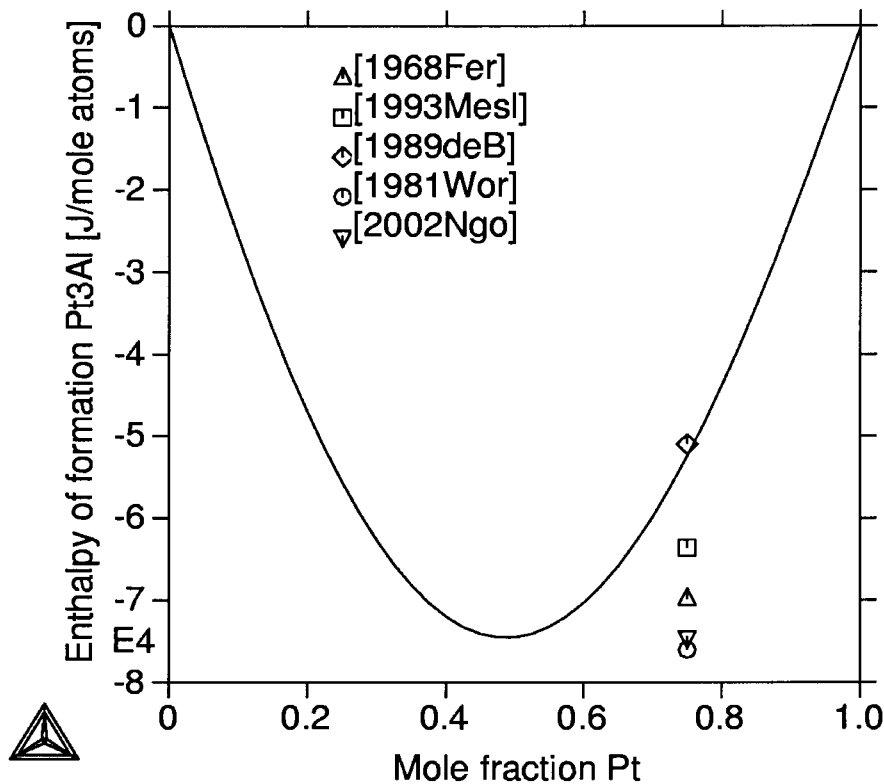


Figure 4. Comparison of the calculated, experimental [1968Fer, 1981Wor], Miedema estimated [1993Mes] and *ab initio* predicted [2002Ngo] enthalpy of formation at 298 K for the ordered Pt_3Al phase.

XRD study of phases in an investigation of the Al-Pt-Ru system. S.N.Prins^a, P.S. Boucher^a and L.A. Cornish^b, ^a CSIR-NML, PO Box 395, Pretoria 0001, RSA, ^b Physical Metallurgy Division, Mintek, Private Bag X3015, Randburg, 2125, RSA.

Keywords: Al-Pt-Ru, Pt-based alloys, XRD

As part of a study for the development of alloys based on Pt for high temperature applications [1], the Al-Pt-Ru phase diagram has been investigated. Both arc-melted and annealed samples have been characterised using scanning electron microscopy (SEM) with energy dispersive X-ray spectroscopy (EDS) [2]. The samples were annealed in argon at 600°C for 160 hours. The phases were initially identified by their compositions and morphology, and X-ray diffraction was used to identify the structures and verify the phase identification.

Bulk polished halves of the as-cast and annealed button samples were scanned in a Philips XRD with Cu K α radiation using a continuous scan from 4 to 90° 2 θ .

Initially, it was thought that the experimentally recorded spectra could be matched with standard spectra from the ICDD database [3] for the expected phases. However, many phases were not yet included in the ICDD database. Even for the binary phases that were in the database, the presence of the third element shifted the diffraction patterns of the phases significantly, rendering identification difficult, especially for non-cubic structures.

A lattice parameter refinement procedure was followed to identify the phases, as well as to calculate the modified lattice parameters for the phases. Where prototypes for the phases were given in the literature, and the prototype was included in the ICDD, the prototype structure was used as a starting point.

A ternary phase of composition \sim Ru₁₂Pt₁₅Al₇₃ was observed to be stable to room temperature. By employing a search-and-match method, it was found that the ternary phase exhibited a primitive cubic structure and lattice parameter of \sim 0.7721 nm, and was of similar type to IrAl_{2.75} and RhAl_{2.63}.

XRD confirmed most of the phase identification from the SEM/EDS results, and also showed that the \sim Ru₁₂Pt₁₅Al₇₃ phase was a true ternary phase, and not an extension of Ru₄Al₁₃ as initially thought.

The Platinum Development Initiative and Department of Science and Technology are acknowledged for supporting this work.

- [1] L.A. Cornish, J. Hohls, P.J. Hill, S.N. Prins, R. Süß and D.N. Compton, 34th International October Conference on Mining and Metallurgy Proceedings, Ed. Z.S. Markovic and D.T. Zivkovic, 545-550, 30 September – 3 October 2002, Bor Lake, Yugoslavia.
- [2] S.N. Prins, L.A. Cornish, P.S. Boucher and W.E. Stumpf, submitted to J. Alloys and Compounds.
- [3] International Center for Diffraction Data (ICDD). 'Powder Diffraction File', Pennsylvania, USA, 2001.



Thermodynamic Assessments of the Pt-Cr and Cr-Ru Systems with an Extrapolation into the Pt-Cr-Ru

U. Glatzel¹ and S.N. Prins²

¹University Jena, Loebdergraben 32, D - 07743 Jena, Germany

²CSIR-NML, PO Box 395, Pretoria, 0001, South Africa

A CALPHAD-like assessment of the Pt-Cr system has been carried out, starting with the data obtained from an assessment by Oikawa et al. [2001Oik]. The Pt₃Cr phase was not included in their assessment. A four sublattice model has been incorporated in order to add the L1₂ ordered Pt₃Cr phase. This phase shows an ordered-disordered transition from L1₂ to fcc at about 1403 K.

Within the Cr-Ru system a sigma phase (Strukturbericht D8b) has been modelled. The sigma model with 10:4:16 sites was used [2003Sun].

An extrapolation to the ternary system Pt-Cr-Ru has been made, with an emphasis on L1₂ ordered phases close to the Pt-rich side.

Financial assistance of the Department of Science and Technology, South Africa and the Platinum Development Initiative is gratefully acknowledged.

References

- [2001Oik] K. Oikawa, G.W. Qin, T. Ikeshoji, O. Kitakami, Y. Shimada, K. Ishida and K. Fukamichi, *J. Magnetism and Magnetic Materials* 236 (2001) 220-233
- [2003Sun] B. Sundman, private communication



A STUDY OF THE Pt-Al-Ru SYSTEM AT 600°C

S.N. Prins,* L.A. Cornish** and P.S. Boucher*

* CSIR-National Metrology Laboratory, PO Box 395, Pretoria, 0001, South Africa

** Physical Metallurgy Division, Mintek, Private Bag X3015, Randburg, 2125, South Africa

The Pt-Al-Ru system is being studied as part of a larger project to develop and optimise Pt-based alloys for high temperature use [1]. These alloys are based on a two-phase microstructure of $\sim\text{Pt}_3\text{Al}$ in a (Pt) matrix, analogous to the γ/γ' microstructure of Ni-based superalloys. Work has been done on the Pt-Al-Ru system [2,3] and the liquidus surface has been derived from as-cast alloys [3].

Six alloys were selected from the alloys so as to contain the phases of interest. The samples were sealed in silica tubes backfilled with argon and annealed at 600°C for 3 weeks. They were prepared metallographically and studied with a LEO 1525 SEM and Oxford INCA EDS. The phases were confirmed, as far as possible, using a Philips XRD with Cu K alpha radiation on solid samples.

The $\sim\text{Pt}_{51}:\text{Al}_{21}:\text{Ru}_{28}$ sample comprised coarse needles of (Ru) in a binary eutectic of fine (Ru) needles and $\sim\text{Pt}_3\text{Al}$. Compared to the as-cast sample, the fine needles had coarsened, and there were no traces of the (Pt) component. Thus the heat treatment had removed the ternary eutectic which appeared due to non-equilibrium cooling. There was precipitation of $\sim\text{Pt}_3\text{Al}$ in the coarse (Ru) needles; this indicated that the (Ru) solvus slopes to lower Ru contents at lower temperatures, and agrees with Obrowski's observations in the Al-Ru system [4].

The as-cast $\sim\text{Pt}_{25}:\text{Al}_{46}:\text{Ru}_{29}$ sample comprised very cored $\sim\text{RuAl}$ dendrites in a matrix of $\sim\text{PtAl} + \text{Pt}_5\text{Al}_3$ which had originated from solid state decomposition of the high temperature beta phase. The heat treated sample showed much reduced coring (Fig. 1) and coarsening in the matrix phases.

The $\sim\text{Pt}_{39}:\text{Al}_{52}:\text{Ru}_9$ sample in the as-cast condition had a complex structure that revealed primary formation of cored $\sim\text{RuAl}$ followed by the formation of PtAl and Pt_2Al_3 . The actual reactions were difficult to interpret since the PtAl and Pt_2Al_3 phases were extremely fine. Annealing at 600°C reduced the coring in $\sim\text{RuAl}$ and coarsened the microstructure so that a eutectic between $\sim\text{RuAl}$ and $\sim\text{PtAl}$ was revealed. The $\sim\text{PtAl}$ within the eutectic had a higher Ru content, and so had a slightly darker contrast as indicated by the arrow in Fig. 2.

As-cast $\sim\text{Pt}_{14}:\text{Al}_{54}:\text{Ru}_{32}$ was another complex sample and was not at equilibrium since it contained four phases: $\sim\text{RuAl}$, $\sim\text{RuAl}_2$, $\sim\text{PtAl}_2$, and $\sim\text{Ru}_{12}\text{Pt}_{15}\text{Al}_{73}$, a new ternary phase [3]. The annealed sample only had three phases: $\sim\text{RuAl}$, $\sim\text{RuAl}_2$ and $\sim\text{PtAl}_2$. In addition, there was precipitation of $\sim\text{RuAl}_2$ within $\sim\text{PtAl}_2$

The as-cast $\sim\text{Pt}_{28}:\text{Al}_{64}:\text{Ru}_8$ specimen contained dendrites of $\sim\text{Ru}_{12}\text{Pt}_{15}\text{Al}_{73}$ surrounded by $\sim\text{PtAl}_2$, in a eutectic comprising $\sim\text{PtAl}_2$ and $\sim\text{Ru}_{12}\text{Pt}_{15}\text{Al}_{73}$. In the annealed condition, there was much less of the $\sim\text{Ru}_{12}\text{Pt}_{15}\text{Al}_{73}$ phase and the eutectic had coarsened.

In the as-cast condition, the $\sim\text{Pt}_8:\text{Al}_{85}:\text{Ru}_7$ alloy had two distinct microstructures locally and the primary phase was different in each: $\sim\text{Ru}_{12}\text{Pt}_{15}\text{Al}_{73}$ and $\sim\text{Pt}_5\text{Al}_{21}$ respectively. The other phases were

$\sim\text{RuAl}_6$ and (Al). Although the annealed sample contained regions which appeared different, the $\sim\text{Pt}_5\text{Al}_{21}$ phase had disappeared, and the $\sim\text{RuAl}_6$ phase was not discerned. However, since the $\sim\text{Ru}_{12}\text{Pt}_{15}\text{Al}_{73}$ phase still showed coring, it is likely that the $\sim\text{RuAl}_6$ phase was still present and was in local equilibrium with the less Pt-rich composition of $\sim\text{Ru}_{12}\text{Pt}_{15}\text{Al}_{73}$, but too fine to detect.

The phase and alloys' EDS analyses were plotted and compared to the as-cast values. The alloys suffered minimal aluminium loss on annealing. Pt_3Al had lost all discernible Ru, which agrees with other work [2]. Similarly, RuAl_2 had negligible Pt after annealing, showing that the solubility for Pt decreases with temperature. The composition of $\sim\text{Ru}_{12}\text{Pt}_{15}\text{Al}_{73}$ moved to slightly lower Pt contents at lower temperatures. Two samples exhibited a similar and a higher Ru composition for the $\sim\text{PtAl}_2$ phase than in the as-cast samples, indicating that the solubility increased with temperature. Both the PtAl and Pt_2Al_3 phase compositions shifted to more stoichiometric values after annealing, indicating a contraction in phase width at lower temperatures. At 600°C , the penetration of the $\sim\text{RuAl}$ phase was reduced compared to the as-cast samples: from ~ 26 at. % Pt to ~ 22 at. % Pt. In addition, the phase width narrowed at lower temperatures.

Annealing the samples at 600°C equilibrated them to some degree; no sample had more than three phases, and the compositions had changed to more stoichiometric values. The only unexpected result was that the $\sim\text{PtAl}_2$ phase extended to higher ruthenium contents.

References

- [1] L.A. Cornish, J. Hohls, P.J. Hill, S.N. Prins, R. Süß and D.N. Compton, 34th International October Conference on Mining and Metallurgy Proceedings, Ed. Z.S. Markovic and D.T. Zivkovic, 545-550, 30 September - 3 October 2002, Bor Lake, Yugoslavia.
- [2] T. Biggs, P.J. Hill, L.A. Cornish and M.J. Witcomb, *J. Phase Equilibria*, 22 (2001) 214-215.
- [3] S.N. Prins, L.A. Cornish, P.S. Boucher and W.E. Stumpf, submitted to *J. Alloys and Compounds*.
- [4] W. Obrowski, *Metallwissenschaft und Technik* (Berlin), 17 (1960) 108-112.
- [5] This research was supported by the PDI and the DS&T, South Africa.

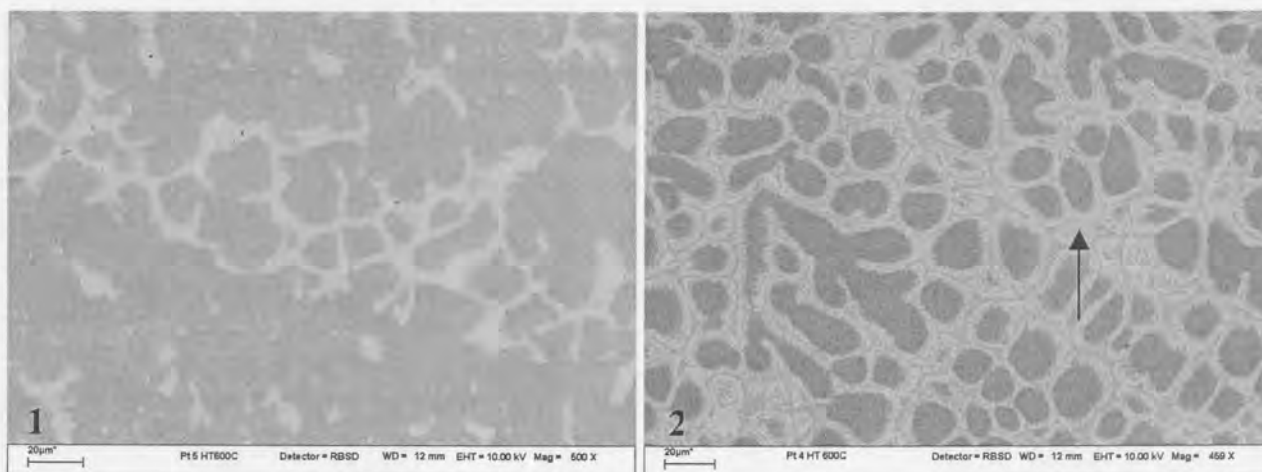


Fig. 1. $\sim\text{Pt}_{25}:\text{Al}_{46}:\text{Ru}_{29}$: BSE image showing $\sim\text{RuAl}$ (dark) in a matrix of $\sim\text{PtAl} + \text{Pt}_5\text{Al}_3$ (light).
Fig. 2. $\sim\text{Pt}_{39}:\text{Al}_{52}:\text{Ru}_9$: BSE image showing $\sim\text{RuAl}$ (dark), $\sim\text{PtAl}$ (light) and Pt_2Al_3 (medium grey).

Appendix B

XRD lattice parameter refinement on sample PAR4.

The XRD spectrum for sample PAR4 is shown in Figure 1, and the d-values and intensities of the spectrum as recorded on a Philips XRD are listed in Table 1.

From EDS analysis, it was proposed that the phases present in this sample are RuAl, PtAl and Pt₂Al₃. Initial XRD spectrum matching showed that PtAl₂ are possibly present in the sample. Furthermore, neither the PtAl nor Pt₂Al₃ phases are included in the ICDD. However, PdAl and Pd₂Al₃ are similar to PtAl and Pt₂Al₃, respectively, in crystal structure and lattice parameter and are included in the ICDD. The presence of the PtAl₂ phase found in the XRD is in contradiction to the EDS results. It was further found that it is difficult to distinguish between PtAl₂ and RuAl, since the standard diffraction patterns overlap almost completely.

For each of the four phases, a lattice refinement was done with the WinCell program [2000Raj]. To do the refinement, the hkl values for each phase and the observed corresponding two theta values (from Table 1) were entered into the program. WinCell does not take the peak intensities into account. An estimate of the lattice parameter is also entered.

The WinCell input screen for the PdAl phase is shown in Figure 2. The software then calculates through a non-linear regression the lattice parameter and the corresponding R² of the phase. The presence of a third element in the binary structures shifted the two theta values in some cases, and more than one attempt was then needed to identify the relevant two theta values to obtain the best R² value.

The WinCell output sheets for the four phases are attached. Output 2 is for PtAl₂, which is actually NOT present in the sample, but it is interesting to note that both RuAl and PtAl₂ gave a good fit (factor R at the bottom of each output sheet). As can be seen from the input values listed in Table 2, RuAl overlaps completely with PtAl₂. On closer investigation, comparing the input data with the ICDD standard reflections, the (311) reflection for PtAl₂ is absent. The (311) reflection for PtAl₂, which appeared at 51.010 two theta, initially gave a bad fit in the refinement and was removed. The pattern then gave a much better R² value. However, since this is a major reflection for the PtAl₂ phase and the (311) reflection should not have been removed in the first place. Following the EDS analysis that suggested RuAl, a good fit was obtained for RuAl. It can be seen that there are many overlaps and that the relative intensities of the reflections should be considered where doubt exists.

This shows the power of using lattice refinement to confirm the presence of the phase. However, care should be taken since WinCell does not take into account the intensities of the reflections. It also be stated that WinCell does not ensure that space group conditions are met, and the operator must check the selected hkl values to make sure that they are not conflicting the space group rules.

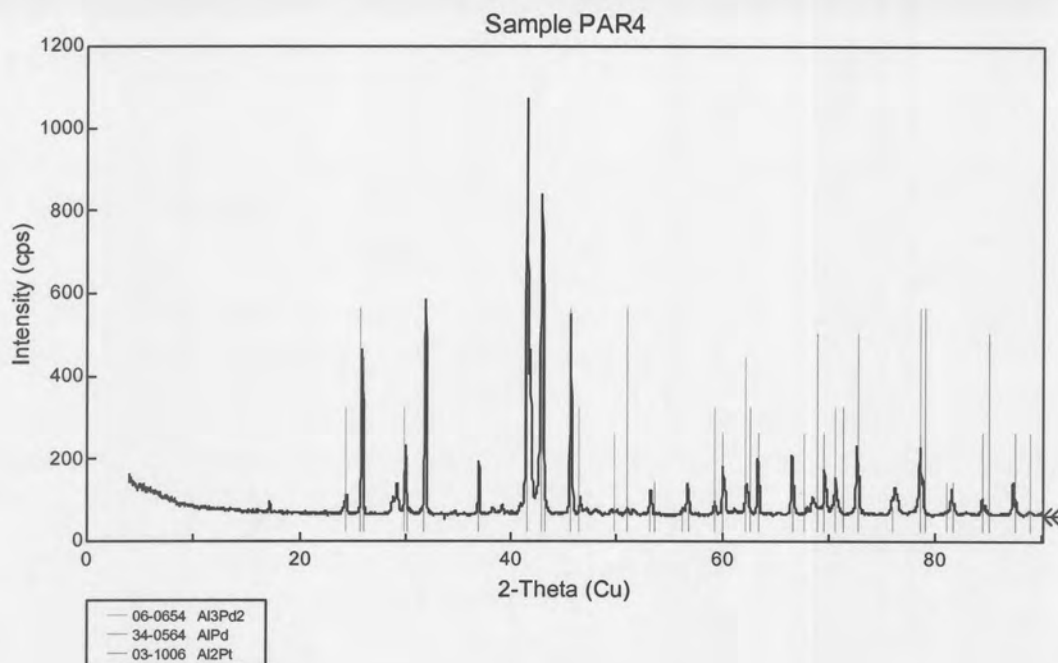


Figure 1. XRD spectrum for sample PAR4.

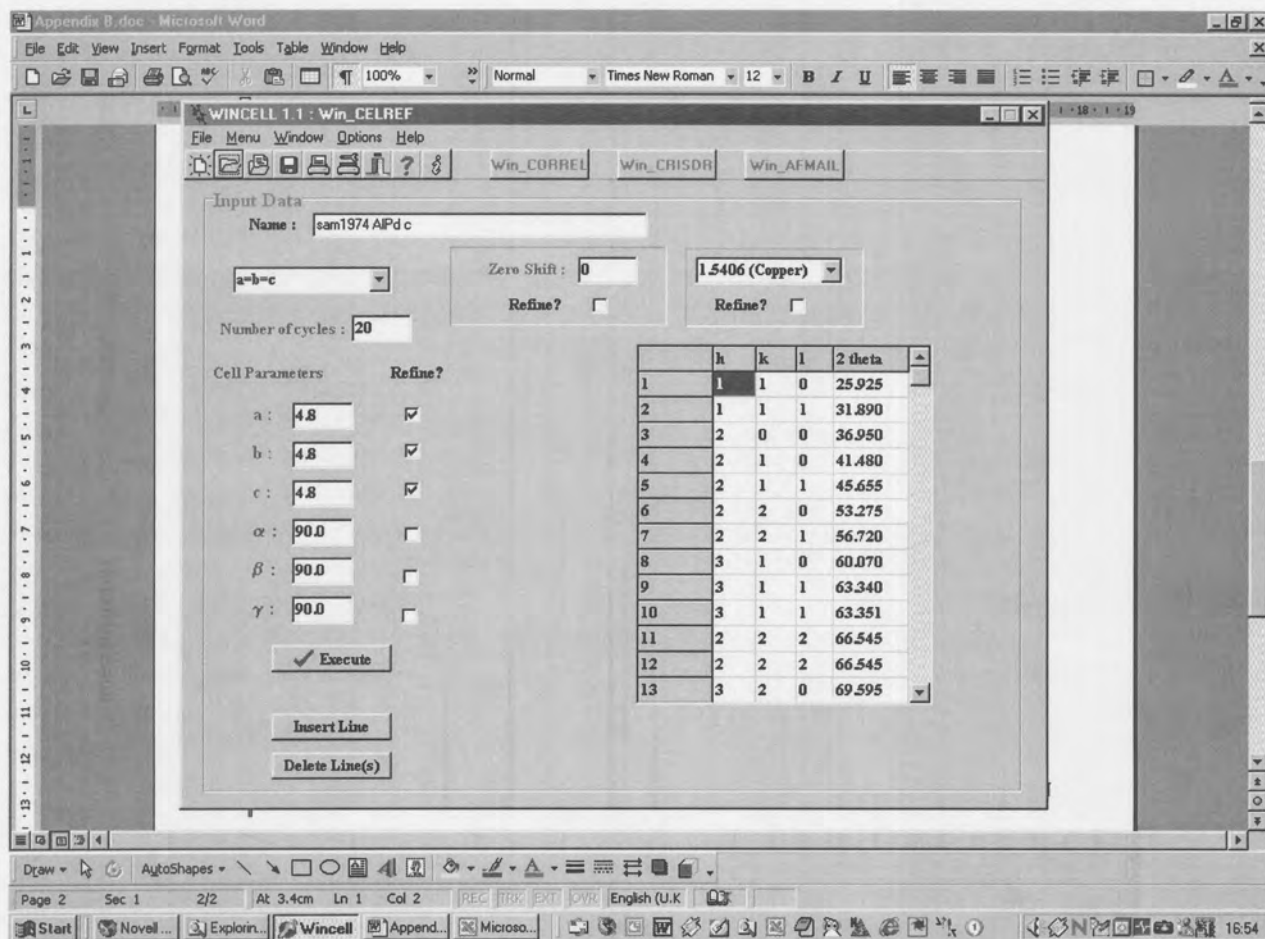


Figure 2. Input screen for the PdAl phase into WinCell.

Table 1. Comparison of WinCell input for RuAl and PtAl₂.

RuAl				PtAl ₂			
h	k	l	2 theta	h	k	l	2 theta
1	0	0	30.000	1	1	1	25.925
1	1	0	42.965	2	0	0	30.000
1	1	1	53.275	2	2	0	42.965
2	0	0	62.260	2	2	2	53.275
2	1	0	70.260	4	0	0	62.260
2	1	1	78.595	3	3	1	68.515
2	1	0	78.579	4	2	0	70.675
				4	2	2	78.595
				4	2	2	78.579
				5	1	1	84.360

Appendix C

Thermodynamic database for Al-Pt-Ru



This database was extrapolated from the binaries, and no ternary parameters have been optimised yet.

The metastable parameters for Pt-bcc and Pt-hcp were added to the bcc and hcp phase descriptions. Due to the additions to the disorder descriptions, the ordered phases had to be stabilised. Pt was added as a third element to the B2 sublattices and Ru was added to the L12 sublattices to stabilise these two phases in the ternary, but no interaction parameters were included for these additions.

No ternary parameters were included for any phases.

```
ELEMENT /- ELECTRON_GAS      0.0000E+00 0.0000E+00 0.0000E+00!
ELEMENT VA VACUUM            0.0000E+00 0.0000E+00 0.0000E+00!
ELEMENT AL FCC_A1            2.6982E+01 4.5773E+03 2.8322E+01!
ELEMENT PT FCC_A1            1.9508E+02 5.7237E+03 4.1631E+01!
ELEMENT RU HCP_A3            1.0107E+02 4.6024E+03 2.8535E+01!

FUNCTION GHSERPT  2.98150E+02 -7595.631+124.38828*T-24.5526*T*LN(T)
-.00248297*T**2-2.0138E-08*T**3+7974*T**(-1); 1.30000E+03 Y
-9253.174+161.52962*T-30.2527*T*LN(T)+.002321665*T**2-6.56947E-07*T**3
-272106*T**(-1); 2.04210E+03 Y
-222518.97+1021.2109*T-136.42269*T*LN(T)+.020501692*T**2
-7.60985E-07*T**3+71709819*T**(-1); 4.00000E+03 N!
FUNCTION GHSERRU  2.98150E+02 -7561.873+127.86623*T-22.914329*T*LN(T)
-.004062566*T**2+1.7641E-07*T**3+56377*T**(-1); 1.50000E+03 Y
-59448.103+489.51621*T-72.324122*T*LN(T)+.018726245*T**2
-1.952433E-06*T**3+11063885*T**(-1); 2.60700E+03 Y
-38588773+168610.52*T-21329.705*T*LN(T)+5.221639*T**2
-2.4024599E-04*T**3+1.3082993E+10*T**(-1); 2.74000E+03 Y
-55768.304+364.48231*T-51.8816*T*LN(T); 4.50000E+03 N!
FUNCTION GHSERAL  2.98140E+02 -7976.15+137.093038*T-24.3671976*T*LN(T)
-.001884662*T**2-8.77664E-07*T**3+74092*T**(-1); 7.00000E+02 Y
-11276.24+223.048446*T-38.5844296*T*LN(T)+.018531982*T**2
-5.764227E-06*T**3+74092*T**(-1); 9.33470E+02 Y
-11278.378+188.684153*T-31.748192*T*LN(T)-1.230524E+28*T**(-9);
2.90000E+03 N!
FUNCTION GHCPAL  2.98150E+02 +5481-1.799*T+GHSERAL#; 6.00000E+03 N!
FUNCTION GHCPPT  2.98150E+02 +2500+.1*T+GHSERPT#; 4.00000E+03 N!
FUNCTION GBCCPT  2.98150E+02 +15000-2.4*T+GHSERPT#; 4.00000E+03 N!
FUNCTION GBCCAL  2.98150E+02 +10083-4.813*T+GHSERAL#; 6.00000E+03 N
!
FUNCTION GBCCRU  2.98150E+02 +26500-6.2*T+GHSERRU#; 4.50000E+03 N!
FUNCTION GFCCRU  2.98150E+02 +12500-2.4*T+GHSERRU#; 4.50000E+03 N!
FUNCTION UAB     2.98150E+02 -13595+8.3*T; 6.00000E+03 N!
FUNCTION UPT3AL  2.98150E+02 +3*UAB#-3913; 6.00000E+03 N!
FUNCTION UPTAL   2.98150E+02 +4*UAB#; 6.00000E+03 N!
FUNCTION UPTAL3  2.98150E+02 +3*UAB#; 6.00000E+03 N!
FUNCTION UL0     2.98150E+02 +1412.8+5.7*T; 6.00000E+03 N!
```

FUNCTION USRO 2.98150E+02 +UAB#; 6.00000E+03 N!
 FUNCTION ULD0 2.98150E+02 -110531-22.9*T; 6.00000E+03 N!
 FUNCTION ULD1 2.98150E+02 -25094; 6.00000E+03 N!
 FUNCTION ULD2 2.98150E+02 21475; 6.00000E+03 N!
 FUNCTION DG0 2.98150E+02 +UPTAL3#+1.5*UPTAL#+UPT3AL#; 6.00000E+03
 N!
 FUNCTION DG1 2.98150E+02 +2*UPTAL3#-2*UPT3AL#; 6.00000E+03 N!
 FUNCTION DG2 2.98150E+02 +UPTAL3#-1.5*UPTAL#+UPT3AL#; 6.00000E+03
 N!
 FUNCTION UN_ASS 2.98150E+02 0.0; 3.00000E+02 N!

TYPE_DEFINITION % SEQ *!
 DEFINE_SYSTEM_DEFAULT ELEMENT 2!
 DEFAULT_COMMAND DEF_SYS_ELEMENT VA!

PHASE LIQUID:L % 1 1.0!
 CONSTITUENT LIQUID:L :AL,PT,RU : !

PARAMETER G(LIQUID,AL;0) 2.98140E+02 +11005.553-11.840873*T
 +7.9401E-20*T**7+GHSERAL#; 9.33600E+02 Y
 +10481.974-11.252014*T+1.234264E+28*T**(-9)+GHSERAL#; 2.90000E+03 N
 REF0!

PARAMETER G(LIQUID,PT;0) 2.98150E+02 +12520.614+115.11473*T
 -24.5526*T*LN(T)-.00248297*T**2-2.0138E-08*T**3+7974*T**(-1); 6.00000E+02
 Y
 +19019.913+33.017485*T-12.351404*T*LN(T)-.011543133*T**2+9.30579E-07*T**3
 -600885*T**(-1); 2.04210E+03 Y
 +1404.968+205.86191*T-36.5*T*LN(T); 4.00000E+03 N REF0!

PARAMETER G(LIQUID,RU;0) 2.98140E+02 +19918.743+119.467485*T
 -22.9143287*T*LN(T)-.004062566*T**2+1.7641E-07*T**3+56377*T**(-1);
 8.00000E+02 Y
 +50827.232-179.818561*T+19.539341*T*LN(T)-.026524167*T**2
 +1.667839E-06*T**3-3861125*T**(-1); 2.60700E+03 Y
 -17161.807+349.673561*T-51.8816*T*LN(T); 4.50000E+03 N REF0!

PARAMETER G(LIQUID,AL,RU;0) 2.98150E+02 -73000-14*T; 6.00000E+03 N
 REF0!

PARAMETER G(LIQUID,AL,RU;1) 2.98150E+02 -56000; 6.00000E+03 N REF0!

PARAMETER G(LIQUID,AL,PT;0) 2.98150E+02 -352536+114.8*T; 6.00000E+03
 N REF0!

PARAMETER G(LIQUID,AL,PT;1) 2.98150E+02 +68566-53*T; 6.00000E+03 N
 REF0!

PARAMETER G(LIQUID,PT,RU;0) 2.98140E+02 -8000; 4.00000E+03 N REF0!

\$ THIS PHASE HAS A DISORDERED CONTRIBUTION FROM BCC_A2

PHASE B2 % 3.5 .5 3!

CONSTITUENT B2 :AL%,PT,RU,VA : AL,PT%,RU%,VA : VA% : !

PARAMETER G(B2,AL:AL:VA;0) 298.15 0; 6000 N!

PARAMETER G(B2,PT:AL:VA;0) 2.98150E+02 +V50#+V51#*T; 6.00000E+03 N
 REF0!

PARAMETER G(B2,RU:AL:VA;0) 2.98150E+02 -87600; 6.00000E+03 N REF0!

PARAMETER G(B2,VA:AL:VA;0) 298.15 0; 6000 N!

PARAMETER G(B2,AL:PT:VA;0) 2.98150E+02 +V50#+V51#*T; 6.00000E+03 N

REF0 !

PARA G(B2,PT:PT:VA;0) 298.15 0; 6000 N!
 PARA G(B2,RU:PT:VA;0) 298.15 0; 6000 N!
 PARA G(B2,VA:PT:VA;0) 298.15 0; 6000 N!
 PARAMETER G(B2,AL:RU:VA;0) 2.98150E+02 -87600; 6.00000E+03 N REF0 !
 PARA G(B2,PT:RU:VA;0) 298.15 0; 6000 N!
 PARA G(B2,RU:RU:VA;0) 298.15 0; 6000 N!
 PARA G(B2,VA:RU:VA;0) 298.15 0; 6000 N!
 PARA G(B2,AL:VA:VA;0) 298.15 0; 6000 N!
 PARA G(B2,PT:VA:VA;0) 298.15 0; 6000 N!
 PARA G(B2,RU:VA:VA;0) 298.15 0; 6000 N!
 PARA G(B2,VA:VA:VA;0) 298.15 0; 6000 N!
 PARAMETER G(B2,AL,RU:AL:VA;0) 2.98150E+02 -73000; 6.00000E+03 N

REF0 !

PARAMETER G(B2,AL,PT:AL:VA;0) 2.98150E+02 +V52#+V53#*T; 6.00000E+03 N REF0 !

PARAMETER G(B2,AL,PT,RU:AL:VA;0) 2.98150E+02 +V54#+V55#*T; 6.00000E+03 N REF0 !

PARAMETER G(B2,AL:AL,RU:VA;0) 2.98150E+02 -73000; 6.00000E+03 N REF0 !

PARAMETER G(B2,AL:AL,PT:VA;0) 2.98150E+02 +V52#+V53#*T; 6.00000E+03 N REF0 !

PARAMETER G(B2,AL:AL,PT,RU:VA;0) 2.98150E+02 +V54#+V55#*T; 6.00000E+03 N REF0 !

PARAMETER G(B2,VA:AL,RU:VA;0) 2.98150E+02 +80*T; 6.00000E+03 N REF0 !

PARAMETER G(B2,VA:AL,PT:VA;0) 2.98150E+02 +80*T; 6.00000E+03 N REF0 !

PARAMETER G(B2,VA:PT,RU:VA;0) 2.98150E+02 +80*T; 6.00000E+03 N REF0 !

PARAMETER G(B2,AL,RU:VA:VA;0) 2.98150E+02 +80*T; 6.00000E+03 N REF0 !

PARAMETER G(B2,AL,PT:VA:VA;0) 2.98150E+02 +80*T; 6.00000E+03 N REF0 !

PARAMETER G(B2,PT,RU:VA:VA;0) 2.98150E+02 +80*T; 6.00000E+03 N REF0 !

TYPE_DEFINITION & GES AMEND_PHASE_DESCRIPTION B2 DIS_PART BCC_A2,,!

TYPE_DEFINITION 'GES A_P_D BCC_A2 MAGNETIC -1.0 4.00000E-01 !

PHASE BCC_A2 %&' 2 1 3 !

CONSTITUENT BCC_A2 :AL,PT,RU,VA : VA : !

PARAMETER G(BCC_A2,AL:VA;0) 2.98140E+02 +GBCCAL#; 2.90000E+03 N REF0 !

PARAMETER G(BCC_A2,PT:VA;0) 2.98140E+02 +GBCCPT#; 4.50000E+03 N REF0 !

PARAMETER G(BCC_A2,RU:VA;0) 2.98140E+02 +GBCCRU#; 4.50000E+03 N REF0 !

PARA G(BCC_A2,VA:VA;0) 298.15 0; 6000 N!

PARAMETER G(BCC_A2,AL,RU:VA;0) 2.98150E+02 -176000+32*T; 6.00000E+03 N REF0 !

PARAMETER G(BCC_A2,AL,VA:VA;0) 2.98150E+02 +120*T; 6.00000E+03 N REF0 !

PARAMETER G(BCC_A2,PT,RU:VA;0) 2.98140E+02 0.0; 4.00000E+03 N REF0 !

PARAMETER G(BCC_A2,PT,RU:VA;1) 2.98140E+02 0.0; 4.00000E+03 N REF0 !

PARAMETER G(BCC_A2,PT,VA:VA;0) 2.98150E+02 +120*T; 6.00000E+03 N REF0 !

PARAMETER G(BCC_A2,RU,VA:VA;0) 2.98150E+02 +120*T; 6.00000E+03 N REF0 !

PHASE BETA % 2.48 .52 !

CONSTITUENT BETA :AL : PT : !

PARAMETER G(BETA,AL:PT;0) 2.98150E+02 -92723+23.88*T+.48*GHSERAL#
+.52*GHSERPT#; 6.00000E+03 N REF0 !

TYPE_DEFINITION (GES A_P_D FCC_A1 MAGNETIC -3.0 2.80000E-01 !
PHASE FCC_A1 %(2 1 1 !
CONSTITUENT FCC_A1 :AL,PT,RU : VA : !

PARAMETER G(FCC_A1,AL:VA;0) 2.98140E+02 +GHSERAL#; 2.90000E+03 N REF0 !
PARAMETER G(FCC_A1,PT:VA;0) 2.98150E+02 +GHSERPT#; 4.50000E+03 N REF0 !
PARAMETER G(FCC_A1,RU:VA;0) 2.98150E+02 +4938.127+125.46623*T
-22.914329*T*LN(T)-.004062566*T**2+1.7641E-07*T**3+56377*T**(-1);
1.50000E+03 Y
-46948.103+487.11621*T-72.324122*T*LN(T)+.018726245*T**2
-1.952433E-06*T**3+11063885*T**(-1); 2.60700E+03 Y
-38576273+168608.12*T-21329.705*T*LN(T)+5.221639*T**2-2.4024599E-04*T**3
+1.3082993E+10*T**(-1); 2.74000E+03 Y
-43268.304+362.08231*T-51.8816*T*LN(T); 4.50000E+03 N REF0 !
PARAMETER G(FCC_A1,AL,PT:VA;0) 2.98150E+02 +ULD0#+DG0#+1.5*USRO#;
6.00000E+03 N REF0 !
PARAMETER G(FCC_A1,AL,PT:VA;1) 2.98150E+02 +ULD1#+DG1#; 6.00000E+03
N REF0 !
PARAMETER G(FCC_A1,AL,PT:VA;2) 2.98150E+02 +ULD2#+DG2#-1.5*USRO#;
6.00000E+03 N REF0 !
PARAMETER G(FCC_A1,AL,PT,RU:VA;0) 2.98150E+02 +V10#+V11#*T;
6.00000E+03 N REF0 !
PARAMETER G(FCC_A1,AL,RU:VA;0) 2.98150E+02 -10000-10*T; 6.00000E+03
N REF0 !
PARAMETER G(FCC_A1,PT,RU:VA;0) 2.98140E+02 -17249.639-2.745999*T;
4.00000E+03 N REF0 !
PARAMETER G(FCC_A1,PT,RU:VA;1) 2.98140E+02 13184.597; 4.00000E+03 N
REF0 !

TYPE_DEFINITION) GES A_P_D HCP_A3 MAGNETIC -3.0 2.80000E-01 !
PHASE HCP_A3 %) 2 1 .5 !
CONSTITUENT HCP_A3 :AL,PT,RU : VA : !

PARAMETER G(HCP_A3,AL:VA;0) 2.98140E+02 +GHCPAL#; 2.90000E+03 N REF0 !
PARAMETER G(HCP_A3,PT:VA;0) 2.98150E+02 -5095.631+124.48828*T
-24.5526*T*LN(T)-.00248297*T**2-2.0138E-08*T**3+7974*T**(-1); 1.30000E+03
Y
-6753.174+161.62962*T-30.2527*T*LN(T)+.002321665*T**2-6.56947E-07*T**3
-272106*T**(-1); 2.04210E+03 Y
-220018.97+1021.3109*T-136.42269*T*LN(T)+.020501692*T**2-7.60985E-07*T**3
+71709819*T**(-1); 4.00000E+03 N REF0 !
PARAMETER G(HCP_A3,RU:VA;0) 2.98150E+02 +GHSERRU#; 4.50000E+03 N REF0 !
PARAMETER G(HCP_A3,AL,RU:VA;0) 2.98150E+02 -105000+30*T; 6.00000E+03
N REF0 !
PARAMETER G(HCP_A3,AL,PT:VA;0) 2.98150E+02 50000; 6.00000E+03 N
REF0 !
PARAMETER G(HCP_A3,AL,PT,RU:VA;0) 2.98150E+02 +V15#+V16#*T;
6.00000E+03 N REF0 !
PARAMETER G(HCP_A3,PT,RU:VA;0) 2.98140E+02 +8629.8149-7.889606*T;

4.00000E+03 N REF0 !

PARAMETER G(HCP_A3,PT,RU:VA;1) 2.98140E+02 -5283.9355; 4.00000E+03 N
REF0 !

\$ THIS PHASE HAS A DISORDERED CONTRIBUTION FROM FCC_A1
TYPE_DEFINITION * GES AMEND_PHASE_DESCRIPTION L12 DIS_PART FCC_A1,,,
PHASE L12 %* 5 .25 .25 .25 .25 1 !
CONSTITUENT L12 :AL,PT,RU : AL,PT,RU : AL,PT,RU : AL,PT,RU : VA : !

PARAMETER G(L12,AL:AL:AL:AL:VA;0) 298.15 0; 6000 N!
PARAMETER G(L12,PT:AL:AL:AL:VA;0) 2.98150E+02 +UPTAL3#; 3.00000E+03 N
REF0 !

PARAMETER G(L12,RU:AL:AL:AL:VA;0) 298.15 0; 6000 N!
PARAMETER G(L12,AL:PT:AL:AL:VA;0) 2.98150E+02 +UPTAL3#; 3.00000E+03 N
REF0 !

PARAMETER G(L12,PT:PT:AL:AL:VA;0) 2.98150E+02 +UPTAL#; 3.00000E+03 N
REF0 !

PARAMETER G(L12,RU:PT:AL:AL:VA;0) 298.15 0; 6000 N!

PARAMETER G(L12,AL:RU:AL:AL:VA;0) 298.15 0; 6000 N!

PARAMETER G(L12,PT:RU:AL:AL:VA;0) 298.15 0; 6000 N!

PARAMETER G(L12,RU:RU:AL:AL:VA;0) 298.15 0; 6000 N!

PARAMETER G(L12,AL:AL:PT:AL:VA;0) 2.98150E+02 +UPTAL3#; 3.00000E+03 N
REF0 !

PARAMETER G(L12,PT:AL:PT:AL:VA;0) 2.98150E+02 +UPTAL#; 3.00000E+03 N
REF0 !

PARAMETER G(L12,RU:AL:PT:AL:VA;0) 298.15 0; 6000 N!

PARAMETER G(L12,AL:PT:PT:AL:VA;0) 2.98150E+02 +UPTAL#; 3.00000E+03 N
REF0 !

PARAMETER G(L12,PT:PT:PT:AL:VA;0) 2.98150E+02 +UPT3AL#; 3.00000E+03 N
REF0 !

PARAMETER G(L12,RU:PT:PT:AL:VA;0) 298.15 0; 6000 N!

PARAMETER G(L12,AL:RU:PT:AL:VA;0) 298.15 0; 6000 N!

PARAMETER G(L12,PT:RU:PT:AL:VA;0) 298.15 0; 6000 N!

PARAMETER G(L12,RU:RU:PT:AL:VA;0) 298.15 0; 6000 N!

PARAMETER G(L12,AL:AL:RU:AL:VA;0) 298.15 0; 6000 N!

PARAMETER G(L12,PT:AL:RU:AL:VA;0) 298.15 0; 6000 N!

PARAMETER G(L12,RU:AL:RU:AL:VA;0) 298.15 0; 6000 N!

PARAMETER G(L12,AL:PT:RU:AL:VA;0) 298.15 0; 6000 N!

PARAMETER G(L12,PT:PT:RU:AL:VA;0) 298.15 0; 6000 N!

PARAMETER G(L12,RU:PT:RU:AL:VA;0) 298.15 0; 6000 N!

PARAMETER G(L12,AL:RU:RU:AL:VA;0) 298.15 0; 6000 N!

PARAMETER G(L12,PT:RU:RU:AL:VA;0) 298.15 0; 6000 N!

PARAMETER G(L12,RU:RU:RU:AL:VA;0) 298.15 0; 6000 N!

PARAMETER G(L12,AL:AL:AL:PT:VA;0) 2.98150E+02 +UPTAL3#; 3.00000E+03 N
REF0 !

PARAMETER G(L12,PT:AL:AL:PT:VA;0) 2.98150E+02 +UPTAL#; 3.00000E+03 N
REF0 !

PARAMETER G(L12,RU:AL:AL:PT:VA;0) 298.15 0; 6000 N!

PARAMETER G(L12,AL:PT:AL:PT:VA;0) 2.98150E+02 +UPTAL#; 3.00000E+03 N
REF0 !

PARAMETER G(L12,PT:PT:AL:PT:VA;0) 2.98150E+02 +UPT3AL#; 3.00000E+03 N
REF0 !

PARAMETER G(L12,RU:PT:AL:PT:VA;0) 298.15 0; 6000 N!

PARAMETER G(L12,AL:RU:AL:PT:VA;0) 298.15 0; 6000 N!



PARA G(L12,PT:RU:AL:PT:VA;0) 298.15 0; 6000 N!
PARA G(L12,RU:RU:AL:PT:VA;0) 298.15 0; 6000 N!
PARAMETER G(L12,AL:AL:PT:PT:VA;0) 2.98150E+02 +UPTAL#; 3.00000E+03 N
REF0 !
PARAMETER G(L12,PT:AL:PT:PT:VA;0) 2.98150E+02 +UPT3AL#; 3.00000E+03 N
REF0 !
PARA G(L12,RU:AL:PT:PT:VA;0) 298.15 0; 6000 N!
PARAMETER G(L12,AL:PT:PT:PT:VA;0) 2.98150E+02 +UPT3AL#; 3.00000E+03 N
REF0 !
PARA G(L12,PT:PT:PT:PT:VA;0) 298.15 0; 6000 N!
PARA G(L12,RU:PT:PT:PT:VA;0) 298.15 0; 6000 N!
PARA G(L12,AL:RU:PT:PT:VA;0) 298.15 0; 6000 N!
PARA G(L12,PT:RU:PT:PT:VA;0) 298.15 0; 6000 N!
PARA G(L12,RU:RU:PT:PT:VA;0) 298.15 0; 6000 N!
PARA G(L12,AL:AL:RU:PT:VA;0) 298.15 0; 6000 N!
PARA G(L12,PT:AL:RU:PT:VA;0) 298.15 0; 6000 N!
PARA G(L12,RU:AL:RU:PT:VA;0) 298.15 0; 6000 N!
PARA G(L12,AL:PT:RU:PT:VA;0) 298.15 0; 6000 N!
PARA G(L12,PT:PT:RU:PT:VA;0) 298.15 0; 6000 N!
PARA G(L12,RU:PT:RU:PT:VA;0) 298.15 0; 6000 N!
PARA G(L12,AL:RU:RU:PT:VA;0) 298.15 0; 6000 N!
PARA G(L12,PT:RU:RU:PT:VA;0) 298.15 0; 6000 N!
PARA G(L12,RU:RU:RU:PT:VA;0) 298.15 0; 6000 N!
PARA G(L12,AL:AL:AL:RU:VA;0) 298.15 0; 6000 N!
PARA G(L12,PT:AL:AL:RU:VA;0) 298.15 0; 6000 N!
PARA G(L12,RU:AL:AL:RU:VA;0) 298.15 0; 6000 N!
PARA G(L12,AL:PT:AL:RU:VA;0) 298.15 0; 6000 N!
PARA G(L12,PT:PT:AL:RU:VA;0) 298.15 0; 6000 N!
PARA G(L12,RU:PT:AL:RU:VA;0) 298.15 0; 6000 N!
PARA G(L12,AL:RU:AL:RU:VA;0) 298.15 0; 6000 N!
PARA G(L12,PT:RU:AL:RU:VA;0) 298.15 0; 6000 N!
PARA G(L12,RU:RU:AL:RU:VA;0) 298.15 0; 6000 N!
PARA G(L12,AL:AL:PT:RU:VA;0) 298.15 0; 6000 N!
PARA G(L12,PT:AL:PT:RU:VA;0) 298.15 0; 6000 N!
PARA G(L12,RU:AL:PT:RU:VA;0) 298.15 0; 6000 N!
PARA G(L12,AL:PT:PT:RU:VA;0) 298.15 0; 6000 N!
PARA G(L12,PT:PT:PT:RU:VA;0) 298.15 0; 6000 N!
PARA G(L12,RU:PT:PT:RU:VA;0) 298.15 0; 6000 N!
PARA G(L12,AL:RU:PT:RU:VA;0) 298.15 0; 6000 N!
PARA G(L12,PT:RU:PT:RU:VA;0) 298.15 0; 6000 N!
PARA G(L12,RU:RU:PT:RU:VA;0) 298.15 0; 6000 N!
PARA G(L12,AL:AL:RU:RU:VA;0) 298.15 0; 6000 N!
PARA G(L12,PT:AL:RU:RU:VA;0) 298.15 0; 6000 N!
PARA G(L12,RU:AL:RU:RU:VA;0) 298.15 0; 6000 N!
PARA G(L12,AL:PT:RU:RU:VA;0) 298.15 0; 6000 N!
PARA G(L12,PT:PT:RU:RU:VA;0) 298.15 0; 6000 N!
PARA G(L12,RU:PT:RU:RU:VA;0) 298.15 0; 6000 N!
PARA G(L12,AL:RU:RU:RU:VA;0) 298.15 0; 6000 N!
PARA G(L12,PT:RU:RU:RU:VA;0) 298.15 0; 6000 N!
PARA G(L12,RU:RU:RU:RU:VA;0) 298.15 0; 6000 N!
PARAMETER G(L12,AL,PT:*.*:VA;0) 2.98150E+02 +UL0#; 3.00000E+03 N
REF0 !
PARAMETER G(L12,*.AL,PT:*.*:VA;0) 2.98150E+02 +UL0#; 3.00000E+03 N
REF0 !
PARAMETER G(L12,*.*.AL,PT:*.VA;0) 2.98150E+02 +UL0#; 3.00000E+03 N

REF0 !

PARAMETER G(L12,*,*:AL,PT:VA;0) 2.98150E+02 +UL0#; 3.00000E+03 N

REF0 !

PARAMETER G(L12,AL,PT:AL,PT:*:VA;0) 2.98150E+02 +USRO#; 3.00000E+03

N REF0 !

PARAMETER G(L12,AL,PT:*,AL,PT:*,VA;0) 2.98150E+02 +USRO#; 3.00000E+03

N REF0 !

PARAMETER G(L12,AL,PT:*,AL,PT:VA;0) 2.98150E+02 +USRO#; 3.00000E+03

N REF0 !

PARAMETER G(L12,*,AL,PT:AL,PT:*,VA;0) 2.98150E+02 +USRO#; 3.00000E+03

N REF0 !

PARAMETER G(L12,*,AL,PT:*,AL,PT:VA;0) 2.98150E+02 +USRO#; 3.00000E+03

N REF0 !

PARAMETER G(L12,*,*:AL,PT:AL,PT:VA;0) 2.98150E+02 +USRO#; 3.00000E+03

N REF0 !

PHASE PT2AL % 2.334 .666 !

CONSTITUENT PT2AL :AL : PT : !

PARAMETER G(P2AL,AL:PT;0) 2.98150E+02 -84989+24.9*T+.334*GHSERAL#
+.666*GHSERPT#; 6.00000E+03 N REF0 !

PHASE PT2AL3 % 2.6 .4 !

CONSTITUENT PT2AL3 :AL : PT : !

PARAMETER G(P2AL3,AL:PT;0) 2.98150E+02 -89885+21.5*T+.6*GHSERAL#
+.4*GHSERPT#; 6.00000E+03 N REF0 !

PHASE PT5AL21 % 2.8077 .1923 !

CONSTITUENT PT5AL21 :AL : PT : !

PARAMETER G(P5AL21,AL:PT;0) 2.98150E+02 -56873+14.8*T+.8077*GHSERAL#
+.1923*GHSERPT#; 6.00000E+03 N REF0 !

PHASE PT5AL3 % 2.375 .625 !

CONSTITUENT PT5AL3 :AL : PT : !

PARAMETER G(P5AL3,AL:PT;0) 2.98150E+02 -87260+24*T+.375*GHSERAL#
+.625*GHSERPT#; 6.00000E+03 N REF0 !

PHASE PT8AL21 % 2.7242 .2759 !

CONSTITUENT PT8AL21 :AL : PT : !

PARAMETER G(P8AL21,AL:PT;0) 2.98150E+02 -82342+23.7*T+.7242*GHSERAL#
+.2759*GHSERPT#; 6.00000E+03 N REF0 !

PHASE PTAL % 2.5 .5 !

CONSTITUENT PTAL :AL : PT : !

PARAMETER G(PTAL,AL:PT;0) 2.98150E+02 -94071+24.1*T+.5*GHSERAL#
+.5*GHSERP#; 6.00000E+03 N REF0 !

PHASE PTAL2 % 2.666 .334 !
CONSTITUENT PTAL2 :AL : PT : !

PARAMETER G(PTAL2,AL:PT;0) 2.98150E+02 -87898+23.3*T+.666*GHSERAL#
+.334*GHSERP#; 6.00000E+03 N REF0 !

PHASE RU2AL3 % 3 3 2 1 !
CONSTITUENT RU2AL3 :AL : AL,RU : RU,VA : !

PARAMETER G(RU2AL3,AL:AL:RU;0) 2.98150E+02 +V15#+5*GBCCAL#+GBCCRU#;
6.00000E+03 N REF0 !
PARAMETER G(RU2AL3,AL:RU:RU;0) 2.98150E+02 -312631.26+30.5*T+3*GBCCAL#
+3*GBCCRU#; 6.00000E+03 N REF0 !
PARAMETER G(RU2AL3,AL:AL:VA;0) 2.98150E+02 +5*GBCCAL#; 6.00000E+03
N REF0 !
PARAMETER G(RU2AL3,AL:RU:VA;0) 2.98150E+02 -312631.26+30.5*T+3*GBCCAL#
+2*GBCCRU#; 6.00000E+03 N REF0 !

PHASE RU4AL13 % 3.6275 .235 .1375 !
CONSTITUENT RU4AL13 :AL : RU : AL,VA : !

PARAMETER G(RU4AL13,AL:RU:AL;0) 2.98150E+02 -35100+1.65*T+.765*GHSERAL#
+.235*GHSERRU#; 6.00000E+03 N REF0 !
PARAMETER G(RU4AL13,AL:RU:VA;0) 2.98150E+02 -35100+1.65*T
+.6275*GHSERAL#+.235*GHSERRU#; 6.00000E+03 N REF0 !

PHASE RUAL2 % 3 2 1 1 !
CONSTITUENT RUAL2 :AL : RU : AL,RU,VA : !

PARAMETER G(RUAL2,AL:RU:AL;0) 2.98150E+02 -136500+8*T-1368.28
+3*GHSERAL#+GHSERRU#; 6.00000E+03 N REF0 !
PARAMETER G(RUAL2,AL:RU:RU;0) 2.98150E+02 -136500+8*T-1412.41
+2*GHSERAL#+2*GHSERRU#; 6.00000E+03 N REF0 !
PARAMETER G(RUAL2,AL:RU:VA;0) 2.98150E+02 -136500+8*T+2*GHSERAL#
+GHSERRU#; 6.00000E+03 N REF0 !

PHASE RUAL6 % 2 6 1 !
CONSTITUENT RUAL6 :AL : RU : !

PARAMETER G(RUAL6,AL:RU;0) 2.98150E+02 -156000+7*T+6*GHSERAL#+GHSERRU#;
6.00000E+03 N REF0 !

LIST_OF_REFERENCES
NUMBER SOURCE
REF0
!